UNIVERSITAT DE BARCELONA

Vibrational properties of ZnO, group III-nitrides and dilute nitride alloys

Esther Alarcón Lladó

Vibrational Properties of ZnO, Group III-Nitrides and Dilute Nitride Alloys

Esther Alarcón Lladó

Thesis submitted for the degree of
Doctor of Philosophy

Barcelona, July 2009

Tutor: Blas Garrido Fernández
Departament d'Electrònica
Universitat de Barcelona

Director: Lluís Artús Surroca
Insitut Jaume Almera
Consell Superior d'Investigacions Científiques

Programm: Microsystems, Sensors and Actuators
2005/2007

The works presented in this PhD thesis have been developed at the Optical Properties of Solids Group from the Institut Jaume Almera (CSIC) under the FPI Programm of the Ministerio de Educación y Ciencia. The research work has been funded by the projects MAT2004-00664 and MAT2007-63617.

Els treballs que es presenten a aquesta Tesi s'han dut a terme al Laboratori de Propietats Òptiques dels Sòlids de l'Institut Jaume Almera (CSIC) dins el programa de Formació de Personal Investigador (FPI) del *Ministerio de Educación y Ciencia*. La recerca s'ha enmarcat dins els projectes MAT2004-00664 i MAT2007-63617.

Acknowledgements

Primer de tot, voldria agrair al Dr. Lluís Artús Surroca, director d'aquesta tesi, haver dipositat la seva confiança en mi (fins i tot més que jo mateixa) i posar a la meva disposició els mitjans per dur a terme aquest treball. Gràcies a ell he tingut la oportunitat de donar la meva primera passa en el món de la recerca, a la qual ha aconseguit que m'hi *enganxi*. Ell m'ha ajudat a conèixer la ciència d'arreu i formar-ne part. Finalment, a en Lluís li he d'agraïr la seva tenacitat, dedicació i paciència durant aquests anys.

Voldria donar un agraïment molt especial al Dr. Ramon Cuscó Cornet i al Dr. Jordi Ibáñez Insa per totes les aportacions en aquest treball. Ells han sigut els meus *gurús*. Tant l'un com l'altre han mostrat una gran paciència en contestar les meves inesgotables preguntes i en escoltar les meves idees extravagants. Ells han aconseguit que gaudís de la física i que les hores passéssin sense adonar-me'n fent càlculs i anàlisis. Per altra banda, a en Jordi no puc deixar d'agraïr-li haver pogut gaudir d'una amistat com la seva i d'innumerables xerrades i consells, els quals m'han ajudat tant a nivell personal. En Jordi m'ha ajudat a mantenir el meu esperit revolucionari, m'ha fet veure que encara queda molt a fer, i que tot és possible.

Querría agradecer al Prof. Juan Jiménez López (Dpto de Física de la Matéria Condensada de la Universidad de Valladolid) por el suministro de muestras de ZnO, que son la base de un tercio de ésta tesis. También quiero agradecerle esas pequñas charlas en las conferencias donde nos hemos encontrado y donde me encontraba ligeramente perdida.

Quiero agradecer al Prof. Enrique Calleja Pardo (ISOM-Departamento de Ingeniería Electrónica de la Universidad Politécnica de Madrid) por el suministro de muestras de nitruros. As well, I would like to acknowledge Prof. Mark Hopkinson (Department of Electronic and Electrical Engineering at the University of Sheffield, UK) and Dr. Sergei Novikov (School of Physics and Astronomy at the University of Nottingham, UK) for the supply of samples.

También quiero agradecer al Prof. Germán González Díaz y a Pablo Fernández (Dpto de Física Aplicada III de la Universidad Complutense de Madrid) por no desesperar tras implantar casi toda la tabla periódica en muestras milimétricas. En general, quiero agradecer a todo el grupo de Láminas Delgadas y Microelectrónica por su paciencia, acogida y explicaciones durante esa fugaz visita a Madrid.

I would like to aknowledge Prof. Jürgen Christen for giving me the opportunity to join their group for a few months at the University Otto-von-Güericke (Magdeburg, Germany) and the opportunity to attend for the first time a scientific meeting conference. I owe him all the faith he put in me when I had to give my first talk in public. I would also like to thank Dr. Frank Bertram, who tought me everything I know about cathodoluminescence and electron microscopy. I am very grateful for him having the patience to answer all my questions (eventhough I was always standing). Besides, I would like to mention all the people from Magdeburg, Martin Noltemeyer, Alex Franke, Sebastian Metzner (Basti), Anja Dempelwolf, Barbara Bastek and again Frank Bertram (Berti), for showing me the beauty of living in Magdeburg and working in their team.

En aquests agraïments, no voldria pas oblidar-me dels meus companys de despatx, Rafael Bartolí (en Rafa), Josep Elvira (en Pep), Miquel àngel González i Jesús Parga. Gràcies a ells he après el funcionament de les institucions públiques estatals. Ha sigut un plaer conviure amb vosaltres (i disculpeu que us hagui donat tant la tabarra!).

Tampoc voldria oblidar-me dels dos veïns que he tingut al llarg d'aquesta tesi. Primer de tot, a l'avui dia Dr. David Pastor Pastor, al qual li dec un principi de doctorat ple d'alegries, experiències, bon humor i humanitat. El dia a dia de treball al seu costat es feia més lleuger i agradable. La seva inquietud per oportunitat que m'ha donat de conèixer la ciència d'arreu i formar-ne part.la ciència va fer que m'adonés de com aquesta m'agrada a mi també. *Te acuerdas de cuándo comía de tu mano...?* Segon, a en Marc Ollé, que tot i la seva visita fugaç, li agraeixo haver-me donat un punt de vista diferent, peculiar i pràctic de les coses.

En aquests agraïments no hi poden faltar tots els companys que han estat al meu costat durant anys, ja siguin coneguts de fa temps o persones que m'ha permès conèixer el doctorat durant aquests últims quatre anys.

Per començar, agraeixo al Dr. Sergi Hernández tota la seva vitalitat, dinamisme

i esperit de Cornellà que m'ha animat i ajudat en tants moments desesperants.

Vull donar les gràcies als companys de facultat, tots ells unes grans persones amb els quals sempre és un plaer quedar i escoltar les seves opinions i històries. D'entre molts voldria destacar en Martí, l'Anna, en Dani, la Cristina, la Laia, la Sònia, la Mariona, en David, ... no pararia! He tingut una gran sort d'haver-vos trobat. Grcies a vosaltres, fer la carrera de física no ha sigut només obtenir un títol.

No hi poden faltar tampoc els meus amics d'Arenys (de Munt!), els quals m'han donat sempre suport, alegries, confiança, consells i amor al llarg de molts anys (tot i el meu *frikisme*). A més a més, a la Lu també li vull donar les gràcies per aconseguir sempre que les meves presentacions siguin presentables.

En aquests agraïments no puc oblidar d'anomenar les persones amb qui he conviscut al llarg dels anys. Primer de tot, a la meva família. Sense el seu suport i confiança no hagués ni tan sols fet una carrera i encara menys un doctorat. A ells i al seu amor els dec felicitat, el que sóc avui dia i el que seré demà.

Segon, les meves estupendes companyes de pis, en especial l'Anna i la Dàmaris. He tingut la gran sort de conèixer a fons dos bellíssimes persones, de les quals n'he après i disfrutat. Ha estat un plaer haver convisut amb vosaltres tots aquests anys de facultat i doctorat.

Tercer (i espero que últim), he de donar les gràcies a en Sergi per haver tingut la paciència de suportar-me durant tant de temps i seguir estant al meu costat dia rere dia. M'has animat en tots els moments baixos i pujat l'autoestima quan altres la reduïen. Sense el teu suport no podria seguir dins d'aquest món tan difícil de la recerca. Sense el teu amor no podria seguir.

Aquesta tesi us la vull dedicar a tots vosaltres, que heu fet possible que tot això hagi tirat endavant.

A tots els que m'estimo,

Contents

"Give me the place to stand,
and I shall move the earth."

Archimedes of Syracuse

1 Introduction

In the recent years, researchers working in the field of microelectronics have paid much attention to find new materials to satisfy the non-stop demanding market. The revolution in the electronic industry that took place over the last decades has changed our daily life in a way never envisaged when the transistor was invented. This was a breakthrough in the discovery and basic understanding of semiconductors which enabled mankind to develop the electronics that we have become so used to over the years.

The comercial market in integrated circuits for computing, power switching, data storage and communication is basically dominated by silicon (Si). The fabrication technology of this semiconductor has come to fruition over the years resulting in low-cost manufacture Si industry. However, semiconducting Si has an indirect band-gap, which makes gallium arsenide (GaAs) better suited for optoelectronic devices, such as laser diodes and solar cells, apart from the fact that GaAs presents higher carrier mobilities and higher effective carrier velocities than Si [1].

Nevertheless, the entire spectral range cannot be covered by GaAs-based materials. Indeed, bandgap engineering allows to develop GaAs-based optoelectronic devices from the infrared to the yellow. Therefore, investigations on materials with larger band gaps to pursue the UV/blue/green emitter devices are essential.

Silicon carbide (SiC), zinc selenide (ZnSe), gallium nitride (GaN) and zinc oxide (ZnO) are some examples of wide band gap materials (band gaps larger than ~ 2 eV). In addition to their interesting band gap energy for operating in the UV/blue spec-

tral range, they offer tremendous advantages in terms of power capability, radiation sensitivity as well as in terms of high temperature and high frequency operation [2].

The interest in wide band-gap materials began to grow in the late eighties, when the first comercial blue LED was made of SiC [3]. Leaving aside SiC and Diamond, which have inderect band-gaps and consequently show a reduced optical efficiency, there are three main types of wide band-gap semiconductors: group II chalcogenides, such as ZnSe; group II oxides, such as ZnO; and group III nitrides, like GaN. In the early nineties, the first pulsed blue laser diode was obtained with ZnSe [4]. Despite advances on this material, the degradation of ZnSe-based devices is still a challenge due to the weak ionic bonds of the compound [5–7].

Since then GaN has recieved most attention in the research areas of blue/UV lasers and LEDs. The first high brightness blue-UV LED was achieved by Shuji Nakamura in 1993 by using InGaN as emitter material [8]. By contrast, interest in ZnO appeared few years later, when new growth technologies were developed for the fabrication of high quality single crystal and epitaxial layers. During the last decade, high quality large-area bulk [9, 10], films [11–16] and ZnO nanostructures [17] have been achieved. After being used for many years in the cosmetic industry, as gas sensor and in transistors, ZnO was thought to be a good candidate for optoelectronic applications. The first UV emission of ZnO was obtained by Zu *et al.* [18] in 1997 for ZnO microcrystalline thin films.

Both GaN and ZnO have very close properties. While the band gap of ZnO at room temperature is 3.37 eV, that of GaN is 3.39 eV. Since their lattice parameters are also very similar, they can be used as suitable substrates for epitaxial growth to each other. Although ZnO and GaN -based devices cover almost the same wavelegth range, ZnO is expected to enable the fabrication of lower threshold laser diode devices, using excitons to operate at higher efficiencies and temperatures. Indeed, the exciton binding energy of ZnO is about 60 meV, which is twice larger than that of GaN (26 meV), [2] and paves the way for an intense near-band-endge excitonic emission at room and higher temperatures. So far, optically pumped UV lasing have been demonstrated at room temperature using highly textured ZnO films [19].

Besides, in the past decade numerous studies have been made on both growth and application of low-dimensional ZnO structures [20]. These structures are promising candidates for biosensors, UV detectors, and single-chip devices [17]. Nevertheless, one important problem should be overcome before ZnO could potentially make inroads into the world of optoelectronics: to obtain reproducible *p*-type conductive layers. It is believed that defects intrinsic to the crystal compensate *p*-type

Figure 1.1: Christmas lighting with GaN-based blue LEDs in Tokyo Midtown. Source: *www.eurotechnology.com*, December 2008.

dopants [21–23]. In fact, interstitial zinc and oxygen vacancies have been demonstrated to have low formation entalpies [24]. Despite all the progress that has been made in *p*-type ZnO, a reliable and reproducible high quality *p*-type conductive layers have not been achieved yet [20]. In order to overcome this bottleneck and to control the material properties, a clear understanding of the physical processes in doped ZnO is necessary. Also, the obtaintion of high-quality ZnO with low *n*-type background conductivity is a pursued aim.

In spite of the great interest of ZnO, researchers have not ceased to investigate III-nitrides. Quite the opposite, III-nitride semiconductors are recognized, at present, as the most important technological material system for the fabrication of optoelectronic devices operating in the green, blue, and UV spectral regions. Actually, the world's highest output blue-violet laser diode, which has been recently produced by Sanyo, is based on GaN [25].

To extend the fabrication of detectors and emitters operating deeper in the UV spectral range we must rely on other nitride systems as active layers. One of the main candidates is the AlGaN system [26]. When adding aluminium to GaN, the

band-gap energy varies from 3.39 to 6.2 eV (band gap of hexagonal AlN), being direct for any Al content [27]. AlGaN/GaN heterostructures are commonly used for large power HFETs and HEMTs [28–31]. AlGaN is also very attractive for its feasibility to be integrated into the Si technology [32]. The main drawback of the AlGaN alloy system is the presence of strain, threading dislocations, inversion domains and hexagonal dips on the surface, which worsen the electronic and optoelectronic properties of the layers [33].

Another potential candidate for band-gap engineering is boron. Similar to the AlGaN alloy, BGaN is expected to have a larger energy band-gap than gallium nitride since the band gap of BN at room temperature is 5.5 eV. With the proper fraction of boron, the alloy system is lattice mismatched to 6H-SiC substrates. However, the large lattice mismatch between the two binaries GaN and BN, makes difficult to grow single phase BGaN for boron compositions above 2% [34–36]. This ternary alloy is highly novel and in a development stage yet. Few data are available on the physical properties of this new system. Taking into account the increasing interest on BGaN alloys, it seems likely that higher quality layers having higher boron concentration will be produced soon.

On the other hand, not only GaN alloying with group III species is interesting, but also it is of interest to introduce group-V atoms into GaN. Since the manufacturing costs of GaAs-based components are low, their processing techniques are well developed, and many advances have been made in the nitride-technology, bridge the gap between the wide band-gap nitrides and medium band-gap arsenides was the natural progression. If GaNAs alloys could be grown over the whole composition range, they could be used for optical devices operating from the ultraviolet (0.4 μm) to the infra-red (2 μm).

The introduction of arsenic into the GaN lattice was found to cause a localized state in the valence-band of the GaN matrix, which results in a band gap reduction with a large negative bowing in the band gap energy [37, 38]. It is worth noting that blue luminescence intensity of one order of magnitude stronger than the band edge emission in undoped samples has been reported in As-doped GaN prepared by ion implantation and in GaNAs films grown by metal organic vapor phase epitaxy [39], which corroborates the potential applications of these compounds. Besides, As acts as a surfactant in GaN, which improves device performance. However, the growth of ordered GaNAs alloys is not a trivial issue and only small amounts of As have been successfully incorporated before phase separation occurs [38]. Theoretical calcula-

tions suggest that the incorporation of As may be strongly favored by increasing the Ga flux during growth [40].

Likewise, the addition of nitrogen to GaAs could have been thought to result in an increase of medium band-gap of gallium arsenide. Surprisingly, Weyers *et.al.* in 1992 [41] found the opposite effect when added small amounts of nitrogen to GaAs, thus resulting in a pronounced reduction of the band gap. This unusual behavior sparked considerable interest from a fundamental physics point of view as well as for potential narrow-gap applications. The band gap reduction has been observed even at nitrogen fraction as low as 0.0032% [41]. These new hybrid alloys with unusual physical properties have become known as *dilute nitrides*. The interest on the study of dilute nitrides has increased unceasingly. Many early epilayers presented low optical efficiency due to poor crystal quality [42], which is hardly surprising in a new material system. The main drawback is that the addition of N into GaAs alloys notoriously reduces the crystal quality. The big difference in size between N and As introduces strain into the lattice, which severely compromises the functionality of the material. To compensate the small atomic size of N, In is introduced into the GaAsN system. This causes an additional reduction in the band-gap energy and makes InGaAsN a promising material for optoelectronics in the telecommunication spectral range (1.3-1.5μm) [43]. Besides, when the In mole fraction is three times larger than the nitrogen fraction, this quaternary alloy results lattice-matched to GaAs [43]. This makes this quaternary alloy very suitable for the GaAs technology, once a good knowledge of its physical properties is achieved.

Although impressive results have already been demonstrated and the prospects of any of these materials look very promising, a large amount of research and development work still remains to be carried out. Further research work is required to better understand the mechanisms ruling their physical properties, to improve growth systems and to consequently optimize device performance.

The phonon spectrum of any of these materials is one of their most fundamental characteristics. Raman spectroscopy is a powerful non-destructive technique well suited to probe the vibrational properties of crystals. Raman measurements can give information about the crystal quality [44–46] as well as to analyze more specific aspects of the lattice dynamics, such as isotopic effects [47–50], anharmonicity [49, 51], phonon lifetimes [52], defects and their local environment [53–55]. In alloys and heterostructures, Raman is extremely useful to reveal information about the alloying, strain and intermixing status [56]. Besides, in the presence of free carriers

it provides information about carrier-phonon interactions and phonon-assisted optical transitions [57], which are of great importance for device performance. Therefore, a study of the lattice dynamics of these materials is not only of fundamental interest but results in a better understanding of structural parameters responsible for the efficiency in devices for microelectronics, optoelectronics, heat transport, quantum electronics, and even superconductivity.

1.1 This thesis

This thesis is focused on the vibrational properties of semiconductors of interest for optoelectronic devices in both the UV (ZnO and GaN-related alloys) and telecommunication spectral range (GaAsN and InGaAsN). For this purpose Raman spectroscopy is used as the characterization technique to probe their lattice dynamics. Raman selection rules and peak widths will give us information about crystal quality. We will assess the degree of incorporated impurities in a host lattice and their local enviroment. Also, we will deal with the interaction between phonons and free carriers in doped semiconductors.

While the crystal structure of dilute nitrides is the cubic zinc blende, ZnO and GaN can grow in both zinc blende and in the hexagonal wurtzite structures. **Chapter II**, introduces the zinc-blende and wurtzite structures and their basic vibrational properties. Next, a review of the theoretical aspects of the Raman scattering process in crystals is described, from both a semi classical and a quantum-mechanical point of view.

Chapter III describes the equipment used to perform Raman scattering measurements. Other vital equipment, such as low-temperature stages, is also reported.

The results obtained during my PhD and their discussion is presented from **chapters IV** to **VI**. In particular, **chapter IV** is a deep insight into the vibrational properties of high-quality bulk ZnO. High-quality bulk ZnO has become available only very recently and has not been studied extensively. An accurate study of the first and second order Raman modes of hydrothermal bulk ZnO is shown. Temperature dependent Raman scattering measurements were performed for understanding the basic lattice dynamics in ZnO. Theoretical modeling of the temperature dependence of the phonon line widths, frequencies and lifetimes is presented. Also, ion implantation-induced lattice damage in bulk ZnO is assessed by means of disorder activated Raman modes. Next, the origin of certain vibrational modes in N-doped ZnO is discussed.

The results were used to cease with the existing controversy with these modes.

Although GaN-based devices are in a much advanced level of development than that based on ZnO, nitride systems still need further research in growth methods and impurity incorporation. In this regard, **chapter V** is focused on the vibrational properties of GaN-related materials. First, we discuss how the III/V ratio in the Molecular Beam Epitaxy growth affects the cubic and hexagonal GaN crystal quality. Also, we investigate the III/V ratio effects in the introduction of arsenic impurities into the GaN lattice. A deep study of the optical phonon modes of the ternary AlGaN system and the two binaries GaN and AlN is performed. Since Raman efficiency of AlGaN is very low, IR transmission measurements at oblique incidence is assessed as a complementary tool for the analysis of AlGaN thin films. Optical phonons behavior of the BGaN alloy system is investigated as a function of boron content. We observe alloying effects for this novel BGaN system.

Chapter VI discusses the vibrational properties of dilute nitrides by means of Raman scattering. First, the optical phonon behavior of strain-free GaAsN is presented, and its relationship with alloying effects and disorder is discussed. Afterwards, heavily doped GaAsN samples are investigated. In particular, we study how the free carrier oscillations couple to the lattice vibrations. A non-destructive way to find the electron effective mass, mobility and carrier density of GaAsN is obtained. The feasibility of the BAC model to calculate optical effective masses is assessed. Finally, the best GaAs substrate orientation to grow InGaAsN thin films by Molecular Beam Epitaxy is also investigated by means of Raman scattering.

To conclude, the last two chapters summarize the results of the work presented in this thesis and the current topics under study are introduced. These studies involve the Raman spectra of ZnO nanostructures, the introduction of Mn to GaN (which is of interest for spintronic applications), and carrier-phonon interactions in the narrow band-gap InN and GaInAsSb semiconductors.

References

[1] Z. I. Alferov, "The double heterostructure: Concept and its application in physics, electronics and technology," 2000. Nobel Lecture.

[2] K. Takahashi, A. Yoshikawa, and A. Sandhu, *Wide Band Gap Semiconductors: Fundamental properties and modern photonic and electronic devices*. Springer, Berlin, Germany, 2007.

[3] `http://www.cree.com/about/milestones.asp`.

[4] M. A. Haase, J. Qiu, J. M. DePuydt, and H. Cheng *Appl. Phys. Lett.*, vol. 59, p. 1272, 1991.

[5] G. C. Hua, N. Otsuka, D. C. Grillo, Y. Fan, J. Han, M. D. Ringle, R. L. Gunshor, M. Hovinen, and A. V. Nurmikko *Appl. Phys. Lett.*, vol. 65, p. 1331, 1994.

[6] S. Gundel, D. Albert, J. Nurberger, and W. Faschinger *Phys. Rev. B*, vol. 60, p. R16271, 1999.

[7] A. Ishibashi *J. Cryst. Growth*, vol. 159, p. 555, 1996.

[8] S. Nakamura, T. Mukai, and N. Iwasa, 1993. United Stated Patent.

[9] M. Suscavage, M. Harris, D. Bliss, P. Yip, S. Q. Wang, D. Schwall, L. Bouthillete, J. Bailey, M. Callahan, D. C. Look, D. C. Reynolds, R. L. Jones, and C. W. Litton *MRS Internet J. Nitride Semicond. Res.*, vol. 4S1, p. G3.40, 1999.

[10] D. C. Look, D. C. Reynolds, J. R. Sizelove, R. Jones, C. W. Litton, G. Cantwell, and W. C. Harsch *Solid State Commun.*, vol. 105, p. 399, 1998.

[11] Y. Chen, D. M. Bagnall, H. J. Koh, K. T. Park, K. Hiraga, Z. Zhu, and T. Yao *J. Appl. Phys.*, vol. 84, p. 3912, 1998.

[12] P. Fons, K. Iwata, S. Niki, A. Yamada, and K. Matsubara *J. Cryst. Growth*, vol. 201/202, p. 627, 1999.

[13] R. D. Vispute, V. Talyansky, Z. Trajanovic, S. Choopun, M. Downes, R. P. Sharma, T. Venkatesan, M. C. Woods, R. T. Lareau, K. A. Jones, and A. A. Iliadis *Appl. Phys. Lett.*, vol. 70, p. 2735, 1997.

[14] M. Kasuga and S. Ogawa *Jpn. J. Appl. Phys.*, vol. 22, p. 794, 1983.

[15] A. M. P. Santos and E. J. P. Santos *Matt. Lett.*, vol. 61, p. 3432, 2007.

[16] J. S. Park, S. K. Hong, T. Minegishi, I. H. Im, S. H. Park, T. Hanada, J. H. Shang, M. W. Cho, and T. Yao *Appl. Surf. Science*, vol. 254, p. 7786, 2008.

[17] Z. L. Wang *Mat. Today*, vol. 7, p. 26, 2004.

[18] P. Zu, Z. K. Tang, G. K. L. Wong, M. Kawasaki, A. Ohtomo, H. Koinuma, and Y. Segawa *Solid State Commun.*, vol. 103, p. 459, 1997.

[19] Y. Chen, N. T. Tuan, Y. Segawa, H. J. Ko, S. K. Hong, and T. Yao *Appl. Phys. Lett.*, vol. 78, p. 1469, 2001.

[20] C. Jagadish and S. J. Pearton, eds., *Zinc Oxide, Bulk, Thin Films and Nanostructures*. Elsevier, Oxford, UK, 2006.

[21] S. B. Zhang, S. H. Wei, and A. Zunger *Phys. Rev. B*, vol. 63, p. 075205, 2001.

[22] A. Janotti *Am. Phys. Soc. Annual March Meeting*, p. S18018, 2005.

[23] T. . Barnes, K. Olson, and C. A. Wolden *Appl. Phys. Lett.*, vol. 86, p. 112112, 2005.

[24] D. C. Look, J. Hemsky, and J. Sizelove *Phys. Rev. Lett.*, vol. 82, p. 2552, 1999.

[25] *Compund Semiconductor*, vol. 14, pp. No. 10, 309, 2008.

[26] S. Nakamura and G. Fasol, *The Blue Laser Diode*. Springer, Berlin, Germany, 1997.

[27] W. Shan, J. W. Ager, K. M. Yu, W. Walukiewicz, E. E. Haller, M. C. Martin, W. R. McKinney, and W. Yang *Appl. Phys. Lett.*, vol. 85, p. 8505, 1999.

[28] R. Gaska, Q. Chen, J. Yang, A. Osinsky, M. Asif Khan, and M. S. Shur *Electron Dev. Lett.*, vol. 18, p. 492, 1997.

[29] S. Yoshida, D. Wang, and M. Ichikawa *Jpn. J. Appl. Phys.*, vol. 41, p. L820, 2002.

[30] A. Jiménez, J. M. Tirado, A. F. B. na, E. M. noz, E. Calleja, Z. Bougrioua, and I. Moerman *Appl. Phys. Lett.*, vol. 82, p. 4827, 2003.

[31] U. K. Mishra, P. Parkin, and Y. F. Wu *IEEE Proceedings*, vol. 90, p. 1022, 2002.

[32] P. Javorka, A. Alam, M. Marso, M. Wolter, J. Kuzmik, A. Fox, M. Heuken, and P. Kordoc *Microelectronics J.*, vol. 34, p. 435, 2003.

[33] H. Amano and I. Akasaki *Opt. Mater.*, vol. 19, p. 219, 2002.

[34] C. H. Wei and J. H. Edgar *J. Cryst. Growth*, vol. 217, p. 109, 2000.

[35] L. K. Teles, J. Furthmuller, L. M. R. Scolfaro, A. Tabata, J. R. Leite, F. Bechstedt, T. Frey, D. J. As, and K. Lischka *Physica E*, vol. 13, p. 1086, 2002.

[36] A. Ougazzaden, S. Gautier, C. Sartel, N. Maloufi, J. Martin, and F. Jomard *J. Cryst. Growth*, vol. 298, p. 316, 2007.

[37] B. Monemar *J. Phys. Condens. Matter*, vol. 13, p. 7011, 2001.

[38] A. Kimura *Appl. Phys. Lett.*, vol. 84, p. 1489, 2004.

[39] A. J. Winser, S. V. Novikov, C. S. Davis, T. S. Cheng, C. T. Foxon, and I. Harrison *Appl. Phys. Lett.*, vol. 77, p. 2506, 2000.

[40] C. G. Van de Walle and J. Neugebauer *Appl. Phys. Lett.*, vol. 76, p. 1009, 2000.

[41] M. Weyers and H. Ando *Jpn. J. Appl. Phys.*, vol. 31, p. L853, 1992.

[42] E. K. Rao, A. Ougazzaden, Y. Le Bellego, and M. Juhel *Appl. Phys. Lett.*, vol. 72, p. 1409, 1998.

[43] M. Pessa, C. S. Peng, T. Jouhti, E. M. Pavelescu, W. Li, S. Karirinne, H. Liu, and O. Okhotnikov *IEE Proceedings- Optoelectronics*, vol. 150, p. 12, 2003.

[44] N. Hasuike, H. Fukumura, K. Kisoda, H. Matsui, H. Saeki, and H. Tabata *J. Phys. Condens. Matter*, vol. 16, p. S5807, 2004.

[45] W. Limmer, W. Ritter, R. Sauer, B. Mensching, C. Liu, and B. Rauschenbach *Appl. Phys. Lett.*, vol. 72, p. 2589, 1988.

[46] D. Pastor, R. Cuscó, L. Artús, G. González-Díaz, S. Fernández, and E. Calleja *Semicond. Sci. Technol.*, vol. 20, p. 374, 2005.

[47] J. M. Zhang, T. Ruf, M. Cardona, O. Ambacher, M. Stutzmann, J. M. Wagner, and F. Bechsted *Phys. Rev. B*, vol. 56, p. 14399, 1997.

[48] A. Gobel, T. Ruf, C. . Lin, M. Cardona, J. C. Merle, and M. Joucla *Phys. Rev. B*, vol. 56, p. 210, 1997.

[49] J. Serrano, F. J. Manjón, A. H. Romero, F. Widulle, R. Lauck, and M. Cardona *Phys. Rev. Lett.*, vol. 90, p. 055510, 2003.

[50] M. Cardona and M. L. W. Thewalt *Rev. Mod. Phys.*, vol. 77, p. 1173, 2005.

[51] J. G. Tischler and J. A. Freitas *Appl. Phys. Lett.*, vol. 85, p. 1943, 2004.

[52] L. Bergamnn, D. Alexson, P. L. Murphy, R. J. Nemanich, M. Dutta, M. A. Stroscio, C. Balkas, H. Shin, and R. F. Davis *Phys. Rev. B*, vol. 59, p. 12977, 1999.

[53] A. K. Arora and A. K. Ramdas *Phys. Rev. B*, vol. 35, p. 4345, 1987.

[54] H. Siegle, A. Kaschner, A. Hoffmann, I. Broser, C. Thomsen, S. Einfeldt, and D. Hommel *Phys. Rev. B*, vol. 58, p. 13619, 1998.

[55] R. S. Berg, N. Mavalvala, H. Warriner, and B. Zhang *Phys. Rev. B*, vol. 39, p. 6201, 1989.

[56] J. I. nez, R. Cuscó, L. Artús, M. Hennini, A. Patané, and L. Eaves *Appl. Phys. Lett.*, vol. 88, p. 141905, 2006.

[57] M. Cardona and G. Guntherodt, eds., *Light Scattering in Solids IV*. Springer, Berlin, Germany, 1984.

"I learned very early the difference between knowing the name of something and knowing something."

Richard Feynman

2

Theoretical Framework: Phonons and Raman Scattering

Reflection, refraction, absorption, and scattering are the processes that may be suffered by light when impinging on a material. With regards to the scattered light, two different processes should be taken into account. While Rayleigh scattering is the classic elastic scattering of light by matter, inelastic scattering can also occur although is typically a factor of 10^6 times weaker than the elastically scattered light. The study of inelastic light scattering due to excitation or absorption of fluctuations of a system (vibrational or rotational modes, spin or plasma waves, etc.) is known as Raman scattering, named after the person who first reported this phenomena. Today resonant and non-resonant Raman scattering have become standard spectroscopic tools not only in the study of semiconductors but also in other condensed media. In this chapter we introduce the fluctuations of interest in this thesis: phonons in the zinc-blende and wurtzite structure. We will explain the Raman theory from both a semi-classical and quantum point of view, and we present some of the scattering mechanisms that take place in the Raman process. Also, we will discuss the Raman scattering by collective oscillations of a plasma and its coupling to phonons.

2.1 Phonons in the zinc-blende structure

The excitation of a crystalline solid causes the collective vibration of N atoms that constitute the crystal lattice, giving rise to $3N$ normal modes of vibration. By means

of quantum theory for harmonic crystals, a phonon is described as a normal mode of vibration of the system and is defined by its energy $\hbar\omega_q$ and wavevector $\vec{q}$. The phonon wavevector accounts for the periodicity and direction of propagation of the atomic vibrations. The total vibrational energy of the system is given by

$$E = \sum_q \hbar\omega_q(n_q + \frac{1}{2}), \tag{2.1}$$

where n_q is the number of phonons in the crystal with energy $\hbar\omega_q$ and wavevector q. In crystals with a basis of at least two atoms, acoustic and optical phonons exist. In acoustic phonons the atoms within a primitive cell move in-phase, and therefore have zero frequency for $q = 0$. In contrast, optical phonons involve atomic movements out of phase which conserve the center of mass. When the atoms vibrate transverse to the propagation of the vibration, the phonon is called transverse. Opposite, when the atoms vibrate parallel to the propagation, the phonon is called longitudinal.

In polar crystals, cations and anions in the lattice carry opposite effective charges (e^*) as a result of the redistribution of the charge associated with the polar bonding. Then, in the dynamical force equations of the harmonic oscillator for longitudinal optical (LO) phonons, appears an additional eletric field that changes the restorting force in the ionic movement. This different restorting forces between TO and LO phonons breaks the mode degeneracy yielding an energy difference between the two modes. This energy difference is called the TO-LO splitting. The magnitude of the TO-LO splitting is related to the ionicity of crystal bonds and can be obtained from the macroscopic dielectric constants by the Lyddane-Sachs-Teller relationship

$$\frac{\varepsilon_0}{\varepsilon_\infty} = \frac{\omega_{LO}^2}{\omega_{TO}^2}. \tag{2.2}$$

Here, the ε_0 and ε_∞ are the low and high frequency dielectric constants of the material, respectively.

On the other hand, lattice vibrations and the electronic band structure of a material highly depend on its crystalline structure and symmetries. While ZnO and GaN-related materials crystallize both in hexagonal and cubic structures depending on the growth conditions, dilute nitrides have usually a cubic structure. The cubic structure of any of these materials is zinc-blende, the same as for the well-known GaAs.

The zinc-blende structure may be regarded as two face-centered cubic lattices displaced relative to each other by a vector $a_0/4 \cdot (1, 1, 1)$, where a_0 is the lattice parameter and the edge of the conventional cell (figure 2.1a). The vectors that

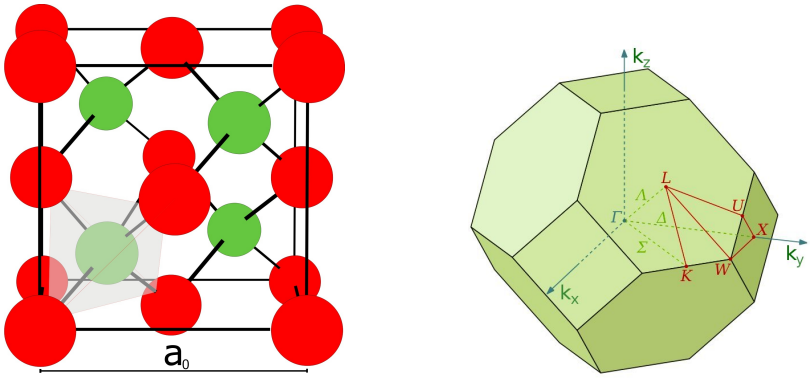

(a) Sketch of the zinc-blende unit cell.

(b) First Brillouin zone of the zinc-blende structure.

Figure 2.1: Zinc-blende structure.

describe its primitive cell are given by $\vec{a_1} = a_0/2 \cdot (0,1,1)$, $\vec{a_2} = a_0/2 \cdot (1,0,1)$, and $\vec{a_3} = a_0(1,1,0)$, and those describing the reciprocal lattice are $\vec{h_1} = 2\pi/a_0 \cdot (-1,1,1)$, $\vec{h_2} = 2\pi/a_0 \cdot (1,-1,1)$, $\vec{h_3} = 2\pi/a_0 \cdot (1,1,-1)$. It should be noted that in zinc-blende structures, the cation is tetrahedrally surrounded by four anions, and viceversa (see figure 2.1a).

Group theory is used in order to classify and study the symmetries of phonons and electronic states [1, 2]. The symmetry operations of the zinc-blende crystal can be found for the different points in the Brillouin zone, i.e. different wavevectors $\vec{q}$ (see figure 2.1b, where the different high-symmetry points and lines of the first Brillouin zone of the zinc-blende are illustrated). By finding the symmetry operations of a wavevector one can obtain the irreducible representations and the table of characters for the litle group of $\vec{q}$. As will be mentioned in section 2.3, first order Raman scattering only probes phonons with $q \sim 0$, i.e. at the Γ point. For this reason, we will only analyze this high-symmetry point, Γ.

The point group of the zinc-blende structure is the T_d (or $\bar{4}3m$), which is also the point group of the tetrahedron. The operations that transform all the atoms of the unit cell into another of the same type and surrounding are called symmetry operations and are writen as $\{R|\vec{a}\}$, where R stands for an inversion axis, rotation axis or symmetry plane and $\vec{a}$ is a fractional translation vector. The symmetry operations at the Γ point coincide with the symmetry operations of the unit cell. They can be classified in conjugacy classes, such that two symmetry operations R_i and R_j belong to the same conjugacy class if

$$R_i = K^{-1} \cdot R_j \cdot K \tag{2.3}$$

where K is a symmetry operation of the group. One can divide all the symmetry elements of the group into classes. It can be shown that the symmetry operations and conjugacy classes at the high-symmetry point Γ for the zinc-blende structure are [3]

E The identity $\{E|0\}$

S_4 Three quaternary rotation axes along the three cartesian axes, followed by an inversion, giving rise to six symmetry operations $\{S_{4i}|0\}$ and $\{S_{4i}^{-1}|0\}$, where i subindex denotes the axis direction. The rotation direction is given by the (-1) superscript, meaning anticlockwise when appearing and clockwise when omitted.

C_2 Three binary axes that coincide with the quaternary axes, which give rise to three symmetry operations $\{C_{2i}|0\}$.

C_3 Four ternary axes along the diagonals of the fundamental cubic cell, giving rise to eight symmetry operations $\{C_{3ijk}|0\}$ and $\{C_{3ijk}^{-1}|0\}$, where $i,j,k = \pm x, \pm y, \pm z)$

σ_p Six symmetry planes perpendicular to the diagonals of each face of the fundamental cubic cell. They give rise to six symmetry operations $\{\sigma_{ij}|0\}$ and $\{\sigma_{i-j}|0\}$, where $i,j = x,y,z$ and $i \neq j$.

A representation of a group, $\mathscr{D}$, is a collection of square non-singular matrices $\mathscr{D}^\alpha$ associated with the symmetry elements R_i of this group. For example, the unit matrix is assigned to the identity element $\{E|0\}$. Any representation $\mathscr{D}$ can be decomposed into a number of inequivalent irreducible representations $\mathscr{D}^\alpha$ (which cannot be reduced by similarity transformations), such that $\mathscr{D} = \sum_\alpha n_\alpha \mathscr{D}^\alpha$, where n_α indicates the number of times the α-irreducible representation is contained in $\mathscr{D}$, i.e. its degeneracy, and it can be shown that $\sum_\alpha n_\alpha^2 = h$, where h is the order of the group ($h = 24$ for the zinc-blende). The total number of irreducible representations of a group is equal to the number of conjugacy classes. For the zinc-blende structure, the symmetry elements at the Γ point are classified in five conjugacy classes, which means that the group has five irreducible representations (Γ_1, Γ_2, Γ_{12}, Γ_{15}, and Γ_{25}).

The trace of the collection of matrices of a representation $\mathscr{D}^\alpha(R)$ associated to an element R, are the so-called group characters, $\chi^\alpha(R)$, and it can be shown that $\chi(R) = \sum_\alpha n_\alpha \chi^\alpha(R)$, where $\chi(R)$ is the character of the total representation $\mathscr{D}(R)$ of an element R. Symmetry elements belonging to the same conjugacy class will

Table 2.1: Character table for the point group T_d at the symmetry point Γ

	$\{E\|0\}$	$3\{C_2\|0\}$	$3\{S_4\|0\}$ $3\{S_4^{-1}\|0\}$	$3\{\sigma_{ij}\|0\}$ $3\{\sigma_{i-j}\|0\}$	$4\{C_3\|0\}$ $4\{C_3^{-1}\|0\}$	Basis
Γ_1	1	1	1	1	1	x^2+y^2, z^2
Γ_2	1	1	-1	-1	1	
Γ_{12}	2	2	0	0	-1	$\{(x^2-y^2),$ $z^2-\frac{1}{2}(x^2+y^2)\}$
Γ_{15}	3	-1	-1	1	0	$(x,y,z),(xy,xz,yz)$
Γ_{25}	3	-1	-1	-1	0	

give rise to equal values for the character of a representation. For the zinc-blende structure, the characters of the irreducible representations associated to the different symmetry elements listed above are represented in table 2.1.

The set of functions which transform according to each irreducible representation is called its basis and are also displayed in the table. Regarding the vibrational properties of a crystal, the basis of an irreducible representation determines if the mode associated to this representation is Raman and/or infrared active. When the basis functions of a representation are linearly dependent of x, y, z, the associated mode is able to absorbe infrared radiation of its own frequency (IR active). An example would be the Γ_{15} representation. Besides, this irreducible representation is Raman active, since at least one of its basis is a second order function of x, y, z, such as x^2, xy, zy, etc. Irreducible representations whose basis are higher order functions of x, y, z, are neither Raman nor IR active, as is the case of Γ_2, and Γ_{25}, and are called silent modes.

Decomposing the total reducible representation of the zinc-blende crystal at $q = 0$ following the *Orthogonality Theorem* described in reference [1], it can be shown that

$$\Gamma_{total} = 2\Gamma_{15}^{(3)}, \tag{2.4}$$

where the (3) superscript denotes the triple degeneration of the Γ_{15} mode, as expected from the isotropy of the crystal structure. Since the zinc-blende structure has two atoms in the unit cell, 6 normal modes of vibration are expected. Each of these normal modes are associated to an irreducible representation of Γ_{total}. Hence, the six normal modes expected for zinc-blende crystals belong to the Γ_{15} representation and are called Γ_{15} modes. Among the six normal modes, one set of three Γ_{15} modes are acoustic, while the remaining are optical. While two of these optical modes are degenerate and correspond to transverse modes, the remaining one corresponds to a

longitudinal optical mode. The frequencies of the transverse and longitudinal optical modes for the materials of interest in this work with zinc-blende structure are listed in table 2.2.

	TO	LO
GaAs	268.2	291.5
GaN	555.0	742.0

Table 2.2: Zone-center Raman active phonon frequencies [cm^{-1}] for cubic GaAs [2] and GaN [4] at room temperature.

2.2 Phonons in the wurtzite structure

The wurtzite structure is a non-centrosymmetric hexagonal crystal structure (see figure 2.2) and is the thermodynamical stable structure of several wide-band gap semiconductors such as ZnO, GaN, and AlN. Since the cohesive energy of the wurtzite structure is very close to that of the zinc-blende, depending on the growth conditions, these semiconductors can occur in both wurtzite and zinc-blende structures.

The difference between the zinc-blende and the hexagonal structure is the stacking order of the anion-cation bilayers along the hexagonal (0001) direction, which coincides with the cubic (111) direction.

As can be seen in figure 2.2b, the vectors that describe the primitive cell of a wurtzite crystal in terms of cartesian axes are given by $\vec{a_1} = a_0/2 \cdot (1, -\sqrt{3}, 0)$, $\vec{a_2} = a_0/2 \cdot (1, \sqrt{3}, 0)$, and $\vec{a_3} = c_0(0, 0, 1)$, and it has four atoms per unit cell. The structure is characterized by two interconnected hexagonal sublattices displaced by $\vec{u} = [(2\vec{a_1} + \vec{a_2})/3 + \vec{c}/2]$, where a_0 and c_0 are the lattice parameters. It is worth noting that the bonding coordination between nearest neighbors is tetrahedral (figure 2.2a) like in zinc-blende crystals. The arrangement of these tetrahedra gives rise to polar symmetry along the hexagonal axis (c-axis) and is a key factor in crystal growth, etching and defect generation, appart from the origin of piezoelectricity and spontaneous polarization. Concerning the wurtzite reciprocal lattice, it is defined by the vectors $\vec{b}_1 = 2\pi/\sqrt{3}a_0 \cdot (\sqrt{3}, -1, 0)$, $\vec{b}_2 = 2\pi/\sqrt{3}a_0 \cdot (-\sqrt{3}, 1, 0)$, $\vec{b}_3 = 2\pi/c_0 \cdot (0, 0, 1)$. The first Brillouin zone of the wurtzite structure is depicted in figure 2.2c, as well as its high-symmetry points and lines.

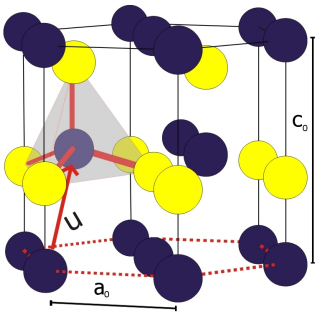

(a) Conventional cell. The tetrahedral coordination between anions and cations is reflected by the shadowed area.

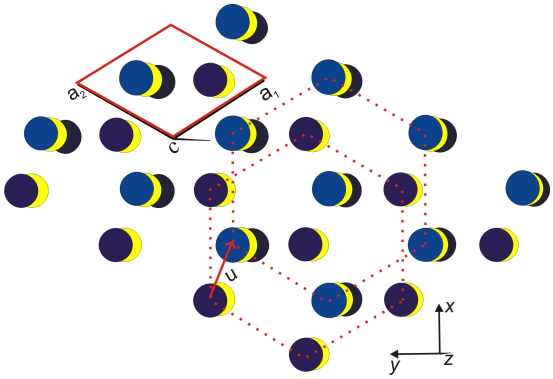

(b) In-plane projection. The primitive cell is highlighted by solid red lines. Dotted red lines indicate the two hexagonal sublattices. Different blue brightness is set for prespective clarity.

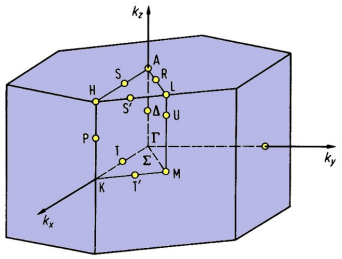

(c) First Brillouin zone of the wurtzite hexagonal lattice. The high-symmetry points and lines are shown.

Figure 2.2: Unit cell, in-plane projection and first Brillouin zone of the wurtzite crystalline structure. Blue/yellow colors are used to differenciate between anions and cations.

The space group of the wurtzite structure is the C_{6v}^4 (or $P6_3mc$), which is a non-symorphic group with a screw axis along the c axis and is homomorphic to the point symmetry group C_{6v} ($6mm$). Parallel to the case of the zinc-blende, the symmetry operations for the wurtzite structure at the Γ point are [2]:

E The identity $\{E|0\}$

C_6 A senary axis in the z direction (c-axis), giving rise to two six-fold rotations about the c-axis followed by the $\vec{c}/2 = (0, 0, c_0/2)$ translation, $\{C_6|\vec{c}/2\}$ and $\{C_6^{-1}|\vec{c}/2\}$.

C_3 A ternary axis in the z direction, giving rise to two symmetry operations, $\{C_3|0\}$ and $\{C_3^{-1}|0\}$.

Table 2.3: Character table of the Γ point for the point group C_{6v}

	$\{E\|0\}$	$2\{C_6\|\vec{c}/2\}$	$2\{C_3\|0\}$	$\{C_2\|\vec{c}/2\}$	$3\{\sigma_v\|0\}$	$3\{\sigma_d\|\vec{c}/2\}$	Basis
A_1	1	1	1	1	1	1	x^2+y^2, z^2, z
A_2	1	1	1	1	−1	−1	
B_1	1	−1	1	−1	1	−1	
B_2	1	−1	1	−1	−1	1	
E_1	2	1	−1	−2	0	0	$(xz, yz), (x, y)$
E_2	2	−1	−1	2	0	0	(x^2-y^2, xy)

C_2 A binary axis along the z direction and an additional translation with the symmetry operation $\{C_2|\vec{c}/2\}$.

σ_d Three symmetry planes normal to $\vec{a}_1$, $\vec{a}_2$ and $\vec{a}_1 + \vec{a}_2$, respectively, with a $(0, 0, c_0/2)$ associated translation. This results into the three symmetry operations, $\{\sigma_{d1}|\vec{c}/2\}$, $\{\sigma_{d2}|\vec{c}/2\}$, and $\{\sigma_{d3}|\vec{c}/2\}$.

σ_v Three symmetry planes perpendicular to the three σ_d planes, giving rise to three symmetry operations, $\{\sigma_{v1}|0\}$, $\{\sigma_{v2}|0\}$, and $\{\sigma_{v3}|0\}$.

Following group theory, the symmetry elements listed above are classified in six conjugacy classes. Hence, six irreducible representations are given for the wurtzite structure, labelled as A_1, A_2, B_1, B_2, E_1 and E_2. The characters of these representations associated to the symmetry elements at the Γ point are represented in table 2.3, where the basis of the representations are also displayed. Analyzing the basis functions of the representations, it can be noted that while the mode associated to the E_2 irreducible representation is Raman active, those associated to the A_1 and E_1 are both IR and Raman active and the modes with B_1 and B_2 symmetry are silent modes.

The wurtzite structure has four atoms in the unit cell (figure 2.2), hence 12 normal modes are expected. Using group theory, the total representation at the Γ point can be decomposed into

$$\Gamma_{total} = 2A_1 + 2B_1 + 2E_1^{(2)} + 2E_2^{(2)}, \tag{2.5}$$

where the (2) superscript denotes double degeneracy of representations E_1 and E_2. Contrary to the zinc-blende structure, the normal modes in wurtzite crystals are associated to representations with different symmetries. Among them, one set of A_1 and $E_1^{(2)}$ modes are acoustic, while the remaining modes are optical. While the

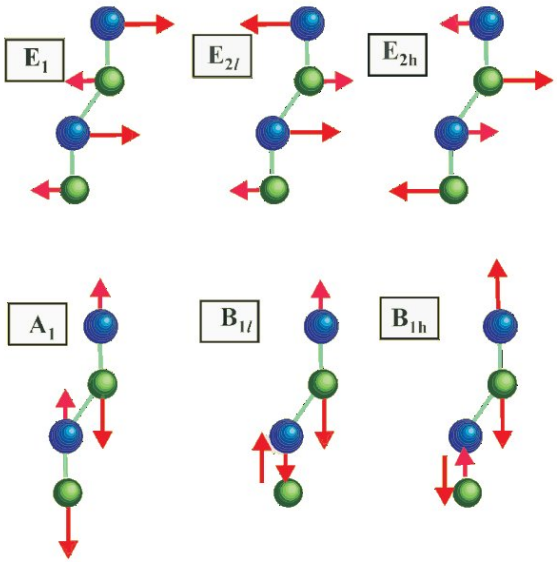

Figure 2.3: Representation of the atomic displacements for the optical phonon modes in the wurtzite structure

A_1 and E_1 modes are both infrared and Raman active, the doubly degenerate E_2 mode is only Raman active and the doubly degenerate B_1 mode is neither infrared nor Raman active.

The atomic displacement scheme for these optical modes is shown in figure 2.3. One can note that while the E_2 and E_1 have in-plane atomic vibrations, the atomic motion of the A_1 mode is in the c-axis direction. The zone-center Raman active phonon frequencies of wurtzite bulk ZnO and GaN are listed in table 2.4.

	E_2^{low}	A_1 (TO)	E_1(TO)	E_2^{high}	A_1 (LO)	E_1(LO)
ZnO	99	375	410	438	575	590
GaN	144	532	559	567	734	742

Table 2.4: Zone-center Raman active phonon frequencies [cm^{-1}] for bulk ZnO and GaN at room temperature. ZnO frequencies are taken from our studies, while GaN frequencies are from reference [4].

2.3 The Raman effect

2.3.1 Semi-classical approximation

From a semiclassical point of view, scattering of light by a material can be regarded as the emission of radiation by oscillating dipoles which are induced by the electric field of the incident light. In this framework, classical electrodynamics describe the radiation emission by dipoles.

Classically, when a molecule is placed in an electric field, its valence electrons will be displaced relative to its nuclei, thus developing an electric dipole moment. For small fields, the introduced dipole moment $\vec{P_i}$ is proportional to the field strength $\vec{\xi}$, where the proportionality constant α is the polarizability tensor of the molecule. This polarizability is a measure of how the electron cloud of the molecule can be distorted by an external electric field. If we assume that the electron field fluctuates sinusoidally with a radiation frequency ω_i, the molecule placed under such field will result in the same fluctuating scatter of frequency ω_i (Rayleigh scattering). Then, the intensity of the emitted light polarized in a given direction $\hat{e_s}$ is proportional to $|\hat{e_s}\vec{P_i}|^2 = |\hat{e_s}\alpha\hat{e_i}|^2$, where $\hat{e_i}$ is the polarization direction of the incident electric field.

A similar treatment stands for a crystalline solid and its harmonic vibrations (phonons). In this case, the molecular polarizability has to be changed by the electric susceptibility $\chi(\omega_i, \vec{k_i})$ of the crystal, which is determined by its electronic structure. For small ionic vibrational amplitudes and for phonon frequencies (ω_q) small compared to the characteristic frequencies of the electronic states (quasistatic approximation), it is possible to expand the crystal susceptibility in terms of the atomic normal coordinates η

$$\chi(\omega_i, \vec{k_i}, \eta) = \chi(\omega_i, \vec{k_i}) + \frac{\partial\chi(\omega_i, \vec{k_i})}{\partial\eta} \cdot \eta + \ldots, \tag{2.6}$$

with $\eta = \eta_0 cos(\vec{q}\cdot\vec{r} - \omega_q t)$. As seen in Eq. (2.6), the vibration of the ions in a crystal induced by an incident electric field, $\vec{\xi_0} cos(\vec{k_i}\cdot\vec{r_i} - \omega_i t)$, changes the susceptibility of the material. Now, the polarization strength of the crystal in the presence of ionic vibrations (or any other fluctuations) will be of the form

$$\begin{aligned} P_i =& \chi(\omega_i, \vec{k_i})\xi_0 cos(\vec{k_i}\cdot\vec{r_i} - \omega_i t) + \frac{\partial\chi(\omega_i, \vec{k_i})}{\partial\eta}\eta_0\xi_0 \\ & \times cos(\vec{k_i}\cdot\vec{r} - \omega_i t) cos(\vec{q}\cdot\vec{r} - \omega_q t) \end{aligned} \tag{2.7}$$

Hence, the scattered radiation contains, along with the elastic contribution of frequency equal to the incident light ω_i, further terms known as Raman terms. The elastic scattering is known as Rayleigh scattering and is represented by the term in which the polarization oscillates in phase with the incident electric field. The remaining terms of Eq. (2.7) represent the polarization induced by the primary radiation, which is modulated by the lattice vibrations up to first order (P_v). The polarization term P_v and can be rearrenged as

$$P_v(\vec{r},t) = \frac{\partial\chi(\omega_i,\vec{k_i})}{\partial\eta}\frac{\eta_0\xi_0}{2} \times \{cos[(\vec{k_i}+\vec{q})\vec{r}-(\omega_i+\omega_q)t] + cos[(\vec{k_i}-\vec{q})\vec{r}-(\omega_i-\omega_q)t]\} \quad (2.8)$$

As can be seen, the polarization P_v is also sinusoidal but with two different wavevectors ($\vec{k_i}\pm\vec{q}$) and frequencies ($\omega_i\pm\omega_q$). The cosine term containing the wavevector sum corresponds to the absorption of a vibrational state of the lattice (phonon) with energy $\hbar\omega_q$ and wavevector $\vec{q}$ by light (anti-Stokes process), whereas the cosine term containing the wavevector difference describes the excitation of the same vibrational state (energy $\hbar\omega_q$ and wavevector $\vec{q}$) by the scattered light (Stokes process). Higher order terms in the expansion of the susceptibility give rise to higher-order processes. For a sinusoidal electric field, sinusoidal terms are obtained with frequency and wavevector $\omega_i\pm2\omega_q$ and $\vec{k_i}\pm2\vec{q}$ for second-order processes, $\omega_i\pm3\omega_q$ and $\vec{k_i}\pm3\vec{q}$ for third-order processes, and so on. These are the overtone scattering processes, where the positive sign stands for excitation of vibrational states (Stokes) and the negative for their absorption (anti-Stokes).

The total intensity S of inelastically scattered light in a direction $\hat{e_s}$ (S) is given by the time-averaged power radiated by the polarization induced by the system fluctuations, $<|\hat{e_s}\cdot\vec{P_v}|>$, which leads to

$$S \propto \left|\hat{e_s}\cdot\frac{\partial\chi(\vec{k_i},\omega_i)}{\partial\eta}\cdot\hat{e_i}\right|^2\cdot<\eta\eta^*> \quad (2.9)$$

for the Stokes component, and to the same expression with $<\eta^*\eta>$ intead of $<\eta\eta^*>$, for the anti-Stokes. Substituing the normal displacements η and η^* by the creation (a) and the anihilation ($a^\dagger$) operators, respectively, the average in time can be evaluated using second-quantization arguments. Then

$$<aa^\dagger>=\frac{\hbar}{2\omega_q}(n+1) \qquad <a^\dagger a>=\frac{\hbar}{2\omega_q}n \quad (2.10)$$

where $n=[e^{\hbar\omega_q/k_BT}-1]^{-1}$ is the Bose-Einstein occupation factor. From Eq. 2.9, we conclude that vibrations are essential for inelastic scattering, since the scattering

intensity is proportional to the vibrational state η. The occupational factor is different for the two processes, since the phonon creation (Stokes process) is more likely to happen than the phonon absorption (anti-Stokes process). The latter process requires that a population of phonons already exists previous to the Raman process. Therefore, for low temperatures, the occupational factor n tends to zero and the intensity of the anti-Stokes lines is much reduced. Moreover, it should be stressed that the ratio between the Stokes and anti-Stokes Raman intensity only depends on the crystal temperature.

Finally, the observation of Raman lines occurs when the susceptibility has a non-vanishing derivative with respect to the coordinate η of the elementary excitation. The properties and mechanisms of these elementary excitations (phonons) depend on the crystal symmetry. In general, the quantity $\partial\chi/\partial\eta$ for a given elementary excitation frequency is a symmetric second-rank tensor, and is known as Raman tensor R of the elementary mode. The tensor coeficients are known as Raman polarizabilities and are related to the scattering probability. These coefficients depend on the different scattering mechanisms that occur in the Raman process and we will deal with them in section 2.3.3.

2.3.2 Quantum-mechanical approach

From a quantum-mechanical point of view, a first-order Raman process consists in the interaction between the incident photon and a elementary excitation, e.g. phonon, giving rise to the scattered photon. However, direct photon-phonon interaction is unlikely unless the energy of the incident photon is comparable to the energy of the excited or absorbed phonon. While the typical phonon energy is about tenths of meV, the energy of the commonly used exciting lasers is of the order of 1 eV or higher. Hence, the Raman process is mediated by conduction and valence electrons of the material. By using time-dependent perturbation theory it is possible to visualize a first-order Raman process as a three-step process (see Feynman diagram of figure 2.4).

In the initial state of the system ($|i>$), there are $N(\omega_i)$ photons with energy $\hbar\omega_i$, $N(\omega_s)$ photons with energy $\hbar\omega_s$, N_q phonons present in the crystal and all the electrons are in their ground state (E_i).

In the first step, the incident photon excites the crystal towards an intermediate state ($|a>$) of energy E_a by creating a virtual electron-hole pair (exciton), via the electron-radiation interaction Hamiltonian $\mathscr{H}_{e-R}$.

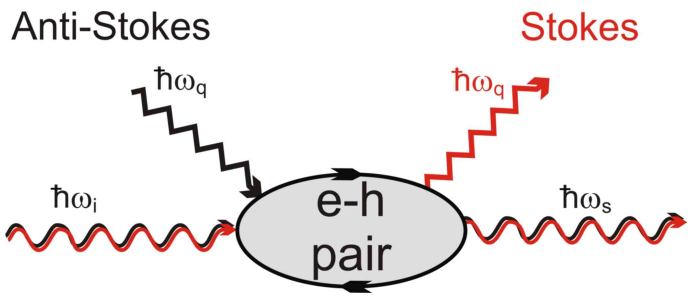

Figure 2.4: Feynman diagram for a first-order Raman process.

Second, the virtual electron or hole interacts with a phonon by exciting (Stokes) or absorbing (anti-Stokes) it via the electron-phonon interaction Hamiltonian $\mathscr{H}_{e-ph}$, leaving the system in a state denoted $|b>$ of energy E_b.

Third, the electron-hole pair recombines radiatively, giving rise to the emitted photon via $\mathscr{H}_{e-R}$. In the final state $|f>$, the number of photons with energy $\hbar\omega_i$ has decreased by one, while $N(\omega_s)$ and N_q have both increased by one. However, the electron state remains unchanged after the whole process, although the electrons mediate the Raman scattering by phonons. Then, the final electronic state is the same than the initial one ($|f>=|i>$) and $E_i = E_f$.

Within this framework, Fermi's Golden Rule allows one to calculate the transition rate probability from a quantum state into a continuum of energy eigenstates of a system due to a perturbation. Then, the probability that the Raman process described above, which is also depicted in figure 2.4, occurs is

$$Pr_{fi} = \left(\frac{2\pi}{\hbar}\right)\left|\sum_{a,b}\frac{<i|\mathscr{H}_{e-R}(\omega_i)|a><a|\mathscr{H}_{e-ph})|b><b|\mathscr{H}_{e-R}(\omega_s)|i>}{[\hbar\omega_i-(E_a-E_i)][\hbar\omega_i\mp\hbar\omega_q-(E_b-E_i)]}\right|^2 \times\delta(\hbar\omega_i-\hbar\omega_q-\hbar\omega_s), \tag{2.11}$$

where $E_{a/b}$ is the intermediate energy from the electronic state $|a/b>$. The $(\mp)$ sign stands for Stokes/anti-Stokes process, respectively. Then, in order to obtain Pr_{fi} we shall evaluate the different Hamiltonians involved in the Raman process.

The electron-radiation Hamiltonian, neglecting the quadratic dependence in the field, is given by

$$\mathscr{H}_{e-R} = \frac{e}{mc}\vec{A}\cdot\vec{p}, \tag{2.12}$$

where $\vec{p}$ is the momentum operator $(\hbar/i)\vec{\nabla}$, and $\vec{A}$ is the potential vector of the electromagnetic field which in the Coulomb gauge is defined by $\vec{\xi} = -c^{-1}(\partial\vec{A}/\partial t)$ and $\vec{B} = \vec{\nabla} \wedge \vec{A}$. As the matrix elements $< i|\vec{A} \cdot \vec{p}|a/b >$ are usually not strongly dependent on the wavevector, we shall replace them by constants.

On the other hand, the electron-phonon Hamiltonian requires a more extended analysis since there exist different interaction mechanisms between electrons and phonons, such as via deformation potentials, Fröhlich interaction, intervalley electron-phonon interaction, etc. Hence, the probability of the first-order Raman scattering depends on which mechanisms and interferences between them take place.

2.3.3 Electron-phonon interactions

As already mentioned, lattice vibrations in a crystal and electrons can interact through many mechanisms. In this work, we focus on the electron-phonon interactions through the deformation potential and Fröhlich mechanisms. We must bear in mind that for both mechanisms two different scattering processess can take place (intraband and interband) depending on the number of electronic bands involved. In intraband scattering, only two electronic bands are involved in the process and is represented by diagonal-terms in the electron-ion interaction tensor. In interband scattering, three electronic bands are involved and is represented by non-diagonal elements of the Raman tensor.

Deformation potential

Within the Born-Oppenheimer approximation, the motion of electrons and atoms in the crystal can be separated and the electronic wavefunction only depends on the respective position of electrons and atoms. This means that the bond lengths and angles affect the energy of the different electronic transitions. Therefore when the interatomic distances vary (as is the case for crystal vibrations) the energy of the electronic transitions is modulated. Assuming that electrons respond instantaneously to the atomic motion, the Hamiltonian for this particular electron-phonon interaction can be expressed as a Taylor series expansion of the electronic Hamiltonian, so that

$$\mathscr{H}_{e-ph} \propto \frac{\partial E_e}{\partial \eta} \cdot \eta + \ldots, \tag{2.13}$$

where E_e is the energy of an electronic state. This is known as deformation potential mechanism since the crystal potential modulation is induced by the atomic displacements. In solids, the energy band structure is intimately connected to the complex

dielectric function and thus to the susceptibility. Therefore, equations 2.9 and 2.11 are conceptually equivalent when the electron-phonon interactions are mainly due to deformation potential. A deformation potential contribution to the Raman polarizability (Raman tensor coeficients) must be taken into account, and the resulting Raman tensor has the same symmetry of the phonon involved in the process.

In zinc-blende crystals, the triply-degenerate optical mode Γ_{15} has the set of functions (xy,yz,xz) as Raman active basis. Consequently, only Raman tensors that transform like these functions give a non-zero result when contracted to the light polarization vectors. Besides, the triply degenerate mode is also infrared active, which means that its Raman tensor for each crystallographic direction must transform like the functions x, y and z, respectively. Such Raman tensors are

$$\mathrm{LO}_x = \begin{pmatrix} 0 & 0 & 0 \\ 0 & 0 & a \\ 0 & a & 0 \end{pmatrix}, \qquad \mathrm{LO}_y = \begin{pmatrix} 0 & 0 & a \\ 0 & 0 & 0 \\ a & 0 & 0 \end{pmatrix}, \qquad \mathrm{LO}_z = \begin{pmatrix} 0 & a & 0 \\ a & 0 & 0 \\ 0 & 0 & 0 \end{pmatrix},$$

where a is the Raman polarizability. Each of these tensors corresponds to lattice vibrations polarized along x, y and z, respectively. This means, that the first Raman tensor corresponds to a LO phonon propagating along the x direction or either to a TO phonon propagating through the y or z directions. In general, for a phonon propagating in a given direction defined by the vector $\hat{e}_q = (e_x, e_y, e_z)$, the Raman tensors for LO and TO phonons are given by

$$R_{LO} = e_x R_x + e_y R_y + e_z R_z \tag{2.14}$$

$$R_{TO} = e_x^T R_x + e_y^T R_y + e_z^T R_z \tag{2.15}$$

where $\hat{e}_q^T$ is a vector perpendicular to $\hat{e}_q = (e_x, e_y, e_z)$.

For wurtzite crystals, the Raman tensors for each of the Raman active modes are

$$E_1(\mathrm{LO}_x) = \begin{pmatrix} 0 & 0 & c \\ 0 & 0 & 0 \\ c & 0 & 0 \end{pmatrix}, E_1(\mathrm{LO}_y) = \begin{pmatrix} 0 & 0 & 0 \\ 0 & 0 & c \\ 0 & c & 0 \end{pmatrix}, A_1(\mathrm{LO}_z) = \begin{pmatrix} a' & 0 & 0 \\ 0 & a' & 0 \\ 0 & 0 & b \end{pmatrix},$$

$$E_2^{(1)} = \begin{pmatrix} d & 0 & 0 \\ 0 & -d & 0 \\ 0 & 0 & 0 \end{pmatrix}, \qquad E_2^{(2)} = \begin{pmatrix} 0 & d & 0 \\ d & 0 & 0 \\ 0 & 0 & 0 \end{pmatrix}, \tag{2.16}$$

Similar to the zinc-blende structure, the A_1 and E_1 polar modes of the wurtizte strucutre have different tensors depending on their polarization.

Geometry	Zinc-Blende	
	TO	LO
$z(xx)\bar{z}$		
$z(xy)\bar{z}$		A
$z(x'x')\bar{z}$		A
$z(x'y')\bar{z}$		
$y(zy)x$	A	

Geometry	Wurtzite				
	E_2	A_1(LO)	A_1(TO)	E_1(LO)	E_1(TO)
$z(xx)\bar{z}$	A	A			
$z(xy)\bar{z}$	A				
$x(yy)\bar{x}$	A		A		
$x(zy)\bar{x}$					A
$y(zy)x$				A	A

Table 2.5: Selection rules for zinc-blende and wurtzite crystals in backscattering and 90° configurations due to deformation potential. x, y, and z are the high-symmetry axes of the structures according to Porto's notation, and x' and y' correspond to the (110) and $(1\bar{1}0)$.

From the Raman tensors and the polarization vectors of the incident and scattered light, the selection rules for Raman scattering are obtained, since $S \propto |\hat{e}_i R \hat{e}_s|^2$. Using this expression and the Raman tensors above, the selection rules for first-order Raman scattering in zinc-blende and wurtzite crystals can be obtained. The symmetry-allowed Raman modes for several scattering geometries are summarized in table 2.5.

Finally, we have mentioned that two different contributions of the phonon modulation may exist depending on the number of electronic bands involved in the scattering process. While in the intraband scattering (2-band process) the band-gap is modulated by phonons, in interband scattering (3-band process) the electron momentum is also modulated. However, in both cases the Raman tensors have the same symmetries and the Raman polarizability a, a', b, c and d include both scattering rates.

Fröhlich interaction

Deformation potential interactions described above naturally occur in both non-polar and polar crystals. However, in the latter additional interactions may take place. Phonons in polar crystals induce both polarization and electrostatic fields. In the case of polar optical phonons, their electrostatic field increase the frequency of the long-wavelength longitudinal optical (LO) mode above those of the corresponding transverse optical (TO) mode, giving rise to the TO-LO splitting.

Under resonance conditions (i.e. when the excitation energy coincides with an interband electronic transition), the intermediate state in the Raman process is real, an exciton. In this case, the electron/hole and the longitudinal electric field induced

by LO phonons are subject to a Coulomb interaction. This long-range phenomena is called the Fröhlich mechanism.

The Hamiltonian for the Fröhlich process is simply given in terms of the scalar potential of the LO phonon longitudinal field (ϕ_{LO})

$$\mathscr{H}_{Fr} = -e\phi_{LO} = -\frac{iC_F}{qV^{1/2}}\left(\frac{\vec{q}}{|q|}\hat{e_{LO}}\right)(a_q + a^{\dagger}_{-q})e^{i\vec{q}\vec{r}}, \tag{2.17}$$

where V is the crystal volume and C_F is the Fröhlich constant given by

$$C_F^2 = 2\pi e^2 \hbar\omega_{LO}\left(\frac{1}{\varepsilon_\infty} - \frac{1}{\varepsilon_0}\right) \tag{2.18}$$

While the deformation potentials are difficult to calculate, the Frölich interaction can be calculated in terms of macroscopic parameters such as the low- and high-frequency dielectric constants, ε_0 and ε_∞ respectively.

It is worth noting that the Fröhlich interaction depends inversely on the phonon wavevector q. Therefore, it diverges as q approaches to zero. However, energy and momentum conservation prevent electrons from undergoing intraband scattering via $q \equiv 0$ optical phonons, since they have a nonvanishing energy at the Γ point. Nevertheless, this mechanism is still strongly resonant for small wavevectors. The contribution of the Fröhlich interaction to the Raman tensor has also different symmetry than that of the deformation potential, and is represented by a diagonal tensor. Another difference between the two mechanisms, is that while the Fröhlich interaction is long-range, deformation potential is a short-range interaction.

In the Fröhlich interband process, the Raman tensor has the same symmetry than the corresponding to deformation potential. In this case, the mechanism is known as electro-optic (EO) mechanism. The EO interaction is the origin of the difference between Raman intensities of the TO and LO modes in polar semiconductors and the ratio between these two intensities is given by the Faust-Henry coeficient C_{FH}.

2.4 Raman scattering by phonon modes

Raman spectroscopy is a very effective and versatile technique for probing phonons in semiconductors. So far, we have studied the normal modes depending on the crystal symmetry and some mechanisms (deformation potential, electro-optic and Fröhlich) that may affect the Raman scattering process. The Raman peaks observed in the spectra are broadened by the finite lifetime of the modes that participate in the scattering process. To analyze the actual response of the system in a light scattering experiment, it is necessary to relate the frequency-dependent cross-section $S(\omega)$ to the total susceptibility of the system. For this purpose we can use the fluctuation-dissipation theory. This theory lies within the framework of non-equilibrium statistical mechanics. It relates the fluctuations, or generalized displacements, of a physical quantity present at equilibrium, to a dissipative process which is given when the system is perturbed by an external force.

The application of the fluctuation-dissipation theory to inelastic light-scattering processes was carried out by Hon and Faust [5] and also by Klein *el al.* [6] in early seventies. In Raman scattering, the dissipative process is related to the emission of the scattered light. While Hon and Faust used classical electrodynamic equations to define the driving forces and displacements, Klein *et al.* dealt with a Hamiltonian that includes first-order changes in the polarizability. Although both get together to the same expression for the Raman efficiency, the theory developed by Hon and Faust also allows the incorporation of charge-density fluctuations as an additional term in the dynamical equations, although including the intraband Fröhlich mechanism is not straightforward. By contrast, the Fröhlich interaction can be easily incorporated within the approach of Klein *et al.*, since the Hamiltonian of this interaction is known.

We will fundamentally study the Raman cross-section of isotropic and anisotropic ionic crystals taking into account the deformation potential and electro-optic mechanisms. In this case, scattering cross-section (Stokes) for the LO vibrations is [5]

$$S^{LO} \propto \Im\left\{\frac{-1}{\varepsilon(\omega,q)}\left[1+2C_{FH}\mathcal{L}(\omega)-C_{FH}^2\mathcal{L}(\omega)\mathcal{A}\right]\right\}\times[n(\omega)+1], \qquad (2.19)$$

where C_{FH} is the Faust-Henry coefficient described in the previous section, $\varepsilon(\omega,q)$ is the dielectric function, $\mathcal{A}=\omega_{TO}^2\cdot[\omega_{LO}^2-\omega_{TO}^2]^{-1}$, and $\mathcal{L}(\omega)$ is the normalized lorentzian response of an oscillator $\mathcal{L}(\omega)=\omega_{TO}^2\cdot[\omega_{TO}^2-\omega^2-i\omega\Gamma_{ion}]^{-1}$. ω_{LO} and ω_{TO} are the frequencies of the longitudinal and transverse optical modes, respectively, and Γ_{ion} represents the spectral width of the phonons, which decay due to anharmonic

effects (this will be explained in detail in chapter 4).

The dielectric function relates the electric field $\vec{\xi}$ originated from the total charge in the medium, to the electric displacement $\vec{D}$ originated by the external free charge. Similarly, the susceptibility tensor $\chi(\omega, \vec{q})$ relates the electric field with the polarization $\vec{P}$, which arises from the charge induced by the external perturbation. In isotropic materials (as is the case of zinc-blende crystals) the dielectric function and the susceptibility are related by

$$\varepsilon(\omega, q) = \varepsilon_\infty + 4\pi\chi(\omega, q). \tag{2.20}$$

For anisotropic crystals, such as hexagonal ZnO and GaN, both the scalar dielectric function and the susceptibility must be replaced by diagonal tensors.

Within the framework of response theory, the dielectric function has to include the contribution of all the possible excitations in the medium, which can be very different in nature depending on the frequency range considered. In the frequency range of vibrational modes and in polar crystals, the susceptibility has basically an atomic contribution (i.e. lattice vibrations). The contribution of the polar lattice arises from the dipole moments induced by the longitudinal optical modes, and is given by [7, 8]

$$\chi_{ion}(\omega) = \frac{\varepsilon_\infty}{4\pi} \frac{\omega_{\mathrm{LO}}^2 - \omega_{\mathrm{TO}}^2}{\omega_{\mathrm{TO}}^2 - \omega^2 - i\Gamma_{ion}\omega}. \tag{2.21}$$

Hence, the expression 2.19 can be rewritten in terms of the susceptibility

$$S^{LO} \propto \Im\left\{\frac{-1}{\varepsilon(\omega, q)}\left[\frac{\varepsilon_\infty}{4\pi} + 2C_{FH}\mathcal{A}\chi_{ion} - C_{FH}^2\mathcal{A}^2\chi_{ion}\right]\right\} \times [n(\omega) + 1]. \tag{2.22}$$

For the TO vibrations, a polariton term (qc/ω) has to be included in the dynamical force equations, within the framework of Hon and Faust theory. For visible light and in backscattering geometry $qc = (4\pi n_r c/\lambda_i) >> \omega_{TO}$, where n_r is the refractive index of the crystal, and hence the Raman cross-section for TO vibration reduces to

$$S^{TO} \propto \Im\{\mathcal{L}(\omega)\} \cdot C_{FH}^2\mathcal{A} \times [n(\omega) + 1], \tag{2.23}$$

or, in terms of the ionic susceptibility,

$$S^{TO} \propto \Im\{\chi_{ion}\} \cdot C_{FH}^2\mathcal{A}^2 \times [n(\omega) + 1]. \tag{2.24}$$

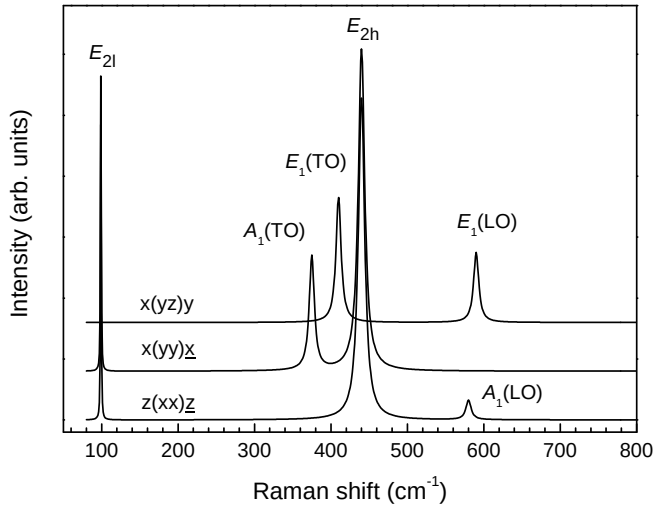

Figure 2.5: Simulated Raman spectra of ZnO in several geometries

In wurtzite crystals, we have seen that not only polar modes exist, but also non-polar (E_2 modes). In this case, the Raman cross-section is simply proportional to $\mathcal{L}(\omega)$, in which ω_{TO} must be replaced by the frequency of the non-polar mode in question. Considering the expressions above, we can simulate the Raman spectra of ZnO for several configurations geometries, as shown in figure 2.5.

2.5 Raman scattering by LO phonon-plasmon coupled modes

Free carriers can be present in a semiconductor by doping or by thermal or optical excitation. Light can be also scattered by free carriers, giving rise to several types of excitations: collective excitations, due to charge density fluctuations (plasmons), and single particle excitations (SPE). The scattered light yields considerable information about these phenomena, depending on the experimental conditions. For example, under excitation resonance the intensity of some of the scattering mechanisms is enhanced.

In particular, collective plasma oscillations, or plasmons, form electric fields that interact with the electric field of the LO phonons in polar crystals. As a result of this interaction, a bound state of two elemental excited particles, LO phonon and plasmon, is formed giving rise to the LO phonon-plasmon coupled modes (LOPCMs). These modes have phonon-plasmon mixed character and their excitation occurs via contribution of the mechanisms that take place in the excitation of the bare modes. Apart from its evident basic interest, Raman scattering by LOPCMs is also a sensitive, contactless and non-destructive technique that allows determining carrier concentrations in polar semiconductors, as well as electron/holes effective masses and mobilities.

We shall describe LO-plasmon coupled modes in one-component plasmas. For this purpose we must first describe the natural plasma mode of the carriers. Supose an electron gas in a crystalline solid, superimposed on the *fixed* equal and opposite positive charges of the ion cores. Any displacement of the electron gas with respect to the core assembly will set up a restorting electric field. This restorting electric field is $\vec{\xi_R} = (4\pi/\varepsilon_\infty) n_0 e\vec{r}$, where n_0 is the static electron density, $\vec{r}$ is the displaced distance vector, and ε_∞ is the high-frequency dielectric constant of the material, which arises from the screening produced by the valence electrons of the ionic lattice. Thus, the force equation for each electron with effective mass m^* in the gas is [7, 8]

$$m^* \frac{\partial^2 \vec{r}}{\partial t^2} = -e\vec{\xi_R} = -\frac{4\pi}{\varepsilon_\infty} n_0 e^2 \vec{r} \qquad (2.25)$$

This equation describes a simple longitudinal harmonic motion at a natural frequency

$$\omega_p^2 = \frac{4\pi n_0 e^2}{\varepsilon_\infty m^*} \qquad (2.26)$$

Hence, the electron gas oscillates about its equilibrium position at a natural plasma frequency ω_p. Similar to simple harmonic oscillations, the energy of plasma oscillations is quantized into units of $\hbar\omega_p$. The quantized entities are known as plasmons. Plasma frequency is usually in the infrared spectral region for doped semiconductors (carrier densities $\sim 10^{18}$ cm^{-3}), and in the ultraviolet for plasmas in metals (carrier densities $\sim 10^{28}$ cm^{-3}).

In a doped polar semiconductor, in addition to the LO phonon modes of the lattice, plasma oscillations of the free carriers are also longitudinal waves. Because of the polar character of the crystal, the LO mode interacts with the macroscopic electric field of the plasmon, giving rise to the formation of coupled modes, L^+ and L^-. For longitudinal waves of frequency ω_{LO}, Maxwell's equations and the driven-oscillator equations result in a $\varepsilon(\omega_{LO}, q)$ that must be equal to zero [7, 9]. This means that a non-zero electric field can exist without a displacement vector $\vec{D}$, i.e. without external sources. Hence, the frequencies of the longitudinal coupled modes are to be obtained from the zeroes of the real part of the total dielectric function, which includes a contribution from both the lattice and the free electrons. In order to predict the frequencies of the coupled modes, the dielectric function must include the contribution of the lattice and the free carriers [9],

$$\varepsilon(\omega, q) = \varepsilon_\infty + 4\pi(\chi_{ion} + \chi_e) \tag{2.27}$$

where χ_{ion} and χ_e are the ionic (described previously) and electronic susceptibilities, respectively.

Similar to the case for undoped crystals, the Raman scattering cross-section can be also determined from the fluctuation-dissipation theory developed by Hon and Faust [5] by adding the free carrier term. This gives rise to the following expression, which is equivalent to equation 2.22,

$$S \propto \Im\left\{\frac{-1}{\varepsilon(\omega, q)}\left[\frac{\varepsilon_\infty}{4\pi} + 2C_{FH}\mathcal{A}\chi_{ion} - C_{FH}^2\mathcal{A}^2\chi_{ion}\{1 + \frac{4\pi}{\varepsilon_\infty}\chi_e\}\right]\right\} \times [n(\omega)+1] \tag{2.28}$$

Hence, the key issue is to determine the electronic susceptibility of the material. Different models with different level of accuracy and complexity exist to describe χ_e.

The Drude model

The Drude Model [7, 8] lies within the framework of classical description of the plasma oscillations and is the simplest model which gives a rough approximation to the coupling between LO phonons and plasmons. The Drude model does not take

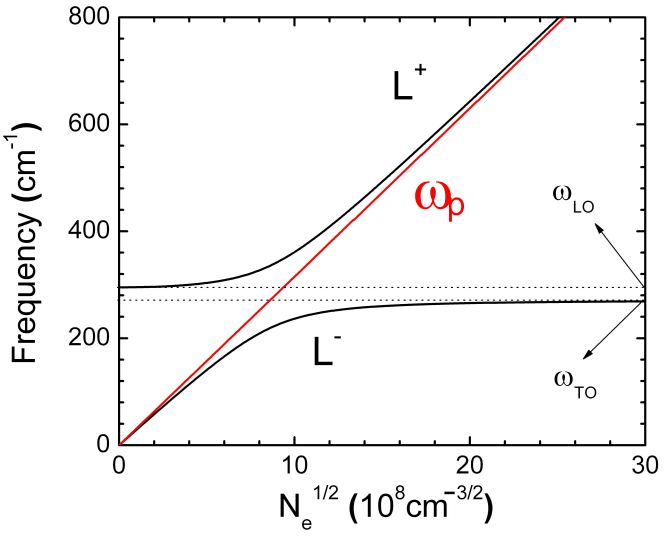

Figure 2.6: Frequency of the L^+ and L^- coupled modes in *n*-type GaAs with respect to the electron charge density, obtained by the zeroes of the real part of the dielectric function. The Drude model was used to describe the electronic susceptibility. The bare-plasma frequency ω_p is also plotted.

into account the spatial dispersion of the plasmons, neither the statistics of the free carriers, nor the non-parabolicity of the conduction band. The electronic contribution to the susceptibility given by this model is

$$\chi_e(\omega) = -\frac{\varepsilon_\infty}{4\pi}\frac{\omega_p^2}{\omega^2 + i\omega\Gamma_e} \tag{2.29}$$

where ω_p is the natural frequency of the plasma (equation 2.26) and Γ_e is a phenomenological damping constant related to the lifetime of the plasmons. From this expression for the dielectric function, one can obtain the frequencies for the coupled modes, L^+ and L^-, from the zeroes of the total dielectric function. Neglecting ionic and electronic dampings, the frequencies of the coupled modes are given by the expression

$$\omega^4 - \omega^2(\omega_p^2 + \omega_{LO}^2) + \omega_p^2\omega_{TO}^2 = 0 \tag{2.30}$$

This equation gives a rough approximation for the frequencies of the LOPCMs in a low damping regime (see chapter 6 for highly damped regimes). The dependence of the coupled frequencies on N_e obtained from equation 2.30 is plotted in figure 2.6 for *n*-type GaAs. It can be observed that at low carrier densities (the dilute regime)

the low frequency branch L^- follows the plasma frequency, and the L^+ branch is very close to the frequency of the LO lattice mode. Contrariwise, at high carrier densities (the degenerate regime) the L^+ branch tends to the plasma frequency and the L^- branch assymptotically approaches the frequency of the TO lattice mode, instead of that of the LO mode. This means that the high density of free carriers yields a screening of the extra Coulombic restorting force induced by the LO phonon displacement, so that the longitudinal oscillation frequency is not splitted from the transverse one. For intermediate values of N_e, the plasma frequency is in the range of the lattice modes, and plasmons strongly interact with the LO phonons. The resulting coupled modes have a mixed phonon-plasmon character.

It should be noticed that the behavior of the LOPCM frequencies as a function of the electron density depicted in figure 2.6 was calculated assuming zero damping. When damping cannot be neglected, the zeroes of the real part of the dielectric function does not provide reliable results for the frequencies of LOPCM. In this case, the frequency of the coupled modes are obtained by calculating the Raman lineshapes. The maxima of the calculated peaks thus provide the frequency of the coupled modes. The damping effects on the Raman lineshapes and LOPCM frequencies are discussed in chapter 6.

The Hydrodynamical model

The Drude model is a simple classical model which neglects wavevector dispersion of the plasmons and single-particle excitations. An improvement to the Drude model is provided by the Hydrodynamical model (HD), which includes wavevector dependence and temperature effects [10]. The HD model is also a classical model and includes a force term in the dynamical equation of electrons of the form $-(1/N_e)\vec{\nabla}P$, where P is the pressure of the electron gas. From kinetic theory, the hydrostatic pressure P can be related to the electron mean-square velocity $< v^2 >$ by the relation $P = \frac{1}{3}N_e m^* < v^2 >$, where m^* is the electron effective mass and N_e the electron gas density. Thus, the additional force term is proportional to the density gradient, which means that the spatial dispersion is taken into account. The electric susceptibility then becomes

$$\chi_e(q,\omega) = -\frac{\varepsilon_\infty}{4\pi}\frac{\omega_p^2}{\omega^2 - < v^2 > q^2 + i\omega\Gamma} \qquad (2.31)$$

It must be noted that when the dispersion effects are negligible ($q \sim 0$), the hydrodynamical expression for the electronic susceptibility reduces to that given by the

Drude model.

Once the dispersion of the electronic band is known, the mean square velocity can be evaluated for a Fermi-Dirac distribution through the expression

$$< v^2 >= \frac{1}{\hbar N_e} \int_0^\infty \left(\frac{\partial E}{\partial k}\right)^2 n_{FD} g(E) dE \qquad (2.32)$$

where $g(E) = (k/\pi)^2(dk/dE)$ is the density of states, $n_{FD} = 1/(1 + e^{(E-E_F)/k_BT})$ is the Fermi-Dirac distribution function, and E_F is the Fermi energy. Assuming a parabolic conduction band, the mean square velocity can be expressed in terms of the Fermi integrals $\mathscr{F}_{1/2}$ and $\mathscr{F}_{3/2}$ by

$$< v^2 >= \frac{3k_bT}{m^*} \frac{\mathscr{F}_{3/2}(\eta)}{\mathscr{F}_{1/2}(\eta)} \qquad (2.33)$$

where $\eta = E_F/k_bT$ is the reduced Fermi energy. The Fermi integrals are defined as [11]

$$\mathscr{F}_j(\eta) = \frac{1}{\Gamma(j+1)} \int_0^\infty \frac{x^j dx}{1 + e^{(x-\eta)}} \qquad (2.34)$$

where $\Gamma(1 + \frac{1}{2}) = \sqrt{\pi}/2$ and $\Gamma(1 + \frac{3}{2}) = 3\sqrt{\pi}/4$.

In the classical and degenerate limits, the expression 2.33 gives the well-known results $< v^2 >_{cl}= 3k_bT/m^*$ and $< v^2 >_{dg}= \frac{3}{5}v_F^2$, respectively. Usually, the classical and degenerate limits are considered to simplify calculations. However, these approximations can affect the determination of the coupled frequencies.

When the collision damping Γ_e is neglected, the frequencies of the coupled modes can be again obtained from the zeroes of the dielectric function. The resulting expression is equivalent to the equation 2.30 but in this case the plasma frequency is wavevector dependant and is given by $\omega_p^2(q) = \omega_p^2(0) + < v^2 > q^2$, where $\omega_p(0)$ is the natural plasma frequency used in the Drude model.

To emphasize the spatial dispersion of plasmons, which is neglected by the Drude model, the wavevector dependence of the L^+ and L^- frequencies is plotted in figure 2.36 for *n*-type GaAs with an electron density of $N_e = 1 \times 10^{18}$ cm^{-3} and $\Gamma_e = 0$ cm^{-1}. As can be seen, the coupled mode frequencies substantially shift upwards with increasing the wavevector. Hence, for a specific electron density, frequency shifts of the coupled modes are expected in measurements carried out by using different excitation wavelengths.

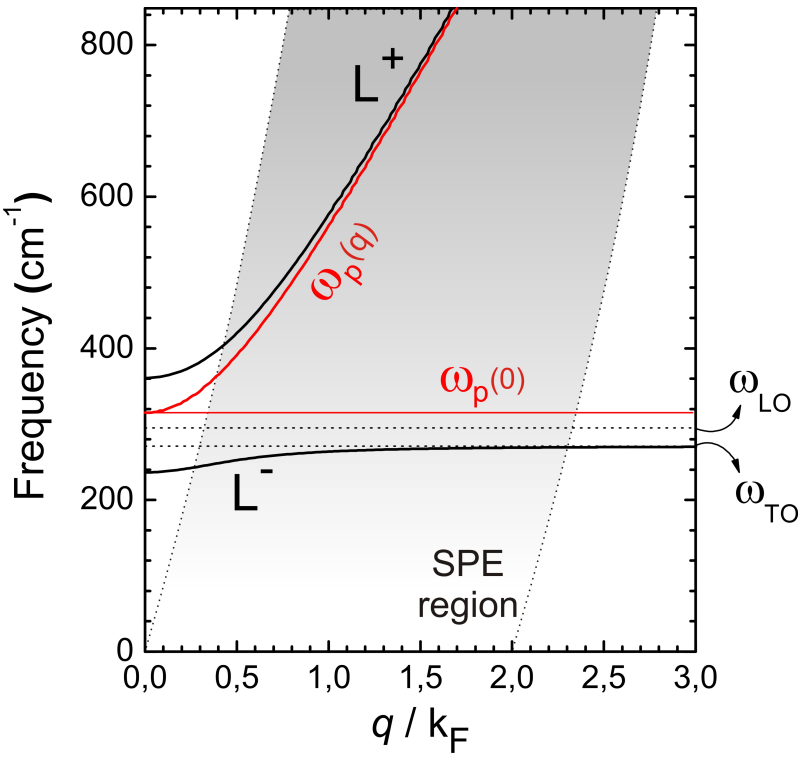

Figure 2.7: Frequency of the L^+ and L^- coupled modes in *n*-type GaAs as a function of the wavevector, calculated by the Hydrodynamical model in the degenerate limit. The electron charge density is $N_e = 1 \times 10^{18}$ cm^{-3} and the electron and ionic dampings have been neglected. The hatched region corresponds to that affected by the Landau damping. The red curve describes the frequency of the plasma oscillations as a function of the wavevector.

Although the Hydrodynamical model gives a better description of the coupled LO phonon-plasmon modes than the Drude model, it must be borne in mind that the model presents some limitations. One of the limits of applicability of the HD model is defined by the Landau damped region, since Landau damping is neglected in this model.

Landau damping and the Lindhard-Mermin model

When the phase velocity is comparable to that of the thermal speed of the free charge, the wave is able to *catch* the charged particles and transfer energy between them, which is known as the Landau damping. This process must fulfill energy and momentum conservation, which is expressed by

$$\frac{\hbar^2}{2m^*}k^2 + \hbar\omega_p(q) = \frac{\hbar^2}{2m^*}(\vec{k}+\vec{q})^2, \qquad (2.35)$$

where $\vec{q}$ is the plasmon wavevector and $\vec{k}$ is the particle wavevector. In the case of a degenerate electron gas, the wavevector $\vec{k}$ must be smaller than the Fermi wavevector k_F. Hence, the excitation energy $\hbar\omega_p$ must lie within the interval

$$\left[\frac{\hbar^2}{2m^*}(q^2 - 2qk_F), \frac{\hbar^2}{2m^*}(q^2 + 2qk_F)\right] \tag{2.36}$$

The region defined by equation 2.36 is represented in figure 2.36 by the hatched region. This region frames the SPE regime, in which the collective modes cease to be well defined by the Hydrodynamical model because energy transfer from the collective excitation to a single electron is possible. Therefore the lifetime of plasmons is reduced due to their decay into single-particle excitations. The Landau damping cannot be reproduced by higher values of the phenomenological damping parameter Γ_e used in the Hydrodynamical model, since they are different in nature.

Mermin [12] proposed a more complete description of the response of the free-charge system, called the Lindhard-Mermin (LM) model. The LM susceptibility is obtained from a quantum mechanical approach, which includes dispersion of the collective excitations, statistics of the free carriers as well as non-parabolicity effects, and is given by

$$\chi_e(q,\omega) = \frac{(1 + i\Gamma_e/\omega)\chi_e^L(q, \omega + i\Gamma_e)}{1 + i\Gamma_e\chi_e^L(q, \omega + i\Gamma_e)[\omega\chi_e^L(q,0)]^{-1}} \tag{2.37}$$

where the Lindhard susceptibility $\chi_e^L(q,\omega)$ is given by

$$\chi_e^L(q,\omega) = \frac{e^2}{2\pi^3 q^2}\int n_{FD}(E_f, T, k)\frac{E(\vec{q}+\vec{k}) - E(\vec{k})}{[E(\vec{q}+\vec{k}) - E(\vec{k})]^2 - (\hbar\omega)^2}d^3k \tag{2.38}$$

and $E(\vec{k})$ is the conduction band dispersion.

Although the LM model only considers the intraband contribution, its formulation is powerful enough to describe coupled modes at all wavevectors, including those in the SPE regime. However, the main drawback for the Lindhard-Mermin model is the complexity of the calculations involved. By contrast, the Drude and Hydrodynamical models yield simple analytical expressions for the electronic susceptibility.

In the small-q limit and far from the Landau damping regime, the expression for the free-charge susceptibility given by either the LM or the HD models coincides. In the studies dealing with LOPCMs presented in this thesis, the optical modes lie far from the Landau damping regime and thus we will use the Hydrodynamical model to keep analytical expressions and to avoid computing intensive calculations.

References

[1] F. Bassani and G. P. Parravicini, *Electronic States and Optical Transitions in Solids*. Pergamon, Oxford, 1975.

[2] P. Yu and M. Cardona, *Fundamentals of Semiconductors*. Springer-Verlag, Berlin, Germany, 1998.

[3] H. Montgomery *Proc. Roy. Soc. A.*, vol. 309, p. 521, 1969.

[4] H. Harima *J. Phys. Condens. Matter*, vol. 14, p. R967, 2002.

[5] D. T. Hon and W. L. Faust *Appl. Phys.*, vol. 1, p. 241, 1973.

[6] M. V. Klein, N. Ganguly, and P. J. Colwell *Phys. Rev. B*, vol. 6, p. 2380, 1972.

[7] N. W. Ashcroft and N. D. Mermin, *Solid State Physics*. Holtz, Rinehart & Winston, Philadelphia, USA, 1976.

[8] B. K. Ridley, *Quantum Processes in Semiconductors*. Oxford University Press, Oxford, UK, 1988.

[9] M. Cardona and G. Guntherodt, eds., *Light Scattering in Solids IV*. Springer, Berlin, Germany, 1984.

[10] U. Nowak, W. Richter, and G. Sachs *Phys. Status Solidi B*, vol. 108, p. 131, 1981.

[11] J. S. Blakemore *J. Appl. Phys.*, vol. 53, p. R123, 1982.

[12] N. D. Mermin *Phys. Rev. B*, vol. 1, p. 2362, 1970.

"Nothing is too wonderful to be true, if it is consistent with the laws of nature, ain't in such things as these, experiment is the best test of such consistency."

Michael Faraday

3

Experimental: Raman set-up

The main experimental technique employed in this thesis is the Raman spectroscopy. In this chapter, we will explain in detail the experimental set-up used in our studies.

3.1 The Jobin Yvon T64000 spectrometer

All the Raman spectra presented in this thesis were carried out using a Jobin-Yvon T64000 spectrometer, which is set at the *Institut Jaume Almera* (CSIC), in Barcelona. Figure 3.1 is a detailed sketch of the experimental set-up. All the equipment is placed on a optical table with pneumatic legs, which isolates the system from external vibrations.

For backscattering measurements in the macrocamera configuration, the laser light is directed towards the sample by the backscattering mirror (BM) and focused by a convergent lens (CL). The spot on the sample has an area of about $185 \times 285\ \mu m^2$ for the Ar^+ laser. For non-backscattering analysis, the excitation laser light is directed towards the sample through a mirror with adjustable angle of incidence (MO). In both cases, the scattered light is collected by the CL and focused at the spectrometer entrance slit (S_0). Previous to S_0, a polarizer (P) permits to select the polarization of the collected light.

Micro-Raman experiments were also carried out in this work. For this configuration, the laser beam is directed towards an *Olympus* BX41 microscope, instead of the macrocamera stage. A set of objectives with 10, 50, 80 and 100 magnifica-

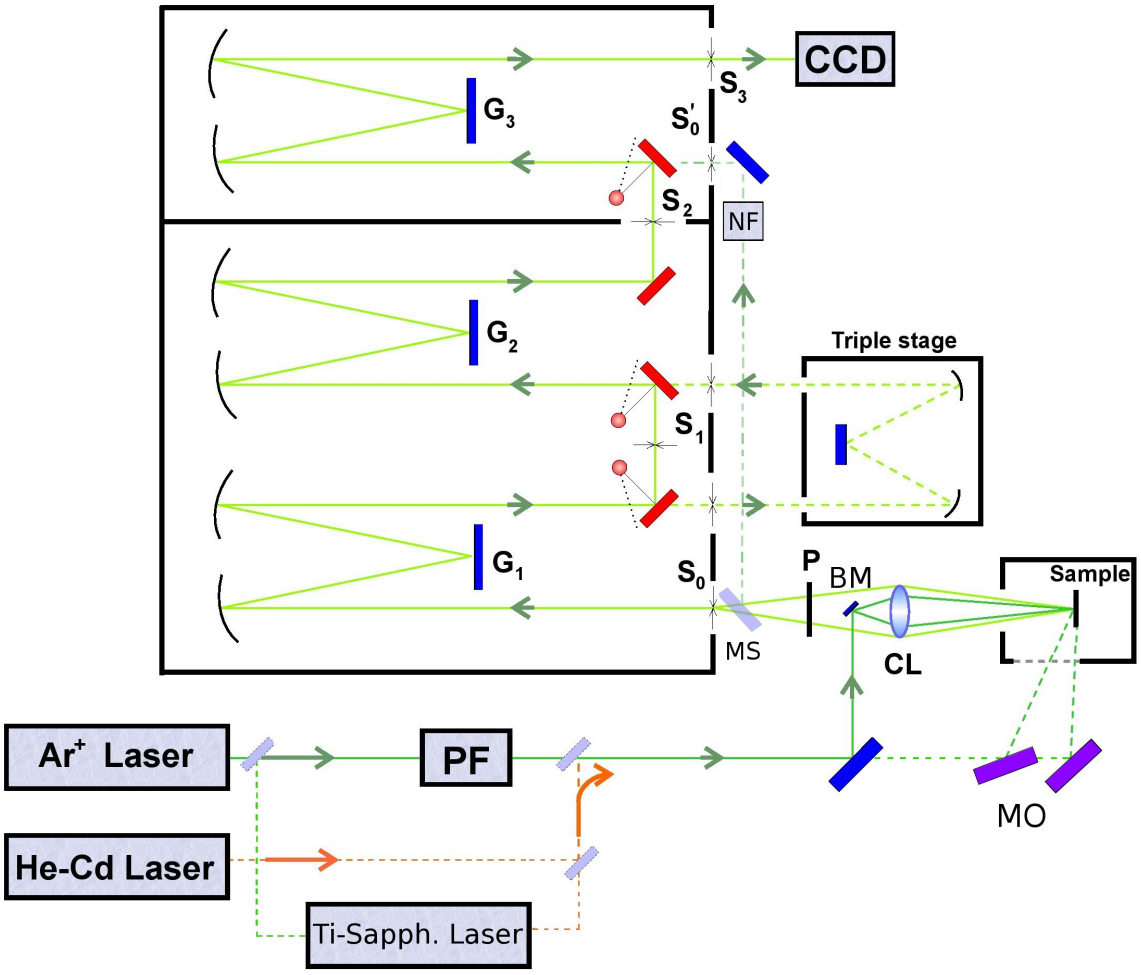

Figure 3.1: Sketch of the Raman spectrometer used in this work

tions are available for experiments in the visible spectral range. For measurements using the UV laser source, a 40 magnification objective is available. A micrometer pinhole at the microscope output can be regulated in order to adjust the signal depth profile. For a 100 μm-diameter pinhole, the depth resolution is about 1μm. By reducing the pinhole diameter to 50 μm, the probing depth reduces to nearly 0.5 μm.

Inside the spectrometer, a set of gratings is used to scatter the collected light and redirect it to the detector. The available grating lines per millimiter and blaze wavelegths are:

1. three 1800 grooves/mm gratings blazed at 500 nm, with a spectral range from 450 to 900nm. These gratings are used for Raman scattering measurements

in the visible range.

2. three 2400 grooves/mm gratings with the blaze wavelength at 400 nm, which are used for UV-Raman experiments. Their spectral range is from 300 to 800 nm.

3. a 1200 grooves/mm grating blazed at 330nm, for UV-photoluminescence (PL) measurements.

4. a 600 grooves/mm grating with the blaze wavelength at 500 nm, for PL measurements in the visible range.

The Raman spectrometer is equiped with a front-illuminated open electrode Charged Coupled Device (CCD) detector. It consists of a 1024×256 array of 26×26μm^2 silicon photodiodes that allow multichannel detection of visible, infrared and ultraviolet light (from 200 to 1000 nm with an average quantum efficiency of 40%). The outstanding sensitivity, high speed and low noise CCD detector is optimal-working at about 140K. Hence, the CCD is cryogenically cooled with liquid nitrogen and warmed up by means of a resistance.

The Jobin-Yvon T64000 Raman spectrometer can be employed in three different configurations depending on the number of gratings used, with a maximum of three (G_1, G_2, and G_3). In the double subtractive configuration, the first grating (G_1) is used to scatter the light and the intermediate slit (S_1) blocks the wavelengths close to the excitation laser light. This avoids to damage the CCD detector. A second grating (G_2) is then used to re-focus the resultant light into the second slit (S_2). Finally, the third grating (G_3) scatters the light to be detected by the CCD. This is the conventional configuration, which allows to detect Raman signal with frequencies down to 3 cm^{-1} and with a spectral resolution of $\sim$2 cm^{-1} (for a 100μm entrance slit using visible light).

In the triple additive configuration, an alternative optical path for the scattered light inside the spectrometer is used. The optical path now includes the triple stage chamber, as depicted in fiure 3.1. Contrary to the double subtractive arrangement, the three gratings are used to scatter the collected light in the triple additive configuration. The intermediate and the final slits (S_1 and S_2) do not act in the triple configuration. This configuration offers the best spectral resolution (0.7 cm^{-1} for 100μm slit using visible light), so it can be assumed that the Raman peaks directly reflect the intrinsic width of the vibrational modes. On the counterpart, signal below 200 cm^{-1} cannot be detected.

In the single configuration, the scattered light is directly guided to the third grating by the MS mirror and enters the spectrometer through a secondary entrance slit (S_0'). In this case, a notch filter (NF) is needed previous to S_0' to block the reflected excitation laser light. This configuration is mainly used for IR-Raman, UV-Raman or photoluminescence measurements.

3.2 Excitation sources

Different lasers have been used as exciton source. First, an Ar^+ laser (*Spectra-Physics* M2045-15) with its characteristic spectral lines from the green to the near ultraviolet region. The laser can be operated in single- or multi-line. For the latter, an output power up to 15 W is available in the visible spectral range and to 2 W in the UV range. The beam diameter is down to 1.65 mm. For single-line operation, undesired lines related to electronic transitions of the ionized argon are avoided by a difraction plasma filter (PF) with 1 nm bandpass, which is placed at the laser output.

Second, for UV measurements, a *Kimmon* TEM_{00} He-Cd laser is employed, which provides wave illumination at 325nm with a source power of 50 mW. The laser beam diameter is of 1.15 mm.

Finally, near infrared experiments are performed with a continuous wave tunable Ti-Sapphire laser (*Spectra-Physics* M3900S) pumped with the Ar^+ laser in the multi-line configuration. The tunning range is from 700 to 980 nm, where the maximum output intensity is obtained at the wavelegth of 780nm. The beam diameter is 0.95 mm.

3.3 Temperature-dependent measurements

Temperature-dependent Raman measurements are carried out with any of the two cryostat systems, whose pictures are shown in figure 3.2. For the macrocamera configuration, a TBT-*Air Liquide* nitrogen cryostat is used to vary the sample temperature from 80 to 380 K.

For micro-Raman measurements, a Linkam freeze drying cryo stage (FDCS196) is employed. The Linkam stage allows samples to be held at temperatures from 80 K up to 400 K. The temperature is measured by a Pt100 resistor mounted close to the sample, and its stability range is less than 0.1° at low temperatures. The top lid which seals the sample chamber has an ultra-thin lid window mounted above a ceramic crucible. A tube carrying recycled warm N_2 is placed over the lid, to prevent

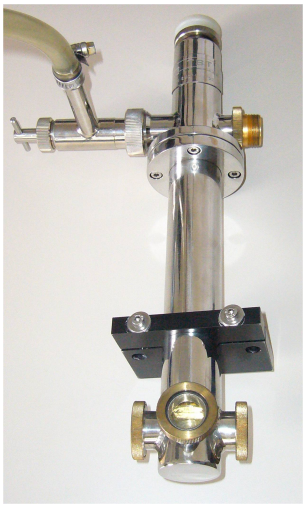

(a) TBT nitrogen cryostat for macro-Raman measurements.

(b) Linkam cryo-stage for micro-Raman measurements.

Figure 3.2: Cryostat systems used in this thesis.

condensation forming on the lid window. A Linkam high-temperature stage was also used in this thesis to extend the temperature range up to 750 K for the micro-Raman configuration. Both stages, the high and low-temperature stages, are designed to operate with a long working-distance (w.d. $= 4.5$ mm) $80\times$ objective to focus the light through the cryostat window. A cooling jacket is used to protect the objective for the high-temperature measurements.

The sample is normally glued to any of the mountings (in macro or micro- camera configurations) with thermally conductive silver paint, and external control units monitor and mantain the sample temperature set by the user.

3.4 Angular dependent measurements

For angular dependent Raman measurements, two special sample-holders were fabricated for the macrocamera stage (figure 3.3). The aim was to vary the scattering geometry from $x(zy)\bar{x}$ to $z(xy)\bar{z}$, and from $x(yy)\bar{x}$ to $z(yy)\bar{z}$, considering z to be parallel to the c-axis of the wurtzite structure (see chapter 4). For the first (second) configuration, sample holder in the left (right) picture was used. The angular resolution of either sample holders is less than 5°.

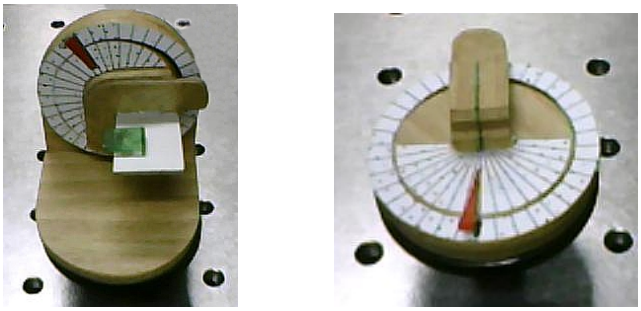

Figure 3.3: Picture of the home-made goniometre sample-holders fabricated for the angular dependence of ZnO optical phonons study.

3.5 Spectrometer calibration

Raman measurements are very sensitive to the optical alignment of the system and to the laboratory temperature. Since accurate frequency shifts of the Raman signal are often required, a careful calibration of the spectrometer is thus needed.

Crystalline silicon exhibits a strong and sharp first-order Raman mode at 521 cm^{-1} at room temperature for visible light excitation. The calibration procedure throughout all the experimental work of this theses was carried out with the same piece of silicon wafer.

For measurements performed by exciting with the UV laser source, a second frequency calibration method is available from the laser plasma lines, which are sharp and have very well defined frequencies. Finally, it should be noted that the Raman measurements are performed in a darkened laboratory with stable temperature controlled by an air conditioner.

"A man should look for what is, and not for what he thinks should be."

Albert Einstein

4

Raman scattering in as-grown and implanted ZnO

4.1 Introduction

The study of vibrational properties of ZnO dates back to the late sixties and seventies [1–3], when the quality of ZnO crystals was still low. The full set of the wurtzite ZnO optical modes (E_1, A_1 and E_2) were firstly observed and identified according to their polarization selection rules by Arguello *et al.* [2]. Resonance Raman scattering of first and second order modes were investigated by Calleja *et al.* [3]. These early studies were affected by the low spectral resolution of the available equipment and low crystal qualities, which has led to some controversies, including the assignment of second order modes, mode frequencies and assymetries.

So far, the knowledge of the lattice dynamics of ZnO still remains rather limited. In fact, only recent Inelastic Neutron Scattering (INS) measurements of the acoustical and optical phonon branches through some high symmetry points of the Brillouin zone have been reported [4]. Before the availabity of these experimental data, Density Functional Theory (DFT) calculations of the phonon dispersion in ZnO [5] have been the guide for the interpretations of the experimental data concerning lattice dynamics.

In the last few years major advances have been made in growth techniques, which

have made available high-quality large-area bulk ZnO single crystals and epitaxial layers. The recent adoption of ZnO as a technological key material demands a reliable, accurate and fundamental study of its lattice dynamics. The Raman analysis of high-quality samples makes possible a better understanding of the ZnO vibrational properties, which are greatly altered by crystal quality and disorder.

Besides, many fields of semiconductor science and technology are highly affected by phonon decay mechanism and lifetimes. For example, the E_2^{low} mode of ZnO has been recently found by means of impulsive stimulated Raman scattering to have a lifetime of 200 ps [6]. This long lived phonons could be drawn to mediate interactions between q-bits and hence, to be used for quantum cryptography and computing. Hence, the study of phonon decay mechanisms and lifetimes is noteworthy for the development and improvement of devices, and can be assessed by studying the Raman lineshapes.

On the other hand, longitudinal optical phonons play also a major role in the fundamental and practical limits of devices. Their lifetimes and interactions with carriers determine important parameters such as saturation velocities and carrier thermalization dynamics. While lifetimes of LO phonons in AlN and GaN have been already reported [7, 8], data for ZnO is very scarce. Phonon lifetimes and decay mechanisms can be evaluated by temperature-dependent Raman measurements. The evolution of Raman line shapes with temperature has also been used to monitor the local temperature in AlGaN/GaN HFETs [9].

Also, optical phonons exhibit unique characteristics in anisotropic crystals. When the crystal high-symmetry axes are tilted relative to the phonon propagation direction, a mixing of the polar modes takes place. This gives rise to the so-called quasimodes [10] and their frequency changes depending on the light propagation direction. Apart from their intrinsic interest from a fundamental point of view, the dependence of quasimodes on light incidence is of relevant importance in the phonon analysis of ZnO nanostructures [11], where the high symmetry axes might be randomly oriented. Raman spectroscopy is the technique of choice for many studies of semiconductor nanostructures [12–14] in order to assess their vibrational and optical properties, and to extract further information about strain, composition, confinement, temperature, electron-phonon coupling, etc. However, ignoring the excitation of quasimodes in nanostructures could result into a misleading analysis of any of the mentioned properties.

Some works dealing with quasimodes in bulk AlN and GaN have been published [1, 2, 15, 16]. Considering the importance of either bulk and nanostructures

ZnO for high-speed, high-power and optoelectronic devices, similar information is in high demand for this material. Early works on quasimodes in ZnO were performed in the late 1960s, but only showed spectra for a 45° phonon propagation direction [1,2].

Nevertheless, in order to perform ZnO-based devices it is essential to achieve both *n*-type and *p*-type doping of ZnO. In the first chapter of this thesis, the problematic with *p*-type doping in ZnO was introduced. Many techniques are used to introduce dopants in semiconductors. Ion implantation represents a very attractive processing tool for several technological steps, including selective-area doping and good control of incorporated dopants [17]. However ion-beam-induced lattice disorder is undesirable for technological applications and the crystal lattice must be subsequently recovered, usually by thermal annealing.

Most studies on ion-implantation processes in solids focus on understanding several fundamental aspects, such as the degree of crystal damage and the nature of the ion-beam-induced defects [18, 19], the degree of lattice incorporation of the implanted ions [20], etc. While the implantation-induced damage and the subsequently crystal recovery by thermal annealing is difficult to assess by the customary optical characterization techniques such as PL, Raman scattering can provide this information [21]. The usefulness of Raman scattering in the study of damaged implanted and annealed wide band-gap semiconductors has been demonstrated in previous studies [21–23]. Disorder related modes due to longitudinal optical branches have been observed for ion-damaged ZnO [24], which are healed with high-temperature thermal annealings.

Thermal annealing steps are also performed to relax the implanted impurities into substitutional positions and to electrically activate them. Hall measurements give information about the free-carrier density and mobility in the implanted layers. In ZnO, it has been found that the electrical activation rate in ZnO is usually small because of the high activation energies, self-compensation by native defects, and formation of electrically inactive stable complexes [25]. In this regard, the lattice incorporation of the impurities and the formation of impurity complexes can be qualitatively studied by Raman scattering. In particular, the observation of local vibrational modes (LVMs) can be used as a fingerprint of impurity incorporation and/or complex formation.

N is one of the most important candidates for *p*-type doping ZnO [26]. Nevertheless, the thermodynamics of N incorporation into the ZnO lattice is complicated [27]. Considerable number of vibrational studies have focused on the characterization of the impurity incorporation and formation of complexes that may reduce the dop-

ing efficiency of ZnO:N [24, 28–32]. These studies have revealed that the Raman spectrum of N-doped ZnO shows some characteristic features associated with N doping at 275, 510, and 644 cm^{-1}. The origin of these features is still controversial. While references [24, 28, 31, 33] attributed the emerging peaks to N local vibrational modes, Bundesmann *et al.* [34] claimed that their origin is intrinsic to the lattice, since they observed the same modes for Fe, Sb, and Al implanted ZnO without nitrogen. Accordingly, Manjon *et al.* [30] suggested that the observed modes correspond to wurtzite-ZnO silent modes, which are allowed by the breakdown of the translational crystal symmetry induced by defects and impurities. Theoretical calculations combined with experimental measurements presented by Wang *et al.* [31] indicated the lowest frequency mode (275 cm^{-1}) to be induced by zinc-related complexes, and the rest to be disorder induced. So far, no experimental evidence has been given for the participation of N motion in the additional modes observed in ZnO:N.

In this chapter, we will investigate the first and second order Raman modes of bulk ZnO, by probing a high-quality ZnO single crystal by means of high-resolution Raman spectroscopy. We will study in detail second order and first order optical modes and their decay mechanisms by using several configuration geometries and sample temperatures. We will also assess the effects of ion implantation on the Raman spectrum of ZnO and we will give some insight into the origin of certain LVMs observed in N implanted ZnO.

4.1.1 Aim

The aim of this chapter can be arranged around the main following points:

- To present a comprehensive and accurate study of the first and second order modes of high-quality bulk ZnO. This includes selection rules, line-shapes, lifetimes, and angular and temperature dependence of the phonon modes.
- To characterize the effects of ion implantation on ZnO.
- To evaluate the effectiveness of Rapid Thermal Annealing for the lattice recovery of implanted ZnO.
- To give a contribution to unravel the origin of possible additional Raman modes in the N-implanted ZnO by means of an isotopic study.

4.2 Groundwork

In order to accomplish the aims of this chapter, a theoretical background is required to understand, analyze and discuss the experimental results. For this reason, in this section we introduce the theory involved in the temperature dependence of phonons in terms of anharmonic decay. Also, we will introduce the Loudon's model for uniaxial crystals, which describes the angular dependence of optical phonons in anisotropic crystals. Finally, we present the main effects of non-pure crystals to its Raman spectrum, from local defects to amorphisation.

4.2.1 Temperature dependence and anharmonic decay of phonons

Raman shift, line width and peak intensity are expected to vary with temperature. The common features observed when increasing the sample temperature are a broadening of the Raman lines accompanied by a blue (red) frequency shift of the Stokes (anti-Stokes) peaks. That is, the phonon frequencies decrease with increasing the temperature. The amount of shift and broadening varies for different phonons and samples. These features can be qualitatively understood in terms of the anharmonic forces in the crystal lattice and thermal expansion of the lattice. In this section we will explain how the anharmonic decay of phonons account for the finite widths of Raman peaks, the temperature effects on Raman frequencies and widths, and the way to obtain a value for the phonon lifetimes.

Up to now, we have studied phonons within the harmonic approximation, i.e. we have kept only quadratic terms of the atomic displacements in the lattice total energy. This harmonic approximation represents phonons as *particles* with infinite lifetime. If we add third and higher order terms in the atomic displacements to the lattice energy, the harmonic functions are no longer eigensolutions of the vibrational Hamiltonian. Unfortunately, the mathematical treatment is no longer as simple as in the harmonic case. To solve the equations of motion is not a trivial issue. Thus, in the anharmonic case one can consider the solutions for the harmonic potential as a first approximation to the true solution, which becomes progressively less accurate with time.

In other words, phonons may have a finite lifetime τ, which is related to the

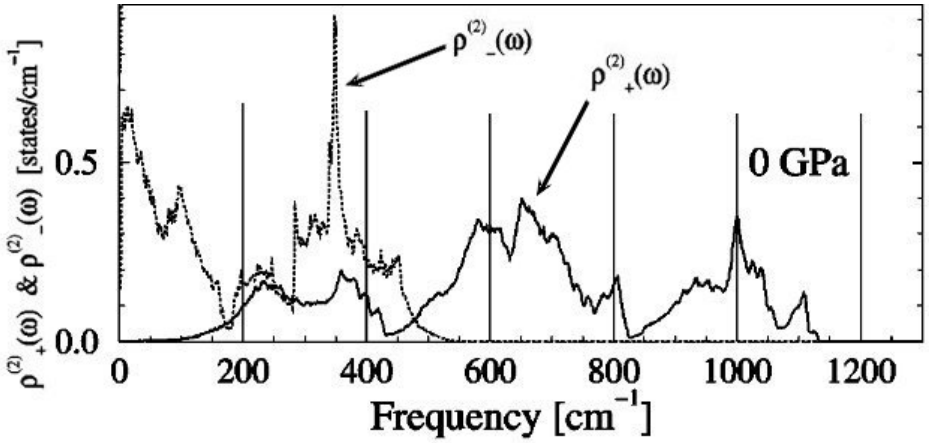

Figure 4.1: ZnO two-phonon DOS calculated by Serrano *et al.* using Density Functional Theory [5].

spectral width of the phonon (full width at half maximum) by the energy-time uncertainty relation $\Gamma\tau \sim \hbar$, where $\hbar$ is the reduced Planck constant (5.3×10^{-12} s cm^{-1}). For this reason, in modern language phonons are referred to as *quasiparticles*, which have a complex frequency dependent contribution to the total energy due to interactions with the system, which is called self-energy [$\Sigma(\omega)$]. This complex self-energy can be written as $\Sigma(\omega) = \Delta(\omega) - i\Sigma_i(\omega)$. In semiconductors, $\Sigma(\omega)$ is induced by phonon-phonon interactions, isotopic mass disorder (when several isotopes of a given element are present in the crystal) and by phonon-electron interactions (in doped semiconductors). The complex self-energy is specific for each phonon and, for a given phonon, it is a function of frequency and temperature.

The phonon self-energy has been discussed in many theoretical papers since the early days of quantum mechanics. To lowest order in perturbation theory, the so-called first Born approximation, phonons decay into the creation of two lower energy phonons (ω_1 and ω_2) or into the anihilation and creation of two phonons (ω_1' and ω_2', respectively). This third order anhamonicity leads to the imaginary part of the self-energy to be proportional to the two phonon density of states (DOS) according to

$$\Sigma_i(\omega, T) = |V_3^+|^2[1 + n(\omega_1) + n(\omega_2)]\rho^+(\omega) + |V_3^-|^2[n(\omega_2') - n(\omega_1')]\rho^-(\omega), \quad (4.1)$$

where $V_3^{\pm}$ are the average third-order anharmonic coupling constants and $\rho^{\pm}(\omega)$ are the two-phonon sum and difference DOS, with the restrictions of energy and momentum conservation. The superscript in the anharmonic coupling constants

stand for the decay into a phonon sum (+) and difference (-). $n(\omega_i)$ is the Bose-Einstein occupation factor for the decaying modes. ω_i are the frequencies of the two decay phonons. The determination of these frequencies will be described later on.

Once the imaginary part of the self-energy is determined, we can find an expression for the real part $\Delta(\omega)$. Since the real and imaginary parts of the self-energy satisfy the Kramers-Kronig relation, $\Delta(\omega)$ can be expressed as

$$\Delta(\omega, T) = -\frac{\omega}{\pi}\mathscr{P}\int_0^\infty \frac{\Sigma_i(\omega')}{\omega'^2 - \omega^2}d\omega' \tag{4.2}$$

where $\mathscr{P}$ is the Cauchy principal value. This expression does not take into account the energy shift due to the thermal expansion of the lattice. Hence, an additional term must be added to the real part of the self-energy, so that $\Delta(\omega, T) = \Delta(\omega) + \Delta_0(T)$. The parameter that relates the thermal expansion of the lattice ($\alpha = \Delta a/a$) with the associated phonon frequency shift is the Grüneisen parameter γ, which is defined as $\gamma = -\partial(In\omega)/\partial(InV)$, where V is the volume of the unit cell. Then, the thermal expansion contribution to the frequency shift is

$$\Delta_0(T) = -\omega_{S0}\gamma\int_0^T [\alpha_c(T') + 2\alpha_a(T')]dT'. \tag{4.3}$$

For frequencies close to a specific phonon mode, the spectral function of this mode can be written as

$$I(\omega, T) \propto \frac{\Sigma_i(\omega, T)}{[\omega - \omega_{S0} - \Delta(\omega, T)]^2 + \Sigma_i^2(\omega, T)} \tag{4.4}$$

where ω_{S0} is the theoretical phonon frequency at zero temperature.

If the two 2-phonon DOS, $\rho^+(\omega)$ and $\rho^-(\omega)$, are virtually constant with frequency, then Σ_i and Δ become only temperature dependent, and the Raman scattering efficiency function describes a Lorentzian distribution about the frequency $\omega_{S0} + \Delta(T)$ and full width at half maxima $\Gamma(T) = 2\Sigma_i(T)$, so that

$$I(\omega, T) \propto \frac{\Gamma(T)}{[\omega - \omega_{S0} - \Delta(T)]^2 + (\Gamma(T)/2)^2} \tag{4.5}$$

with

$$\begin{aligned}\Gamma(T) &= A^+[1 + n(\omega_1) + n(\omega_2)] + A^-[n(\omega_2) - n(\omega_1)] \qquad \text{and} \\ \Delta(T) &= B^+[1 + n(\omega_1) + n(\omega_2)] + B^-[n(\omega_2) - n(\omega_1)] + \Delta_0(T).\end{aligned} \tag{4.6}$$

$A^\pm$ and $B^\pm$ are the anharmonic parameters and are related to the anharmonic coupling constants by $A^\pm = 2|V_3^\pm|^2\rho^\pm$ and $B^\pm = -(\mathscr{P}/2)|V_3^\pm|^2\rho^\pm$.

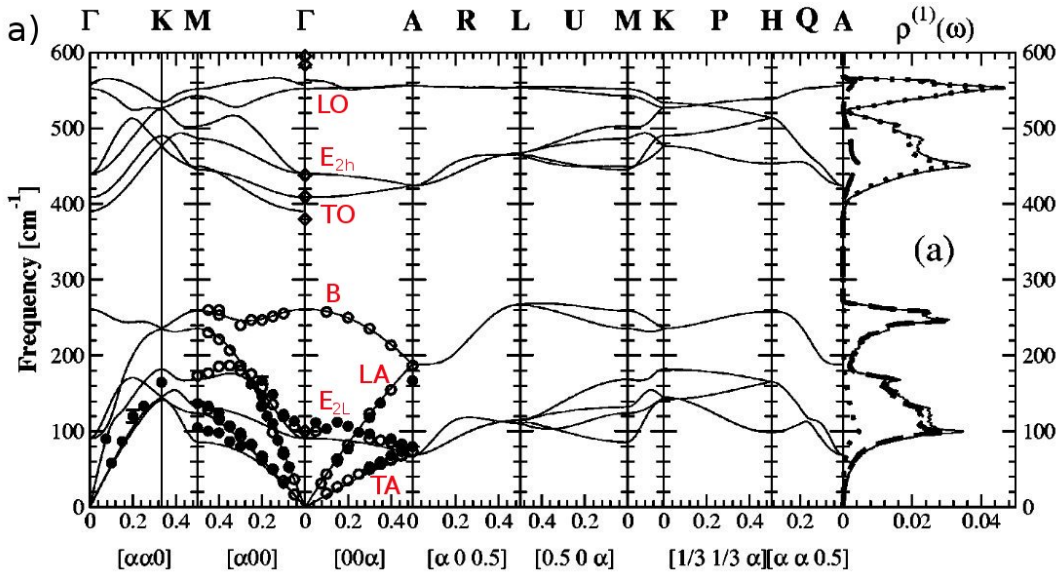

Figure 4.2: Calculated phonon dispersion relations and one-phonon DOS of the wurtzite ZnO. The solid and open circles display early inelastic neutron scattering data. Figure extracted from reference [5].

Conservation of energy requires that $\omega_1 + \omega_2 = \omega$ and $\omega_2' - \omega_1' = \omega$. Klemmens proposed the symmetric two-phonon decay process, in which $\omega_1 = \omega_2 = \omega/2$. However, this symmetry is hardly found in experiments. Hence, the assymmetric Klemmens channel was suggested, in which ω_1 and ω_2 are two acoustic modes whose frequency is determined by the one-phonon density of states and the dispersion curves of the material. This means that first-order phonons are more likely to decay into modes with high one-phonon DOS intensity obeying energy and momentum conservation.

For example, the ZnO phonon dispersion curve calculated by Serrano *et al.* [5] shown in figure 4.2, suggests that the most probable decay mechanisms for the E_2^{high} in ZnO (440 cm^{-1}) are into the sum of two acoustic modes at 190 cm^{-1} (TA[K]) and 250 cm^{-1}(LA[K]), and into difference between a longitudinal optical mode at 550 cm^{-1} (LO[M]) and acoustic mode at 110 cm^{-1} (TA[M]).

In contrast, for LO phonons does not exist any first-order phonon with enough energy to obey energy conservation in the decay into a difference. Concerning the decay into the sum of two modes in the wurtzite ZnO, LO phonons have higher energies than twice the energy of any available acoustic phonon. In this case, the typical decay channel of LO modes is found to be the Ridley channel [35], where the LO phonon decays into a transverse acoustic (TA) phonon and a transverse optical

(TO) phonon. Similarly to the E_2^{high} mode and assuming the Ridley channel as the decay route, the A_1(LO) mode of ZnO may decay into a TO at 455 cm^{-1} and a LA at 120 cm^{-1} from the branches along the L-M points. Similarly, the E_1(LO) mode may decay into the TO[L-M] at 490 cm^{-1} and a LA[L-M] at 100 cm^{-1}.

Correction of the spectrometer response function

Phonon lifetimes and the analysis of temperature dependence are extremely related to the Raman line shapes and frequency position. Unfortunately accurate determination of the true Raman line widths cannot be directly obtained from the measured widths in the experiments. All spectrometers have a limited spectral resolution and an associated broadening function. Also, frequency measurements must be sufficiently precise and stable to give reliable frequency shifts. In this sense, in our studies we probed high-quality bulk ZnO with the highest spectral resolution configuration available for our spectrometer(see chapter 3), as well as we evaluated the spectrometer induced broadening to the real Raman line widths.

The Raman signal measured is convoluted by the spectrometer broadening function. Some authors have used the extrapolation to zero spectrometer slit width to obtain the true phonon line width. Others, use Voigt functions for the spectral response, which allow to separate the processes that contribute to the line width, so that they can be independently evaluated. The two main contributions to be considered are: the natural Lorentzian line-shape of a Raman phonon signal, and the Gaussian instrument broadening function. Kielkopf developed a deep study in the convolution/deconvolution of response functions and gave an expression for the deconvoluted Lorentzian contribution to the full width at half maxima (FWHM) Γ_L [36, 37]

$$\Gamma_L = \Gamma_m - \frac{\Gamma_G^2}{\Gamma_m} \tag{4.7}$$

where Γ_m is the measured FWHM and Γ_G is the gaussian contribution due to the experimental equipment. Then, for extremely narrow emission lines, $\Gamma_L \sim 0$ and the measured FWHM is approximately Γ_G.

For our Jobin Yvon T64000, we used the 546.07 nm emission line of a Hg lamp. The peak was fitted by a Gaussian line shape, and we obtained a FWHM of $\Gamma_G = 0.44$ cm^{-1} for a 50μm entrance slit. According to the described procedure, we find corrections up to a 1% of the intrinsic FWHM of the phonons in ZnO, except for the E_2^{low} mode. This result means that the high-resolution Raman spectra with

50μm slits can be assumed to reflect the intrinsic FWHM of the ZnO modes. In the case of the E_2^{low} mode, the Raman peak observed is too narrow to be detected by standard Raman scattering experiments, and its width is actually an image of the slits. As mentioned earlier, this mode can be only resolved by impulsive stimulated Raman scattering (ISRS) [6].

The phonon lifetime and anharmonic decay of phonons are also relevant in other frameworks. For example, the energy loss rate of a carrier in a polar semiconductor is determined by both the rate at which the carrier's energy is lost by phonon emission and the rate at which the carrier gains energy from phonon absorption. The latter can be very important in low dimensional systems and structures, since the phonons emitted by energetic carriers (hot phonons) can accumulate and be re-adsorbed by electrons. Hence, the energy loss rate of carriers would decrease, preventing the good functionality of devices. Clearly, the total energy loss rate for such hot carriers highly depends on both lifetime and decay channels of optical phonons. Note that if the LO phonons decay into the typical Ridley channel, any of the decaying modes (TA and TO) are not available for absorption by carriers, which is of benefit for high-power devices. Hence, it is important to study phonon lifetimes and decay mechanisms in ZnO, as it is considered to be a good candidate for high-power devices.

4.2.2 Angular dependence of optical phonons

Optical phonons in anisotropic crystals require a further analysis than in isototropic materials. In 1964, Loudon predicted a model for the optical modes in uniaxial crystals [10]. In this section we will describe Loudon model in order to account for the dependence of optical phonons on the phonon propagation direction in anisotropic media.

As scarcely mentioned before, the dielectric function in anisotropic media must be expressed as a tensor. Wurtzite crystals, such as ZnO, are anisotropic media which exhibit an extraordinary index (n_e) for light propagating perpendicular to the c-axis and an ordinary index for light propagating along this axis. Then, the dielectric tensor can be expressed by

$$\varepsilon(\omega) = \begin{pmatrix} \varepsilon_{\parallel}(\omega) & 0 & 0 \\ 0 & \varepsilon_{\parallel}(\omega) & 0 \\ 0 & 0 & \varepsilon_{\perp}(\omega) \end{pmatrix} = \begin{pmatrix} n_o^2 & 0 & 0 \\ 0 & n_o^2 & 0 \\ 0 & 0 & n_e^2 \end{pmatrix} \tag{4.8}$$

Due to the anisotropy of the crystal, the TO and LO vibrations in which the atoms

are displaced parallel to the c-axis (A_1 modes) have different frequencies to the two degenerate vibrations in which the atomic displacements lie perpendicular to the c-axis (E_1 modes). The expression for each dielectric function is exactly the same as in equation 2.20, but replacing ε_∞, ω_{LO} and ω_{TO} by their corresponding values in the directions parallel and perpendicular to the c-axis. Similarly, Maxwell's equations must be doubled, and hence we obtain two types of phonon waves in uniaxial crystals: ordinary and extraordinary waves.

In ordinary waves, both the electric field and the polarization are perpendicular to the wave vector and also to the c-axis. By contrast, in extraordinary waves, the macroscopic electric field and the polarization are not simply parallel or perpendicularly polarized relative to the wave vector or the c-axis. In this case, the frequencies of the extraordinary waves depend on the angle θ between the wave vector $\vec{k}$ and the c-axis, according to the expression

$$\left[\frac{\omega_\perp^2\varepsilon_{0\perp}-\omega^2\varepsilon_{\infty\perp}}{\omega_\perp^2-\omega^2}\right]\cos^2\theta+\left[\frac{\omega_\parallel^2\varepsilon_{0\parallel}-\omega^2\varepsilon_{\infty\parallel}}{\omega_\parallel^2-\omega^2}\right]\sin^2\theta=0, \tag{4.9}$$

where $\omega_\perp$ and $\omega_\parallel$ stand for the TO frequencies vibrating along the c-axis or $\mathrm{in\text{-}plane}$, respectively. Making use of the Lyddane-Sachs-Teller relation for each direction, we can re-write equation 4.9

$$\left[\frac{\omega_{LO\perp}^2-\omega^2}{\omega_{TO\perp}^2-\omega^2}\right]\varepsilon_{\infty\perp}\cos^2\theta+\left[\frac{\omega_{LO\parallel}^2-\omega^2}{\omega_{TO\parallel}^2-\omega^2}\right]\varepsilon_{\infty\parallel}\sin^2\theta=0, \tag{4.10}$$

This equation gives rise to two solution branches, $\omega_1(\theta)$ and $\omega_2(\theta)$, which satisfy the modified Lyddane-Sachs-Teller relation

$$\left(\frac{\omega_1\omega_2}{\omega_\perp\omega_\parallel}\right)^2=\frac{\varepsilon_{0\perp}\cos^2\theta+\varepsilon_{0\parallel}\sin^2\theta}{\varepsilon_{\infty\perp}\cos^2\theta+\varepsilon_{\infty\parallel}\sin^2\theta}. \tag{4.11}$$

There are two limiting cases for equation 4.10:

(a) Strong anisotropy: $|\omega_{TO\perp}-\omega_{TO\parallel}|\gg(\omega_{LO\perp}-\omega_{TO\perp})$ and $|\omega_{TO\perp}-\omega_{TO\parallel}|\gg(\omega_{LO\parallel}-\omega_{TO\parallel})$. This means that the anisotropy is predominant over the long-range electrostatic forces that cause the TO-LO splitting. In this case, one of the solutions to equation 4.10 always lies in the vicinity of $\omega_{TO\perp}$ and $\omega_{LO\perp}$, and the other solution in the vicinity of $\omega_{TO\parallel}$ and $\omega_{LO\parallel}$. An approximate expression for the two solution branches to equation 4.10 is

$$\begin{aligned}\omega_1^2(\theta)&\approx\omega_{TO\perp}^2\sin^2\theta+\omega_{LO\perp}^2\cos^2\theta\\ \omega_2^2(\theta)&\approx\omega_{TO\parallel}^2\cos^2\theta+\omega_{LO\parallel}^2\sin^2\theta.\end{aligned} \tag{4.12}$$

Table 4.1: Typical phonon frequencies (cm^{-1}) at 300 K for optical modes in ZnO, GaN and AlN. ZnO data are extracted from our studies. The values for GaN and AlN derive from reference [20].

	A_1(TO)	E_1(TO)	A_1(LO)	E_1(LO)
ZnO	378	410	574	590
GaN	531	560	734	741
AlN	611	671	890	912

While the polarization of the high frequency branch $\omega_1(\theta)$ is approximately perpendicular to the c-axis for any angle θ, the polarization for the low frequency branch $\omega_2(\theta)$ lies nearly parallel to the c-axis. Hence, the solutions are called quasi-E_1 and quasi-A_1 modes, respectively.

(b) Strong bonding polarity: $|\omega_{TO\perp}-\omega_{TO\parallel}| \ll (\omega_{LO\perp}-\omega_{TO\perp})$ and $|\omega_{TO\perp}-\omega_{TO\parallel}| \ll (\omega_{LO\parallel}-\omega_{TO\parallel})$. In this case, the frequency difference caused by anisotropy $(\omega_{A_1}-\omega_{E_1})$ is small compared to that caused by the electrostatic forces$(\omega_{LO}-\omega_{TO})$. Similarly to the previous case, the two solution branches to equation 4.10 are approximately

$$\omega_1^2 \approx \omega_{TO\perp}^2 \sin^2\theta + \omega_{TO\parallel}^2 \cos^2\theta$$
$$\omega_2^2 \approx \omega_{LO\perp}^2 \cos^2\theta + \omega_{LO\parallel}^2 \sin^2\theta. \qquad (4.13)$$

Now the predominance of electrostatic forces over the anisotropy ensures that the polarization of the high frequency solution $\omega_1(\theta)$ slightly deviates from the longitudinal polarization. Also, the polarization of the lower frequency solution $\omega_2(\theta)$ does not significantly depart from the transverse polarization. In this limit, we talk about quasi-LO and quasi-TO modes, respectively.

ZnO lies within the second limit (long range distant forces are predominant over anisotropy), together with GaN and AlN (see table 4.1). Thus, quasi-LO and quasi-TO are expected for these semiconductors, rather than quasi-E_1 and quasi-A_1 modes. Effectively, the quasi-TO and quasi-LO behaviour in AlN and GaN layers can be observed in figure 4.3. So far, the angular dependence of quasimodes has not been reported. This dependence is of high importance for nanostructured material, for which the experimental configuration geometry of the Raman measurements is not

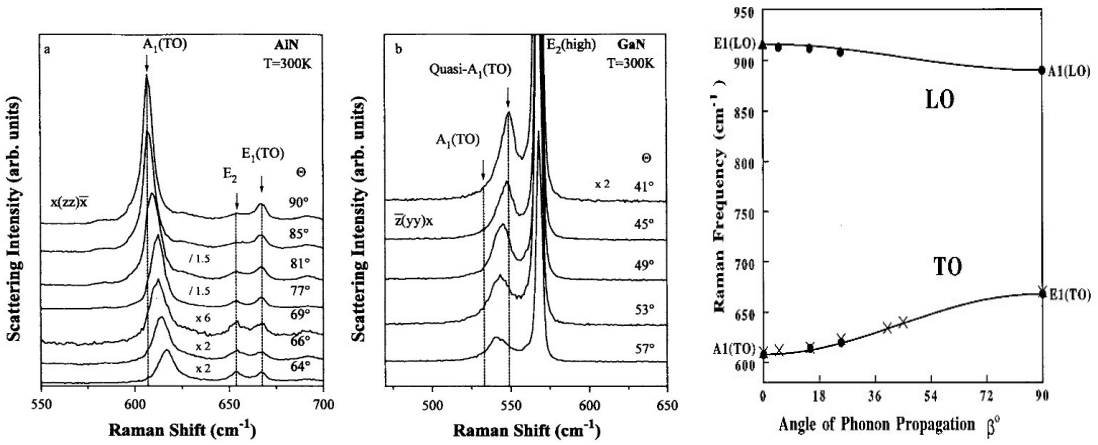

Figure 4.3: Angular dependence of the optical modes in a) AlN and b) and c) in GaN for different phonon propagation angles. θ in a) and b) is relative to the *c*-axis, while β in c) is relative to the *a*-axis. [15, 16]

well defined. With increasing interest of nanostructured ZnO, it is relevant to study quasimodes in ZnO.

4.2.3 Ion-implanted ZnO: Disorder Activated Raman Scattering and Local Vibrational Modes

Although ion-implantation is a very interesting technique to dope semiconductors, it induces structural damage to the crystal. This damage depends on the host material resistance as well as on the energy and atomic mass of the implanted ions. Highly energetic and heavy ions could even induce the amorphisation of the implanted layer in the host crystal.

Subsequent annealing treatments are essential for the lattice recovery and also for the lattice incorporation of the implanted ions. For ion-implantation doping processes, the position of the implanted species in the lattice determines the electrical and optical properties of the material. Because ZnO exhibits a strong dynamic annealing, defect migration is expected to promote the incorporation of implanted species into energetically favorable lattice sites. Hence, a high fraction of implanted dopants in substitutional positions even directly after implantation at room temperature is not unexpected (see reference [25] and references therein).

Disorder Activated Raman Scattering (DARS)

In order to understand the physics in ion implanted crystals, we can regard them as mildly imperfect crystals, with a small concentration of defects and/or any kind of disturbance of the translation symmetry. In this system, wave vector conservation rule in the Raman process breaks down. From the quantum mechanics point of view, we could say that the Bloch theorem does not apply, and hence the wave vector is not a good quantum number anymore. In this case, Raman spectrum is expected to display features reflecting the density of states (DOS). In particular, intense peaks in the DOS usually come mainly from flat regions in the LO, TO, LA, TA branches.

For instance, the DOS of ZnO (figure 4.2) shows a peak at around 580 cm^{-1}, which is mainly due to contributions of the flat LO branches around this frequency. For this reason, in the Raman spectrum of disordered ZnO a band around this frequency is expected. These bands related to disorder in the crystal lattice, which are mainly due to LO, TO, LA or TA branches, are called DALO, DATO, DALA or DATA bands, respectively.

For a completely amorphized material, its Raman spectrum directly reflects the one phonon DOS [38].

Local Vibrational Modes (LVMs)

When the density of defects/impurities is low enough to preserve translation symmetry in the crystal lattice, we deal with point or local defects. From the vibrational point of view, point defects may be regarded as isolated atoms (implying vacancies, interstitial atoms, antisites, impurities, etc.) in localized regions of the host crystal. The point defect is thus a perturbation on the dynamical matrix of the perfect crystal, representing the change of force constants and atomic masses. The resulting frequency for the new localized dynamic equations corresponds to the LVM frequency.

As a first approximation, we can assume that the force constants are not significantly changed by the point defect. Hence, in ZnO and for the case of an impurity in the O site, I_o, the LVM frequency can be roughly estimated by the empirical diatomic model, resulting in

$$\frac{\omega_{\mathrm{LVM}}}{\omega} \sim \sqrt{\frac{\mu(\mathrm{Zn}-I_o)}{\mu(\mathrm{Zn}-\mathrm{O})}}, \tag{4.14}$$

where $\mu(\mathrm{Zn}-I_o)$ and $\mu(\mathrm{Zn}-O)$ are the relative masses for the pairs $\mathrm{Zn}-I_o$ and $\mathrm{Zn}-O$, respectively. Hence, if the atomic mass of the vibrating atoms changes, the

frequency of the related LVM is expected to shift accordingly.

As we have seen, the frequency of the LVMs is very sensitive to the impurity chemical nature, its local environment and to the formation of complexes. Therefore Raman scattering of LVMs can provide useful information about the incorporation of impurities in a host lattice.

4.3 The ZnO samples

Bulk ZnO can be mainly grown by three methods: melt grown, vapor phase, and hydrothermal. Because of the high vapor pressure of ZnO, the first two growth techniques are difficult to control.

The ZnO samples used in our studies are single crystals grown by the hydrothermal growth method. Possible advantages of this method over other types of crystal growth include the ability to create crystalline phases which are not stable at the melting point. Also, materials which have a high vapor pressure near their melting points can also be grown by the hydrothermal method.

4.3.1 Hydrothermal ZnO

Hydrothermal synthesis consists in the growth of single crystals using a seed and nutrients solved in water. The crystallization vessels used in this technique are autoclaves (see picture in figure 4.4). These are usually thick-walled steel cylinders

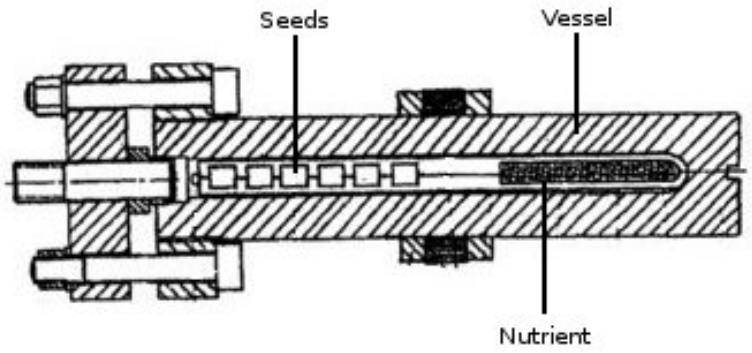

Figure 4.4: Experimental set-up for hydrothermal growth. The scheme is rotated 90° with respect to reality.

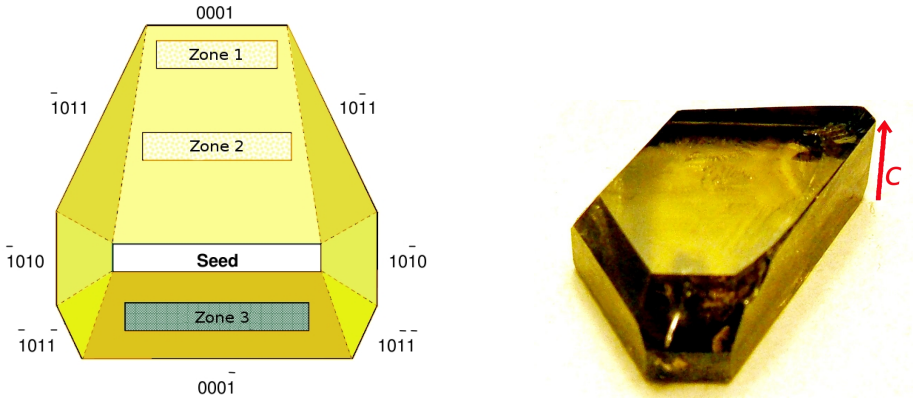

Figure 4.5: Growth scheme section of a hydrothermal ZnO (left) and picture of a hydrothermal ZnO sample (right) used in some of our studies.

with a hermetic seal which must withstand high temperatures and pressures for long periods of time. In order to isolate crystal growth environment from the walls of the autoclave, a sealed platinum lining is used.

The mineralizer solution, or nutrient, for the growth of our ZnO samples is a mixture of Li_2CO_3, 4NKOH, and 4NNaOH as solvent with the fill quantity at 80%, and the nutrient is prepared from 99.99% ZnO (Alfa Aesar) powder having particle size smaller than 3μm, which is sintered for 4 hours in air at 1350°C in a platinum crucible.

The nutrient and solvent are placed in the lower part of the autoclave, whereas the seeds (usually more than one) are hanged in its upper part. In our case, the seeds are (0001) plates of ZnO from previous hydrothermal growth runs.

The supersaturation is achieved by reducing the temperature in the crystal growth zone. The autoclave is heated in order to create two temperature zones. During growth, the nutrient zone is at 355°C with a temperature gradient of -10°C towards the seed zone. The nutrient dissolves in the hotter zone and the saturated aqueous solution in the lower part is transported to the upper part by convective motion of the solution. The cooler and denser solution in the upper part of the autoclave descends while the counterflow of solution ascends. The solution becomes supersaturated in the upper part as the result of the reduction in temperature. At this time, crystallization starts. The result is a ZnO single crystal, as depicted in figure 4.5. The polygonal shape of the crystal is due to the difference in growth rates between different crystallographic directions. The highest growth rate is found to be in the *c*-axis (10 mm per day). This growth is however anisotropic. A growth rate differ-

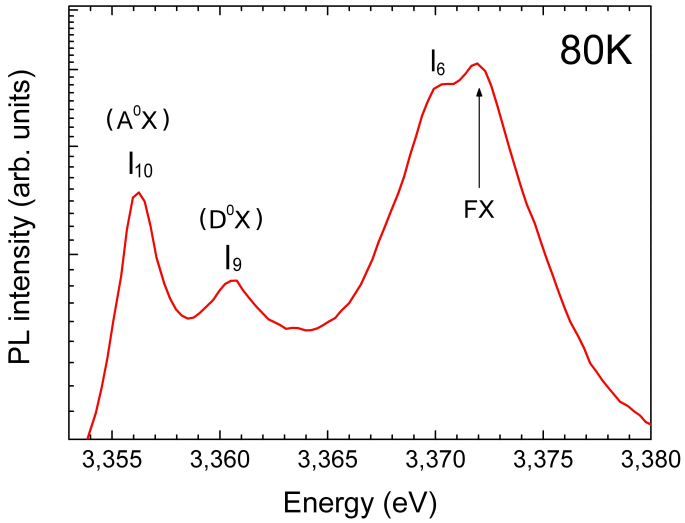

Figure 4.6: PL spectrum at 80 K from the reference hydrothermal ZnO sample.

ence exists between the Zn-terminated (C^+) and O-terminated (C^-) surface. The growth rate for the latter is 3 times slower than the first.

Right picture of figure 4.5 shows one of the samples that have been used in our studies. This sample is about a half of the as-grown single crystal, in which can be still observed the platinium ring that holds the seed in the autoclave. Hydrothermal ZnO used for our studies have been grown in either *Air Force Research Laboratory* (Hanscom, MA, USA) or *Tokyo Denpa Co.* (Japan). Appart from the sample in the picture, the samples studied here are slices of the as-grown crystals obtained from the zone labeled 1 in figure 4.5.

We checked the optical properties of all the samples by photoluminescence (PL) measurements at 80 K. In high quality bulk ZnO crystals, its optical spectrum is usually characterized by intense luminescence intensity with rich structure of excitonic lines. Appart from the free exciton lines, a neutral shallow donor bound exciton often dominates in the PL spectrum at 80 K because of the presence of donors due to unintentional impurities and/or shallow donor-like defects. One of the main impurity found in hydrothermal ZnO is hydrogen, whose fingerprint in the luminescence spectra was labelled I_4 [39]. Figure 4.6 shows a PL spectrum of the band edge region at 80 K for one of the hydrothermal ZnO samples. Free and the donor bound excitonic emissions are the predominant in our spectra. While the emission peak I_6 is attribut-

ted to the Al impurity, the I_9 and I_{10} peaks have not been yet associated to a specific chemical origin but proved to be neutral donor and neutral acceptor bound excitons, respectively [39]. Hydrogen related emission peaks (I_4 lines) are not observed in our PL spectra for any of our ZnO samples, which confirm the high-quality of the studied samples.

4.3.2 Sample treatments

Ion Implantation and RTA processes

For the doped ZnO studies we ion-implant hydrothermal ZnO with several species: N^+, P^+, Zn^+, and O^+. The first two are the potential candidates to obtain *p*-type ZnO, while the latter were chosen to give information about intrinsic lattice defects.

Multiple implantations at different energies were carried out to achieve a doping

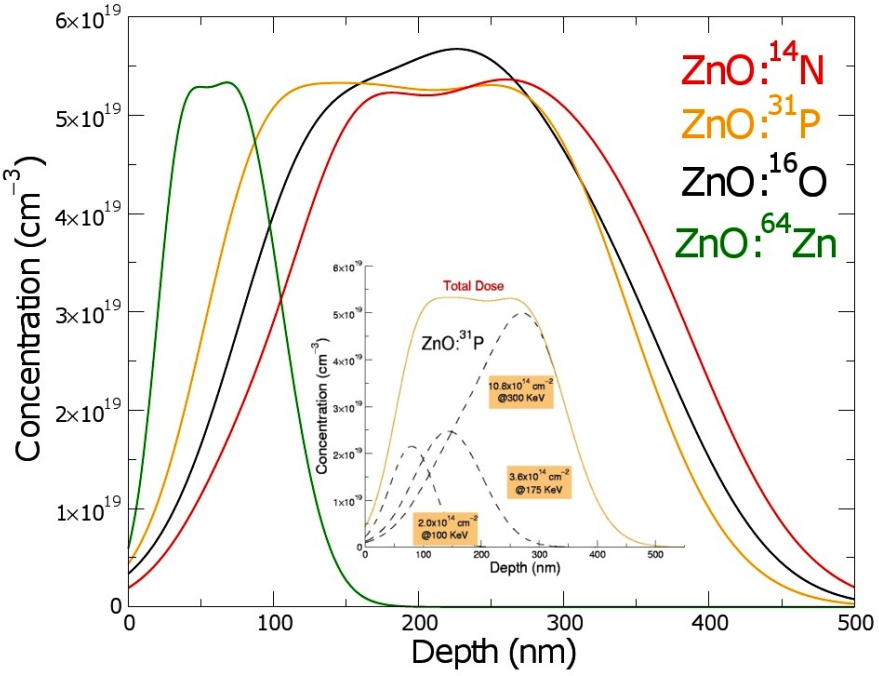

Figure 4.7: SRIM total depth profile simulation for ZnO implanted with N^+, P^+, O^+, and Zn^+. Inset: SRIM depth profiles for the individual implantations at different energies and the total doping profile for P-implanted ZnO.

profile with a flat homogeneous region and doping densities around 5×10^{19} cm^{-3} for about 220 nm. SRIM simulations were used to determine the corresponding implantation energies and doses for the selected ions (figure 4.7). For P^+ the implantation profile with higher energy (300 KeV) was achieved using double ionized P. For the heaviest ion implanted, Zn^+, double ionization was not available and a narrower profile with a 50 nm flat region was obtained.

The samples were all implanted at the *Departamento de Física Aplicada III* of the *Universidad Complutense* (Madrid), with a Varian CF3000 implantation system modified by the IBS (Ion Beam Services) company.

After ion implantation, the crystal lattice must be recovered. Usually, the recovery is achieved by thermal treatments. Semiconductors typically need annealing temperatures which are $\sim 2/3$ of their melting temperature to completely remove the ion-implantation-induced defects. Given the melting temperature of ZnO to be of $\sim$ 1975°C [25], this wide band-gap semiconductor is expected to recover form ion-bombardment damage at temperatures above $\sim$ 1300°C. However, it was found in As-implanted ZnO that annealings with temperatures above $\sim$ 1000°C leads to the decomposition and evaporation of the heavily-damaged layer, instead of the expected defect recovery and recrystallization [40]. Studies on ion-implantation in ZnO of different atomic species find that lattice defects can be removed by thermal annealing at temperatures between $\sim$ 800 and $\sim$ 1000°C [41–43]. In our experiments, we annealed the implanted bulk ZnO by the RTA method at 950°C for 10 s under a constant oxygen flux. Thermal annealings were also performed at the *Departamento de Física Aplicada III* of the *Universidad Complutense* (Madrid) using an ADDAX.RM system with a SiC susceptor.

Surface beveling processes

Although Raman scattering measurements do not require any special sample preparation, for the angular dependence of the optical modes sloping edged surfaces are essential. Due to Snell's law, phonon propagation angles larger than 30° with respect to the high-symmetry axes are not available when probing the typical (0001) / $(10\bar{1}0)$ / $(01\bar{1}0)$ faces. Fortunately, hydrothermal ZnO shows a natural beveled surface with an angle of 30° relative to the *a*-plane (see the growth scheme in figure 4.5). Probing this naturally beveled surface we are able to propagate light with angles up to 60° relative to the *a*-axis. In order to propagate light in any direction

between the *c* and *a*-axis, we need to bevel and polish a ZnO bulk crystal with a larger slope.

A depicted sketch of the resulted beveled sample is shown in figure 4.8. The 70°-beveled surface was polished by a chemomechanical process at NovaSiC, the leading company in ZnO polishing proceedures. This choice was made in order to reduce the effects on the optical properties of the sample, as we will explain in the following section.

Polishing effects on the optical properties

ZnO is known as a very soft material. Hence, the optical properties of ZnO might be affected by mechanical pressure and polishing procedures. For this purpose, we performed a two-step mechanical polish to hydrothermal ZnO. The first step consisted of a polish with consecutive grain sizes from 15μm to 5μm. This step was performed to remove the possible optically dead layer. Second, the sample was more accurately polished with diamond powder paste down to 1 μm particle size. The total removed layer was about 20μm thick.

Optical properties were checked by means of spatial-resolved Cathodoluminescence (CL) spectroscopy at 5 K. This technique offers not only in-plane resolution, but also a good control of the probing depth by adjusting the beam acceleration voltage and electron current.

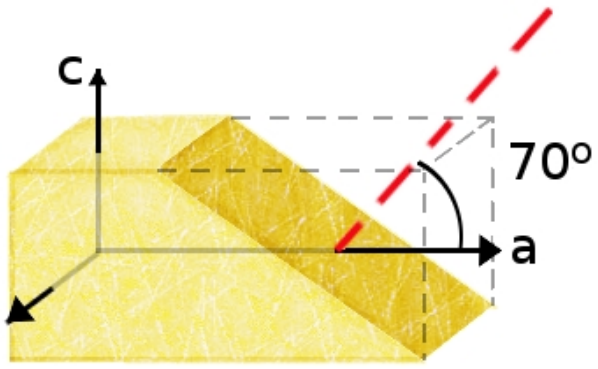

Figure 4.8: Sketch of a ZnO crystal with a beveled surface (dark region) of 70° relative to the *a*-plane.

At 5 K, the optical spectrum of ZnO is usually characterized by an intense luminescence intensity with a rich structure of excitonic lines. Up to 20 emission lines are listed so far [39]. Nevertheless, the polished surface under study shows only a weak luminescence intensity mainly influenced by the polishing. The averaged CL spectrum of the probed area (figure 4.9) shows a dominating near band edge luminescence and a broad defect band around 2.2 eV, which is typical from ZnO crystals.

The origin of this band is quite controversial and it is believed to be composed mainly by two bands: the green (GL) and yellow (YL) luminescence bands. While copper impurities, oxygen vacancies and interstitial zinc are the potential candidates to be responsible for the green band [44, 45], the yellow band is believed to be originated by Li impurities [46].

Spatially resolved cathodoluminescence measurements on a home-made mechanical polished surface is shown in figure 4.10. CL panchromatic image represents a mapping of the total light detected at each point of the surface region analyzed. Yellow color represents the maximum of light intensity, and black stands for zero

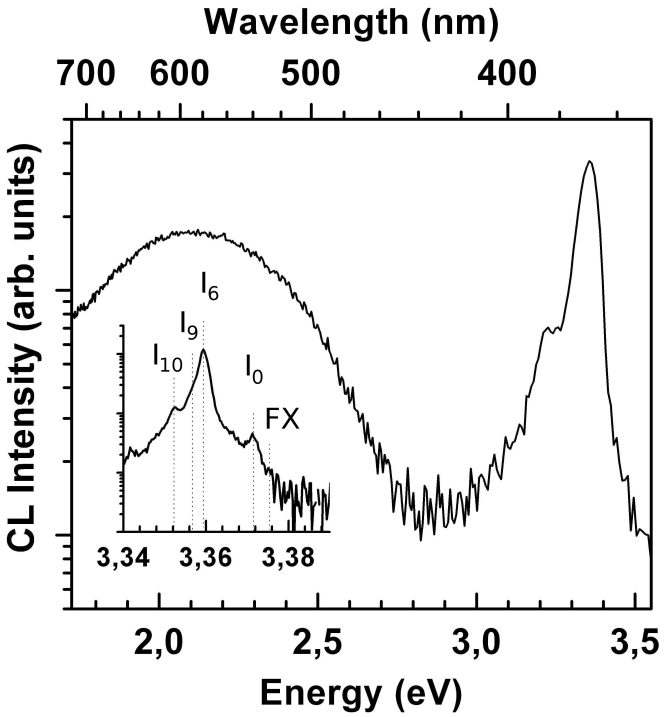

Figure 4.9: Laterally averaged CL spectrum of the polished ZnO surface. Inset: Detailed spectrum of the near band edge luminescence spectral region.

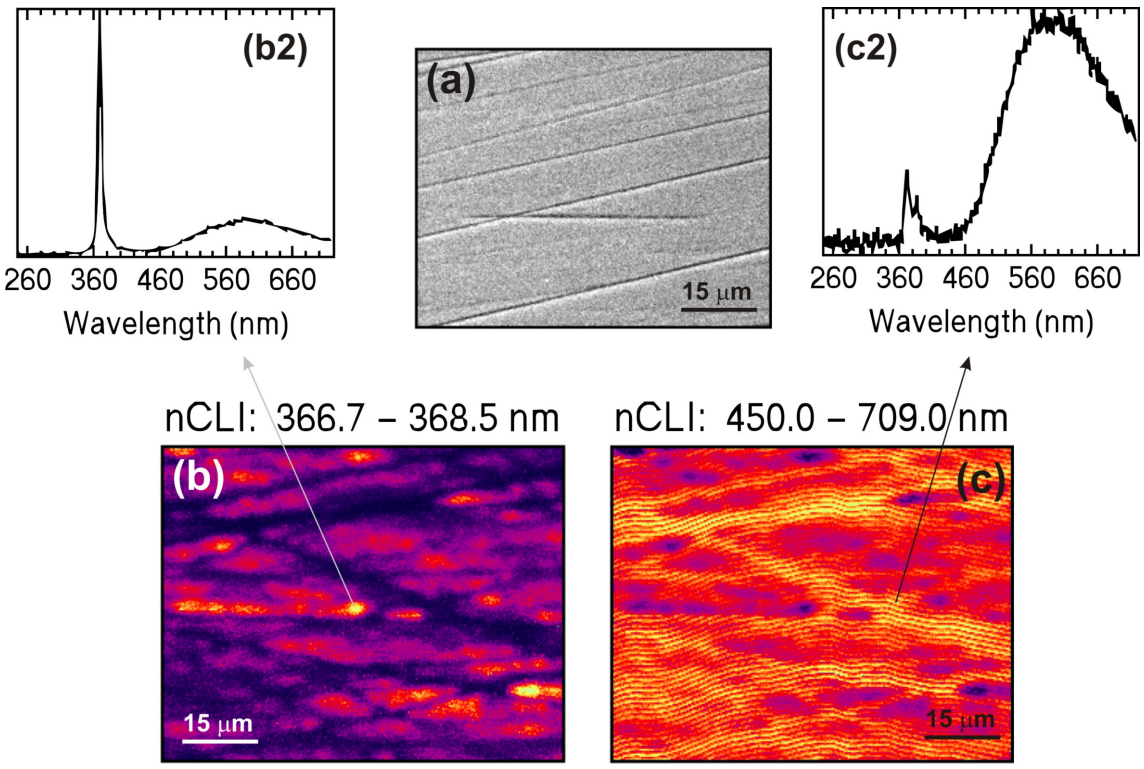

Figure 4.10: Spatially resolved CL of a mechanical polished surface of hydrothermal ZnO. Figure (a) is the SE image of the probed area and (b) and (c) are the normalized CL intensity mappings for the near band-edge and visible regions, respectively. (b2) and (c2) are local spectra of the indicated points.

intensity.

A strong correlation between the CL intensity of the excitonic lines and the morphology was observed. The NBE luminescence strongly quenches at the position of the scratches (see figures 4.10(a) and (b)). However, no spectral shift is observed while approaching these marks. It is worth noting that even in the regions without any features on the SE image, monochromatic CL images show dark lines running through. These lines mark the position of removed scratches from the top polishing procedures, indicating long-range/distant-acting damage of the scratches. In contrast, a complementary behavior is observed for the defect-related luminescence band (figure 4.10(c)). The band shows its highest normalized intensity at the scratches. This correlation suggests that the mechanical polishing processes induces a new radiative recombination channel related to the visible luminescence. Confocal Raman spectra of the polished surface confirms the defects at the sample surface by the presence of disorder-related features for around 1μm depth, which are not observed

in surfaces chemomechanical polished by the NovaSiC company. Consequently, any polishing procedure required in the ZnO studies have been performed at the NovaSiC company.

4.4 Results and Discussion: Related Publications

The results of the studies concerning Raman scattering in doped and undoped ZnO can be found in the following publications:

Study of the temperature dependence of E2 and A1(LO) modes in ZnO
Mater. Res. Soc. Symp. Proc. **957** K07-11 (2007)

Temperature dependence of Raman scattering in ZnO
Physical Review B **75** 165202 (2007)

Raman scattering of quasimodes in ZnO
Journal of Physics: Condensed Matter **20** 445211 (2008)

Raman scattering characterization of implanted ZnO
Mater. Res. Soc. Symp. Proc. **957** K07-24 (2007)

Isotopic study of the nitrogen-related modes in N^+-implanted ZnO
Applied Physics Letters **90** 181911 (2007)

Mater. Res. Soc. Symp. Proc. Vol. 957 © 2007 Materials Research Society 0957-K07-11

Study of the Temperature Dependence of E2 and A1(LO) Modes in ZnO

Esther Alarcon-Llado[1], Ramon Cusco[1], Jordi Ibanez[1], Luis Artus[1], Juan Jimenez[2], Buguo Wang[3], and Michael Callahan[4]

[1]Inst. Jaume Almera, C.S.I.C., C. Sole Sabaris sn, Barcelona, 08028, Spain

[2]Departamento Física Materia Condensada, Univ. Valladolid, P. del Cauce sn, Valladolid, 47011, Spain

[3]Solid State Scientific Corporation, 27-2 Wrigth Road, Hollis, NH, 03049

[4]Sensors Directorate, Air Force Research Laboratory, Hanscom AFB, MA, 01731-2909

ABSTRACT

Raman scattering measurements were carried out on a bulk, single crystal of wurtzite ZnO over a temperature range from 80 to 760 K and the temperature-dependent shift and broadening of the E_2^{high} and A_1(LO) modes was analyzed. The E_2^{high} mode exhibits a visibly asymmetric line shape that can be related to the interaction with the continuum of acoustic two-phonon density of states. A Fermi resonance model was used to describe the E_2^{high} temperature dependence. On the other hand, the anharmonic shift and broadening of the A_1(LO) mode are adequately accounted for by a decay model with a dominating Ridley channel involving TO and LA modes. Phonon lifetimes of ~0.9 and 0.5 ps are found for the E_2^{high} and A_1(LO) modes, respectively, which corroborates that anharmonic decay involves in both cases a three-phonon process. The A_1(LO) lifetime is one order of magnitude lower than that of GaN, which suggests that hot phonon effects should be expected to play a less relevant role in carrier relaxation in ZnO as compared with GaN.

INTRODUCTION

ZnO is a wide band gap semiconductor with great potential as an alternative to GaN for optoelectronic devices operating in the blue and UV spectral region, since it has a much higher free exciton binding energy (60 meV), it is more resistant to radiation damage and large native substrates are available. The achievement of large-area bulk growth of high-quality ZnO single crystals has renewed the interest on this semiconductor. While the dynamics of the phonon population strongly affect the performance of high-speed optoelectronic devices, our knowledge of ZnO lattice dynamics is still rather limited. Detailed measurements of the optical phonon branch by neutron scattering are still lacking, and only recently a density functional theory (DFT) calculation of the phonon dispersion in ZnO has been published [1]. Raman scattering measurements are well suited to obtain information about the sample quality as well as to analyze more specific aspects of lattice dynamics, such as isotopic effects and phonon lifetimes [2]. In the present study, we present the temperature dependence of Raman scattering in ZnO. We analyze the anharmonic shift and broadening of the E_2^{high} and A_1(LO) modes as a function of temperature, and we obtain phonon lifetime values for both modes.

EXPERIMENT

The experiments were performed on a high quality ZnO single crystal obtained by the hydrothermal growth method [3]. The Raman spectra were excited with the 514.5-nm line of an Ar^+ laser in the usual backscattering configuration. The scattered light was analyzed by means of a Jobin-Yvon T64000 triple spectrometer equipped with a LN_2-cooled charge-coupled device (CCD) detector. The triple additive configuration of the spectrometer with 50 μm slit was used to obtain high-resolution spectra of the E_2^{high} and A_1(LO) modes. Under these experimental conditions, the instrumental broadening correction [2] was found to be less than 1% for the narrowest line shape considered in this work (E_2^{high} peak at 80 K), and therefore it is assumed that the high-resolution Raman spectra reflect the intrinsic linewidth of the modes without need of further corrections. A LN_2 cryostat was used to vary the sample temperature from 80 to 380 K. To extend the temperature range up to 750 K, we used a Linkam high-temperature stage and the measurements were performed using a confocal microscope with a long working-distance ×80 objective.

DISCUSSION

Figure 1(a) shows *z(xx)-z* Raman spectra of the E_2^{high} mode recorded at temperatures in the 80 – 750 K range. The E_2^{high} mode exhibits a visibly asymmetric line shape with a low-frequency tail, which significantly broadens and shifts to lower frequencies as temperature increases. The asymmetry of the E_2^{high} line shape can be explained by the anharmonic interaction

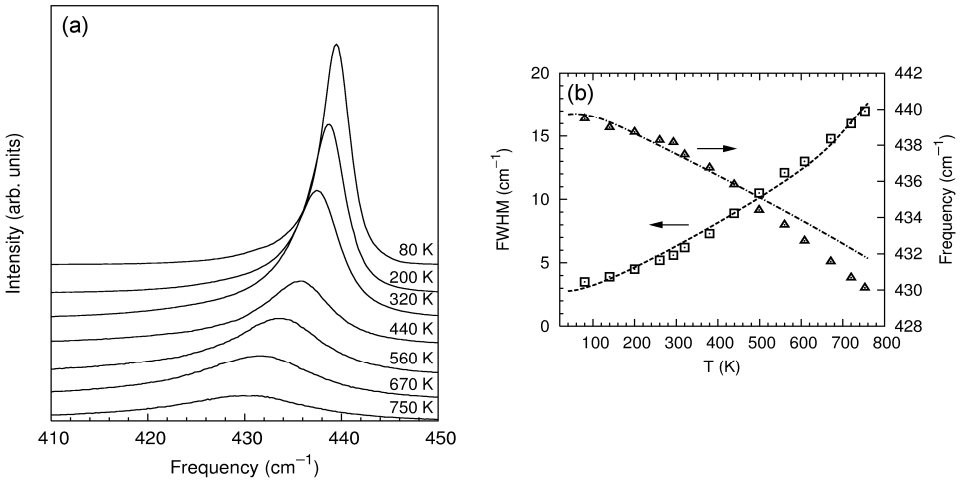

Figure 1. (a) Raman spectra of the E_2^{high} mode for temperatures in the 80 – 750 K range. (b) Temperature dependence of the linewidth (squares) and frequency (triangles) of the E_2^{high} mode. The dashed line is a fit of the anharmonic decay model to the FWHM data. The temperature dependence of the E_2^{high} frequency given by the model is plotted as a dot-dashed line.

with a continuum of transverse and longitudinal acoustic phonon combinations (Fermi resonance) [4]. The resulting anharmonic broadening can be written as [2]

$$\Gamma(\omega) = |V_3^+|^2 [1 + n_1 + n_2] \rho^+(\omega) + |V_3^-|^2 [n_2 - n_1] \rho^-(\omega), \quad (1)$$

where V_3^+ and V_3^- are, respectively, the effective third-order anharmonic constant for decay into phonon sums and phonon differences, $\rho^+(\omega)$ and $\rho^-(\omega)$ are the phonon-sum and phonon-difference DOS, and n_1, n_2 are the Bose-Einstein factors for the decay modes. The associated anharmonic shift, $\Delta(\omega)$, is related to Eq. (1) by a Hilbert transform [4]. For small anharmonic corrections, the Raman line shape can be written as [4]

$$I(\omega) \propto \Gamma(\omega) / \{[\omega_0 + \Delta_0 + \Delta(\omega) - \omega]^2 + \Gamma(\omega)^2\}, \quad (2)$$

where ω_0 is the harmonic frequency of the mode and Δ_0 is the frequency shift due to the thermal expansion of the lattice [5]. According to the DFT calculations, the two-phonon sum DOS presents a ridge-like structure around the E_2^{high} frequency [1,2]. Then, Eq. (1) yields a frequency dependent anharmonic broadening that gives rise to a distorted Lorentzian line shape, as given by Eq. (2). Inspection of the DFT phonon dispersion suggests that the most likely decay channels for the E_2^{high} are the decay into two acoustic modes around 190 and 250 cm^{-1}, and into a difference between a longitudinal optical phonon at ~550 cm^{-1} and an acoustic mode at ~110 cm^{-1}. In Fig. 1(b) we plot the FWHM and frequency measured on the E_2^{high} Raman spectra as a function of temperature. The temperature dependence of the FWHM of the line shape given by Eq. (2) was fitted to the experimental data, with $|V_3^+|^2$, $|V_3^-|^2$ and Γ_0 as fitting parameters, where Γ_0 is a constant background contribution due to impurity/defect scattering. The best fit is obtained for $|V_3^+|^2 = 39$ cm^{-2}, $|V_3^-|^2 = 3.8$ cm^{-2}, and $\Gamma_0 = 1.3$ cm^{-1}. The result of the fit is plotted in Fig. 1(b) as a dashed line. For the same set of parameters, the calculated frequency shift is plotted as a dot-dashed line in Fig. 1(b). For $T \geq 500$ K, the measured E_2^{high} frequency falls slightly below the calculated one. This discrepancy may be explained by the increasing importance at higher temperatures of the higher order terms neglected in Eq. (1) [6].

In contrast with the E_2^{high} mode, the $A_1(LO)$ mode occurs at a frequency where the two-phonon DOS does not exhibit significant variations. Then, the anharmonic broadening [Eq. (1)] is nearly constant and as a consequence the resulting Raman line shape is well described by a symmetric Lorentzian. Inspection of the calculated phonon dispersion [1] suggests that the main decay channel for these modes is the so-called generalized Ridley channel, which involves the decay into a transverse optical mode and a transverse acoustic mode. Taking into account the phonon DOS, the $A_1(LO)$ mode most probably decays in pairs of TO and TA modes clustered around $\omega_1 = 455$ cm^{-1} and $\omega_2 = 120$ cm^{-1}, respectively. Then, the temperature dependence of the FWHM and frequency of the $A_1(LO)$ mode can be modeled by [5]

$$\Gamma(T) = \Gamma_0 + A [1 + n(\omega_1,T) + n(\omega_2,T)] \quad (3)$$
$$\omega(T) = \omega_0 + \Delta_0(T) + B [1 + n(\omega_1,T) + n(\omega_2,T)] \quad (4)$$

where A and B are the effective anharmonic coefficients, $n(\omega,T)$ is the Bose-Einstein distribution function, ω_0 is the harmonic frequency, $\Delta_0(T)$ is the frequency shift due to lattice expansion and Γ_0 is a constant background contribution associated with impurity/defect scattering.

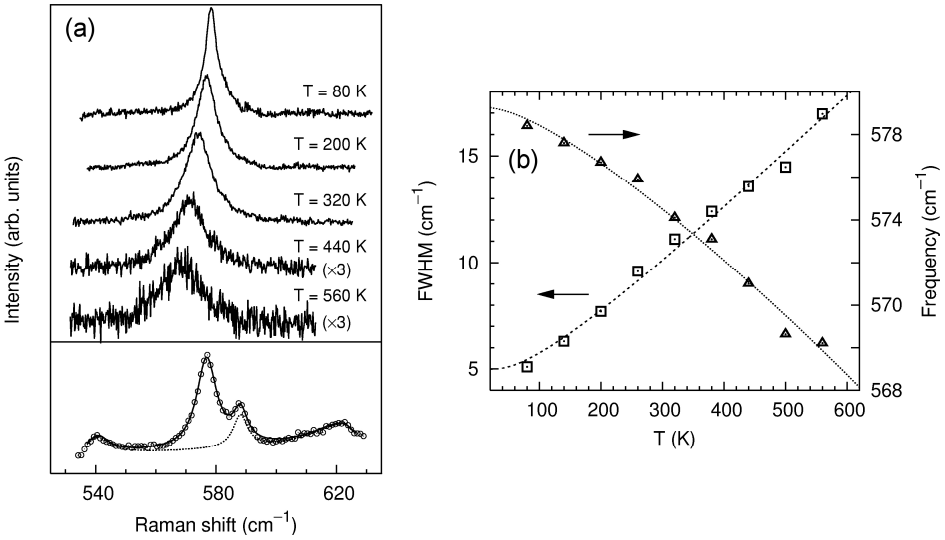

Figure 2. (a) Raman spectra of the A_1(LO) mode for temperatures in the 80 – 560 K range after background subtraction. Lower panel: fit to the Raman data (circles) used to determine the baseline (dotted line) for the spectrum at T = 200 K. (b) Temperature dependence of the FWHM (squares) and frequency (triangles) of the A_1(LO) mode as determined from the Raman spectra. The dotted and dashed lines are fits of Eqs. (3) and (4) to the experimental data.

The A_1(LO) mode is very weak and it emerges on a background of second-order acoustic and optical phonon combinations. Long integration times were required in order to obtain adequate signal-to-noise ratio to perform a reliable line shape analysis. Careful background subtraction was carried out by fitting a suitable combination of Lorentzian line shapes plus a linear baseline. Figure 2(a) displays *z(xx)-z* Raman spectra of the A_1(LO) mode recorded at temperatures in the 80 – 560 K range. For T ≥ 440 K the measurements were performed using the microscope hot stage and therefore the signal is lower owing to the smaller depth of focus of the setup. Measurements at T >560 K were discarded as the signal-to-noise ratio did not allow a reliable determination of the FWHM. The lower panel of Fig. 2(a) illustrates the background subtraction for the spectrum at T = 200 K, where, besides the second-order bands, an additional peak close to the A_1(LO) mode is already resolved. In Fig. 2(b) we plot the measured values of FWHM (squares) and frequency (triangles). Eqs. (3) and (4) were fitted to the experimental data, using Γ_0, ω_0, A, and B as adjustable parameters. The best fit to the data is obtained for $\Gamma_0 = 1.3$ cm^{-1}, $\omega_0 = 581.4$ cm^{-1}, A = 3.7 cm^{-1} and B = –2.1 cm^{-1}. While the coincidence of the values found for the impurity/defect broadening Γ_0 in the case of the E_2^{high} and the A_1(LO) modes is somehow fortuitous, similar Γ_0 values are indeed expected.

The phonon lifetime τ can be obtained from the Raman linewidth via the energy-time uncertainty relation $\tau = \hbar / \Gamma$, where Γ is the Raman FWHM and $\hbar$ is the Plack constant. Phonon lifetime is mainly limited by anharmonic decay into two or more phonons, with characteristic decay time τ_A, and by the loss of translational symmetry due to impurities and defects, with a characteristic decay time τ_I. Then, the measured FWHM is $\tau^{-1} = \tau_A^{-1} + \tau_I^{-1}$. An estimation of the decay time associated with impurities and defects can be obtained from the values of the Γ_0

Table I. Phonon lifetimes of the E_2^{high} and the A_1(LO) modes of ZnO at 80 and 300 K. The characteristic decay time associated with impurities/defects τ_I is estimated from the background broadening parameter Γ_0 used to fit the temperature dependence of the FWHM.

Phonon mode	T = 80K Γ (cm^{-1})	T = 80K τ (ps)	T = 300K Γ (cm^{-1})	T = 300K τ (ps)	Γ_0 (cm^{-1})	τ_I (ps)
E_2^{high}	3.5	1.5	6.0	0.88	1.3	4.1
A_1(LO)	5.1	1.0	9.7	0.54	1.3	4.1

parameter provided by the FWHM temperature-dependence fits. The results are summarized in Table I. The E_2^{high} lifetime at room temperature is in good agreement with the value reported by Bergman *et al.*[7]. No lifetime values for the A_1(LO) mode were reported in that work, but the value we find for ZnO is similar to that reported for high-quality AlN crystals [7]. On the other hand, the A_1(LO) lifetime found for ZnO is one order of magnitude lower than the one reported for GaN [8]. This suggests that hot phonon effects should be expected to play a less relevant role in carrier relaxation in ZnO as compared to GaN. The values found for both E_2^{high} and A_1(LO) phonon lifetimes corroborate that the anharmonic decay involves in both cases a three-phonon process; four-phonon processes are ruled out as the main decay mechanism, as this would yield phonon lifetimes two or three orders of magnitude longer.

CONCLUSIONS

The temperature dependence of the E_2^{high} and A_1(LO) modes has been studied over a wide temperature range. The E_2^{high} mode exhibits a visibly asymmetric line shape that can be explained by the interaction with a continuum of transverse and longitudinal acoustic phonon combinations. The E_2^{high} line shape asymmetry results from the ridge-like structure in the two-phonon DOS around the E_2^{high} frequency. On the other hand, the A_1(LO) mode exhibits a nearly symmetrical line shape, and its temperature dependence can be adequately described with a generalized Ridley channel that involves the decay into a transverse optical and longitudinal acoustic phonon pair. The phonon lifetimes can be extracted from the FWHM of the Raman line shapes. A typical value of 0.5 ps is found for the lifetime of the polar A_1(LO) mode, which corroborates the three-phonon process as the main decay channel for this mode. This polar mode lifetime is one order of magnitude higher than in GaN. The background impurity/defect contribution to the phonon lifetime is found to be the same for both the E_2^{high} and A_1(LO) modes.

ACKNOWLEDGMENTS

This work has been supported by the Spanish Ministry of Education and Science under contract MAT2004-0664 and Ramón y Cajal Program. The work performed by the United States Air Force Research Laboratory at Hanscom Air Force Base was partially supported by the Air Force Office of Scientific Research.

REFERENCES

1. J. Serrano, A. H. Romero, F. J. Manjón, R. Lauck, M. Cardona and A. Rubio, Phys. Rev. B **69**, 094306 (2004).
2. J. Serrano, F. J. Manjón, A. H. Romero, F. Widulle, R. Lauck and M. Cardona, Phys. Rev. Lett. **90**, 055510 (2003).
3. M. Suscavage, M. Harris, D. Bliss, P. Yip, S. Q. Wang, D. Schwall, L. Bouthillette, J. Bailey, M. Callahan and D. C. Look, Internet J. Nitride Semicond. Res. 4S1, G3.40 (1999).
4. F. Widulle, R. Ruf, A. Göbel, E. Schönherr and M. Cardona, Phys. Rev. Lett. **82**, 5281 (1999).
5. J. Menéndez and M. Cardona, Phys. Rev. B **29**, 2051 (1984).
6. A. Debernardi and M. Cardona, Physica B **263–264**. 687 (1999).
7. L. Bergman, D. Alexson, P. L. Murphy, R. J. Nemanich, M. Dutta, M. A. Sctroscio, C. Balkas, H. Shin and Robert F. Davis, Phys. Rev. B **59**, 12977 (1999).
8. K. T. Tsen, R. P. Joshi, D. K. Ferry, A. Botchkarev, B. Sverdlov, A. Salvador, and H. Morkoç, Appl. Phys. Lett. **68**, 2990 (1996).

PHYSICAL REVIEW B **75**, 165202 (2007)

Temperature dependence of Raman scattering in ZnO

Ramon Cuscó, Esther Alarcón-Lladó, Jordi Ibáñez, and Luis Artús
Institut Jaume Almera, Consell Superior d'Investigacions Científiques (CSIC), Lluís Solé i Sabarís s.n., 08028 Barcelona, Spain

Juan Jiménez
Dept. Física de la Materia Condensada, ETSII, Universidad de Valladolid, Spain

Buguo Wang
Solid State Scientific Corporation, 27-2 Wright Road, Hollis, New Hampshire 03049, USA

Michael J. Callahan
Air Force Research Laboratory, Sensors Directorate, Electromagnetics Technology Division, Optoelectronic Technology Branch, Hanscom AFB, Massachusetts 01731-2909, USA

(Received 22 November 2006; published 6 April 2007)

We present a Raman scattering study of wurtzite ZnO over a temperature range from 80 to 750 K. Second-order Raman features are interpreted in the light of recent *ab initio* phonon density of states calculations. The temperature dependence of the Raman intensities allows the assignment of difference modes to be made unambiguously. Some weak, sharp Raman peaks are detected whose temperature dependence suggests they may be due to impurity modes. High-resolution spectra of the E_2^{high}, $A_1(\text{LO})$, and $E_1(\text{LO})$ modes were recorded, and an analysis of the anharmonicity and lifetimes of these phonons is carried out. The E_2^{high} mode displays a visibly asymmetric line shape. This can be attributed to anharmonic interaction with transverse and longitudinal acoustic phonon combinations in the vicinity of the K point, where the two-phonon density of states displays a sharp edge around the E_2^{high} frequency. The temperature dependence of the linewidth and frequency of the E_2^{high} mode is well described by a perturbation-theory renormalization of the harmonic E_2^{high} frequency resulting from the interaction with the acoustic two-phonon density of states. In contrast, the $A_1(\text{LO})$ and $E_1(\text{LO})$ frequencies lie in a region of nearly flat two-phonon density of states, and they exhibit a nearly symmetric Lorentzian line shape with a temperature dependence that is well accounted for by a dominating asymmetric decay channel.

DOI: 10.1103/PhysRevB.75.165202 PACS number(s): 78.30.Fs, 78.30.−j, 63.20.−e

I. INTRODUCTION

The interest in ZnO has been renewed by its potential applications in transparent electronics and UV optoelectronic devices. Its large exciton binding energy (60 meV) makes it highly attractive for applications as blue and ultraviolet light emitters, where it may become an advantageous alternative to GaN.[1] Good knowledge of the vibrational properties of this material is essential to understand transport properties and phonon interaction with the free carriers, both of which have great impact on optoelectronic device performance. Today this is made possible by the availability of high-quality, large-area bulk ZnO single crystals. In polar semiconductors, carriers excited high in the conduction band relax toward their ground state mainly by Fröhlich interaction with the longitudinal optical phonons. Thus, the dynamics of the phonon population strongly affects the performance of high-speed optoelectronic devices.[2] Raman scattering measurements are well suited to obtain information about the sample quality in wide band gap semiconductors[3–5] as well as to analyze more specific aspects of lattice dynamics, such as isotopic effects[6,7] and phonon lifetimes.[8,9] The temperature dependence of the phonon modes has also been used to determine the local temperature of a GaN diode as a function of the operating voltage,[10] and therefore Raman scattering has proven to be well suited to monitor the local temperature during device operation.

Wurtzite-type ZnO belongs to the space group C_{6v}^4 with two formula units in the primitive cell. The zone-center optical phonons can be classified according to the following irreducible representations: $\Gamma_{\text{opt}}=A_1+E_1+2E_2+2B_1$. The B_1 modes are silent modes, the A_1 and E_1 modes are polar modes and are both Raman and infrared active, whereas the E_2 modes are nonpolar and Raman active only. Polarized right-angle Raman scattering of ZnO was measured by Damen *et al.*[11] back in 1965. Arguello *et al.*[12] reported Raman spectra of ZnO obtained in a variety of geometries, which allowed them to identify all Raman active modes from their selection rules. A few years later, a detailed study of the resonant behavior of the high frequency E_2 mode (E_2^{high}), $A_1(\text{TO})$, and $E_1(\text{TO},\text{LO})$ modes as well as several second-order features was presented by Calleja and Cardona.[13] Data on temperature dependence of ZnO phonons also date back to the late 1970s.[14] In the past few years, the availability of bulk ZnO crystals of very high optical quality and the technological relevance of this material have spurred the realization of fundamental and more detailed studies on ZnO lattice dynamics. However, our knowledge of the lattice dynamics of ZnO is still rather limited, as few experimental data are available on phonon dispersion in this material. In fact, detailed measurements of the optical phonon branch by inelastic neutron scattering are still lacking. Only recently have *ab initio* density-functional theory (DFT) calculations of lattice-dynamical properties been published,[15] which have made a

TABLE I. Symmetry allowed Raman modes for the scattering geometries considered in this work.

	Raman active modes				
Scattering geometry	E_2	A_1(LO)	A_1(TO)	E_1(LO)	E_1(TO)
$z(xx)\bar{z}$	A	A			
$z(xy)\bar{z}$	A				
$x(yy)\bar{x}$	A		A		
$x(zy)\bar{x}$					A
$x(zy)y$				A	A

more accurate interpretation of the experimental data possible. Thus, the unusual variations of the E_2^{high} phonon linewidth with the isotopic composition and with pressure have been accounted for by fine features of the phonon density of states (DOS) revealed by the DFT calculations.[8] Recently, the low-frequency E_2 phonon lifetime has been measured in ZnO by means of impulsive stimulated Raman scattering experiments, and it has been found to be longer than 200 ps at low temperature.[16] It has been suggested that such long-lived optical phonons could have applications in quantum cryptography and quantum computing.[16]

In this work we present a study of the first- and second-order Raman spectra of ZnO and their dependence on temperature. Second-order Raman features are discussed in the light of recently available DFT calculations of phonon DOS. To analyze the temperature dependence of optical phonons in ZnO, high spectral resolution measurements of the E_2^{high}, A_1(LO), and E_1(LO) modes have been carried out at different temperatures. A visible line-shape asymmetry is observed for the E_2^{high} mode, which can be explained by the features of the two-phonon DOS around the E_2^{high} frequency. We discuss the temperature effects on the phonons in terms of third-order anharmonic decay. Whereas the behavior of the A_1(LO) and E_1(LO) modes is well described by a dominant decay channel localized around a single set of frequencies, the description of the E_2^{high} temperature dependence requires a more detailed analysis that takes into account the two-phonon DOS.

II. EXPERIMENT

The experiments were performed on a high-quality ZnO single crystal obtained by the hydrothermal growth method. Growth details as well as x-ray and photoluminescence (PL) characterization of ZnO crystals obtained by this method have been published elsewhere.[17] After chemomechanical polish, PL spectra obtained at 2.1 K revealed emission from excitonic transitions with narrow line shapes, indicating the high quality of these hydrothermally grown samples.[17]

The Raman spectra were excited with the 514.5 nm line of an Ar^+ laser in different scattering geometries (see Table I). The scattered light was analyzed by means of a Jobin-Yvon T64000 triple spectrometer equipped with a LN_2-cooled charge-coupled device (CCD) detector. Full-range spectra were obtained in the subtractive configuration of the spectrometer with 100 μm slits, corresponding to a spectral slit width of $\approx$2.5 cm^{-1}. The triple additive configuration with 50 μm slit was utilized to obtain high resolution spectra of the E_2^{high}, A_1(LO), and E_1(LO) modes. The spectrometer spectral broadening for this configuration was checked by measuring the λ=546.07 nm emission line of Hg, which was fitted by a Gaussian line shape with a full width at half maximum (FWHM) of Γ_G=0.44 cm^{-1}. Then, following Ref. 8, the instrumental broadening was estimated from $\Gamma_L=\Gamma-\Gamma_G^2/\Gamma$, where Γ and Γ_L are, respectively, the FWHM measured on the Raman spectrum and the intrinsic FWHM of the mode. Using this relation, we find that the instrumental broadening correction for the narrowest mode studied (the E_2^{high} mode at 80 K) amounts to less than 1% of the measured FWHM, and therefore we can assume that the high-resolution Raman spectra reflect the intrinsic FWHM of the modes.

A LN_2 cryostat was used to vary the sample temperature from 80 to 380 K. Within this temperature range, the spectra were acquired in macrocamera configuration. To extend the temperature range up to 750 K, we used a Linkam high-temperature stage and the measurements were performed using a confocal microscope with a long working-distance $\times$80 objective protected by a cooling jacket. Both sets of measurements yield consistent results in the overlapping temperature range between 290 and 380 K. For each measurement, the temperature was stabilized for 10 min before acquiring a spectrum.

III. RESULTS AND DISCUSSION

A. First- and second-order Raman scattering of ZnO

First, we present an overview of the first-order Raman scattering in ZnO, and compare our results with previously reported data. We have performed polarized Raman scattering measurements in different scattering configurations to identify all Raman active modes of ZnO (see Table I). The Raman tensors for each of these modes are given by

$$E_2^{(1)}=\begin{pmatrix} d & 0 & 0 \\ 0 & -d & 0 \\ 0 & 0 & 0 \end{pmatrix}, \quad E_2^{(2)}=\begin{pmatrix} 0 & d & 0 \\ d & 0 & 0 \\ 0 & 0 & 0 \end{pmatrix},$$

$$E_1(x)=\begin{pmatrix} 0 & 0 & c \\ 0 & 0 & 0 \\ c & 0 & 0 \end{pmatrix}, \quad E_1(y)=\begin{pmatrix} 0 & 0 & 0 \\ 0 & 0 & c \\ 0 & c & 0 \end{pmatrix},$$

$$A_1(z)=\begin{pmatrix} a & 0 & 0 \\ 0 & a & 0 \\ 0 & 0 & b \end{pmatrix}. \tag{1}$$

For polar modes, the coordinate in parentheses denotes the direction of phonon polarization. As derived from the Raman tensors of the respective modes, all Raman active modes can be observed in backscattering geometry except for the E_1(LO) mode, for which only the polarizability components involving z and the direction of phonon polarization

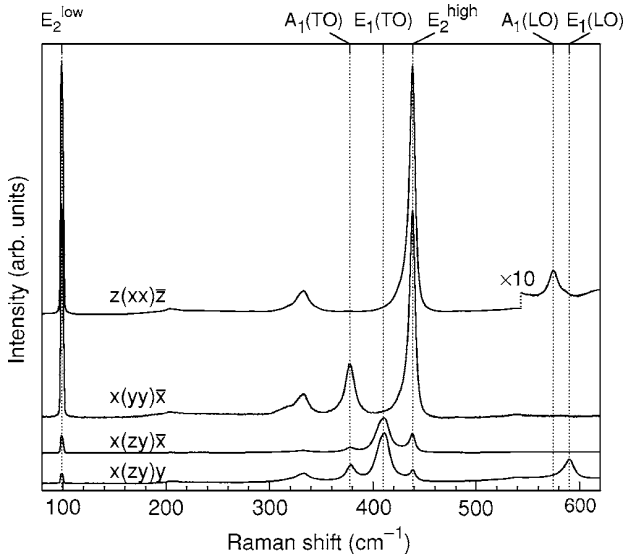

FIG. 1. Room temperature first-order Raman spectra of ZnO in scattering geometries corresponding to A_1+E_2 and E_1 symmetries.

change during the vibration. The symmetry-allowed Raman modes for the scattering geometries considered in this work are summarized in Table I for convenience. Although the E_1(LO) mode was reported in the forbidden configuration $x(zz)\bar{x}$ under 406.7-nm excitation owing to intraband Fröhlich interaction,[13] the unambiguous observation of the E_1(LO) mode requires a scattering configuration with a nonvanishing $x(zy)y$ component.

Figure 1 shows polarized first-order Raman spectra of the ZnO sample obtained at room temperature in four different scattering configurations that allow the observation of all the Raman active modes. Our results are consistent with previous Raman studies.[11–13] The $z(xx)\bar{z}$ spectrum (E_2+A_1 symmetry) is dominated by the two intense, sharp E_2 modes at 99 and 438 cm^{-1}. The low-frequency E_2 mode, involving mainly Zn motion, displays an extremely narrow linewidth, well below the slit width of the subtractive configuration of the spectrometer even for the highest temperature studied. The E_2^{high} mode displays a clear asymmetry toward low frequencies that we shall discuss in more detail in the next section. In contrast with previous works, where the A_1(LO) mode could not be detected for excitation wavelengths longer than 406.7 nm,[13] we can detect a weak A_1(LO) mode at 574 cm^{-1}. The prominent feature at 333 cm^{-1} corresponds to second-order scattering and will be discussed below. In the $x(yy)\bar{x}$ spectrum (E_2+A_1 symmetry), in addition to the strong E_2 modes a new peak appears at 378 cm^{-1}, which can be assigned to the A_1(TO) mode. An additional peak emerges at 410 cm^{-1} in the $x(zy)\bar{x}$ spectrum (E_1 symmetry), which is assigned to the E_1(TO) mode. Finally, the E_1(LO) mode can be observed at 590 cm^{-1} in the $x(zy)y$ spectrum. Therefore, the highest-frequency first-order mode of ZnO corresponds to the E_1(LO) mode, which at zone center is found at a frequency 16 cm^{-1} higher than that of the A_1(LO) mode. It is worth noting that DFT calculations yield inaccurate results regarding the E_1(LO) and A_1(LO) modes, as they give a zone center E_1(LO) frequency 4 cm^{-1} lower than that of the A_1(LO) mode.[15] This fact should be taken into account when discussing the Raman features of ZnO in terms of the calculated phonon DOS. The observed first-order Raman frequencies are reported in Table II.

A residual intensity of the forbidden E_2 modes can be seen in the $x(zy)\bar{x}$ and $x(zy)y$ spectra that could arise from a slight misalignment of the sample introducing a small x component in the z polarization direction or from a lower quality of the sample polishing in the m prismatic face resulting in a relaxation of the selection rules.

Whereas wave-vector conservation restricts the phonons involved in first-order Raman scattering to those with $\mathbf{k}\approx 0$, phonons from the entire Brillouin zone take part in second-order Raman scattering. Therefore, second-order spectra usually display feature-rich structures, which are determined, on the one hand, by the phonon DOS and, on the other hand, by the selection rules of the two-phonon scattering processes. Selection rules for two-phonon Raman scattering in crystals with the wurtzite structure were reported by Siegle *et al.*[18] As a general rule, it was found that overtones always contain the representation A_1 whereas combinations of phonons belonging to different representations do not contain the A_1 representation. According to DFT calculations[15] the phonon DOS of ZnO presents a frequency gap between acoustic and optical modes that extends from 270 to 410 cm^{-1}. The second-order spectra may then be divided into three regions: (i) the low-frequency region (approximately 160–540 cm^{-1}) dominated by acoustic overtones, (ii) the high-frequency region (820–1120 cm^{-1}) formed by optical overtones and combinations, and (iii) the intermediate-frequency region (540–820 cm^{-1}) where optical and acoustic phonon combinations occur.

In the present analysis, we use the phonon dispersion calculated by DFT (Ref. 15) and the symmetry selection rules for two-phonon Raman scattering reported by Siegle *et al.*[18] to aid the identification of the second-order features of the ZnO Raman spectrum. Figure 2 shows the $z(xx)\bar{z}$ polarized second-order Raman spectra of ZnO (A_1+E_2 symmetry) for different temperatures in the 80–300 K range. The second-order features are labeled with their respective frequencies on the RT spectrum. The most prominent second-order features occur in the high-frequency region and correspond to LO overtones and combinations involving LO modes. The broad, intense peak at 1158 cm^{-1}, which is found between the doubled frequencies measured for the A_1(LO) and E_1(LO) modes, contains contributions of $2A_1$(LO) and $2E_1$(LO) modes at the Γ point of the Brillouin zone, and possibly also of 2LO scattering by mixed modes from the rather flat bands along the *A-L-M* line. The weaker peak at 1105 cm^{-1} can be attributed to 2LO at *H* and *K*. Note that the DFT calculations, in addition to giving the wrong ordering for the E_1(LO) and A_1(LO) modes, tend to underestimate the LO frequencies. Thus, the Raman peaks in this region occur at higher frequencies than predicted by DFT results. As mentioned above, all these overtones contain the A_1 representation, and furthermore, they occur in a region with high two-phonon DOS. Two weak shoulders can be observed in the RT spectrum at 1072 and 1044 cm^{-1}, which become more vis-

TABLE II. Room temperature frequencies and symmetries of the first- and second-order Raman spectra observed in ZnO and their assignments. Our results are compared with previous data in Ref. 13. Parentheses indicate symmetries that although being present in the spectra display a much lower intensity than the dominant one.

Frequency (cm^{-1})				
Our data	Ref. 13	Symmetry	Process	Brillouin zone points/lines
99	101	E_2	E_2^{low}	Γ
203	208	$A_1,(E_2)$	2TA; $2E_2^{low}$	$L,M,H;\Gamma$
284		A_1	$B_1^{high}-B_1^{low}$	Γ
333	332	$A_1,(E_2,E_1)$	$E_2^{high}-E_2^{low}$	Γ
378	380	A_1	A_1(TO)	Γ
410	408	E_1	E_1(TO)	Γ
438	437	E_2	E_2^{high}	Γ
483		A_1	2LA	M-K
536	541	A_1	$2B_1^{low}$; 2LA	$\Gamma;L,M,H$
574	574	A_1	A_1(LO)	Γ
590	584	E_1	E_1(LO)	Γ
618		A_1	TA+TO	H,M
657		E_1,E_2	TA+LO	L,H
666		A_1	TA+LO	M
700		A_1	LA+TO	M
723		A_1	LA+TO	L-M
745		A_1	LA+TO	L-M
773		A_1	LA+TO	M,K
812		A_1	LA+LO	L,M
980	990	A_1	2TO	L-M-K-H
1044		A_1	TO+LO	A,H
1072	1080	A_1	TO+LO	M,L
1105		A_1	2LO	H,K
1158	1160	A_1	$2A_1$(LO),$2E_1$(LO); 2LO	$\Gamma;A$-L-M

ible at low temperature. We assign the mode at 1072 cm^{-1} to TO+LO combinations at the M and L points, and the mode at 1044 cm^{-1} to TO+LO combinations at the A and H points. A weak broad band can be observed at about 980 cm^{-1}, which can be attributed to TO overtones. It is noteworthy that the scattering efficiency of processes involving LO modes is much higher than those involving TO modes. As reported by Calleja and Cardona,[13] the 2LO scattering is resonantly enhanced already at photon energies $\sim$1 eV below the fundamental gap.

A multiplicity of structures appear in the low- and intermediate-frequency regions of the spectra, where acoustic overtones and acoustic-optical combinations occur. To aid their identification by analyzing their symmetry, we have recorded polarized Raman spectra in several scattering geometries. In Fig. 3 we display the A_1+E_2, A_1, E_2, and E_1 components of the second-order spectrum. The most intense peak in the intermediate-low-frequency region is observed at 333 cm^{-1}. This mode had been previously assigned to transverse acoustic overtone scattering at M.[13,19] However, the temperature dependence of its Raman intensity (see Fig. 2) clearly indicates that this is a difference mode. The frequency of this mode is in good agreement with the difference between the E_2^{high} and E_2^{low} frequencies measured in our sample. Using the notation of Ref. 18, the $E_2^{high}-E_2^{low}$ difference contains symmetries $\Gamma_6\otimes\Gamma_6\supset A_1,E_2$. This is consistent with the polarized measurements shown in Fig. 3, which indicate that the symmetry of the 333 cm^{-1} mode is predominantly A_1, with a smaller E_2 component and an even smaller E_1 component. According to the calculated phonon dispersion relations,[15] the 333-cm^{-1} mode could also contain contributions from $[\mathrm{TO}-\mathrm{TA}]_{A,L,H}$ differences. These differences, however, yield higher frequencies and all of them contain the E_1 symmetry. To demonstrate the origin of the 333-cm^{-1} mode, we plot in Fig. 4 the Raman intensity of this mode versus temperature, normalized to its intensity at room temperature, and we compare it with the statistical occupation factor for the $E_2^{high}-E_2^{low}$ difference mode (dashed line), which is given by[20]

$$\rho(T)=[1+n(E_2^{high})]n(E_2^{low}), \tag{2}$$

where $n(E)=[\exp(E/k_BT)-1]^{-1}$ is the Bose-Einstein distribution function. For comparison, we also plot (dotted line)

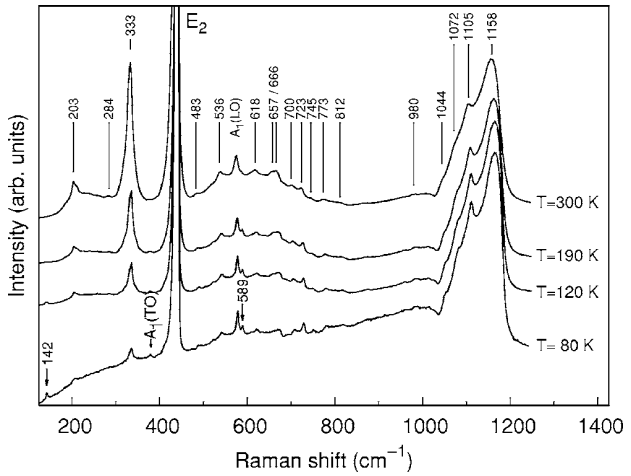

FIG. 2. Second-order Raman spectra of ZnO obtained in $z(xx)\bar{z}$ configuration for temperatures in the 80–300 K range.

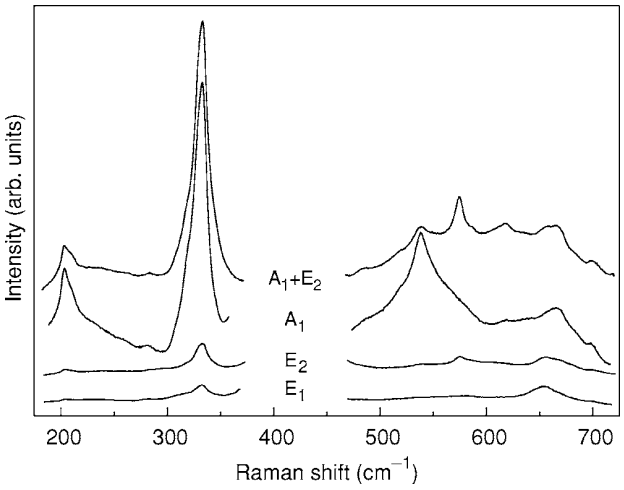

FIG. 3. Second-order Raman spectra of ZnO obtained for various scattering geometries. From top to bottom, $z(xx)\bar{z}$, $x(zz)\bar{x}$, $z(xy)\bar{z}$, and $x(zy)\bar{x}$.

the statistical occupation factor for overtones of TA phonons with $\hbar\omega_{\mathrm{TA}} \approx 160\ \mathrm{cm}^{-1}$ around the M point, $\rho(T)=[1+n(\hbar\omega_{\mathrm{TA}})]^2$, as suggested in Refs. 13 and 19. Clearly, the statistical occupation factor for the difference mode [Eq. (2)] accounts for the observed temperature dependence of the intensity, whereas the corresponding factor for the overtones deviates significantly from the experimental points.

Another prominent peak is observed at 203 cm^{-1}, which as seen from Fig. 3 exhibits A_1 symmetry and thus can be attributed to a TA overtone. In Ref. 15 this mode was assigned to $2\mathrm{TA}_L$, and in Ref. 13 to $2E_2^{\mathrm{low}}$ with possible contributions of 2TA at the M point. We note that the corresponding phonon branch is rather flat at H, so we speculate that the 203 cm^{-1} peak could also have a significant contribution of 2TA scattering at the H point.

A weak peak can be seen at 284 cm^{-1} in the room temperature spectrum, which disappears at lower temperatures (see Fig. 2), and therefore we assign it to a difference mode. As can be seen from Fig. 3, this mode has A_1 symmetry. Several mode differences yield frequencies close to the observed peak: $A_1(\mathrm{LO})-B_1^{\mathrm{low}}$, $E_1(\mathrm{LO})-B_1^{\mathrm{low}}$, $B_1^{\mathrm{high}}-B_1^{\mathrm{low}}$, and $[\mathrm{LO\text{-}LA}]_L$. However, some of them have symmetries which are incompatible with the spectra of Fig. 3. The symmetry of these differences are, respectively, $\Gamma_1\otimes\Gamma_3\supset B_1$, $\Gamma_5\otimes\Gamma_3\supset E_2$, $\Gamma_3\otimes\Gamma_3\supset A_1$, and $L_{\mathrm{I}}\otimes L_{\mathrm{I}}\supset A_1, E_1, E_2$.[18] Therefore, the first two possibilities can be excluded, and the absence of E_1 and E_2 component in this peak suggests that it can be primarily assigned to B_1^{high}-B_1^{low}. The very weak structure detected at 483 cm^{-1}, which as seen from Fig. 3 exhibits A_1 symmetry, can be assigned to LA overtones along M-K, where phonon dispersion is nearly flat and hence the DOS is very high. The peak at 536 cm^{-1} is clearly of A_1 symmetry and can be attributed to $2B_1^{\mathrm{low}}$ and LA overtones along L-M and H.

Above this frequency, we find acoustic and optical combinations. The peak at 618 cm^{-1} could be tentatively assigned to TA+TO at the H and M points. TA+LO combinations give rise to the doublet observed at 657–666 cm^{-1}. The lower component of the doublet has E_2 and E_1 symmetry, whereas the symmetry of the higher component is basically A_1. The highest DOS for combinations in this frequency range is found at the L, M, and H points. Both at the L and H points the TA+LO combination has symmetry E_1, E_2, whereas at the M point combinations of the type $M_i\otimes M_i\supset A_1, E_2$ occur. This suggests the assignment of the 657 cm^{-1} mode to TA+LO combinations at the L and H points and the 666 cm^{-1} mode to TA+LO combinations at the M point. Low intensity modes of mainly A_1 symmetry are detected at 700, 723, 745, 773, and 812 cm^{-1}, which can be attributed to acoustic and optical combinations. Taking into account the predominantly A_1 symmetry of all these modes, we tentatively assign the peak at 700 cm^{-1} to LA+TO combinations at the M point, and the peak at 812 cm^{-1} to LO+LA combinations at the L and M points. The frequencies of the second-order Raman features observed at room temperature are collected in Table II.

It is noteworthy that, in addition to the second-order peaks discussed above, several sharp peaks appear and grow in intensity as the temperature decreases. These peaks are

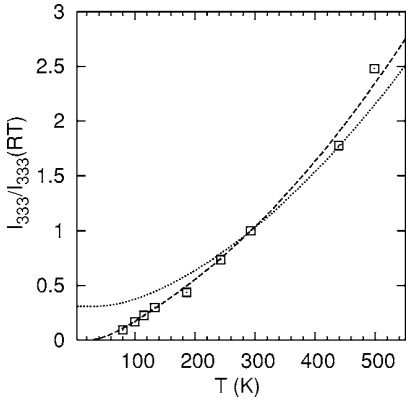

FIG. 4. Intensity of the second-order peak observed at $\approx$333 cm^{-1} as a function of temperature. Dashed line, occupation number factor for the $E_2^{\mathrm{high}}-E_2^{\mathrm{low}}$ difference mode; dotted line, *idem* for TA overtones around the M point.

marked by arrows in the 80 K spectrum shown in Fig. 2. The weak peak at 380 cm^{-1} appears at the same frequency as the A_1(TO) mode in a $x(yy)\bar{x}$ spectrum recorded at 80 K, so we assign it to a leaky A_1(TO) mode. While the peak at 589 cm^{-1} is close to the E_1(LO) mode, its frequency is about 4 cm^{-1} lower than that measured for the E_1(LO) mode at 80 K in the allowed $x(zy)y$ scattering configuration. This peak could be related to local vibrational modes associated with intrinsic lattice defects, similarly to the peak that was observed at 582 cm^{-1} in doped GaN,[3,19,21] which was conjectured to be associated with intrinsic lattice defects favored or activated by doping.[21] The intensity enhancement and sharpening with decreasing temperature observed for this peak as well as for that at 142 cm^{-1} clearly suggest a local mode origin for these peaks. Although Al, Fe, Si, Li, and K impurities were detected by glow discharge mass spectrometry in hydrothermal ZnO samples, their concentration was found to be in the few ppm range,[17] well below the detection limit of Raman spectroscopy. Thus, we speculate that these peaks are related to intrinsic lattice defects, which may be favored by the growth conditions. These crystals present a strong visible luminescence band, which supports the existence of intrinsic point defects. On the other hand, surface effects can be ruled out because of the deep penetration of the excitation light. Further work should be carried out to determine the origin of these Raman peaks.

B. Anharmonic phonon decay and phonon lifetimes

1. The E_2^{high} mode: Fermi resonance model

In the discussion of the first-order Raman spectra of ZnO presented in the preceding section, we noted that the E_2^{high} mode exhibits a visibly asymmetric line shape with a low-frequency tail. This is quite apparent from Fig. 1 when one compares the line shapes of the E_2^{high} and A_1(TO) modes. Given that the A_1(TO) line shape is fairly symmetric, the asymmetry of the E_2^{high} mode cannot be ascribed to lattice disorder. Furthermore, isotopic broadening is negligible for the E_2^{high} mode since it mainly involves O motion, and O is nearly isotopically pure. The line-shape broadening is then mostly determined by anharmonic phonon-phonon interactions. These can result in strongly distorted peaks when resonant interaction with a band of second-order combinations takes place (Fermi resonance), as is the case, for instance, for the GaP TO mode,[22,23] where the presence of van Hove-type singularities in the DOS of the TA+LA combination band gives rise to a highly asymmetric TO mode, which develops a side band at high pressure.[22] A similar situation occurs for the E_2^{high} mode of ZnO, as its frequency lies close to a ridge-like structure of the two-phonon DOS corresponding to TA+LA combinations in the vicinity of the K point.[8]

To evaluate this effect for the E_2^{high} phonon of ZnO we consider the phonon self-energy $\Sigma(\omega)=\Delta(\omega)-i\Upsilon(\omega)$, which expresses the renormalization of the *bare* harmonic frequency of the mode, ω_0, as a result of the interaction with other phonons. To the second order in perturbation theory, the cubic anharmonicity effect on the imaginary part of the self-energy is given by[24]

$$\Upsilon(\omega)=\frac{18\pi}{\hbar^2}\sum_{\mathbf{q}j_1j_2}|V_3(\mathbf{q}j_1,-\mathbf{q}j_2)|^2[(n_1+n_2+1)\delta(\omega_1+\omega_2-\omega)+(n_2-n_1)\delta(\omega_1-\omega_2-\omega)], \tag{3}$$

where $V_3(\mathbf{q}j_1,-\mathbf{q}j_2)$ is the third-order coefficient in the expansion of the lattice potential in normal coordinates and n_1 and n_2 are the Bose-Einstein occupation factors for the modes $\omega(\mathbf{q},j_1)$ and $\omega(-\mathbf{q},j_2)$, respectively ($\mathbf{q}$ is the phonon wave vector and j_i labels the phonon branch). Assuming slowly varying Bose-Einstein factors and V_3 coefficients in the small energy range considered, the imaginary part of the self-energy is proportional to the two-phonon DOS and can be written as

$$\Upsilon(\omega)=|V_3^+|^2(1+n_1+n_2)\rho^+(\omega)+|V_3^-|^2(n_2-n_1)\rho^-(\omega), \tag{4}$$

with $\rho^+(\omega)$ and $\rho^-(\omega)$ the two-phonon sum and difference DOS, and V_3^+ and V_3^- the effective third-order anharmonic constants for decay into phonon sums and phonon differences, respectively. Since real and imaginary parts of the phonon self-energy are related by a Kramers-Kronig transformation, the corresponding real part of the self-energy $\Delta(\omega)$ can be evaluated as

$$\Delta(\omega)=-\frac{2}{\pi}\mathcal{P}\int_0^\infty\frac{\omega'}{\omega'^2-\omega^2}\Upsilon(\omega')d\omega'. \tag{5}$$

This yields a frequency-dependent renormalization of the phonon energy, which has to be added to the constant shift in frequency due to the thermal expansion of the lattice Δ_0. This latter contribution can be written as[25]

$$\Delta_0=-\omega_0\gamma\int_0^T[\alpha_c(T')+2\alpha_a(T')]dT', \tag{6}$$

where α_c and α_a are the linear thermal expansion coefficients along directions parallel and perpendicular to the c axis, respectively, and γ is the Grüneisen parameter of the E_2^{high} mode, which we take as $\gamma=2.02$.[15] We have derived the thermal expansion coefficients for ZnO from the temperature dependence of the lattice parameters determined by x-ray diffraction by Iwanaga *et al.*[26] Although these data are only available for $T\geq 300$ K, we have extrapolated the results down to $T=200$ K. Below this temperature, thermal expansion usually falls rapidly and becomes negligible at $T\sim 50$ K,[27] and consequently the extrapolation of high-temperature values is not a good approximation. Thus, as a more accurate approximation for the thermal expansion coefficients for $T<200$ K we have used the calculated variation for ZnSe,[27] scaled to fit smoothly with the curve derived from experimental results for ZnO. For small self-energy corrections compared to the Raman frequency, the line shape of the Raman peak is

$$I(\omega)\propto\frac{\Upsilon(\omega)}{[\omega_0+\Delta_0+\Delta(\omega)-\omega]^2+\Upsilon(\omega)^2}. \tag{7}$$

If the frequency dependence of the phonon self-energy is neglected, the Raman line shape given by Eq. (7) reduces to

a Lorentzian function. In that case, the imaginary part of the phonon self-energy gives directly the half width of the corresponding line shape $\Upsilon = \frac{1}{2}\Gamma$. Note, however, that because of the frequency dependence of the self-energy, the line shape given by Eq. (7) may deviate substantially from a Lorentzian line shape and the comparison between the Raman linewidth and the theoretical lifetime requires a detailed analysis that involves a calculation of both the real and the imaginary part of the self-energy.[28] We use Eq. (7) with the frequency-dependent self-energy in order to simulate the Raman spectrum of the E_2^{high} mode and explain the observed asymmetric line shape.

To evaluate the imaginary part of the self-energy we have used the two-phonon sum DOS reported by Serrano *et al.*,[8] shifted by -10 cm^{-1} as explained in Ref. 15. Following the approach taken in Refs. 6 and 23, we smooth the calculated DOS in order to avoid spurious artifacts in the calculated line shapes. On the other hand, the two-phonon difference DOS is nearly flat around the E_2^{high} frequency, and can be approximated by a constant value $\rho^-(\omega) \approx 0.25$ states/cm^{-1}, as given in Ref. 8. According to the calculated phonon dispersion of ZnO, the most likely decay channels for the E_2^{high} mode are the decay into two acoustic modes at $\omega_1 \approx 190$ cm^{-1} and $\omega_2 \approx 250$ cm^{-1}, and into a difference between a longitudinal optical mode at $\omega_2 \approx 550$ cm^{-1} and an acoustic mode at $\omega_1 \approx 110$ cm^{-1}.[8] Using the corresponding Bose-Einstein occupation factors in Eq. (4), the line shape of the E_2^{high} mode can be calculated from Eqs. (4)–(7) with two adjustable parameters $|V_3^+|^2$ and $|V_3^-|^2$. We have taken $\omega_0 = 440$ cm^{-1} as given by the *ab initio* calculations reported in Ref. 15. A rigid shift of the two-phonon sum DOS has been included to take into account the thermal expansion effects. This has been obtained from Eq. (6) with the average Grüneisen parameters of the acoustic modes at $\omega_1 \approx 190$ cm^{-1} and $\omega_2 \approx 250$ cm^{-1}, which, based on the values reported in Ref. 15, we take as $\bar{\gamma} \approx 1.1$.

In Fig. 5 we plot the real and imaginary parts of the phonon self-energy and the theoretical line shape (solid line) for room temperature and $|V_3^+|^2 = 39$ cm^{-2} and $|V_3^-|^2 = 5.8$ cm^{-2}. We shall discuss the determination of the anharmonic coupling constants below. The calculated line shape has been upshifted by 2.3 cm^{-1} to bring it into agreement with the experimental spectrum. Such frequency shift is necessary because of the low *bare* harmonic frequency given by the *ab initio* calculations, which was estimated to be about 0.7% too low in Ref. 15. Very good agreement is obtained with the high-resolution Raman spectrum of the E_2^{high} mode (open circles). As can be seen from Fig. 5, the E_2^{high} line shape exhibits an asymmetric broadening toward low frequencies, where it deviates significantly from the Lorentzian line shape fitted to the upper frequency half of the peak (dotted line). The asymmetry in the E_2^{high} line shape stems from the strong frequency dependence of the imaginary part of the phonon self-energy, which is plotted in Fig. 5 (dashed-dotted line) against the left axis over the frequency region where the E_2^{high} mode occurs. Such a strong variation of the imaginary part of the phonon self-energy in the vicinity of the E_2^{high} frequency has been previously shown to give rise to an anomalous behavior of the E_2^{high} linewidth in ZnO crystals with different isotopical compositions and to an unusual pressure dependence of the E_2^{high} linewidth vs hydrostatic pressure.[8] In the present work, we show that this self-energy features are also responsible for the line-shape asymmetry of the E_2^{high} Raman peak.

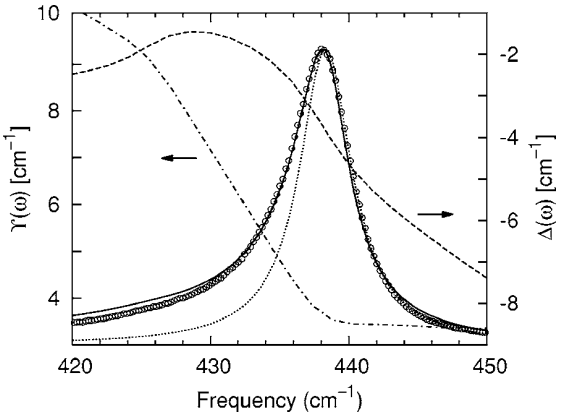

FIG. 5. High-resolution spectrum of the E_2^{high} mode of ZnO at room temperature (open circles). The solid line is the theoretical line shape calculated using the anharmonic decay model described in the text. For comparison, a symmetric Lorentzian line shape fitted to the high-frequency side of the peak is also displayed (dotted line). The real and imaginary parts of the phonon self-energy used in the calculations are plotted as dashed and dot-dashed lines, respectively.

The determination of the anharmonic coupling constants by fitting Eq. (7) to a single Raman spectrum has some degree of arbitrariness, as many combinations of $|V_3^+|^2$ and $|V_3^-|^2$ values yield similarly good visual agreement with the data. Instead of relying on a single Raman spectrum to derive the values of the anharmonic constants, we have measured the E_2^{high} linewidth for the full set of Raman spectra obtained at different temperatures and we have fitted the model to the temperature dependence of the E_2^{high} linewidth. To this end, the FWHM obtained from the theoretical line shape [Eq. (7)] Γ_{LS} was tabulated for a grid of $|V_3^+|^2$ and $|V_3^-|^2$ values. The tabulated values were used to interpolate $\Gamma_{\text{LS}}(T;|V_3^+|^2,|V_3^-|^2)$, which was fitted by the Levenberg-Marquardt method to the experimental linewidths. Including a constant background contribution to the linewidth (Γ_0) to account for defect and impurity scattering improves the fit significantly. The best fit to our data, which is displayed in Fig. 6, is obtained for $|V_3^+|^2 = 39$ cm^{-2}, $|V_3^-|^2 = 3.8$ cm^{-2}, and $\Gamma_0 = 1.3$ cm^{-1}. These results confirm that the decay rate for phonon-difference decay channels is considerably lower than for phonon-sum decay channels, and thus it can be safely neglected at low temperatures.

Estimates of the anharmonic squared matrix elements for the E_2^{high} mode of ZnO were obtained in Refs. 8 and 15 by using the expressions for the imaginary part of the self-energy [Eq. (4)] evaluated at the frequency of the mode and adjusting the anharmonic coefficients to reproduce their measured FWHM. As discussed above, when the frequency dependence is neglected, the imaginary part of the self-energy corresponds to the half width of the Lorentzian line shape, and therefore this procedure yields values for the anharmonic

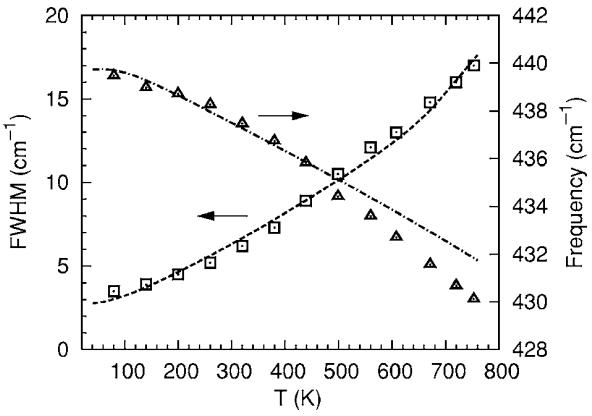

FIG. 6. Temperature dependence of the linewidth (squares, left axis) and frequency (triangles, right axis) of the E_2^{high} mode. The dashed line is a fit of the model discussed in the text to the linewidth data. The dot-dashed line corresponds to the temperature dependence of the frequency given by the model for the same set of parameters.

coefficients which are actually two times the values of the corresponding anharmonic squared matrix elements $[|V_3^+|^2$ and $|V_3^-|^2$ of Eq. (4)]. After correcting for this factor of 2, our values for the anharmonic squared matrix elements are somewhat higher than those given in Refs. 8 and 15 (39 vs 28 cm^{-1} for $|V_3^+|^2$ and 3.8 vs 3.1 cm^{-1} for $|V_3^-|^2$). In those works, no defect and/or impurity contribution to the linewidth was considered. If we do not include the constant contribution Γ_0 in our fits, the resulting $|V_3^-|^2$ value increases appreciably to compensate for the defect and/or impurity broadening, while $|V_3^+|^2$ turns out to be roughly the same. This explains the value $|V_3^-|^2$=5.8 cm^{-2} used to obtain the visual fit displayed in Fig. 5, but cannot account for the lower $|V_3^-|^2$ value reported in Ref. 8. The discrepancies in the $|V_3^+|^2$ and $|V_3^-|^2$ values mentioned above could arise from the simplified model used in Refs. 8 and 15, which does not take into account the actual frequency dependence of the phonon self-energy. Also, one should bear in mind that the higher-order terms neglected in Eq. (3) may lead to deviations in the calculated line shapes that are of increasing importance for higher temperatures. This could explain that the measured E_2^{high} frequency falls slightly below the one calculated from the model for $T>500$ K using the parameters determined above (see Fig. 6).[29]

Figure 7 displays high-resolution E_2^{high} spectra recorded at temperatures in the 80–750 K range. As temperature increases, the E_2^{high} peak is reduced in intensity and broadens significantly, maintaining a visible asymmetry toward lower frequencies. Such behavior is well reproduced by the line shapes calculated according to Eq. (7), which are plotted in the inset of Fig. 7. Note that Eq. (7) does not contain the defect and/or impurity broadening contribution and consequently the calculated line shapes are narrower than the corresponding Raman spectra, which are further broadened by defects and impurities. This is most apparent for the narrowest Raman line shape measured at 80 K.

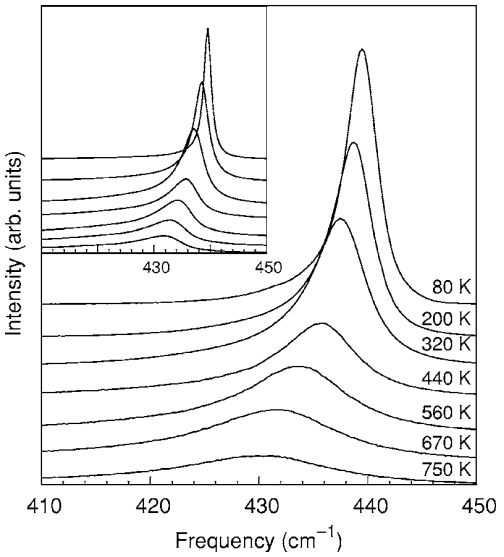

FIG. 7. Raman spectra of the E_2^{high} mode for temperatures in the 80–750 K range. Inset, corresponding line shapes calculated using the Fermi resonance model described in the text.

2. *The A_1(LO) and E_1(LO) modes: Generalized Ridley channel model*

The A_1(LO) and E_1(LO) frequencies of ZnO are very close to each other. Unlike the E_2^{high} mode, these two modes occur at frequencies that lie in a plateau of the two-phonon DOS with a relatively high density of states. Therefore their line shape is not affected by variations of the phonon self-energy and a simpler model can be used to analyze their temperature dependence. Inspection of the phonon dispersion curves[15] suggests that the main decay channel for these modes is the so-called generalized Ridley channel.[30,31] This involves the decay of the longitudinal optical mode into a mode of the transverse acoustic branches and a mode of the transverse optical branches. The anisotropy of the force constants in the wurtzite structure causes the transverse branches to split along the main symmetry lines of the Brillouin zone. Thus, modes from different split TO and TA branches can provide decay channels for both the A_1(LO) and the E_1(LO) modes. In the TA region, the phonon DOS presents a maximum at 100 cm^{-1}, with a significant contribution from the lower TA branch along *L-M*. A secondary maximum can be seen at ≈120 cm^{-1}, with an important contribution from the nearly flat TA branch along *L-M*. Similarly, in the TO region the phonon DOS exhibits a maximum at ≈455 cm^{-1} and a secondary maximum at ≈490 cm^{-1}, both of which contain important contributions from the split TO branches along *L-M*. Taking into account the phonon DOS, the A_1(LO) mode (574 cm^{-1}) decays most probably into pairs of TO and TA modes with frequencies around 455 and 120 cm^{-1}, respectively, whereas the corresponding decay frequencies for the E_1(LO) mode (590 cm^{-1}) are clustered around 490 and 100 cm^{-1}.

Assuming that the most relevant decay channel is the generalized Ridley channel with the main contributions clustered around ω_1 and ω_2, the temperature-dependent FWHM of the phonon mode can be modeled by[28]

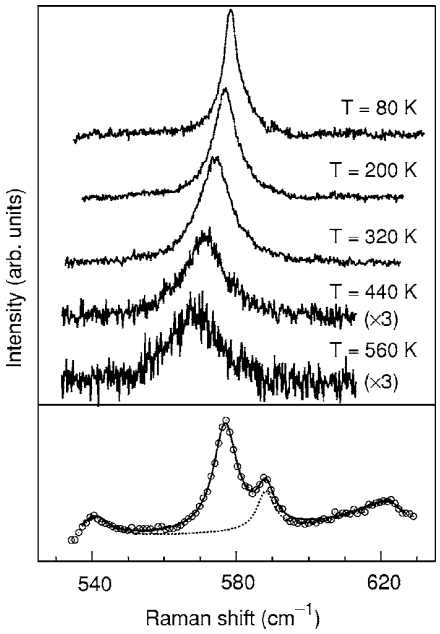

FIG. 8. Raman spectra of the A_1(LO) mode for temperatures in the 80–560 K temperature range, after baseline subtraction. For $T \geq 440$ K the spectra were recorded with the microscope hot stage and therefore the signal is lower due to the smaller depth of focus of the setup. Lower panel, fit to the Raman data (circles) used to determine the baseline (dotted line) to be subtracted, for the spectrum at $T=200$ K, where an additional peak is already resolved.

$$\Gamma(T) = \Gamma_0 + A[1 + n(\omega_1, T) + n(\omega_2, T)], \tag{8}$$

where Γ_0 is a background contribution due to impurity and/or defect scattering and isotopic broadening, A is the anharmonic coefficient, and $n(\omega, T)$ is the Bose-Einstein distribution function. Similarly, the temperature dependence of the frequency of the phonon mode can be written as

$$\omega(T) = \omega_0 + \Delta_0(T) + B[1 + n(\omega_1, T) + n(\omega_2, T)], \tag{9}$$

where $\Delta_0(T)$ is the thermal expansion shift given by Eq. (6) and B is the anharmonic coefficient.

As can be seen in Figs. 2 and 3, the A_1(LO) mode is very weak and emerges on a relatively strong second-order Raman scattering background. Furthermore, at low temperatures a peak at slightly higher frequency is resolved. To perform a linewidth analysis of the A_1(LO) Raman peak both contributions must be subtracted from the spectra. In Fig. 8 we show $z(xx)\bar{z}$ Raman spectra of the A_1(LO) mode for temperatures in the 80–560 K range after background subtraction. To determine the spectra backgrounds, a suitable combination of Lorentzian line shapes plus a linear background were fitted to the spectra, as illustrated in the lower panel of Fig. 8 for the spectrum at 200 K. The A_1(LO) Raman peak exhibits a symmetrical Lorentzian line shape, which redshifts and broadens as temperature increases. For $T \geq 400$ K the microscope hot stage was used, and hence the signal level is lower because of the smaller depth of focus of the setup.

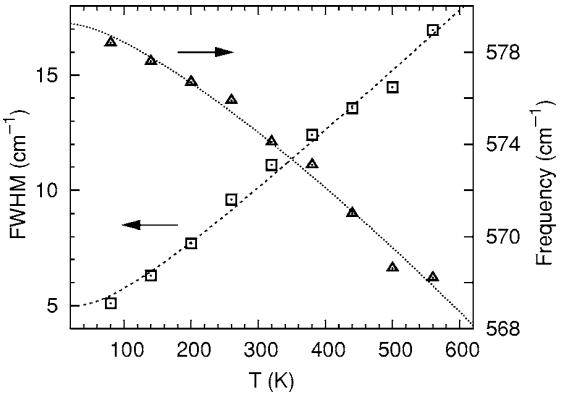

FIG. 9. Measured values of frequency (triangles) and linewidth (squares) of the A_1(LO) mode for temperatures in the 80–560 K range. The dotted lines are fits of $\Gamma(T)$ and $\omega(T)$ given by Eqs. (8) and (9) to the respective data.

Measurements at $T > 560$ K were discarded as the signal-to-noise ratio did not allow a reliable determination of the peak width.

The measured Raman shifts and linewidths of the A_1(LO) mode are plotted in Fig. 9. Equations (8) and (9), with $\omega_1 = 120$ cm^{-1} and $\omega_2 = 455$ cm^{-1}, and Γ_0, A, ω_0, and B as adjustable parameters, were fitted to the respective experimental data. We find $\Gamma_0 = 1.3$ cm^{-1}, $A = 3.7$ cm^{-1}, $\omega_0 = 581.4$ cm^{-1}, and $B = -2.1$ cm^{-1}.

A similar analysis was performed for the E_1(LO) mode. Figure 10 displays the $x(zy)y$ Raman spectra of the E_1(LO) mode for temperatures between 80 and 380 K, after careful subtraction of the background as illustrated in the lower panel for the 320 K spectrum. Since the E_1(LO) mode is

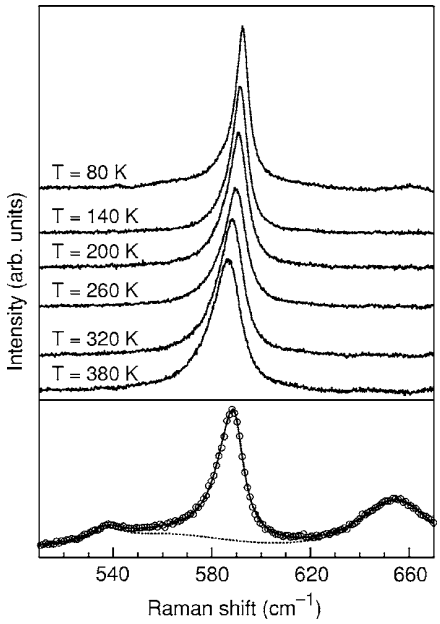

FIG. 10. Raman spectra of the E_1(LO) mode for temperatures in the 80–380 K temperature range, after baseline subtraction. Lower panel, fit to the Raman data (circles) used to determine the baseline (dotted line) to be subtracted, for the spectrum at $T=320$ K.

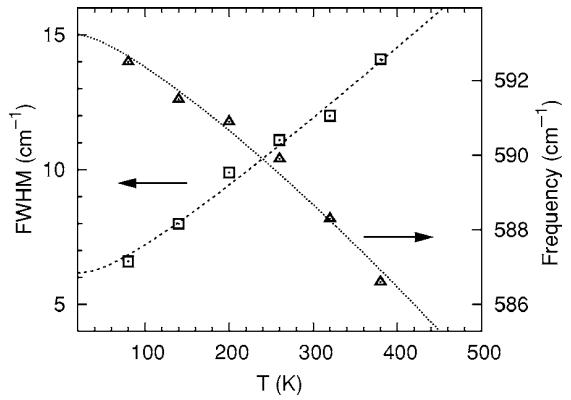

FIG. 11. Measured values of frequency (triangles) and linewidth (squares) of the E_1(LO) mode for temperatures in the 80–380 K range. The dotted lines are fits of $\Gamma(T)$ and $\omega(T)$ given by Eqs. (8) and (9) to the respective data.

forbidden in backscattering configuration, the microscope hot stage could not be used and consequently this set of measurements was only possible on a limited temperature range. Measured E_1(LO) linewidths and frequencies as well as linear-square fits of Eqs. (8) and (9) to the data with $\omega_1 = 100$ cm^{-1} and $\omega_2 = 490$ cm^{-1} are plotted in Fig. 11. The best fit to our data is found for $\Gamma_0 = 2.8$ cm^{-1}, $A = 3.3$ cm^{-1}, $\omega_0 = 595$ cm^{-1}, and $B = -1.7$ cm^{-1}.

By comparing the anharmonic coefficients A and B for the A_1(LO) and E_1(LO) modes of ZnO we can see that the temperature dependence of these modes is very similar. This is not unexpected, as these modes lie close in frequency in a region where the two-phonon DOS does not change appreciably. However, the E_1(LO) mode displays a larger linewidth, which implies a higher value of Γ_0 and suggests that the E_1(LO) mode is more strongly affected by impurity and/or defect scattering than the A_1(LO) mode. As the incorporation of defects in ZnO is known to be highly anisotropic, this could be related to a possible anisotropy in the distribution of defects and the fact that the E_1(LO) mode has an in-plane atomic motion whereas the atomic motion of the A_1(LO) mode takes place along the c axis.

To sum up, in contrast with the E_2^{high} mode where anharmonic decay involves a continuum of TA+LA phonons, the temperature dependence of the A_1(LO) and E_1(LO) modes can be accounted for by a simple model in which the longitudinal phonon decays into a pair of TO and TA phonons whose frequencies correspond to maxima of the phonon DOS.

3. Phonon lifetimes

The phonon lifetime τ can be derived from the Raman spectra via the energy-time uncertainty relation

$$\frac{1}{\tau} = \frac{\Delta E}{\hbar} = 2\pi c\Gamma, \tag{10}$$

where ΔE is the uncertainty in the energy of the phonon mode, $\hbar$ is the Planck constant, and Γ is the FWHM of the Raman peak in units of cm^{-1}.

TABLE III. Phonon lifetimes of the E_2^{high}, A_1(LO), and E_1(LO) modes of ZnO at 80 K and room temperature. The characteristic decay time associated with impurities τ_I is estimated from the background broadening parameter Γ_0 used to fit the FWHM temperature dependence.

	$T=80$ K		$T=300$ K			
Phonon mode	Γ (cm^{-1})	τ (10^{-12} s)	Γ (cm^{-1})	τ (10^{-12} s)	Γ_0 (cm^{-1})	τ_I (10^{-12} s)
E_2^{high}	3.5	1.5	6.0	0.88	1.3	4.1
A_1(LO)	5.1	1.0	9.7	0.54	1.3	4.1
E_1(LO)	6.6	0.80	11.7	0.45	2.8	1.9

Phonon lifetime is mainly limited by two mechanisms: (i) anharmonic decay of the phonon into two or more phonons so that energy and momentum are conserved, with a characteristic decay time τ_A and (ii) perturbation of the translational symmetry of the crystal by the presence of impurities, defects and isotopic fluctuations, with a characteristic decay time τ_I. The phonon lifetime deduced from the Raman measurements is therefore

$$\frac{1}{\tau} = \frac{1}{\tau_A} + \frac{1}{\tau_I}. \tag{11}$$

It is difficult to separate the contribution of both mechanisms, but we can obtain an estimation of the characteristic decay time associated with impurities from the values of the Γ_0 parameter provided by the FWHM temperature-dependence fits. The results are summarized in Table III. We can see that the shortest τ_I corresponds to the E_1(LO) mode. The fact that the E_1(LO) mode has a polar character allows a Fröhlich interaction with charged impurities and defects.[32] As already discussed, owing to a possible anisotropy in the distribution of defects such interaction could affect the E_1(LO) lifetime more severely than the A_1(LO) lifetime, as the E_1(LO) mode has in-plane polarization, whereas the A_1(LO) mode is polarized along the c axis. This would explain that the E_1(LO) linewidth observed both at 80 K and at RT is 1.5–2 cm^{-1} higher than the corresponding A_1(LO) linewidth.

The E_2^{high} lifetime at room temperature is in good agreement with the value reported by Bergman *et al.*[9] No values for the A_1(LO) and E_1(LO) were reported in that work. We find similar lifetime values around 0.5 ps for both modes, which are close to those reported for high-quality AlN crystals.[9] The values found for the E_2^{high}, A_1(LO), and E_1(LO) phonon lifetimes corroborate that the anharmonic decay involves in all three cases a three-phonon process and rules out four-phonon interaction as the main decay mechanism, as this would yield phonon lifetimes 2 or 3 orders of magnitude longer.

IV. SUMMARY AND CONCLUSIONS

We have carried out a detailed study of the first- and second-order Raman scattering of ZnO for temperatures

ranging from 80 up to 750 K. Second-order Raman spectra obtained in different scattering geometries have been discussed in terms of DFT phonon dispersion relations and symmetry analysis. Characteristic second-order Raman peaks have been assigned to overtones and combinations of acoustic and optical phonon branches. The temperature dependence of the 333 cm^{-1} Raman peak, which is often attributed to acoustic overtones at M, has been shown to correspond to a difference mode, and the mode has been assigned to E_2^{high}-E_2^{low}. Several sharp peaks show up at low temperature, which are tentatively related to intrinsic lattice defects. Most notably, a peak is resolved at 589 cm^{-1} in the $z(xx)\bar{z}$ spectra at 80 K, very close to the E_1(LO) frequency. The possibility of a leaky E_1(LO) mode can be ruled out since the frequency of the E_1(LO) mode at 80 K was determined to be 593 cm^{-1} in the allowed $x(zy)y$ configuration.

The anharmonic broadening of the E_2^{high}, A_1(LO), and E_1(LO) phonon modes was studied as a function of temperature. The E_2^{high} mode of ZnO exhibits a visibly asymmetric line shape, which could be successfully explained in terms of resonant anharmonic interaction of the E_2^{high} mode with a band of combined transverse and longitudinal acoustic modes, as the steep variation of the two-phonon DOS around the E_2^{high} frequency leads to a distorted phonon line shape. In contrast, the two-phonon DOS is rather flat in the A_1(LO) and E_1(LO) frequency region and the temperature dependence of these modes can be adequately described with a simple anharmonic decay model via a dominating Ridley channel involving TO and TA modes whose frequencies are clustered around maxima of the DOS. The lifetimes of these modes are determined from the Raman spectra and are found to be around 0.5 ps for both longitudinal modes at room temperature.

ACKNOWLEDGMENTS

This work has been supported by the Spanish Ministry of Education and Science under Contract No. MAT2004-0664 and Ramón y Cajal Program. The work performed by the United States Air Force Research Laboratory at Hanscom Air Force Base was partially supported by the Air Force Office of Scientific Research.

[1] D. C. Look, Mater. Sci. Eng., B **80**, 383 (2001).
[2] B. C. Lee, K. W. Kim, M. A. Stroscio, and M. Dutta, Phys. Rev. B **58**, 4860 (1998).
[3] N. Hasuike, H. Fukumura, H. Harima, K. Kisoda, H. Matsui, H. Saeki, and H. Tabata, J. Phys.: Condens. Matter **16**, S5807 (2004).
[4] W. Limmer, W. Ritter, R. Sauer, B. Mensching, C. Liu, and B. Rauschenbach, Appl. Phys. Lett. **72**, 2589 (1998).
[5] D. Pastor, R. Cuscó, L. Artús, G. González-Díaz, S. Fernández, and E. Calleja, Semicond. Sci. Technol. **20**, 374 (2005).
[6] A. Göbel, T. Ruf, C.-T. Lin, M. Cardona, J.-C. Merle, and M. Joucla, Phys. Rev. B **56**, 210 (1997).
[7] J. M. Zhang, T. Ruf, M. Cardona, O. Ambacher, M. Stutzmann, J.-M. Wagner, and F. Bechstedt, Phys. Rev. B **56**, 14399 (1997).
[8] J. Serrano, F. J. Manjón, A. H. Romero, F. Widulle, R. Lauck, and M. Cardona, Phys. Rev. Lett. **90**, 055510 (2003).
[9] L. Bergman, D. Alexson, P. L. Murphy, R. J. Nemanich, M. Dutta, M. A. Stroscio, C. Balkas, H. Shin, and R. F. Davis, Phys. Rev. B **59**, 12977 (1999).
[10] A. Link, K. Bitzer, W. Limmer, R.Sauer, C. Kirchner, V. Schwegler, M. Kamp, D. G. Ebling, and K. W. Benz, J. Appl. Phys. **86**, 6256 (1999).
[11] T. C. Damen, S. P. S. Porto, and B. Tell, Phys. Rev. **142**, 570 (1966).
[12] C. A. Arguello, D. L. Rosseau, and S. P. S. Porto, Phys. Rev. **181**, 1351 (1969).
[13] J. M. Calleja and M. Cardona, Phys. Rev. B **16**, 3753 (1977).
[14] D. G. Mead and G. R. Wilkinson, J. Raman Spectrosc. **6**, 123 (1977).
[15] J. Serrano, A. H. Romero, F. J. Manjón, R. Lauck, M. Cardona, and A. Rubio, Phys. Rev. B **69**, 094306 (2004).
[16] C. Aku-Leh, J. Zhao, R. Merlin, J. Menéndez, and M. Cardona, Phys. Rev. B **71**, 205211 (2005).
[17] M. Suscavage *et al.*, MRS Internet J. Nitride Semicond. Res. **4S1**, G3.40 (1999).
[18] H. Siegle, G. Kaczmarczyk, L. Filippidis, A. P. Litvinchuk, A. Hoffmann, and C. Thomsen, Phys. Rev. B **55**, 7000 (1997).
[19] A. Kaschner, U. Haboeck, M. Strassburg, G. Kaczmarczyk, A. Hoffmann, C. Thomsen, A. Zeuner, H. R. Alves, D. M. Hofmann, and B. K. Meyer, Appl. Phys. Lett. **80**, 1909 (2002).
[20] *Light Scattering in Solids II*, edited by M. Cardona and G. Güntherodt, Topics in Applied Physics Vol. 50 (Springer-Verlag, Berlin, 1982).
[21] C. Bundesmann, N. Ashkenov, M. Shubert, D. Spemann, T. Butz, E. M. Kaidashev, M. Lorenz, and M. Grundmann, Appl. Phys. Lett. **83**, 1974 (2003).
[22] B. A. Weinstein, Solid State Commun. **20**, 999 (1976).
[23] F. Widulle, T. Ruf, A. Göbel, E. Schönherr, and M. Cardona, Phys. Rev. Lett. **82**, 5281 (1999).
[24] R. A. Cowley, Rep. Prog. Phys. **31**, 123 (1968).
[25] W. J. Borer, S. S. Mitra, and K. V. Namjoshi, Solid State Commun. **9**, 1377 (1971).
[26] H. Iwanaga, A. Kunishige, and S. Takeuchi, J. Mater. Sci. **35**, 2451 (2000).
[27] A. Debernardi and M. Cardona, Phys. Rev. B **54**, 11305 (1996).
[28] J. Menéndez and M. Cardona, Phys. Rev. B **29**, 2051 (1984).
[29] A. Debernardi and M. Cardona, Physica B **263-264**, 687 (1999).
[30] B. K. Ridley, J. Phys.: Condens. Matter **8**, L511 (1996).
[31] S. Barman and G. P. Srivastava, Phys. Rev. B **69**, 235208 (2004).
[32] B. K. Ridley and R. Gupta, Phys. Rev. B **43**, 4939 (1991).

IOP PUBLISHING JOURNAL OF PHYSICS: CONDENSED MATTER

J. Phys.: Condens. Matter **20** (2008) 445211 (4pp) doi:10.1088/0953-8984/20/44/445211

Raman scattering of quasimodes in ZnO

E Alarcón-Lladó[1], R Cuscó[1], L Artús[1], J Jiménez[2], B Wang[3] and M Callahan[4]

[1] Institut Jaume Almera, Consell Superior d'Investigacions Científiques (CSIC), Lluís Solé i Sabarís s.n., 08028 Barcelona, Spain
[2] Departamento de Física de la Materia Condensada, ETSII, Universidad de Valladolid, Spain
[3] Solid State Scientific Corporation, 27-2 Wright Road, Hollis, NH 03049, USA
[4] Air Force Research Laboratory, Sensors Directorate, Electromagnetics Technology Division, Optoelectronic Technology Branch, Hanscom AFB, MA 01731-2909, USA

Received 24 July 2008, in final form 19 September 2008
Published 10 October 2008
Online at stacks.iop.org/JPhysCM/20/445211

Abstract
The angular dependence of the optical phonons of high-quality bulk ZnO has been systematically studied by means of Raman scattering. We report the observation of quasi-TO and quasi-LO modes for propagation directions covering the whole *a*–*c* mixing plane using a beveled ZnO single crystal sample. Scattering experiments performed in two different configuration geometries indicate that birefringence effects are not relevant for the phonon analysis in this material. The observed angular dependence of the quasimode frequencies is in good agreement with Loudon's model.

1. Introduction

ZnO is a direct wide band-gap ($E_g \sim 3.4$ eV) semiconductor with a deep excitonic binding energy of around 60 meV [1], which makes it a promising material in electronics, optics and photonics. With reduction in size, semiconductor structures exhibit novel electronic, mechanical, optical and vibrational properties which are a consequence of surface and quantum confinement effects. Raman scattering has been proven to be a powerful and non-destructive technique to study the vibrational and optical properties of ZnO crystals, thin films and micro and nanostructures [2–4]. In the case of crystals of reduced dimensionality, some peak shifts and broadenings in the Raman spectra may occur. In previous works on ZnO nanocrystals, some authors attribute these changes to confinement effects [5–9], whereas others claim that the shifts are due to local heating rather than to spatial confinement [10, 11]. However, the crystallite orientation also affects the Raman spectra. In these systems, a mixing of the polar modes takes place when the crystal high-symmetry axes are tilted relative to the phonon propagation direction. This gives rise to the so-called quasimodes [12] and their frequency changes depending on the light incidence. Ignoring the excitation of quasimodes in nanostructures could result in a misleading analysis of strain, composition and confinement.

Some works dealing with quasimodes in wide band-gap materials have been published [13–16]. Bergman *et al* [13] studied the quasi-transverse and quasi-longitudinal optical modes in wurtzite AlN for phonon propagation angles lower than 30° relative to the *a*-axis. Early works on quasimodes in ZnO were performed in the late 1960s, but only showed spectra for a 45° phonon propagation direction [15, 16]. To date, no Raman data on the angular dependence of quasimodes in ZnO are available. In this work we present a systematic study of the longitudinal optical (LO) and transverse optical (TO) quasimodes in bulk single crystal ZnO by means of Raman scattering for phonon propagation angles spanning the whole range of propagation directions between the *a* and *c* axis. We discuss the role of birefringence in the determination of the quasimode frequencies in wurtzite crystals and we find that the birefringence effects can be neglected in ZnO. The experimental values of the quasimode frequencies are in good agreement with those predicted by Loudon's model based on the phonon–electrostatic field interaction between polar modes in uniaxial materials.

2. Experiment

The experiments were performed on a ZnO single crystal obtained by the hydrothermal growth method. Growth details as well as x-ray and photoluminescence (PL) characterization of ZnO crystals obtained by this growth method can be found elsewhere [17]. The sample was excited at room temperature with the 514.5 nm line of an Ar^+ laser in the backscattering geometry from an *m*-plane $(10\bar{1}0)$. The scattered light was analyzed with a Jobin-Yvon T64000 spectrometer equipped with a LN_2-cooled charged-coupled device (CCD) detector.

J. Phys.: Condens. Matter **20** (2008) 445211

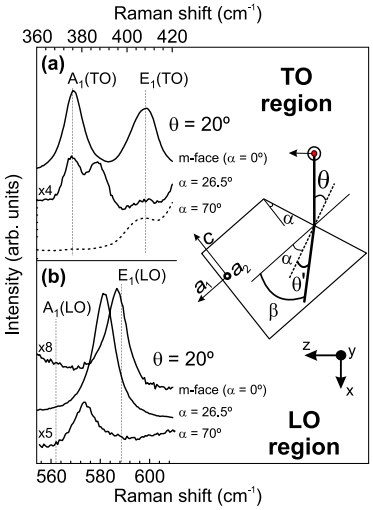

Figure 1. Room temperature $x(z\gamma)\bar{x}$ Raman spectra of single crystal ZnO in the TO (a) and LO (b) frequency regions. The spectra were obtained with an angle of incidence of 20° from various surfaces. The dotted spectrum was recorded in a $x(y\gamma)\bar{x}$ configuration in order to reduce the E_2^{high} tail. The spectra are arbitrarily offset on the intensity scale for clarity. The sketch shows the geometry of the experimental setup and the laboratory coordinate system (x, y, z). θ, θ' and α correspond to the incidence, refracted and surface tilting angles, respectively, and $\beta = \alpha + \theta'$.

Both $x(z\gamma)\bar{x}$ and $x(y\gamma)\bar{x}$ scattering configurations were used, where x, y, and z correspond to the laboratory coordinates as depicted in figure 1, and γ denotes the scattered light polarization which depends on the angle θ and was adjusted by optimizing the quasimode signal. We define a set of orthogonal crystal axes (a_1, a_2, c), where a_1 (a_2) is perpendicular (parallel) to the m-plane and c is along the (0001) crystallographic direction (see sketch in figure 1). The ZnO crystal was rotated in 10° steps through an angle θ in such a way that the quasiphonon propagation direction remains in the mixing c–a_1 plane. In the backscattering geometry, the phonon propagation direction lies along the light propagation direction in the crystal. The maximum phonon propagation angle β is thus limited to around 30° in ZnO by Snell's law. In order to overcome this limitation and to attain higher phonon propagation angles, we also performed measurements on surfaces tilted at an angle $\alpha = 26.5°$ and 70° relative to the m-plane. The former corresponds to the natural growth surface $(10\bar{1}1)$, whereas for the latter a beveled sample was prepared by chemomechanical polishing at NovaSiC.

3. Results and discussion

Figure 1 shows $x(z\gamma)\bar{x}$ Raman spectra performed at an incidence of $\theta = 20°$ relative to the surface normal, for surfaces tilted at an angle $\alpha = 0$, 26.5, and 70°, where β increases from ≈10° for $\alpha = 0°$ to ≈80° for $\alpha = 70°$. In the TO-frequency region (figure 1(a)), three main features can be observed in the spectra: the E_1(TO) mode at 407.1 cm^{-1}, the A_1(TO) mode at 374.7 cm^{-1}, and a peak which shifts upwards with increasing β. In the LO-frequency region (figure 1(b)), a single intense peak dominates the spectrum. This peak shifts to lower frequencies as the propagation angle increases. Given that in ZnO the interaction between polar modes is dominated by the long-range electrostatic field rather than by the short-range interatomic forces, TO (LO) phonons of A_1 and E_1 symmetries mix together, giving rise to quasimodes with large TO–LO splitting. These quasimodes exhibit nearly pure transverse (quasi-TO) or longitudinal (quasi-LO) character and their frequencies shift relative to the frequencies of the pure modes depending on the phonon propagation direction [12]. Therefore we assign the peaks displaying a frequency dependence on the propagation angle in figures 1(a) and (b) to the quasi-TO and quasi-LO modes, respectively. The E_1 character of the quasi-TO mode increases with the phonon propagation angle and therefore it displays a shift to higher frequencies. Conversely, the quasi-LO mode gains A_1 character as the phonon propagation angle increases and as a result it shows a downward frequency shift.

For incidences close to the c-axis the weak quasi-TO mode cannot be well resolved because it is masked by the overlapping E_2^{high} low frequency tail. For this reason, we plot in figure 1(a) the $x(y\gamma)\bar{x}$ spectrum for $\alpha = 70°$ (dotted line). In contrast, the quasi-LO mode intensity becomes comparable with that of the typical second order Raman features in ZnO [2] but can still be unambiguously determined.

As already mentioned, pure E_1(TO) and A_1(TO) peaks show up in the spectra (see figure 1(a)) in spite of the mixing between the A_1 and E_1 modes. The pure E_1(TO) mode observed in the $x(z\gamma)\bar{x}$ Raman spectra corresponds to the E_1 component polarized along the direction orthogonal to the c–a_1 mixing plane. Although the non-degenerate A_1 mode lies in the c–a_1 plane and always mixes with the E_1 mode, a weak pure A_1(TO) mode is also observed in the $x(z\gamma)\bar{x}$ spectra which is attributed to Raman scattering of internal reflections.

In order to collect and show all our experimental data, we present in figure 2 a contour plot of the Raman intensity over the range of incidence and surface tilting angles studied in this work. For convenience, the x-axis range is arranged so that no discontinuities in the phonon propagation angle occur between plots from differently tilted surfaces. The intensity was normalized to the quasimode intensity after a baseline subtraction and the maxima and minima of intensity correspond, respectively, to the red and blue colors in the contour plot. First, we note that both the quasi-TO and the quasi-LO modes do not show a significant variation of their width with the incidence and surface tilting angles. However, the quasi-TO mode seems to broaden asymmetrically to lower frequencies with increasing θ in the $\alpha = 26.5°$ lower panel of figure 2. This broadening can be explained by the presence of a weak pure A_1(TO) mode superimposed to the quasimode whose origin has been discussed above. For $\alpha = 70°$ the quasi-TO mode weakens and shifts upward, allowing the pure A_1(TO) be clearly observed in the contour plot as an independent peak (dark region in the lower right panel). The fact that quasimodes display similar widths for all propagation directions is not surprising, as the A_1 and E_1-symmetry modes have similar widths in ZnO either for the longitudinal and

J. Phys.: Condens. Matter **20** (2008) 445211 E Alarcón-Lladó *et al*

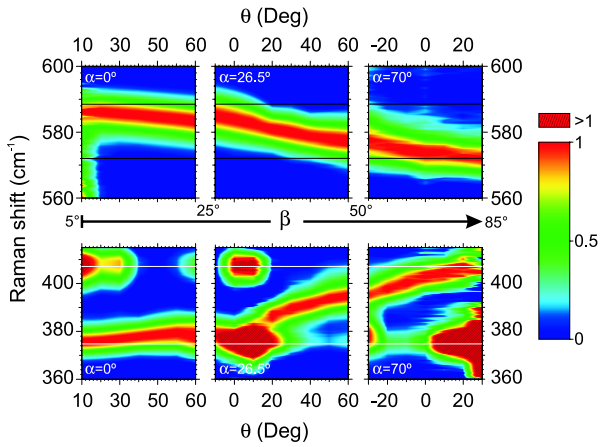

Figure 2. Spectrally resolved contour plots of the $x(z\gamma)\bar{x}$ Raman intensity as a function of the angle of incidence in the LO-frequency region (upper panels) and TO-frequency region (lower panels). Spectra were taken from faces tilted an angle α relative to the m-face. The arrow indicates increasing phonon propagation angle. The spectra were normalized such that the quasimode intensity is unity. Horizontal lines represent the frequency position of the pure polar modes in ZnO.

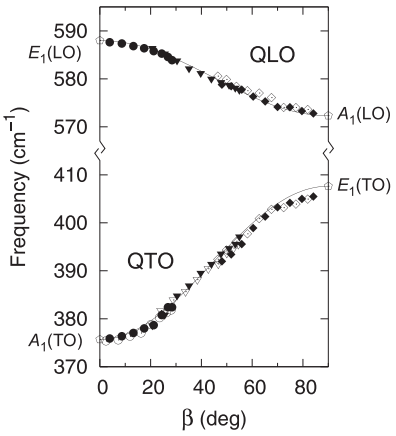

Figure 3. Quasi-LO and quasi-TO mode frequencies as a function of phonon propagation angle β relative to the a_1 axis. The plotted data points were obtained from a m-face (circles) and faces tilted 26.5° (triangles) and 70° (diamonds). Empty (filled) symbols correspond to the $x(y\gamma)\bar{x}$ [$x(z\gamma)\bar{x}$] scattering configuration. Solid lines represent the quasimode frequencies calculated using Loudon's theory.

transverse modes [2]. On the other hand, the quasimode frequency behavior is clearly illustrated in figure 2. The quasi-LO mode frequency ω_{QLO} (upper panels) shifts monotonically from the E_1(LO) mode frequency, $\omega_{E_1(\mathrm{LO})} = 588.5\ \mathrm{cm}^{-1}$, to the A_1(LO) mode frequency, $\omega_{A_1(\mathrm{LO})} = 571.0\ \mathrm{cm}^{-1}$, when changing the phonon propagation direction from a_1 to c. A similar behavior holds for the quasi-TO mode frequency. The mode shows an upward frequency shift from the A_1(TO) to the E_1(TO) mode frequency ($\omega_{A_1(\mathrm{TO})} = 378.0\ \mathrm{cm}^{-1}$ and $\omega_{E_1(\mathrm{TO})} = 410.0\,\mathrm{cm}^{-1}$, respectively). As the longitudinal mode frequencies are closer to each other than the transverse mode frequencies, the dispersion of the quasi-TO mode (~32 cm^{-1}) is larger than that of the quasi-LO mode (~16 cm^{-1}).

The change of the quasimode frequency with β can be modeled by Loudon's theory, considering the long-range electrostatic field as the dominant interaction mechanism between polar phonons. Under this assumption, the theory predicts that the quasi-TO mode frequency should lie between the frequency of the pure A_1(TO) mode and that of the pure E_1(TO) mode according to the relation [12]

$$\omega^2_{\mathrm{QTO}} = \omega^2_{A_1(\mathrm{TO})}\cos^2\beta + \omega^2_{E_1(\mathrm{TO})}\sin^2\beta. \qquad (1)$$

Similarly, the quasi-LO mode should shift from the pure E_1(LO) mode to the pure A_1(LO) mode following the relation [12]

$$\omega^2_{\mathrm{QLO}} = \omega^2_{E_1(\mathrm{LO})}\cos^2\beta + \omega^2_{A_1(\mathrm{LO})}\sin^2\beta. \qquad (2)$$

In the backscattering geometry, β can be derived from the incidence angle θ and the surface tilting angle α via Snell's law: $n_1\sin\theta = n_2\sin(\beta-\alpha)$, where $n_1 = 1$ and n_2 is the ZnO refractive index. As ZnO is a uniaxial crystal, two different refractive indices are to be considered depending on the electric field direction of the incident light. For the electric field parallel (perpendicular) to the c-axis, the extraordinary refractive index n_e (ordinary refractive index n_o) must be used. In the $x(z\gamma)\bar{x}$ configuration geometry, the refractive index varies from n_e for normal incidence to n_o in the $\beta \to 90°$ limit according to the refractive index ellipsoid $1/n^2(\beta) = (\sin\beta/n_o)^2 + (\cos\beta/n_e)^2$. In contrast, in a $x(y\gamma)\bar{x}$ configuration geometry the refractive index is n_o independently of the angle of incidence θ. However, for small β only the quasi-TO mode can be unambiguously detected in this configuration. For this reason, experiments in the two scattering configurations discussed above were carried out.

Figure 3 displays the experimental values of ω_{QTO} and ω_{QLO} as a function of the phonon propagation angle β. The angle β was calculated using $n_2 = n_o = 2.053$ [18] as the refractive index of ZnO for both scattering geometries used in the experiments. If birefringence effects were important, the two sets of data plotted in figure 3 would differ noticeably. On the contrary, a smooth overlapping of the experimental data can be seen in figure 3, from which we conclude that the error made by using the approximation $n(\beta) = n_o$ is negligible and therefore birefringence effects can be ignored in ZnO for the purpose of quasimode analysis. The experimental quasimode frequencies follow closely the theoretical predictions (equations (1) and (2)), also plotted in figure 3 as solid lines. Although at large β the quasi-TO mode frequencies deviate slightly from the theoretical curve, this may be related to the difficulty in determining accurately ω_{QTO} in this limit, given the high intensity of the E_2^{high} peak whose low frequency tail overlaps the weak quasi-TO mode.

4. Conclusions

The quasi-LO and quasi-TO modes of ZnO were observed for the whole range of phonon propagation angles between an a and the c axis. The angular dependence of the

quasimode frequencies is well described by Loudon's model. The agreement between the model and the experimental data obtained under different scattering geometries implies that the birefringence effect can be neglected in ZnO for the phonon analysis. Taking into account this angular dependence is crucial for analyzing Raman spectra of nanostructured ZnO with randomly oriented facets.

Acknowledgments

Work supported by the Spanish Government (project MAT2007-63617 and FPI Program). The work performed by the US Air Force Research Laboratory at Hanscom Air Force Base was partially supported by the Air Force Office of Scientific Research.

References

[1] Thomas D 1960 *J. Phys. Chem. Solids* **15** 86
[2] Cuscó R, Alarcón-Lladó R, Ibáñez J, Artús L, Jiménez J, Wang B and Callahan M 2007 *Phys. Rev.* B **75** 165202
[3] Park D, Tak Y and Yong K 2008 *J. Nanosci. Nanotechnol.* **8** 623
[4] Chen B, HT N and Chen C L 2007 *J. Exp. Nanosci.* **2** 57
[5] Bergman L, Chen X B, Huso J, Morrison J L and Hoeck H 2005 *J. Appl. Phys.* **98** 093507
[6] Zi J, Büscher H, Falter C, Ludwig W, Zhang K and Xie X 1996 *Appl. Phys. Lett.* **69** 200
[7] Campbell I H and Fauchet P M 1986 *Solid State Commun.* **58** 739
[8] Rajalakshmi M, Arora A K, Bendre B S and Mahamuni S 2000 *J. Appl. Phys.* **87** 2445
[9] Geng C, Jiang Y, Yao Y, Meng X, Zapien J A, Lee C S, Lifshitz Y and Lee S T 2004 *Adv. Funct. Mater.* **14** 589
[10] Alim K A, Fonoberov V A, Shamsa M and Balandin A A 2005 *J. Appl. Phys.* **97** 124313
[11] Demangeot F, Paillard V, Chassaing P M, Pagès C, Kahn M L, Maisonnat A and Chaudret B 2006 *Appl. Phys. Lett.* **88** 071921
[12] Loudon R 1964 *Adv. Phys.* **13** 423
[13] Bergman L, Dutta M, Balkas C, Davis R F, Christman J A, Alexson D and Nemanich R J 1999 *J. Appl. Phys.* **85** 3535
[14] Filippidis L, Siegle H, Hoffmann A, Thomsen C, Karch K and Bechstedt F 1996 *Phys. Status Solidi* b **198** 621
[15] Arguello C A, Rousseau D L and Porto S P S 1969 *Phys. Rev.* **181** 1351
[16] Damen T C, Porto S P S and Tell B 1966 *Phys. Rev.* **142** 570
[17] Suscavage M, Harris M, Bliss D, Yip P, Wang S Q, Schwall D, Bouthillette L, Bailey J, Callahan M and Look D C 1999 *MRS Internet J. Nitride Semicond. Res.* **4S1** G3.40
[18] Yoshikawa H and Adachi S 1997 *Japan J. Appl. Phys.* **36** 6237

Mater. Res. Soc. Symp. Proc. Vol. 957 © 2007 Materials Research Society 0957-K07-24

Raman Scattering Characterization of Implanted ZnO

Esther Alarcon-Llado[1], Ramon Cusco[1], Luis Artus[1], German Gonzalez-Diaz[2], Ignacio Martil[2], Juan Jimenez[3], Buguo Wang[4], and Michael Callahan[5]
[1]Inst. Jaume Almera, C.S.I.C., C. Sole Sabaris sn, Barcelona, 08028, Spain
[2]Dep. Fisica Aplicada III, Univ. Complutense, Madrid, 28040, Spain
[3]Dep. Fisica Materia Condensada, Univ. Valladolid, P. del Cauce sn, Valladolid, 47011, Spain
[4]Solid State Scientific Corporation, 27-2 Wright Road, Hollis, NH, 03049
[5]Sensors Directorate, Air Force Research Laboratory, Hanscom AFB, MA, 01731-2909

ABSTRACT

In this work we investigate the lattice damage induced in ZnO implanted with potential group V acceptors by means of Raman scattering. ZnO samples were implanted with N and P to high doses and Raman spectra were obtained prior and after rapid thermal annealing (RTA). Characteristic disorder-activated modes are observed in the spectra that can be used to assess the degree of lattice damage. ZnO samples were also implanted with native Zn^+ and O^+ ions under similar conditions to study specific effects of implantation with N^+ and P^+. As revealed by the intensity of disorder-activated bands, the implantation induced lattice damage is considerably higher for Zn^+ than for the lighter O^+ ion. In samples implanted with N^+ additional Raman peaks emerge that are not observed either in the samples implanted with the native Zn^+ and O^+ ions or in the samples implanted with P^+, thus pointing to a local vibrational mode of N or a N complex as the origin of these modes. Disorder-activated features are fully removed by RTA, indicating a high degree of lattice recovery by RTA even for the heavily damaged ZnO samples implanted with Zn^+.

INTRODUCTION

In recent years there has been a growing interest in ZnO because of its advantageous physical properties –wide band gap and free exciton with a 60 meV binding energy– for applications in integrated optoelectronic devices operating in the ultraviolet and blue spectral range. One of the main challenges for the development of ZnO based devices is the difficulty in obtaining reproducible *p*-type doping. The group V elements N, P and As have been used to make *p*-type ZnO, despite P and As having a much larger ionic radius than that of O. Actually, some of the lowest resistivity *p*-type material has been obtained with P doping [1]. Nevertheless, hole concentrations and mobilities are usually small because of high activation energies, self-compensation by native defects and the formation of electrically inactive stable complexes [2]. Ion implantation is a versatile processing tool for selective doping with a good control of the incorporated dopants. However, the implantation process induces defects and disorder in the lattice that strongly affect the electrical activation of the implanted dopants and usually give rise to heavily compensated implanted *p*-type layers. Therefore, the characterization of the ZnO lattice damage induced by implantation and its recovery by annealing is important for the

development of reliable p-type doping by ion implantation. Recently, p-type doping of ZnO has been achieved by As^+ implantation with activation rates around 5% [3].

In this work we study the lattice damage and subsequent recovery by thermal annealing of implanted ZnO crystals by means of Raman scattering. We investigate N and P as the best candidates to possible acceptor dopants: N has nearly the same ionic radius as O, and P has produced some of the *p*-type ZnO with lowest resistivity so far [1]. Raman scattering spectra of implanted samples prior and after rapid thermal annealing are compared to assess the lattice recovery. ZnO samples implanted with native species, Zn and O, are also examined in order to study the Raman scattering signatures of intrinsic lattice defects.

EXPERIMENT

The experiments were performed on ZnO single crystals obtained by the hydrothermal growth medthod. Growth details as well as x-ray and photoluminescence characterization of ZnO crystals obtained by this method have been published elsewhere [4]. Multiple implantations at different energies were carried out to achieve a doping profile with a flat homogeneous region and doping densities around 5×10^{19} cm^{-3}. SRIM simulations were used to determine the corresponding implantation energies and doses for the selected ions. Both N^+ and O^+ implantations were carried out at 80, 130 and 185 keV, with respective doses of 3×10^{14}, 5.4×10^{14}, and 7.8×10^{14} cm^{-2}. A similar profile for the heavier P impurity was achieved by P^+ implantation at 100 and 175 keV, and under double ionization, at 300 keV, with doses of 2×10^{14},

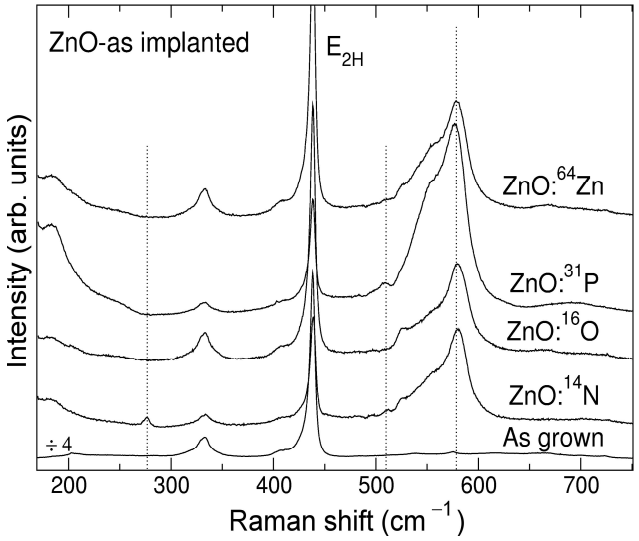

Figure 1. Raman spectra of ZnO samples implanted with N, P, Zn, and O to high doses (~ 5×10^{19} cm^{-3}), compared with the spectrum of an unimplanted ZnO sample. The spectra were excited with the 514.5 nm line of an Ar^+ laser and were recorded in backscattering configuration on a (0001) face. The intensity of the unimplanted sample has been reduced by a factor of four.

3.6×10^{14}, and 1.08×10^{15} cm^{-2}, respectively. In all cases, a nearly homogeneous depth doping profile extending for about 220 nm is obtained. For the heaviest ion implanted, Zn^+, double ionization was not available and a narrower profile with a 50 nm flat region was obtained by implantation at 80 and 185 keV with doses of 9×10^{13} and 4.1×10^{14} cm^{-2}. Rapid thermal annealings were carried out in an ADDAX-RM system with a SiC susceptor at 950 ºC for 10 s. under a continuous O_2 flow.

Raman scattering spectra were recorded in backscattering configuration on a (0001) face using the 514.5 nm line of an Ar^+ laser and the 325 nm line of a He:Cd laser as excitation sources. The scattered light was analyzed using a Jobin-Yvon T64000 spectrometer equipped with a LN_2 cooled CCD detector. The measurements in the visible were performed using a confocal micro-Raman setup, with ×100 objective and lateral and depth resolution of about 1 μm.

DISCUSSION

Figure 1 shows the Raman spectra of the implanted samples compared with the Raman spectrum of the virgin ZnO sample. The spectra are dominated by the strong E_2^{high} mode of ZnO at 438 cm^{-1}. A lower intensity peak is also observed in all spectra at 333 cm^{-1}, corresponding to a second order $E_2^{high} - E_2^{low}$ difference mode. The barely visible peak observed at 574 cm^{-1} in the unimplanted sample is due to the A_1(LO) mode. The intensity of the E_2^{high} mode is reduced roughly by a factor of 4 after N^+, O^+, and P^+ implantation, reflecting the presence of a heavily damaged layer in the first 400 nm of the sample depth. The intensity reduction is much less in the spectrum of the sample implanted with Zn^+ because the implantation profile was much narrower in this case, and the damaged layer extended only to a depth of about 130 nm. In addition to the peaks already mentioned, the spectra of the implanted samples show a prominent band that extends from 520 to 600 cm^{-1}. This band, which reflects the very high density of phonon states in the longitudinal optical branches of ZnO [5], is associated with disorder-activated modes (DALO) that result from the relaxation of the k = 0 selection rule in the damaged crystal [6]. Therefore, the intensity of this band is an indicator of the degree of lattice damage in the implanted layer. Indeed, as can be seen in Fig. 1, the intensity of the DALO band increases with the mass of the implanted ion: it is nearly the same for N and O, but it is twice as much intense for P. It should be noted that this intensity progression is not observed in the spectrum of the Zn^+-implanted sample because, as discussed above, the implantation was substantially narrower in this case. The doping profile cut-off at 1×10^{19} cm^{-3} given by the SRIM simulations for the N^+-implanted sample is 450 nm, whereas for the Zn^+-implanted sample is only 130 nm. Then, to compare the DALO intensity of the Zn^+-implanted sample with those of the rest of the series, the former should be multiplied by a factor of ~3.6. If this correction is applied to the spectra of Fig. 1, we find that the DALO intensity roughly scales linearly with the mass of the implanted ion. The weak broad band observed between 220 and 270 cm^{-1} in the more heavily damaged samples (P^+ and Zn^+ implanted) corresponds to disorder-activated longitudinal acoustic modes, and the bands emerging below 200 cm^{-1} are associated with disorder-activated transverse acoustic modes at zone edge. If we compare the Raman spectra of

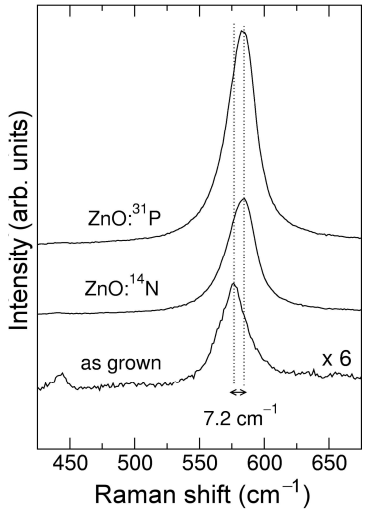

Figure 2. Raman spectra obtained under 325 nm excitation of the ZnO samples implanted with $N^+$and P^+ compared with that of the unimplanted sample.

samples implanted with O^+ and N^+, which according to the DALO intensity have a similar degree of lattice damage, we observe two additional peaks at 277 and 510 cm^{-1} (indicated by vertical dotted lines) in the N^+-implanted sample. These peaks were previously attributed to N local vibrational modes [7] but their origin is still controversial [8,9]. We observe the peaks at 277 and 510 cm^{-1} in the sample implanted with N^+ but not in samples implanted with native species, which appears to indicate that this is a N-related mode as opposed to an intrinsic lattice defect mode. A weak peak is also detected at about 510 cm^{-1} in the more heavily damaged sample implanted with P^+. However, this peak is broader than the one observed at roughly the same frequency in the N^+-implanted sample and, as we shall see below, its annealing behavior is different. This strongly suggests a different origin of the peak at about 510 cm^{-1} in P^+- and N^+-implanted samples.

Raman scattering measurements performed with above band-gap excitation using the 325 nm wavelength were also carried out to specifically probe the damaged layer close to the surface. In Fig. 2 we compare the UV Raman spectra of the samples implanted with N^+ and P^+ with that of an unimplanted ZnO control sample. The 325 nm exitation is close to resonance conditions and a strong enhancement of the polar A_1(LO) mode due to the Fröhlich resonant mechanism occurs. In the unimplanted sample, a weak E_2^{high} is still observed at 438 cm^{-1}, but the spectrum is dominated by the A_1(LO) mode at 574 cm^{-1}. The spectra of the implanted samples exhibit only a very intense A_1(LO) mode shifted to higher frequencies by about 7 cm^{-1}. The A_1(LO) frequency shift indicates the presence of compressive strain in the implanted samples. No significant differences in strain are observed between N^+- and P^+-implantated samples, which suggests that the strain may arise from the presence of heavily damaged regions in the implanted crystal. The compressive strain also increases the band gap energy thus enhancing the resonance conditions for the above band-gap excitation of the experiment. This results in a significant intensity increase of the A_1(LO) modes arising from the compressively strained, less damaged regions of the implanted layers [10], as can be seen in Fig. 2.

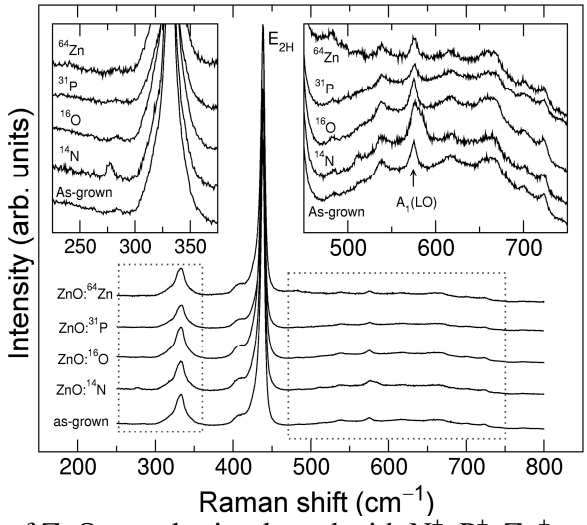

Figure 3. Raman spectra of ZnO samples implanted with N^+, P^+, Zn^+, and O^+ after rapid thermal annealing at 950 ºC under O_2 flux, compared with the spectrum of an unimplanted ZnO sample. The spectra were excited with the 514.5 nm line of an Ar^+ laser and were recorded in backscattering configuration on a (0001) face. The insets are expanded views of the spectral regions within the dashed rectangles.

Figure 3 shows the Raman spectra of the implanted samples after RTA, obtained under 514.5 nm excitation. The spectrum of the unimplanted control sample is also shown at the bottom of the figure. The intensity of the E_2^{high} mode in the annealed samples is recovered to the level observed in the unimplanted sample. In addition, the highly disorder-sensitive DALO band (520 – 600 cm^{-1}) has been completely removed, even for the most heavily damaged layer (Zn^+ implanted). As can be seen in the top-right inset, the rich structure of second-order Raman modes that is observed in the unimplanted sample can also be observed in the implanted samples after RTA in the frequency range where the DALO band occurs. This corroborates the high degree of lattice recovery achieved by RTA at 950 ºC under O_2 flow, even for the heavily damaged Zn^+-implanted ZnO sample. The weak A_1(LO) mode is also detected in all the implanted and subsequently annealed samples. It is interesting to note that the 277 and 510 cm^{-1} peaks that appeared in N^+-implanted samples are still clearly visible after RTA (see top-left inset of Fig. 3), which suggests that these peaks are indeed associated with a N or a N-complex local vibrational modes, in agreement with previous studies [11]. In contrast, the peak about 510 cm^{-1} observed in the P^+-implanted sample has completely vanished after annealing. This suggests that this peak might be related to specific defects induced by the P^+ implantation which are removed by the RTA process. On the other hand, a shoulder on the high-frequency side of the A_1(LO) peak can be seen in the spectrum of the N^+-implanted sample (see top-right inset of Fig. 3). This feature is not observed in any of the other samples, which indicates that it is also probably due to a N-related local vibrational mode as previously suggested [7].

CONCLUSIONS

We have shown that Raman scattering is a powerful tool to assess the implantation-induced lattice damage in ZnO. The intensity of the DALO band that appears in the 520 – 600 cm^{-1} frequency range can be used as a sensitive measure of the degree of lattice damage in implanted samples. Near-resonant Raman experiments revealed an upward frequency shift of the A_1(LO) mode that indicates the presence of compressive strain in the implanted layers. A very high degree of lattice recovery is obtained in the implanted samples by RTA at 950 ºC under O_2 flow, as evidenced by the removal of the Raman scattering signatures of disorder in the spectra of the annealed samples. Characteristic Raman peaks of the N^+ -implanted samples are observed at 277 and 510 cm^{-1} which remain after RTA and are therefore attributed to a N or a N-complex local vibrational modes. A high-frequency shoulder (~582 cm^{-1}) in the A_1(LO) peak of annealed N^+ -implanted samples is also tentatively attributed to a N-related local vibrational mode.

ACKNOWLEDGMENTS

This work has been supported by the Spanish Ministry of Education and Science under contract MAT2004-0664. The work performed by the United States Air Force Research Laboratory at Hanscom Air Force Base was partially supported by the Air Force Office of Scientific Research.

REFERENCES

1. D. C. Look and B. Chaflin, Phys. Stat. Sol. (b) **241**, 624 (2004).
2. E-C Lee, Y-S Kim, Y-G Jin and K. J. Chang, Phys. Rev. B **64**, 085120 (2001).
3. G. Braunstein, A. Muraviev, H. Saxena, N. Dhere, V. Richter, and R. Kalish, Appl. Phys. Lett. **87**, 192103 (2005).
4. M. Suscavage, M. Harris, D. Bliss, P. Yip, S. Q. Wang, D. Schwall, L. Bouthillette, J. Bailey, M. Callahan, D. C. Look, D. C. Reynolds, R. L. Jones, and C. W. Litton, MRS Internet J. Nitride Semicond. Res. **4S1**, G3.40 (1999).
5. J. Serrano, A. H. Romero, F. J. Manjón, R. Lauck, M. Cardona, and A. Rubio, Phys. Rev. B **69**, 094306 (2004).
6. F. Reuss, C. Kirchner, Th. Gruber, R. Kling, S. Maschek, W. Limmer, A. Waag, and P. Ziemann, J. Appl. Phys. **95**, 3385 (2004).
7. A. Kaschner, U. Haboek, M. Strassburg, M. Strassburg, G. Kaczmarczyk, Z. Zeuner, H. R. Alves, D. M. Hoffmann, and B. K. Meyer, Appl. Phys. Lett. **80**, 1909 (2002).
8. C. Bundesmann, N. Ashkenov, M. Schubert, D. Spemann, T. Butz, E. M. Kaidashev, M. Lorentz, and M. Grundmann, Appl. Phys. Lett. **83**, 1974 (2003).
9. J. B. Wang, H. M. Zhong, Z. F. Li, and W. Lu, Appl. Phys. Lett. **88**, 101913 (2006).
10. D. Pastor, J. Ibáñez, R. Cuscó, L. Artús, G. González-Díaz, and E. Calleja, Semicond. Sci. Technol. **22**, 70 (2007).
11. J. Yu, H, Xing, Q. Zhao, H. Mao, Y. Shen, J. Wang, Z. Lai, Z. Zhu, Solid State Commun. **138**, 502 (2006).

APPLIED PHYSICS LETTERS **90**, 181911 (2007)

Isotopic study of the nitrogen-related modes in N^+-implanted ZnO

L. Artús,[a] R. Cuscó, and E. Alarcón-Lladó
Institut Jaume Almera, Consell Superior d'Investigacions Científiques (CSIC), Lluís Solé i Sabarís s.n., 08028 Barcelona, Spain

G. González-Díaz and I. Mártil
Departamento de Física Aplicada III, Facultad de Física, Universidad Complutense, 28040 Madrid, Spain

J. Jiménez
Deptartamento Física de la Materia Condensada, ETSII, Universidad de Valladolid, P. del sn, 47011, Valladolid, Spain

B. Wang
Solid State Scientific Corporation, 27-2 Wright Road, Hollis, New Hampshire 03049

M. Callahan
Air Force Research Laboratory, Sensors Directorate, Electromagnetics Technology Division, Optoelectronic Technology Branch, Hanscom AFB, Massachusetts 01731-2909

(Received 23 March 2007; accepted 3 April 2007; published online 1 May 2007)

Micro-Raman measurements were performed to study the nitrogen-related modes in ZnO samples implanted with N^+. The two stable N isotopes, ^{14}N and ^{15}N, were implanted. Distinct peaks at 277 and 512 cm^{-1} are observed irrespective of the implanted isotope, both before and after rapid thermal annealing. The insensitivity of the mode frequencies to the implanted isotope rules out the explanation of these modes as local vibrational modes involving N motion. These modes were not detected in ZnO samples implanted with Zn^+, O^+, or P^+, which suggests that they may be associated with distortions/defects favored by the presence of N. © *2007 American Institute of Physics*. [DOI: 10.1063/1.2734474]

In recent years there has been a growing interest in ZnO because of its advantageous physical properties—wide band gap and free exciton with 60 meV binding energy—for applications in integrated optoelectronic devices operating in the blue and ultraviolet spectral range.[1] However, as in other wide band gap semiconductors, *p*-type doping of ZnO is proving to be difficult. The demonstration of *p*-type doping in homoepitaxial N-doped ZnO grown by molecular beam epitaxy[2] paved the way to the realization of *p-n* junctions in ZnO based materials. Nevertheless, reproducible *p*-type doping is still a difficult issue and the yields of several approaches and different laboratories vary enormously.[3] Being nitrogen the primary acceptor candidate in ZnO, considerable effort has been devoted to characterize, by means of vibrational spectroscopy, the impurity incorporation and the formation of complexes that may reduce the doping efficiency of N in ZnO.[4–7] Kaschner *et al.*[5] reported the observation of several additional Raman peaks between 275 and 643 cm^{-1} in N-doped GaN epitaxial films grown by chemical vapor deposition. They were attributed to local vibrational modes (LVMs) of N in substitutional O site in the ZnO lattice. As the intensity of those peaks increased linearly with N concentration, it was further suggested that their intensity could be used to determine the N concentration in N-doped ZnO samples.[5] However, Bundesmann *et al.* disputed this interpretation, as they detected similar peaks in ZnO thin films doped with Fe, Sb, and Al, intentionally grown without N incorporation.[6] They attributed the additional Raman peaks to intrinsic host lattice defects. The controversy about the origin of these modes remains, as they have been observed in later works and have been assigned either to LVMs of N (Ref. 8) or to intrinsic host lattice defects.[9] Also, the correlation between N concentration and the intensity of the additional peaks has been confirmed by some works[8,10] and contradicted by others.[9] In a recent study,[10] on the basis of a local phonon density of states calculation, it was suggested that the additional mode observed at 275 cm^{-1} originates from localized vibration of the Zn atoms in a first-neighbor environment where part of the O atoms are replaced by N atoms. No experimental evidence of the participation of N atoms in the LVM observed in N-doped ZnO has been given so far.

In this work, we carry out an isotopic study of N^+-implanted ZnO to investigate the involvement of N vibration in the additional modes observed in N-doped ZnO. In order to check possible effects of the implantation damage inducing intrinsic host lattice defects, ZnO samples implanted with ions of the native species, Zn and O, were also studied. The specificity of the additional modes to N doping was further checked by studying a P^+-implanted sample.

The experiments were performed on ZnO single crystals obtained by the hydrothermal growth method. Growth details as well as x-ray and photoluminescence characterization of ZnO crystals obtained by this method have been published elsewhere.[11] The two stable isotopes of nitrogen, ^{14}N and ^{15}N, were implanted. For comparison purposes, further ZnO samples were implanted with P^+ and with the native species Zn and O. Multiple implantations at different energies were carried out to achieve a doping profile with a flat homogeneous region and doping densities around 5×10^9 cm^{-3}. SRIM simulations[12] were performed to determine the corresponding implantation energies and doses for the selected ions. Both N^+ and O^+ implantations were carried out at 80, 130,

[a]Electronic mail: lartus@ija.csic.es

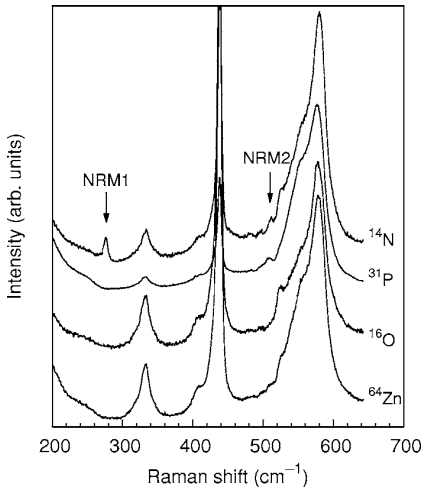

FIG. 1. Raman spectra of ZnO crystals implanted with two potential isoelectronic acceptor ions: N^+ and P^+, as well as with ions of the native species: O^+ and Zn^+.

and 185 keV, with respective doses of 3×10^{14}, 5.4×10^{14}, and 7.8×10^{14} cm^{-2}. A similar profile for the heavier P impurity was achieved by P^+ implantation at 100, 175, and (under double ionization) 300 keV, with doses of 2×10^{14}, 3.6×10^{14}, and 1.08×10^{15} cm^{-2}, respectively. In all cases, a nearly homogeneous depth doping profile extending for about 220 nm is obtained. For Zn^+, double ionization was not available and a narrower profile with a 50 nm flat region was obtained by implanting at 80 and 185 keV with respective doses of 9×10^{13} and 4.1×10^{14} cm^{-2}. Rapid thermal annealings (RTA) were carried out in an ADDAX-RM system with a SiC susceptor at 950 °C for 10 s under continuous O_2 flow.

Raman scattering spectra were recorded in backscattering configuration on a (0001) face using the 514.5 nm line of an Ar^+ laser as excitation source. The scattered light was collected with a confocal microscope with a lateral and depth resolution of about 1 μm and analyzed using a Jobin-Yvon T64000 spectrometer equipped with a LN_2 cooled charge coupled device detector.

Figure 1 shows Raman spectra of the ZnO samples ion implanted with different species. No postimplantation annealing treatment was performed on these samples. The band between 520 and 600 cm^{-1} is due to disorder-activated longitudinal optical (DALO) modes and reflects the lattice disorder in the implanted layer.[8] To facilitate the comparison between the spectra of the implanted layers, the spectra shown in Fig. 1 have been normalized so that all of them display a similar DALO intensity. Besides the DALO band, all spectra show a strong E_2^{high} peak at 438 cm^{-1} and a second-order difference mode at 333 cm^{-1},[13] which primarily arise from the undamaged crystal beyond the implantation profile. Clearly, two additional peaks appear in the spectrum of the N^+-implanted sample at 277 and 512 cm^{-1}. At these frequencies, the layers implanted with ions of the native species do not display any Raman feature and therefore the additional peaks cannot be attributed to intrinsic host lattice defects. As these modes appear to be related to the presence of N in the lattice, we shall refer to them as nitrogen-related modes (NRMs), NRM1 and NRM2, respectively. In the P^+-implanted layer, a weak broad band appears

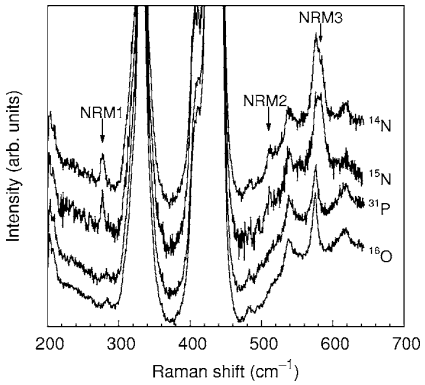

FIG. 2. Raman spectra of ZnO crystals implanted with O^+, P^+, and with ions of the two stable N isotopes: $^{14}N^+$ and $^{15}N^+$ after RTA.

at 508 cm^{-1}, slightly below the NRM2 frequency. Despite their proximity in frequency, these bands have different origins, as they exhibit a different annealing behavior: whereas NRM2 is still detected after RTA, the 508 cm^{-1} mode vanishes in P^+-implanted samples after annealing. The N^+-implanted sample displays a weak feature at 524 cm^{-1}, which is also observed in the spectra of the samples ion implanted with the native species, and hence can be attributed to intrinsic host lattice defects produced by the implantation. The fact that this feature is most prominent in the O^+-implanted sample suggests that it might be related to interstitial O or O antisite defects.[14] This feature is not present in the spectrum of the P^+-implanted sample. Although this is not fully understood, it could be due to the higher degree of damage in the probed region of the P^+-implanted sample, as indicated by the broader DALO band and the higher intensity ratio between the DALO band and the second-order mode at 333 cm^{-1} observed in this sample.

An excellent lattice recovery of the implanted layers is achieved by RTA, as can be seen from the spectra displayed in Fig. 2. The DALO band has been completely removed by the annealing, and the second-order structures revealed by the spectra of the P^+- and O^+-implanted samples are virtually identical to those of the virgin ZnO.[13] In contrast, the samples implanted with N^+ display additional features at 277, 512, and 582 cm^{-1}, labeled as NRM1, NRM2, and NRM3 in Fig. 2. NRM1 and NRM2 correspond to the NRMs already observed in the N^+-implanted samples before annealing. Note that the weak feature displayed by P^+- and O^+-implanted samples at $\approx$284 cm^{-1}, although close to the NRM1 frequency, actually corresponds to a second-order mode previously assigned to $B_1^{high}-B_1^{low}$ in bulk ZnO.[13]

The NRMs show a substantial decrease in intensity after annealing, contrary to what one would expect for substitutional LVMs, and most notably, their frequencies do not change in the sample implanted with $^{15}N^+$. For a substitutional LVM of N, a rough estimate of the expected isotopic shift can be obtained from the empirical diatomic model,[15]

$$\frac{\omega_{LVM}(^{15}N)}{\omega_{LVM}(^{14}N)} \approx \sqrt{\frac{\mu(Zn-{}^{14}N)}{\mu(Zn-{}^{15}N)}}, \quad (1)$$

where μ(Zn–N) is the reduced mass of the Zn–N pair. Using Eq. (1) we obtain for the lowest frequency NRM an expected isotopic shift $\Delta\omega_{NRM1}\approx 8$ cm^{-1}, which is not observed in the spectra of Fig. 2. Even higher shifts should be expected for

NRM2 and NRM3. However, all the NRMs observed in the sample implanted with $^{14}N^+$ lie at the same frequencies as those detected in the sample implanted with $^{15}N^+$. Our isotopic doping experiments indicate that whereas the NRM1, NRM2, and NRM3 modes are clearly related to the presence of N in the ZnO lattice, they cannot be attributed to LVMs of substitutional N in the O site. The insensitivity of the NRM1 frequency to the isotopic mass would be consistent with the attribution of this mode to a vibration of Zn atoms in a local environment, where part of their first-neighbor O atoms are replaced by N atoms in the ZnO lattice.[10] However, one would expect the number of substitutional N atoms to increase after RTA, and hence the intensity of such a mode should be greater in annealed samples, in contrast with the experimental observation. Therefore, our results suggest that these modes are probably due to localized vibrations associated with local distortions of the lattice caused by nonsubstitutional N or to a complex defect favored by the presence of N. It is worth noting that, in contrast with Ref. 6, we observe these additional modes *only* in the spectra of the ZnO samples implanted with N^+ and they are not present in samples implanted with P^+ or with the native species. Therefore, we conclude that, contrary to the suggestion made in Ref. 6, these modes cannot be attributed to intrinsic host lattice defects.

In summary, we have investigated ZnO samples ion implanted with several atomic species as well as with two nitrogen isotopes, ^{14}N and ^{15}N. The Raman spectra of the N^+-implanted samples exhibit additional modes at 277, 512, and 582 cm^{-1} which are not present in the spectra of the samples implanted with other species. The NRMs occur at the same frequencies in samples implanted with $^{14}N^+$ and with $^{15}N^+$. This is an experimental evidence that N motion is not involved in the NRMs of ZnO:N. These modes are not observed in ZnO samples ion implanted with the native species, which indicates that they are not due to intrinsic host lattice defects either. Alternatively, our results suggest that the presence of N in the ZnO lattice induces a local lattice distortion or the formation of a complex defect that does not occur for other potential acceptors such as P.

This work has been supported by the Spanish Ministry of Education and Science under Contract No. MAT2004-0664. The work performed by the United States Air Force Research Laboratory at Hanscom Air Force Base was partially supported by the Air Force Office of Scientific Research.

[1]D. C. Look, Mater. Sci. Eng., B **80**, 383 (2001).
[2]D. C. Look, D. C. Reynolds, C. W. Litton, R. L. Jones, D. B. Eason, and G. Cantwell, Appl. Phys. Lett. **81**, 1830 (2002).
[3]D. C. Look and B. Claflin, Phys. Status Solidi B **241**, 624 (2004).
[4]N. H. Nickel, F. Friedrich, J. F. Rommeluère, and P. Galtier, Appl. Phys. Lett. **87**, 211905 (2005).
[5]A. Kaschner, U. Haboeck, M. Strassburg, M. Strassburg, G. Kaczmarczyk, A. Hoffmann, C. Thomsen, A. Zeuner, H. R. Alves, D. M. Hofmann, and B. K. Meyer, Appl. Phys. Lett. **80**, 1909 (2002).
[6]C. Bundesmann, N. Ashkenov, M. Shubert, D. Spemann, T. Butz, E. M. Kaidashev, M. Lorenz, and M. Grundmann, Appl. Phys. Lett. **83**, 1974 (2003).
[7]U. Haboeck, A. Hoffmann, C. Thomsen, A. Zeuner, and B. K. Meyer, Phys. Status Solidi B **242**, R21 (2005).
[8]F. Reuss, C. Kirchner, T. Gruber, R. Kling, S. Maschek, W. Limmer, A. Waag, and P. Ziemann, J. Appl. Phys. **95**, 3385 (2004).
[9]N. Hasuike, H. Fukumura, H. Harima, K. Kisoda, H. Matsui, H. Saeki, and H. Tabata, J. Phys.: Condens. Matter **16**, S5807 (2004).
[10]J. B. Wang, H. M. Zhong, Z. F. Li, and W. Lu, Appl. Phys. Lett. **88**, 101913 (2006).
[11]M. Suscavage, M. Harris, D. Bliss, P. Yip, S. Q. Wang, D. Schwall, L. Bouthillette, J. Bailey, M. Callahan, D. C. Look, D. C. Reynolds, R. L. Jones, and C. W. Litton, MRS Internet J. Nitride Semicond. Res. **4S1**, G3.40 (1999).
[12]J. P. Biersak and J. F. Siegler, SRIM code, www.srim. org, 2006.
[13]R. Cuscó, E. Alarcón-Lladó, L. Artús, J. Ibáñez, J. Jiménez, B. Wang, and M. J. Callahan, Phys. Rev. B **75**, 165202 (2007).
[14]Q. X. Zhao, P. Klason, M. Willander, H. M. Zhong, W. Lu, and J. H. Yang, Appl. Phys. Lett. **87**, 211912 (2005).
[15]M. D. McCluskey, J. Appl. Phys. **87**, 3593 (2000).

References

[1] T. Damen, S. Porto, and B. Tell *Phys. Rev.*, vol. 142, p. 570, 1966.

[2] C. Arguello, D. Rousseau, and S. Porto *Phys. Rev.*, vol. 181, p. 1351, 1969.

[3] J. Calleja and M. Cardona *Phys. Rev. B*, vol. 16, p. 3753, 1977.

[4] J. Serrano, F. Manjon, A. Romero, A. Ivanov, R. Lauck, M. Cardona, and M. Krisch *Phys. Status Solidi B*, vol. 244, p. 1478, 2007.

[5] J. Serrano, A. Romero, F. Manjon, R. Lauck, M. Cardona, and A. Rubio *Phys. Rev. B*, vol. 69, p. 094306, 2004.

[6] C. Aku-Leh, J. Zhao, R. Merlin, J. Menendez, and M. Cardona *Phys. Rev. B*, vol. 71, p. 205211, 2005.

[7] M. Kuball, J. Hayes, Y. Shi, and J. Edgar *Appl. Phys. Lett.*, vol. 77, p. 1958, 2000.

[8] L. Bergman, D. Alexon, P. Murphy, R. Nemanich, M. Dutta, M. Stroscio, C. Balkas, H. Shin, and R. Davis *Phys. Rev. B*, vol. 59, p. 12977, 1999.

[9] A. Link, K. Bitzer, W. Limmer, R. Sauer, C. Kirchner, V. Schwegler, M. Kamp, D. Ebling, and K. Benz *J. Appl. Phys.*, vol. 86, p. 6256, 1999.

[10] R. Loudon *Advanced Phys.*, vol. 13, p. 423, 1964.

[11] T. Livneh, J. Zhang, G. Cheng, and M. Moskovits *Phys. Rev. B*, vol. 74, p. 035320, 2006.

[12] S. Piscanec, M. Cantoro, A. Ferrari, J. Zapien, Y. Lifshitz, S. Lee, S. Hoffmann, and J. Robertson *Phys. Rev. B*, vol. 68, p. 241312, 2003.

[13] T. Beechem, S. Graham, S. Kearney, L. Phinney, and J. Serrano *Rev. Sci. Instrum.*, vol. 78, p. 061301, 2007.

[14] J. Ye, K. Teoh, X. sun, G. Lo, D. Kwong, H. Zhao, S. Gu, R. Zhang, Y. Zheng, S. Oh, X. Zhang, and S. Tripathy *Appl. Phys. Lett.*, vol. 91, p. 091901, 2007.

[15] L. Bergman, M. Dutta, C. Balkas, R. Davis, J. Christman, D. Alexson, and R. Nemanich *J. Appl. Phys.*, vol. 85, p. 3535, 1998.

[16] L. Filippidis, H. Siegle, A. Hoffmann, C. Thomsen, K. Karch, and F. Bechstedt *Phys. Status Solidi B*, vol. 198, p. 621, 1996.

[17] J. Ziegler, *Handbook of Ion Implantation Technology*. New York, USA: Wiley, 1992.

[18] D. Myers, P. Gourley, and P. Peercy *J. Appl. Phys.*, vol. 54, p. 5032, 1983.

[19] G. Burns, F. Dacol, C. Wie, E. Burstein, and M. Cardona *Solid State Commun.*, vol. 62, p. 449, 1987.

[20] H. Harima *J. Phys. Condens. Matter*, vol. 14, p. R967, 2002.

[21] D. Pastor, R. Cusco, L. Artus, G. Gonzalez-Diaz, S. Fernandez, and E. Calleja *Semicond. Sci. Technol.*, vol. 20, p. 374, 2005.

[22] W. Limmer, W. Rittler, R. Sauer, B. Mensching, C. Liu, and B. Rauschenbach *Appl. Phys. Lett.*, vol. 72, p. 2589, 1998.

[23] N. Wieser, O. Ambacher, R. Dimitrov, M. Stutzmann, B. Stritzker, and J. Lindner *Phys. Status Solidi B*, vol. 216, p. 807, 1999.

[24] F. Reuss, C. Kirchner, T. Gruber, R. Kling, S. Maschek, W. Limmer, A. Waag, and P. Ziemann *J. Appl. Phys.*, vol. 95, p. 3385, 2004.

[25] U. Ozgur, Y. Alivov, C. Liu, A. Teke, M. Reshchikov, S. Dogan, V. Avrutin, S. Cho, and H. Morkoc *J. Appl. Phys.*, vol. 98, p. 041301, 2005.

[26] Y. Yan, S. Zhang, and S. Pantelides *Phys. Rev. Lett.*, vol. 86, p. 5723, 2001.

[27] P. Fons, H. Tampo, A. Kolobov, M. Ohkubo, S. Niki, J. Tominaga, R. Carboni, F. Boscherini, and S. Friedrich *Phys. Rev. Lett.*, vol. 96, p. 045504, 2006.

[28] A. Kaschner, U. Haboeck, M. Strassburg, M. Strassburg, G. Kaczmarczyk, A. Hoffmann, C. Thomsen, A. Zeuner, H. Alves, D. Hofmann, and B. Meyer *Appl. Phys. Lett.*, vol. 80, p. 1909, 2002.

[29] J. Ma, Y. Liu, R. Mu, J. Zhang, Y. Lu, D. Shen, and X. Fan *J. Vac. Sci. Technol. B*, vol. 22, p. 94, 2004.

[30] F. Manjon, B. Mari, J. Serrano, and A. Romero *J. Appl. Phys.*, vol. 97, p. 053516, 2005.

[31] J. Wang, H. Zhong, Z. Li, and W. Lu *Appl. Phys. Lett.*, vol. 88, p. 101913, 2006.

[32] C. Bundesmann, N. Ashenkov, M. Schubert, D. Spemann, T. Butz, E. Kaidashev, M. Lorenz, and M. Grundmann *Appl. Phys. Lett.*, vol. 83, p. 1974, 2003.

[33] J. Yu, H. Xing, Q. Zhao, H. Mao, Y. Shen, J. Wang, Z. Lai, and Z. Zhu *Solid State Commun.*, vol. 138, p. 502, 2006.

[34] C. Bundesmann, N. Ashkenov, M. Schubert, D. Spemann, T. Butz, E. Kaidashev, M. Lorenz, and M. Grundmann *Appl. Phys. Lett.*, vol. 83, p. 1974, 2003.

[35] B. Ridley *J. Phys.: Cond. Matter*, vol. 8, p. L511, 1996.

[36] J. Kielkopf *J. Opt. Soc. Am.*, vol. 63, p. 987, 1973.

[37] J. Serrano, F. Manjon, A. romero, F. Widulle, R. Lauck, and M. Cardona *Phys. Rev. Lett.*, vol. 90, p. 055510, 2003.

[38] M. Wihl, M. Cardona, and J. Tanc *J. Non-Crystalline Solids*, vol. 8-10, p. 172, 1972.

[39] B. Meyer, H. Alves, D. Hofmann, W. Kriegseis, D. Forster, F. Bertram, J. Christen, A. Hoffmann, M. Strassburg, M. Dworzak, U. Haboeck, and A. Rodina *Phys. Status Solidi B*, vol. 241, p. 231, 2004.

[40] V. Coleman, H. Tan, C. Jagadish, J. Zou, G. Li, and A. Titov *Phys. Rev. B*, vol. 64, p. 035202, 2001.

[41] A. Georgobani, A. Gruzintsev, V. Volkov, M. Vorobiev, V. Demin, and V. Dravin *Nucl. Instrum. Meth. A*, vol. 514, p. 117, 2003.

[42] M. Schilling, R. Helbig, and G. Pensl *J. Lumin.*, vol. 33, p. 201, 1985.

[43] E. Alves, E. Rita, U. Wahl, J. Correia, T. Monteiro, J. Soares, and C. Boemare *Nucl. Instrum. Meth. B*, vol. 206, p. 1047, 2003.

[44] N. Garces, L. Wang, L. Bai, N. Giles, L. Halliburton, and G. Cantwell *Appl. Phys. Lett.*, vol. 81, p. 622, 2002.

[45] S. Jeong, B. Kim, and B. Lee *Appl. Phys. Lett.*, vol. 82, p. 2625, 2003.

[46] O. Schirmer and D. Zwingel *Solid State Commun.*, vol. 8, p. 1559, 1970.

'Sometimes the questions are complicated and the answers are simple."

Michael Faraday

5

Raman scattering in GaN-related materials

5.1 Introduction

The growth and properties of ternary semiconductors of the nitride family have been under intense investigation since nitrides emerged as blue-light emitting devices in the 1990s [1]. The particular interest in the ternary and quaternary nitrides results from the fact that they allow adjusting the semiconductor band gap to values not available in the pure compounds. At present, group III-nitrides are the most used materials in optoelectronics and in high-speed devices [1].

Phonons of some GaN-related materials have been widely studied by Raman and far-infrared spectroscopies to investigate their crystal quality, orientation of the as-grown material, free carrier effects, piezoelectric response, etc (see reference [2] and references therein). Room temperature non-resonant $z(xx)\bar{z}$ Raman spectrum of wurtzite GaN is typically dominated by intense E_2^{low} and E_2^{high} modes at 144 and 568 cm^{-1}, respectively, and a less intense $A_1(\text{LO})$ polar mode at 531 cm^{-1}. By performing experiments in several geometry configurations, the remaining Raman active modes are typically found at frequencies $\omega_{A_1(\text{TO})} = 531$ cm^{-1}, $\omega_{E_1(\text{TO})} = 560$ cm^{-1}, and $\omega_{E_1(\text{LO})} = 741$ cm^{-1} [2, 3].

As we have mentioned before, III-V-nitride alloy systems are very attractive for optoelectronics in terms of band gap engineering (see figure 5.1). Although the band gap behavior of the alloy can result from a linear interpolation between those of the

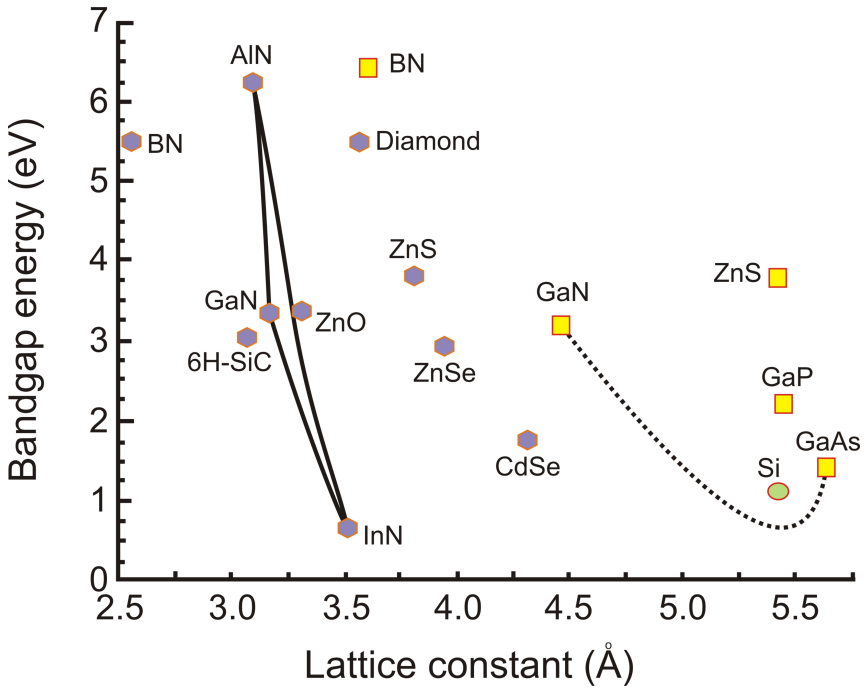

Figure 5.1: Band-gap engineering diagram for III-V-nitride semiconductors.

binary materials (which is the case of the AlGaN alloy), band gap bowing is often important as we will discuss for the GaNAs system.

From the vibrational point of view, phonons of alloys show a specific trend for each system. In alloys, phonon frequencies usually shift with the atomic composition, since the reduced mass of the vibrating atoms changes. There are typically two types of characteristic behavior of frequency dependence with composition [4]. One is the so-called one-mode behavior, in which the zone-center phonon frequencies of the alloy ($A_xB_{1-x}C$) vary continuously from the frequencies of one end-binary BC, to those of the other AC. The other behavior is the two-mode type, in which for an intermediate alloy composition two sets of phonon modes appear with frequencies close to those of the binaries, and their strength is approximately proportional to the mole fraction of each component. This means that two-mode behavior alloys exhibit two sets of LO and TO phonons whose frequencies vary continuously from those of one end-member binary (AC,BC) to the impurity mode in the other end-member binary (BC:A and AC:B, respectively).

Regarding to wurtzite $Al_xGa_{1-x}N$ alloys, the composition dependence of the frequencies for their Raman active modes were traced in detail by Davydov *et al.* [5],

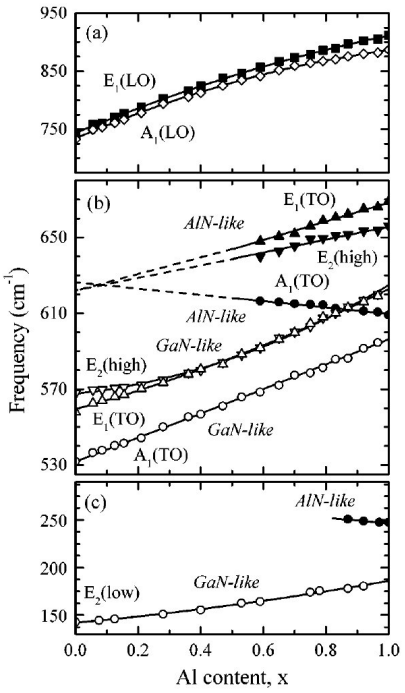

Figure 5.2: Al content dependence of phonon frequencies in $Al_xGa_{1-x}N$ published in reference [5]

probing a large set of thick layers grown on Si(111). They found that while both A_1(LO) and E_1(LO) modes showed a one-mode type behavior, the others, A_1(TO), E_1(TO), E_2^{low} and E_2^{high}, exhibit a two-mode behavior (see figure 5.2).

Wide band gap $Al_xGa_{1-x}N$ thin films are widely used for the fabrication of optoelectronic devices operating in the blue and violet spectral regions. To investigate structures containing very thin films of $Al_xGa_{1-x}N$, visible Raman scattering may not be appropriate due to the low Raman efficiency exhibited by this ternary alloy, in particular for large Al contents. In addition, given that wide band gap compounds are transparent to visible radiation, the Raman spectra may be obscured by intense peaks arising from the substrate.

The Raman signal from the nitride films may be enhanced by using UV, near-resonant laser excitations. However, owing to absorption effects, UV Raman experiments only allow one to probe the shallowest layers of the samples (about the first 100 nm or less). Therefore, IR transmission measurements at oblique incidence may emerge as a complementary tool to Raman scattering for the characterization of structures based on $Al_xGa_{1-x}N$.

IR transmission experiments on wurtzite GaN are scarce [6] since the more widely used substrate is sapphire, which strongly absorbs IR radiation in the 380-900 cm^{-1}

spectral region, and hence transmission dips from the GaN layer are not observed. By contrast, cubic nitrides, which have different electronic, doping and thermal properties than wurtizte GaN [7–9], are usually grown on GaAs substrates. Experiments on cubic GaN are scarce because of the difficulty of sample growth. To obtain higher quality epitaxial layers, an AlN buffer interlayer may be grown between the *c*-GaN and the substrate [10]. Moreover, this buffer layer can help to reduce As diffusion from the GaAs substrate to the GaN layer. Since *c*-GaN layers are usually very thin, their Raman frequencies are affected by strain. The typical TO and LO frequencies for *c*-GaN have been found to be at 555 and 742 cm^{-1}, respectively [2]. Since the restrahlen band of the GaAs lies far from the optical modes of III-nitride materials, IR transmission measurements may give additional information to the study of cubic GaN-based systems on GaAs substrates.

Returning to nitride alloy systems, $B_xGa_{1-x}N$ alloys are novel potential candidates for the production of large energy optical devices. The newness and growth difficulty of $B_xGa_{1-x}N$ alloys result in the lack of information about its physical properties, such as its lattice dynamics. Raman spectra of either cubic [11, 12] or hexagonal [12, 13] BN are scarce, but the frequencies of any of its optical modes are well above 1000 cm^{-1} due to the small size and weight of boron and nitrogen atoms. Therefore, the incorporation of boron into the *w*-GaN lattice is expected to increase the frequencies of its optical modes, even though the hexagonal structure shown by BN at ambient growth conditions does not correspond to the wurtzite.

The actual main problem to grow $B_xGa_{1-x}N$ alloys is that the lattice mismatch between GaN and BN binaries results in a considerable internal strain and in the phase separation that occurs for relatively low boron contents ($\leq 4\%$) [14, 15]. Strain and composition inhomogeneities can be detected by Raman scattering experiments, as observed in InGaN layers with mid-In concentrations [16]. In that study, In inhomogeneities where detected by selective resonance Raman shifts in the polar modes. Under near-resonance conditions, an intensity enhancement of the polar modes occur due to Fröhlich interaction, as well as a very strong scattering by 2LO phonons and higher-order multiphonon scattering. The Fröhlich-induced enhancement highly depends on the difference between the energy of the excitation and the band gap of the material. Closer values of these energies yields much enhanced intensities of the polar modes. Then, spatial inhomogeneities in the band gap energy of the probed region, which arise from inhomogeneities in the alloy composition, give rise to selective resonances. This means that for an specific excitation energy E_L, the

signal detected is mainly from the regions with the band gap closer to E_L. In this sense, near-resonant Raman scattering can give valuable information about boron content inhomogeneities through the probed region.

Finally, the incorporation of As in GaN has been increasingly studied during the last years for three main reasons:

a) The surfactant effects and the promoting of cubic GaN by As. A residual As pressure in the MBE chamber was observed to completely modify the surface reconstructions for cubic GaN [17, 18]. This fact suggested that As-mediated GaN growth would yield larger critical thicknesses for nitride heterostructures.

b) A large band gap reduction for $GaN_{1-x}As_x$ alloys. To bridge together the band gaps of GaN and GaAs is highly interesting for the optoelectronics and its integration to the GaAs technology. However, the incorporation of arsenic has been shown to be low in efficiency and poses a strong perturbation to the GaN lattice. For As contents above 1%, the coexistence of hexagonal N-rich GaAsN and cubic As-rich GaNAs phases is usually observed [19].

c) A strong blue emission at room temperature from As-doped GaN. At the low concentration end of the alloy (isoelectronic impurity regime), GaN:As shows intense blue luminescence centered around 2.6 eV, as observed already in As-implanted GaN and subsequently in MBE As-doped GaN [20,21]. The chemical nature of the 2.6 eV blue luminescence was found to result from optical centers involving As atoms [22].

In MBE grown samples, it is well known that the Ga-to-N flux ratio, or III/V ratio, affects the morphology, crystalline quality, optical and electrical properties of GaN [23]. Also, the transition from As-doped GaN to the $GaN_{1-x}As_x$ alloy has been suggested to be affected by the III/V ratio and temperature growth [24]. Information about the lattice position of As in GaN can be obtained from LVMs and alloying effects on the optical modes in the Raman spectra. So, Raman scattering can provide valuable information about doping-alloying regimes, crystal quality, internal strain, etc., which may contribute to the improvement of the growth of either As-doped GaN or $GaN_{1-x}As_x$ layers.

The local vibrations of As in *w*- and *c*-GaN were theoretically modelled by Kaczmarczyk *et al.* [25], who also compared their values with those reported in previous experimental works [26, 27]. They concluded that As-isolated impurity LVMs in GaN

have frequencies between the 95-200 cm^{-1} frequency region, and As-related clusters give rise to Raman features around 235 cm^{-1}. By contrast, the incorporation of As into the GaN lattice, and subsequent formation of the GaNAs alloy, may shift downwards the optical phonon frequencies of the GaN-like modes. The different behavior of the Raman spectrum for the two regimes (As-doped GaN and GaNAs alloy) evidences the value of Raman scattering to give further information about the doping-alloying regimes in GaNAs.

In this chapter, we will apply IR transmission spectroscopy to study the vibrational properties of cubic and wurtzite GaN and AlN thin films, as well as the wurtzite AlGaN alloy system. We will compare the results with the Raman data of the samples under study and of those reported in the literature for thicker films. We will also present the first UV Raman scattering study of the boron content dependence of the BGaN alloy phonons. Also, the effect of the III/V ratio on the vibrational properties of undoped and As-doped *w*-GaN films will be studied by means of Raman scattering.

5.1.1 Aim

The aim of this section is:

- To comparatively assess the usefulness and the information given by the IR and Raman techniques to probe *w*-AlGaN thin films with mid-Al contents grown by MBE on Si substrates.
- To comparatively assess the usefulness and the information given by the IR and Raman techniques to probe the vibrational properties of *c*-GaN grown by MBE on GaAs substrates. The effects of an AlN buffer layer between the *c*-GaN and the GaAs substrate will be also studied.
- To study the $B_xGa_{1-x}N$ alloy in the dilute regime by means of near resonance UV-Raman scattering. This aim includes the assessment of the crystal quality degree, composition homogeneity and phase separation for the novel material.
- To study the effects of the III/V ratio to the As incorporation and crystal quality for MBE-grown *w*-GaN. For this purpose, we will also analyze undoped *w*-GaN epilayers with similar III/V ratio conditions, as reference.

5.2 Groundwork

In order to accomplish the aim of this chapter, some previous considerations should be taken. Since we will apply far-IR transmission spectroscopy to study group III-nitrides, it is interesting to first introduce the physical process that takes place in isotropic (zinc-blende) and uniaxial (wurtzite) thin films when infrared light propagates through them. We will also discuss how TO and LO modes can be observed in thin films by oblique measurements.

5.2.1 Far-Infrared Transmission spectroscopy

As discussed earlier in this thesis, two types of normal modes of vibration exist in a polar crystal independently of their symmetry: transverse and longitudinal modes. TO and LO mode frequencies can be deduced from infrared reflectivity spectra by curve-fitting procedures, which require intense computing routines. For very thin polar films ($c/\omega \gg d$, being d the thickness of the film, c the speed of light and ω the frequency of the incident IR light), the infrared transmission spectrum recorded in normal incidence can reveal only the TO modes [28]. By contrast, both TO and LO modes are manifested as transmission minima for oblique incidence probing thin films [29], as we will discuss later on.

Isotropic crystals

Consider a free-standing isotropic polar film of thickness d and dielectric function $\varepsilon(\omega) = n^2(\omega)$, and an incident electromagnetic wave of frequency ω on the film at an angle θ_i, with the electric field ($\vec{\xi}$) polarized either perpendicular (s or TE wave) or parallel (p or TM wave) to the plane of incidence. In any case, $|\vec{k}|^2 = (\omega/c)^2$ and $|\vec{\kappa}|^2 = (\omega/c)^2\varepsilon(\omega)$ are the squared wavevectors of the wave propagating through the air and the film, respectively.

From Maxwell's equations and the film boundary conditions, the fraction of an incident TE or TM polarized wave transmitted through this film can be derived, and

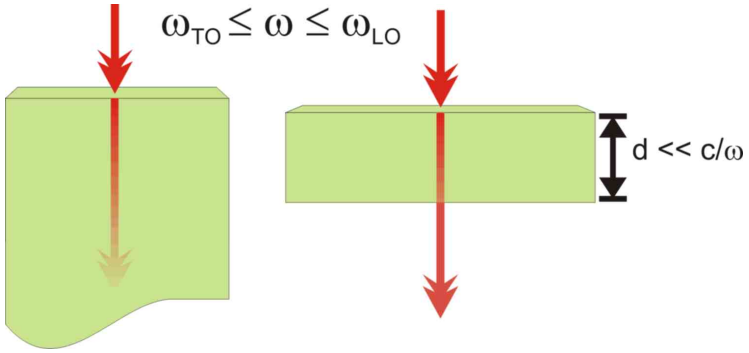

Figure 5.3: Far-IR transmission in bulk and thin films, for radiation energies in the material's restrahlen region (energies between $\hbar\omega_{TO}$ and $\hbar\omega_{LO}$). Within this energy region the material is highly absorbant and hence, radiation can only emerge from very thin films.

are

$$T_{\mathrm{TE}} = \left| \left\{ \cos\kappa_i d - i \left(\frac{\kappa_i^2 + k_i^2}{2\kappa_i k_i} \right) \sin\kappa_i d \right\}^{-1} \right|^2 \tag{5.1}$$

$$T_{\mathrm{TM}} = \left| \left\{ \cos\kappa_i d - i \left(\frac{\kappa_i^2 + n^4 k_i^2}{2n^2\kappa_i k_i} \right) \sin\kappa_i d \right\}^{-1} \right|^2 \tag{5.2}$$

where k_i and κ_i are respectively the components of $\vec{k}$ and $\vec{\kappa}$ perpendicular to the film surface. These are $k_i = (\frac{\omega}{c})\cos\theta_i$ and $\kappa_i = (\frac{\omega}{c})\sqrt{n^2 - \sin^2\theta_i}$ using Snell's law. The expressions of equations 5.1 and 5.2 are general and apply to films of any thickness. For unpolarized waves, the total fractional transmission T_U is simply $T_U = \frac{1}{2}(T_{\mathrm{TE}} + T_{\mathrm{TM}})$.

The frequency dependent dielectric function of a polar semiconductor described in the *Theoretical framework* chapter has a pole and a zero at the frequencies of the TO and LO modes, respectively. Between these two frequencies (called restrahlen region) the dielectric function is negative, giving rise to a complex wavevector κ for the electromagnetic wave, which hence becomes cushioned or evanescent. Therefore, an electromagnetic wave with frequency between that of the TO and LO modes can only be transmitted by films of thickness shorter than κ^{-1}, usually expressed by $d \ll c/\omega$, as depicted in figure 5.3. Films with thicknesses that fulfill this condition, are said to be *thin* within the far-IR spectroscopy framework.

For polar *thin* films, one can visualize two normal modes of polarized lattice vibrations. In one mode the vibrations are parallel to the film surface and the frequency is the corresponding to the TO mode. In the other, vibrations are normal to the

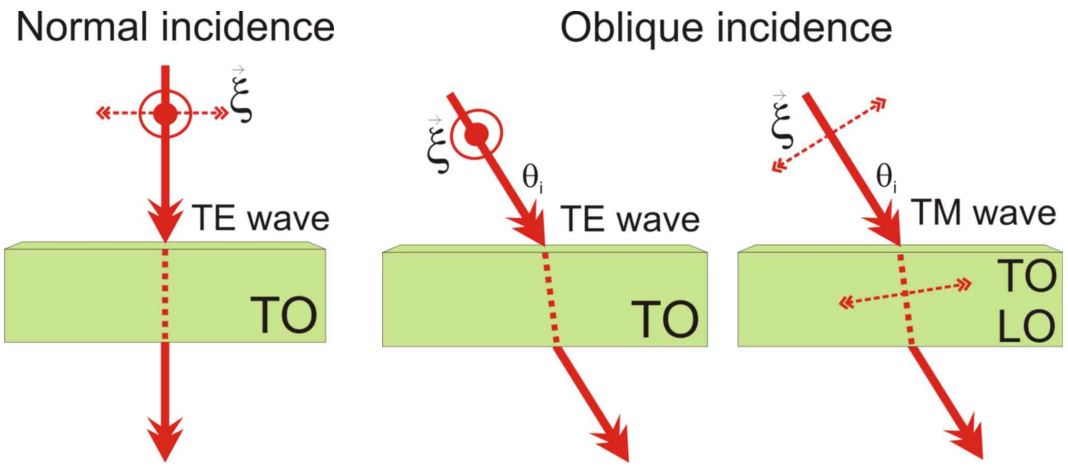

(a) Normal incidence radiation: only TO modes are observed, regardless of the incident polarization.

(b) Oblique incidence radiation: the LO mode is only observed for TM waves.

Figure 5.4: Different IR transmission configurations for a polar thin film, and the corresponding polar modes observed.

film surface and the frequency is ω_{LO} since vibrations polarized perpendicular to the film surface produce a surface polarization so that $\varepsilon = 0$. Consequently, LO modes cannot be excited by TE waves since the electric field is polarized perpendicular to the plane of incidence independently of the angle of incidence.

By contrast, the electric field of a TM wave at an oblique incidence has a component in the direction of the particle motion for both TO and LO modes(see figure 5.4). Hence, both TO and LO modes can be excited. This effect is called the Berreman effect, named after who first predicted and verified it [29].

To illustrate the transmission model outlined above, we consider a binary isotropic polar compound such as *c*-AlN or *c*-GaN, whose frequency dependent refractive index is determined by their TO and LO frequencies using equations 2.20 and 2.21,

$$n^2(\omega) = \varepsilon(\omega) = \varepsilon_\infty + \varepsilon_\infty \frac{\omega_{LO}^2 - \omega_{TO}^2}{\omega_{TO}^2 - \omega^2 - i\omega\Gamma_{ion}} \tag{5.3}$$

The Berreman effect is clearly displayed in figure 5.5a. Computed transmission far-IR transmission spectra of a TM wave are plotted for several angles of incidence to a thin *c*-AlN film. For normal incidence, only a dip at the TO mode frequency is observed. With increasing the angle of incidence of the electromagnetic radiation, a dip at the LO frequency is enhanced.

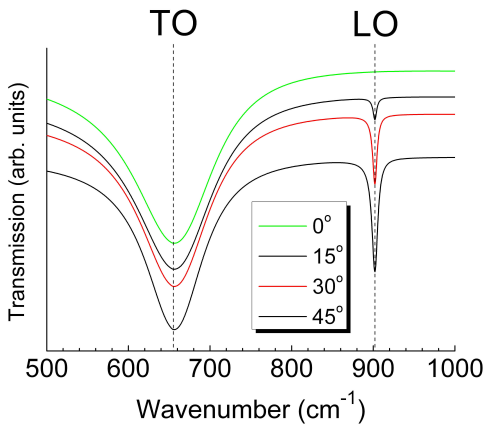

(a) Calculated far-IR transmission spectra of a c-AlN 0.2μm-thick film, assuming a TM wave with different angles of incidence, from 0° to 45°.

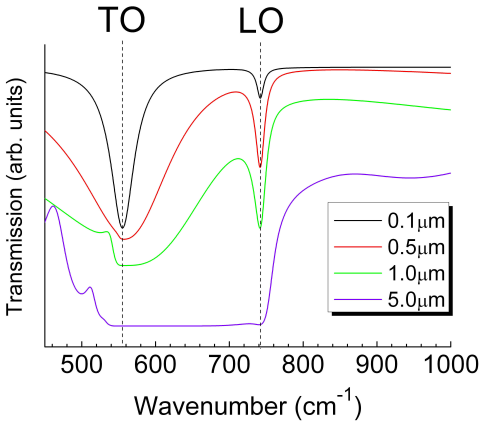

(b) Calculated far-IR transmission spectra for an oblique incident ($\theta = 45°$) TM wave on c-GaN thin films of different thicknesses.

Figure 5.5: Examples of calculated far-IR transmission spectra to illustrate the Berreman and thickness effects for isotropic films.

To evidence the film thickness effects, figure 5.5b shows four calculated spectra of a TM wave at oblique incidence ($\theta_i = 45°$) for c-GaN films of different thicknesses. Transmission minima appear at both the TO and LO frequencies. With increasing the film thickness, interference fringes appear below the TO frequency, which stem from the rapid increase in the dielectric function as the frequency approaches its pole at ω_{TO}. For the thicker film ($d = 5$ μm), the TO and LO frequencies are difficult to be identified since the restrahlen band is already observed.

Anysotropic crystals

In an uniaxial medium, the dielectric function has to be represented by a tensor (equation 4.8), and hence the frequency dependent refractive index is written by

$$n(\omega) = \begin{pmatrix} n_{\parallel}(\omega) & 0 & 0 \\ 0 & n_{\parallel}(\omega) & 0 \\ 0 & 0 & n_{\perp}(\omega) \end{pmatrix} \qquad (5.4)$$

where $n_{\parallel}$ and $n_{\perp}$ are the ordinary and extraordinary refractive indexes, respectively. Following the notation in section 4.2.1, the components of the refractive index tensor

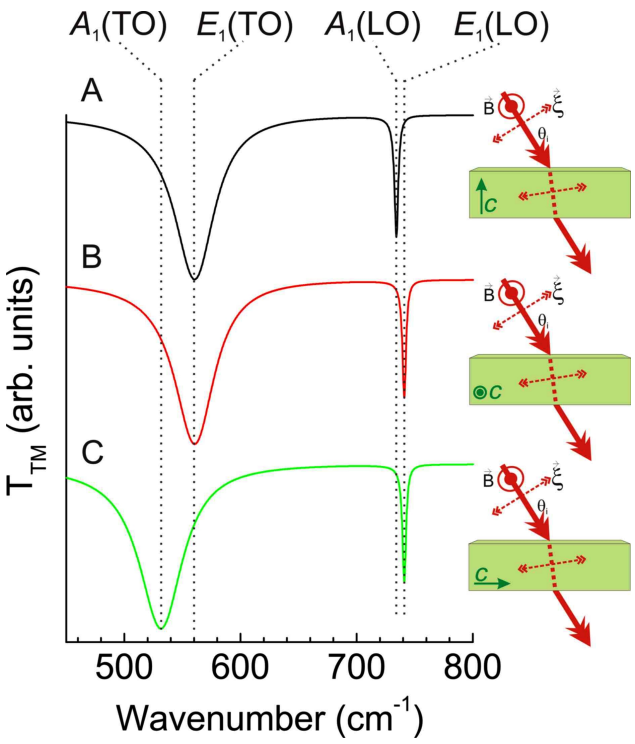

Figure 5.6: Calculated far-IR transmission spectra at oblique incidence for TM waves incident on a *w*-GaN thin film with the *c*-axis oriented perpendicular to the film surface (curve A), parallel to both the film surface and the magnetic field $\vec{B}$ (curve B), and parallel to the film surface and perpendicular to $\vec{B}$ (curve C). The spectra are vertically displaced for clarity. The insets show the different geometries considered.

are given by

$$n_{\parallel}^2 = \varepsilon_{\infty\parallel} + \varepsilon_{\infty\parallel}\frac{\omega_{LO\parallel}^2 - \omega_{TO\parallel}^2}{\omega_{TO\parallel}^2 - \omega^2 - i\omega\Gamma_{ion\parallel}} \tag{5.5}$$

$$n_{\perp}^2 = \varepsilon_{\infty\perp} + \varepsilon_{\infty\perp}\frac{\omega_{LO\perp}^2 - \omega_{TO\perp}^2}{\omega_{TO\perp}^2 - \omega^2 - i\omega\Gamma_{ion\perp}} \tag{5.6}$$

In the wurtzite structure, the optic axis is the crystallographic *c*-axis. Then, $\omega_{TO\parallel}$ and $\omega_{LO\parallel}$ correspond to the frequencies of the E_1 modes, whereas $\omega_{TO\perp}$ and $\omega_{LO\perp}$ correspond to that of the A_1 modes.

It is worth noting that for a TM wave impinging on a wurtzite thin film at an angle θ_i, the wavevector κ depends on the film crystallographic orientation. In this regard, three main cases must be considered:

Case 1: When the *c* axis is perpendicular to the plane of the film (upper inset in figure 5.6), the wavevector component κ_i is given by

$$\kappa_i = \frac{\omega}{c}\left[n_{\parallel}^2 - \frac{n_{\parallel}^2}{n_{\perp}^2}\sin^2\theta_i\right]^{1/2} \tag{5.7}$$

It is worth noting that equation 5.7 reduces to the isotropic expression when $n_{\perp} = n_{\parallel}$. For the geometry considered, the incident radiation can only be polarized perpendicular to the *c*-axis, given that it is in the plane of incidence. Similar to the isotropic

case, the solution to Maxwell's equations shows that the fractional transmission for the TM wave considered is given by

$$T_{\mathrm{TM}} = \left| \left\{ \cos \kappa_i d - i \left(\frac{\kappa_i^2 + n_{\parallel}^4 k_i^2}{2 n_{\parallel}^2 \kappa_i k_i} \right) \sin \kappa_i d \right\}^{-1} \right|^2 \qquad (5.8)$$

Case 2: When the optic axis is parallel to the film surface and perpendicular to the plane of incidence (middle inset in figure 5.6), the polarization of the magnetic field is parallel to the c-axis and the wavevector component is

$$\kappa_i = \frac{\omega}{c} \left[n_{\parallel}^2 - \sin^2 \theta_i \right]^{1/2} \qquad (5.9)$$

The fractional TM wave transmitted to this film is still held by the expression 5.8.

Case 3: When the optic axis is parallel to both the film surface and the plane of incidence, the magnetic field and the optic axis are perpendicular (lower inset in figure 5.6). This gives rise to

$$\kappa_i = \frac{\omega}{c} \left[n_{\perp}^2 - \frac{n_{\perp}^2}{n_{\parallel}^2} \sin^2 \theta_i \right]^{1/2} \qquad (5.10)$$

for the wavevector. Now, $n_{\parallel}$ must be replaced by $n_{\perp}$ for the fractional transmission expression in equation 5.8.

Figure 5.6 shows the calculated far-IR transmitted spectra for a TM wave at oblique incidence on a 160-nm-thick w-GaN thin film, considering the three cases discussed above. One can clearly observe dips at the frequencies of the normal modes of the film which are expected for every geometry. Note that the film orientation determines the *selection rules* for IR transmission through anisotropic thin films. Usually, GaN-related thin films are grown in the c-axis direction. Then, only the E_1(TO) and A_1(LO) modes can be observed by far-infrared transmission spectroscopy.

The IR experimental set-up

The experimental system used to obtain the IR transmission spectra was a BOMEM DA3 rapid scanning Fourier transform IR (FTIR) spectrometer. The BOMEM DA3 is a rapid scanning Michelson interferometer in which three different sources can be selected, according to their intensity over a specific spectral range. For the far-IR

experiments in our work, we used a globar lamp, which consists on an electrically heated silicon carbide rod.

A KBr beam splitter was used to split the unpolarized light beam towards the fixed and scan mirrors. The two beams are recombined again at the beam splitter and directed towards the sample. The angle between the incident beam and the normal to the surface of the samples (θ_i) was adjusted by rotating the sample holder, which could be set to within $\sim 5^\circ$ of the desired angle. After the light beam passes through the sample, it is detected by an MCT (mercury cadmium telluride) detector. The spectra were recorded with a 1 cm^{-1} resolution and 100 coadditions.

5.3 The GaN-related samples

A group of novel technologies relating to the growth and processing of gallium nitride and other group III-nitride epilayers have been developed during the last years. In this chapter, the samples under study are all epitaxial layers, which have been grown by either Molecular Beam Epitaxy, MBE, (radio-frequency and plasma assisted) or Metalorganic Vapor Phase Epitaxy (MOVPE) methods. It must be stressed that all the hexagonal epilayers have the *c* axis normal to the surface.

5.3.1 Molecular Beam Epitaxy grown samples

In MBE, the constituent elements of a semiconductor are in the form of *molecular beams* and are deposited onto a heated crystalline substrate to form thin epitaxial layers. The *molecular beams* are typically from thermally evaporated elemental sources. Other sources for the growth of group-III nitrides include metal-organic group III precursors (MOMBE), gaseous group V hydride or organic precursors (gas-source MBE), or some combination of both (chemical beam epitaxy or CBE). To obtain high-purity layers, it is critical that the material sources are extremely pure and that the entire process be done in an ultra-high vacuum environment.

Cubic GaN layers

Due to the fact that the cubic phase is a quasistable structure in GaN, the growth of high-quality *c*-GaN has mostly been performed by MBE, as is the case of our samples. The cubic layers for our studies were developed at the *Department of Physics* of the *Nottingham University*. The growth facility consists of a *Varian Modular* GEN-II

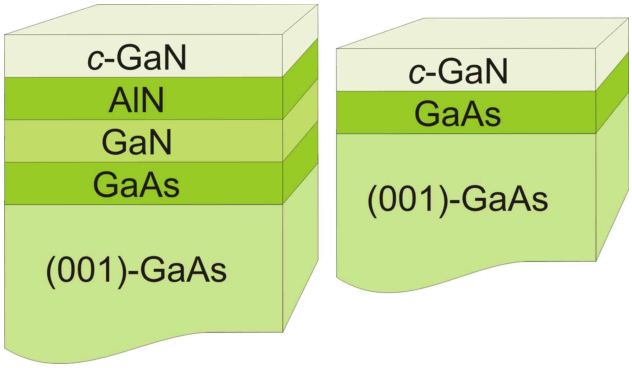

Figure 5.7: Representation of the *c*-GaN samples with and without AlN buffer layer.

equipped with Al, Ga, In, As, C, Mg, Mn and Si sources. The active nitrogen is provided by an Oxford Applied Research CARS25 RF-activated plasma source.

In this work, two different *c*-GaN layers have been studied. They were both grown on (001)-oriented GaAs substrates. Prior to the growth of the GaN layers, a 150 nm-thick GaAs buffer layer was grown on the GaAs substrate in order to improve the properties of the cubic GaN layers. The thickness of the resulting *c*-GaN epilayers is ∼300 nm.

To study the effects of an AlN buffer layer, for one of the samples the GaAs buffer is followed by a 150 nm-thick GaN layer and a 100 nm-thick AlN buffer (see figure 5.7).

$Al_xGa_{1-x}N$ layers

The *w*-AlGaN alloys were grown at the *Instituto de Sistemas Optoelectrónicos y Microtecnología* (ISOM) attached to the *Universidad Politécnica de Madrid*, Spain. The growth facility consists in a MECA 2000 MBE system. The active nitrogen was produced by an Oxford HD25 radio-frequency plasma source, and standard Knudssen

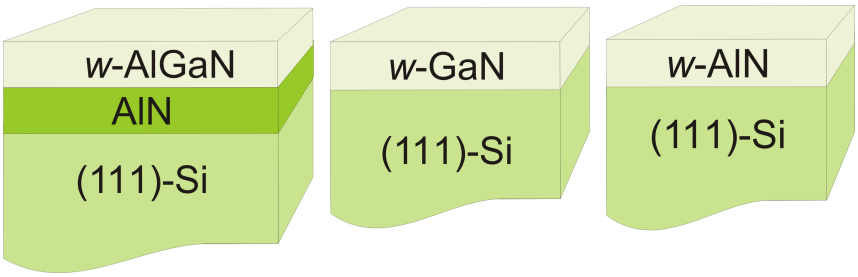

Figure 5.8: Growth scheme of the wurtzite AlGaN, GaN and AlN samples of the present work.

effusion cells were used for the Ga and Al elements.

A representative growth scheme is shown in figure 5.8. As can be seen in the figure, the samples were grown on (111)-oriented Si substrates with a $\sim$ 100 nm-thick AlN buffer interlayer to improve the crystalline quality of the AlGaN epilayer. The reference binary compounds (*w*-AlN and *w*-GaN) were also grown on (111)-Si substrates without any buffer layer. The resulting AlGaN layers have nominal Al contents of 2, 25.5 and 29%, and are $\sim$200 nm thick, which can be categorized as thin film for far-IR spectroscopy.

As-doped *w*-GaN layers with modulated III/V ratio

The samples with modulated III-V ratios used in this study were grown directly on sapphire substrates (see figure 5.10) by PA-MBE in the same laboratory than that for the *c*-GaN samples above, at the *Department of Physics* at *Nottingham University*, United Kingdom.

Arsenic in the form of dimers (As_2) or tetramers (As_4) was produced using a two-zone purpose-made cell. While the nitrogen and arsenic fluxes were intentionally kept constant (beam equivalent pressures, BEP, of $\sim 3\times10^{-5}$ mbar and $\sim 4 \times 10^{-6}$, respectively), the Ga flux was modulated with BEPs from $\sim 2 \times 10^{-8}$ mbar to $\sim 2 \times 10^{-6}$ mbar. Then, the III/V ratio conditions for the doped samples ranges from 1/24 to 1/939. By contrast, the undoped samples were grown with a constant Ga flux and a modulated nitrogen flux with BEPs varying from 1.9×10^{-5} mbar to 1.3×10^{-4} mbar. For these growth conditions, the III/V ratio ranges from 1/23 to 1/162. Although the growth time was 3 hours for all the samples, the final epilayer thicknesses is larger for the samples grown with higher Ga fluxes.

Previous studies on these samples investigated their PL spectra, and also their surface morphology by means of atomic force microscopy (AFM) measurements [30]. In these studies, an increase of the blue luminescence for samples grown with higher

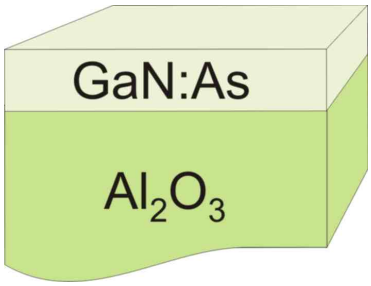

Figure 5.9: Growth scheme of the wurtzite As-doped GaN samples used in this work.

As fluxes was observed, which suggests that the samples are within the doping regime (GaN:As). The AFM images revealed the surfactant effect of As presence on the GaN growth.

5.3.2 Metal Organic Vapor Phase Epitaxy grown samples

The metal organic phase epitaxy (MOVPE) technique is very attractive for the epitaxial growth of compound semiconductors due to its simplicity and flexibility.The epitaxial growth is from the surface reaction of organic compounds or metalorganics and metal hydrides containing the required chemical elements. In contrast to MBE, the growth of MOVPE crystals is by chemical reaction and not by physical deposition. The growth takes place not in a vacuum, but from the gas phase at moderate pressures (15 to 750 Torr). Hence, the MOVPE technique is preferred to grow thermodynamically metastable alloys, such as the BGaN alloy system.

$B_xGa_{1-x}N$ layers

The $B_xGa_{1-x}N$ layers used in this study were grown by Metal-Organic Vapor-Phase Epitaxy (MOVPE) on 4 μm-thick (0001)-GaN template on sapphire substrates. A 200 nm GaN buffer was grown prior to the $B_xGa_{1-x}N$ epilayers, with typical thicknesses between 120 nm and 350 nm. A thick BGaN ($\sim$1.2 μm) epilayer was also grown for comparison purposes.

All the epitaxial growths were performed in a T-shape reactor using 100% nitrogen as the carrier gas, located at the GT-CNRS UMI 2958, an international research unit stablished between the *Georgia Institute of Technology* and the *French National Research Council (CNRS)* in Metz, France.

Triethylborate (TEB), trimethylgallium (TMG) and amonia (NH_3) were used as

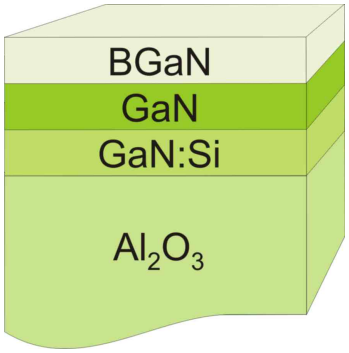

Figure 5.10: Representation of the wurtzite $B_xGa_{1-x}N$ samples.

precursor sources for boron, gallium and nitrogen, respectively. All the growths were performed at 1000° on a 4 μm-thick GaN:Si template on sapphire substrates. A 200 nm-thick GaN buffer was grown prior to the BGaN thin films. The molar ratio of the TEB precursor in the vapor phase with respect to that of the group-III sources (TEB+TMG) TEB/III, was varied to obtain epilayers with different boron contents. The boron composition of the samples was estimated in a previous study from HRXRD and SIMS measurements to be 1.1%, 1.6%, 1.75%, 1.9%, 2.16%, 3.0%, and 3.6% [31]. The SIMS measurements also revealed an homogeneous distribution of the boron along the growth direction througout the $B_xGa_{1-x}N$ layer.

5.4 Results and Discussion: Related Publications

Detailed results of this section and their discussion can be found in the following publications:

Far-infrared transmission in GaN, AlN, and $Al_xGa_{1-x}N$ thin films grown by molecular beam epitaxy
Journal of Applied Physics **104** 033544 (2008)

Phonons in $B_xGa_{1-x}N$/GaN epilayers studied by means of UV Raman scattering
Physica Status Solidi b **DOI** 10.1002/pssb.200743398 (2008)

Raman scattering study of undoped and As-doped GaN grown with different III/V ratios
Semiconductor Science and Technology **22** 1145 (2007)

JOURNAL OF APPLIED PHYSICS **104**, 033544 (2008)

Far-infrared transmission in GaN, AlN, and AlGaN thin films grown by molecular beam epitaxy

J. Ibáñez,[1] S. Hernández,[1] E. Alarcón-Lladó,[1] R. Cuscó,[1] L. Artús,[1,a)] S. V. Novikov,[2] C. T. Foxon,[2] and E. Calleja[3]
[1]*Institut Jaume Almera, Consell Superior d'Investigacions Científiques (CSIC), Lluís Solé i Sabarís s.n, 08028 Barcelona, Catalonia, Spain*
[2]*School of Physics and Astronomy, University of Nottingham, Nottingham NG7 2RD, United Kingdom*
[3]*ISOM-Departamento Ingeniería Electrónica, ETSI Telecomunicación, Universidad Politécnica, 28040 Madrid, Spain*

(Received 3 April 2008; accepted 11 June 2008; published online 15 August 2008)

We present a far-infrared transmission study on group-III nitride thin films. Cubic GaN and AlN layers and *c*-oriented wurtzite GaN, AlN, and $Al_xGa_{1-x}N$ ($x<0.3$) layers were grown by molecular beam epitaxy on GaAs and Si(111) substrates, respectively. The Berreman effect allows us to observe simultaneously the transverse optic and the longitudinal optic phonons of both the cubic and the hexagonal films as transmission minima in the infrared spectra acquired with obliquely incident radiation. We discuss our results in terms of the relevant electromagnetic theory of infrared transmission in cubic and wurtzite thin films. We compare the infrared results with visible Raman-scattering measurements. In the case of films with low scattering volumes and/or low Raman efficiencies and also when the Raman signal of the substrate material obscures the weaker peaks from the nitride films, we find that the Berreman technique is particularly useful to complement Raman spectroscopy. © *2008 American Institute of Physics*. [DOI: 10.1063/1.2968242]

I. INTRODUCTION

Group-III nitride compounds are currently being used to fabricate optoelectronic devices operating in the blue and near-ultraviolet (UV) regions as well as high-power microwave devices and field-effect transistors. Numerous studies have employed Raman scattering and far-infrared (IR) spectroscopies to investigate several physical properties of GaN, AlN, and the ternary alloy AlGaN such as their phonon modes, the crystal quality and the orientation of the as-grown material, free-carrier effects, and the piezoelectric response.[1–18] It is now clear that the longitudinal optic (LO) phonons [A_1(LO) and E_1(LO)] of hexagonal AlGaN display a one-mode behavior, whereas the rest of the Raman or IR active phonon modes [E_2, A_1(TO) and E_1(TO)] exhibit a two-mode behavior.[13,17] Similarly, it has been shown that the LO and transverse optic (TO) phonons of cubic AlGaN exhibit one-mode and two-mode behaviors, respectively.[11]

While visible Raman scattering is a highly sensitive technique for the study of the lattice dynamics in semiconductor alloys, many authors usually rely on IR reflectance to characterize the optical properties of group-III nitride crystals and structures.[1,4–9,12–15] In contrast, only a few works reported IR transmission measurements,[3,9,12,18] most of which were performed in normal-incidence configuration. Reports dealing with oblique-incidence IR transmission to study the phonons of group-III nitrides are scarce.[3]

As first demonstrated by Berreman,[19] the frequency of both zone-center TO and LO phonons of polar materials can be directly measured in far-IR transmission experiments for radiation at oblique incidence and with the electric vector polarized parallel to the plane of incidence (TM waves).[19,20] The observation of transmission minima at the frequency of LO modes (i.e., the Berreman effect) and TO modes is limited to samples that are significantly thinner than the wavelength of the electromagnetic radiation corresponding to the reststrahlen band of the material. This condition, easily fulfilled for epilayers and heterostructures produced by molecular beam epitaxy (MBE) or chemical vapor deposition, provides an alternative means to determine the frequency of both TO and LO phonons in polar compounds and structures.[20,21] The transmission measurements at oblique incidence also allow one to directly measure the frequency of LO-plasmon coupled modes, from which the free-carrier concentration of the samples can be evaluated.[22]

The observation of transmission minima corresponding to TO or LO phonons in group-III nitrides is however limited to samples grown on substrates that are not highly light absorbing in the spectral region of interest. Epitaxial thin films and structures based on GaN or AlN have been grown on many different substrates such as sapphire, Si, or GaAs. While sapphire displays strong absorption in the 380–900 cm^{-1} spectral region[23] and as a consequence it cannot be used for transmission experiments, the reststrahlen band of GaAs (250–350 cm^{-1}) is well separated from the A_1(TO,LO) and E_1(TO,LO) phonon frequencies of GaN and AlN. In turn, owing to its nonpolar nature, Si is IR inactive and absorbs IR radiation very weakly. Hence, Si substrates are very well-suited for IR transmission studies of nitride compounds. Note that, in contrast, Si exhibits very strong first-order and second-order Raman features that may overlap with the phonon modes of the nitrides in the Raman spectra.

a)Electronic mail: lartus@ija.csic.es.

TABLE I. Basic details of the GaN, AlN, and $Al_xGa_{1-x}N$ epilayers studied in this work.

Sample	Epilayer	Substrate	Thickness (μm)	Buffer layers
A	*c*-GaN	GaAs(001)	0.3	GaAs (150 nm)
B	*c*-GaN	GaAs(001)	0.3	AlN (100 nm)/GaN (150 nm)/GaAs (150 nm)
C	*w*-GaN (Be-doped)	Si(111)	0.16	···
D	*w*-$Al_{0.02}Ga_{0.98}N$	Si(111)	0.2	AlN (100 nm)
E	*w*-$Al_{0.25}Ga_{0.75}N$	Si(111)	0.2	AlN (140 nm)
F	*w*-$Al_{0.29}Ga_{0.71}N$	Si(111)	0.2	AlN (100 nm)
G	*w*-AlN	Si(111)	0.4	···

The aim of this work is to apply IR transmission spectroscopy to study group-III nitrides. Two types of samples are investigated: (i) cubic (*c*) GaN and AlN thin films grown on (100)-oriented GaAs substrates and (ii) wurtzite (*w*) GaN, AlN, and $Al_xGa_{1-x}N$ ($x<0.3$) thin films grown on (111)-oriented Si substrates. Our measurements, performed in normal and oblique incidence, allow us to detect transmission minima corresponding to the TO and LO phonons both in the cubic and in the wurtzite samples. We discuss our results in terms of the relevant electromagnetic theory of IR transmission in wurtzite thin films, which differs from the standard theory for isotropic materials. In spite of the uniaxial symmetry of wurtzite compounds, the isotropic approximation has been widely used in the literature to analyze the IR optical response of group-III nitrides.[2,4,6,8]

The bandgap of AlGaN is significantly higher than the energy corresponding to visible laser excitations. As a consequence, the use of visible Raman scattering to investigate structures containing very thin films of AlGaN (i.e., films with very small scattering volumes) may be hampered by the low Raman efficiency exhibited by this ternary alloy, in particular for large Al contents. In addition, given that wide-bandgap compounds are transparent to visible radiation, the Raman spectra may be obscured by intense peaks arising from the substrate. The Raman signal from the nitride films may be enhanced by using UV, near-resonant laser excitations.[24] However, owing to absorption effects, the more involved UV Raman experiments only allow one to probe the shallowest layers of the samples. Therefore, the IR transmission measurements at oblique incidence may emerge as a complementary tool to Raman scattering for the characterization of structures based on Al(Ga)N. Here we compare the IR transmission data with visible Raman-scattering measurements. We show that the IR technique may be particularly useful for the direct observation of phonon peaks from very thin layers with high Al content. In the case of *w*-AlGaN, the transmission spectra reveal the composition behavior of the A_1(LO) and the GaN-like E_1(TO) phonon modes of the ternary alloy. In the composition range investigated, the IR transmission data are in good agreement with Raman and IR reflectance results reported in the literature.

II. EXPERIMENT

IR transmission measurements were performed on different series of *c*-GaN, *w*-GaN, *w*-AlGaN, and *w*-AlN epilayers grown by MBE in different laboratories. Details of the samples such as the substrate material, presence of a buffer layer, and the composition and thickness of the epilayers can be found in Table I. All wurtzite samples were grown with the crystallographic *c* axis parallel to the growth direction.

Room-temperature unpolarized transmission spectra were obtained with a BOMEM DA.8 rapid scanning Fourier transform IR spectrometer. The experiments were performed by using a globar source, a KBr beam splitter, and a HgCdTe [mercury cadmium telluride (MCT)] detector. The spectra were typically recorded with 1 cm^{-1} resolution and 100 coadditions. The angle between the incident beam and the normal to the surface of the samples (θ_i) was adjusted by rotating the sample holder, which could be set to within $\sim 5°$ of the desired angle.

Raman experiments were carried out at RT by using a confocal Raman microprobe with a 100× objective. The typical spot size was of about 1 μm. The spectra were recorded with a Jobin–Yvon T64000 triple-grating spectrometer equipped with a coupled charge detector cooled with liquid nitrogen. The 514.5 nm line of an Ar laser was used as excitation source.

III. THEORETICAL CONSIDERATIONS

From the point of view of far-IR spectroscopy, a polar film of thickness *d* may be considered as *thin* provided that $\omega/c \gg d$, where ω is the frequency of the incident electromagnetic wave and *c* is the speed of light. In a polar thin film, there exist two types of normal modes of vibration: (i) modes with the particle motion parallel to the plane of the film (TO modes) and (ii) modes with the particle motion perpendicular to the plane of the film (LO modes). As is well known, the long wavelength polarization fields associated to the LO modes give rise to the LO-TO splitting.

When an electromagnetic wave is incident on the film with the electric field polarized perpendicular to the plane of incidence [i.e., an *s* wave, also known as transverse-electric (TE) wave], the radiation can only interact with the TO modes regardless of the angle of incidence (θ_i). In contrast, both the TO and LO modes can be excited by radiation that impinges on the film at an angle θ_i with the electric field polarized parallel to the plane of incidence [i.e., a *p* wave, also known as transverse-magnetic (TM) wave].[19,20] In such case, the electric field has a component in the direction of the particle motion for both the TO and LO phonons.

While the optical response of crystals with cubic symmetry is isotropic, the response of crystals with the wurtzite

(uniaxial) structure depends on the orientation of the crystal and on the geometry considered (i.e., optic axis in the plane of incidence or perpendicular to it). To describe the far-IR response of wurtzite crystals, two different refractive indexes for each polarization configuration (i.e., two dielectric functions) are required. Depending on the geometry considered and the angle of incidence, transmission minima corresponding to the A_1(TO), A_1(LO), E_1(TO), or the E_1(LO) modes can be detected.[20]

A. Isotropic thin films

For the sake of completeness, we first revisit the electromagnetic theory for far-IR transmission in an isotropic thin film (see Ref. 20 and references therein for details). In what follows, we focus on TM waves since only this radiation allows the observation of transmission minima at the frequency of LO modes. For isotropic films with complex dielectric function $\epsilon(\omega)=n^2(\omega)$, the fractional transmission for the TM waves is given by[20]

$$T_{\mathrm{TM}} = \left| \left[\cos \kappa d - i \left(\frac{\kappa^2 + n^4 k^2}{2n^2 \kappa k} \right) \sin \kappa d \right]^{-1} \right|^2, \tag{1}$$

where $n(\omega)$ is the refractive index of the material, $k=(\omega/c)\cos\theta_i$ is the wave vector component of the incident radiation parallel to the film, and $\kappa=(\omega/c)[n^2-\sin^2\theta_i]^{1/2}$. The definition of κ originates from the solutions of Maxwell's equations inside the film, which have the form $B_{\parallel}(z)=a\exp^{i\kappa z}+b\exp^{-i\kappa z}$ for the magnetic-field component parallel to the film, where the z direction is perpendicular to the plane of the film and a and b are constants that can be obtained with the appropriate boundary conditions.

For a binary isotropic polar compound such as c-GaN or c-AlN, the frequency-dependent refractive index is determined by the frequency of the TO and LO phonons, ω_{TO} and ω_{LO}:

$$n^2(\omega) = \epsilon_\infty + \epsilon_\infty \frac{\omega_{\mathrm{LO}}^2 - \omega_{\mathrm{TO}}^2}{\omega_{\mathrm{TO}}^2 - \omega^2 - i\Gamma\omega}, \tag{2}$$

where Γ is the phenomenological damping coefficient for the phonon modes. The TO and LO frequencies are related to the static (ϵ_0) and high-frequency (ϵ_∞) dielectric constants through the Lyddane–Sachs–Teller relation. If the investigated material is an isotropic two-mode ternary alloy, Eq. (2) has to be replaced by a dielectric function that includes contributions from the two polar sublattices (see Ref. 22 for details).

To illustrate the transmission model outlined above, we have plotted in Fig. 1 the calculated transmission for a TM wave at oblique incidence for c-AlN thin films of different thicknesses. For the calculations, we have used the phonon frequency values of c-AlN given in Ref. 16 ($\omega_{\mathrm{TO}}=655$ cm^{-1} and $\omega_{\mathrm{LO}}=902$ cm^{-1}) and we have taken $\theta_i=45°$ and $\Gamma=10$ cm^{-1}. For the high-frequency dielectric constant, we have employed the value measured in w-AlN, $\epsilon_\infty=4.77$.[16] Figure 1 shows that transmission minima appear at both ω_{TO} and ω_{LO}. For the thicker films, interference fringes appear below the TO frequency, which results from the rapid increase in the dielectric function for ω values close to the pole at ω_{TO}.[20]

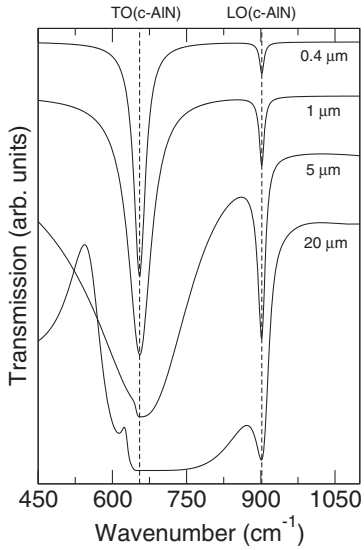

FIG. 1. Calculated far-IR transmission spectra of c-AlN thin films of different thicknesses, ranging from 0.4 μm to 20 μm. Each spectrum was calculated assuming obliquely incident TM waves ($\theta_i=45°$).

B. Uniaxial thin films

For a uniaxial medium such as a thin film with wurtzite crystal structure, the solutions of Maxwell's equations can be found in a similar way to the isotropic case. The dielectric function, however, has to be replaced by the uniaxial dielectric tensor

$$\epsilon(\omega) = \begin{pmatrix} n_\parallel^2 & 0 & 0 \\ 0 & n_\parallel^2 & 0 \\ 0 & 0 & n_\perp^2 \end{pmatrix}, \tag{3}$$

where $n_\parallel$ and $n_\perp$ are the ordinary and extraordinary refractive indexes, respectively. The components of the dielectric tensor are given by

$$n_\parallel^2(\omega) = \epsilon_{\infty\parallel} + \epsilon_{\infty\parallel} \frac{\omega_{\mathrm{LO}\parallel}^2 - \omega_{\mathrm{TO}\parallel}^2}{\omega_{\mathrm{TO}\parallel}^2 - \omega^2 - i\omega\Gamma_\parallel} \tag{4}$$

and

$$n_\perp^2(\omega) = \epsilon_{\infty\perp} + \epsilon_{\infty\perp} \frac{\omega_{\mathrm{LO}\perp}^2 - \omega_{\mathrm{TO}\perp}^2}{\omega_{\mathrm{TO}\perp}^2 - \omega^2 - i\omega\Gamma_\perp}, \tag{5}$$

where $\omega_{\mathrm{TO}\parallel}$ and $\omega_{\mathrm{LO}\parallel}$ correspond to the E_1 phonon modes of wurtzite, while $\omega_{\mathrm{TO}\perp}$ and $\omega_{\mathrm{LO}\perp}$ correspond to the A_1 modes.[13] In Eqs. (4) and (5), $\Gamma_{\parallel,\perp}$ and $\epsilon_{\infty\parallel,\perp}$ represent the corresponding phonon damping and high-frequency dielectric constants, respectively.

For a TM wave impinging on a wurtzite thin film with the c-axis perpendicular to the plane of the film [see inset of Fig. 2(a)], the z dependence of $B_{\parallel}(z)$ is the same as for the isotropic film, but with κ given by[25]

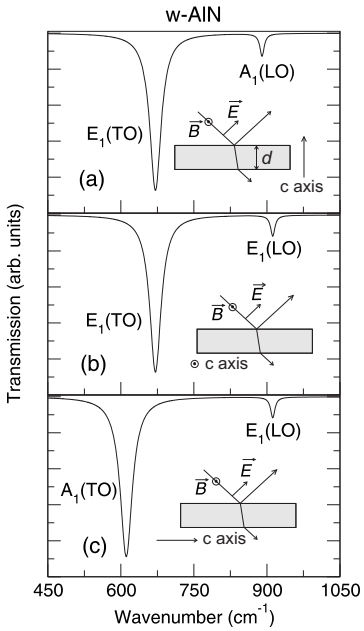

FIG. 2. Calculated far-IR transmission spectra at oblique incidence (θ_i =45°) for TM waves incident on a 400-nm-thick *w*-AlN thin film with the *c*-axis oriented (a) perpendicular to both the magnetic field of the incident radiation ($\vec{B}$) and the film surface, (b) parallel to both $\vec{B}$ and the film surface, and (c) perpendicular to $\vec{B}$ and parallel to the film surface. The insets show the different geometries considered.

$$\kappa = (\omega/c)\left[n_{\parallel}^2 - \frac{n_{\parallel}^2}{n_{\perp}^2}\sin^2\theta_i\right]^{1/2}, \tag{6}$$

where z is perpendicular to the plane of the film ($z \| c$ axis). Note that, as expected, Eq. (6) reduces to the isotropic expression when $n_{\perp}=n_{\parallel}$. In the previous discussion, given that the c axis is in the plane of incidence, the magnetic field of the incident radiation can only be polarized perpendicular to the c axis. In contrast, for a TM wave impinging on a face not oriented along the c axis, care has to be taken about the polarization of the magnetic field, which can be parallel or perpendicular to the optic axis [see insets of Figs. 2(b) and 2(c), respectively]. Correspondingly, the appropriate components of the dielectric tensor have to be considered in Eq. (6) for these geometries.

For a c-oriented thin film, similarly to the isotropic case, the solution of Maxwell's equations shows that the fractional transmission for the TM waves is given by

$$T_{\mathrm{TM}} = \left|\left[\cos\kappa d - i\left(\frac{\kappa^2 + n_{\parallel}^4 k^2}{2n_{\parallel}^2 \kappa k}\right)\sin\kappa d\right]^{-1}\right|^2, \tag{7}$$

with κ given by Eq. (6). For a film with its surface parallel to the c axis, the previous expression still holds provided that the plane of incidence is perpendicular to the optic axis [inset of Fig. 2(b)], since in this case, the electric-field component of the electromagnetic radiation parallel to the plane of the film is also perpendicular to the c axis. In contrast, $n_{\parallel}$ has to be replaced by $n_{\perp}$ when the plane of incidence and the c axis are parallel [inset of Fig. 2(c)], since in this case, the electric-field component in the plane of the film and the optic axis are parallel.

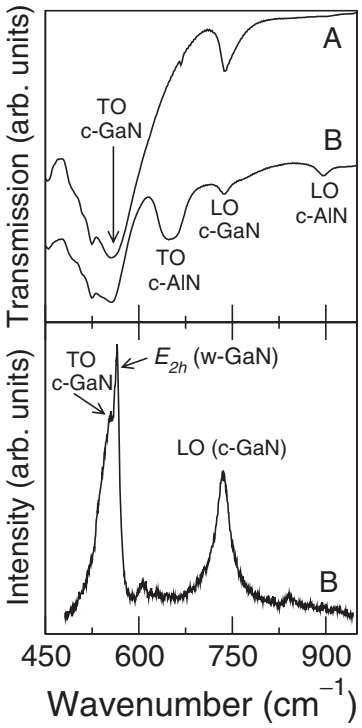

FIG. 3. (Upper panel) Far-IR transmission spectra in oblique incidence of two *c*-GaN epilayers grown on (001)-GaAs with an AlN buffer layer (curve *B*) and without an AlN buffer layer (curve *A*). (Lower panel) Visible Raman spectrum (λ_{exc}=514.5 nm) of the *c*-GaN/GaAs epilayer grown with an AlN buffer layer.

Figures 2(a)–2(c) show the calculated transmission for a TM wave at oblique incidence for a 400-nm-thick *w*-AlN thin film. The three geometries discussed above, depicted in the insets of each figure, have been considered. For the calculations, we have used the phonon frequency values of *w*-AlN given in Ref. 16 ($\omega[E_1(\mathrm{TO})]$=670.8 cm^{-1}, $\omega[E_1(\mathrm{LO})]$=912 cm^{-1}, $\omega[A_1(\mathrm{TO})]$=611 cm^{-1}, and $\omega[A_1(\mathrm{LO})]$=890 cm^{-1}), and we have taken θ_i=45°, $\epsilon_{\infty\parallel}=\epsilon_{\infty\perp}$=4.77,[16] and Γ=10 cm^{-1}. The figure shows that transmission minima corresponding to the normal modes of the film for each configuration, with particle motions parallel (TO) and perpendicular (LO) to the plane of the film, are expected in all the geometries for oblique incidences. In the particular case of *c*-oriented wurtzite films, these are the E_1(TO) and the A_1(LO) modes, respectively [see Fig. 2(a)].

IV. RESULTS AND DISCUSSION

A. Cubic GaN and AlN

The upper panel of Fig. 3 shows IR transmission spectra in oblique incidence ($\theta_i \sim 45°$) of samples A and B, which consist of 0.3-μm-thick *c*-GaN epilayers grown on a (100)-GaAs substrate (see Table I). The epilayer of sample A was grown on a 0.15-μm-thick GaAs buffer layer, while the epilayer of sample B was grown on a 0.15 μm GaAs buffer, followed by a 0.15 μm GaN layer and a 0.10 μm AlN buffer. The reststrahlen band of GaAs, in the 268–292 cm^{-1}

region, does not appear in the figure because it is below the detection range of the MCT detector. The spectra of both samples display transmission dips at 555 and 742 cm^{-1} corresponding to the TO and LO phonon modes of *c*-GaN.[3] As predicted by theory (see Sec. III), the LO modes are not observed in the normal-incidence experiments (not shown). In addition to the GaN-related features, the spectrum of sample B displays transmission dips that can be attributed to the TO and LO modes of *c*-AlN. The positions of these two features, located at 651 and 897 cm^{-1}, are in good agreement with the values obtained by Raman scattering in bulk crystals (655 and 902 cm^{-1}, see Ref. 16). The lower frequency values found for the thin AlN layer of sample B in comparison to bulk samples may be related to tensile strain as a consequence of the lower lattice parameter of AlN with respect to the GaAs substrate.

Next, we compare the IR transmission data obtained from the group-III nitride cubic samples with the results of visible Raman-scattering measurements. The lower panel of Fig. 3 displays the Raman spectrum for sample B, acquired with the 514.5 nm line of an Ar^+ laser. Raman peaks corresponding to the TO and LO modes of *c*-GaN are clearly observed. An additional Raman peak at 565 cm^{-1}, which can be attributed to the E_{2h} mode of *w*-GaN, appears in the spectrum of this sample. The presence of this peak shows that the AlN buffer promotes the growth of wurtzite domains in the GaN epilayer. However, as is evident from the upper panel of Fig. 3, the presence of *w*-GaN domains in sample B is not detected by IR transmission because the frequency of the IR active modes (LO and TO modes) for both phases is very similar. Also, the transmission dips are much broader than the corresponding Raman peaks. In contrast, no signal from the AlN layer appears in the Raman spectra of sample B. Note that for the visible excitation wavelength used to acquire the Raman spectra (514.5 nm), the GaN epilayers are transparent. Thus, the absence of Raman signal from the AlN buffer can be explained by the low Raman efficiency of AlN for this wavelength and also by the relatively small thickness of the AlN buffer (0.10 μm). We would like to emphasize that, given the thickness of the GaN epilayer in sample B, the use of UV, near-resonant wavelengths would not permit one to detect the AlN layer since the excitation radiation would then be absorbed by the GaN epilayer. While the Raman measurements are clearly superior in sensitivity and resolution to study the GaN films of sample B, they fail to detect the weak modes of the AlN buffer layer contained in this sample, which can be otherwise probed unambiguously with the Berreman technique.

B. Wurtzite Al(Ga)N

As discussed in Sec. III, the transmission spectrum of *c*-oriented wurtzite material is dominated by the E_1(TO) mode. This can be seen in Fig. 4 for the case of an AlN thin film grown on Si(111) (sample G). The figure shows four different spectra acquired with different incidence angles (0°, 15°, 30°, and 45°). The strong dip at ~670 cm^{-1} that appears in all the spectra can be assigned to the E_1(TO) mode of AlN. In addition to this feature, a dip at ~890 cm^{-1}, the intensity of which increases with the angle of incidence of the electromagnetic radiation, is also observed. This feature corresponds to the A_1(LO) mode of AlN. Owing to minor deviations from perfect normal incidence, a very weak A_1(LO) dip is also observed in the spectrum acquired with ~0°. More importantly, no dips corresponding to the E_1(LO) mode of *w*-AlN appear in any of the spectra, in agreement with theory.

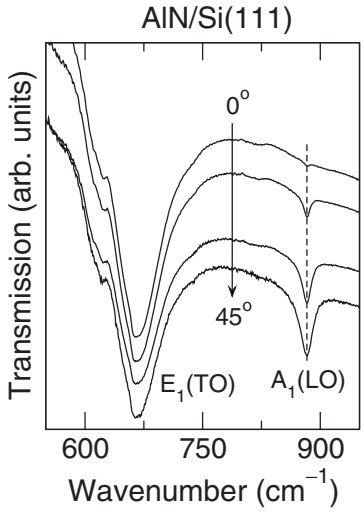

FIG. 4. IR transmission of a *w*-AlN epilayer grown by MBE on Si(111) (sample G) for different angles of incidence. The spectra correspond to θ_i =0°, 15°, 30°, and 45°.

It should be borne in mind that in Raman-scattering experiments on wurtzite AlN, an interaction between the A_1 and E_1 phonons takes place when the crystal high-symmetry axes are tilted relative to the phonon propagation direction. The resulting mixed modes, known as quasi-TO and quasi-LO modes, are shifted with respect to the pure A_1 or E_1 modes.[26] As discussed in Sec. III, no mixing between the A_1 and E_1 modes occurs in the case of the oblique-incidence IR transmission experiments on samples oriented along high-symmetry axes because the symmetry of the respective TO and LO modes of the polar film (i.e., the modes with which TE and TM waves interact, respectively) is not affected by the angle of the incident radiation. Thus, only pure A_1 and E_1 modes are detected with the Berreman technique.

In Fig. 5 we show the transmission spectra at oblique incidence for three different $Al_xGa_{1-x}N$ epilayers grown on Si(111) substrates (samples D–F). These epilayers were grown on an AlN buffer layer. For comparison, in Fig. 5 we have also included IR spectra of GaN and AlN epilayers (samples C and G, respectively). As can be observed in the figure, transmission dips corresponding to the A_1(LO) mode and to the GaN-like E_1(TO) mode appear in all the spectra of the GaN and AlGaN epilayers. In samples D, E, and F we also observe the corresponding E_1(TO) and A_1(LO) modes arising from the AlN buffer layers. Although the E_1(TO) mode appears as a fairly broad dip in the spectra of the AlGaN samples, it can be seen in the figure that this feature displays an upward frequency shift with increasing Al content. In the lower panel of Fig. 6, we plot the frequency of

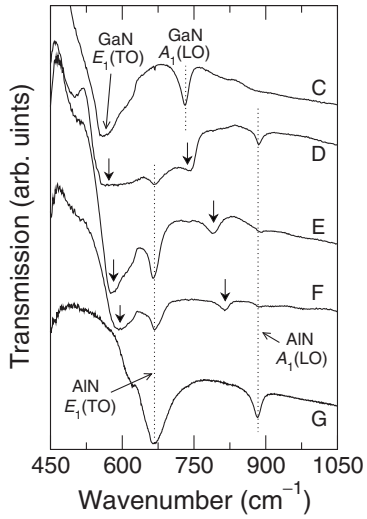

FIG. 5. IR transmission spectra of different $Al_xGa_{1-x}N/AlN/Si(111)$ epilayers grown by MBE with x=2%, 25%, and 29% (curves *D*-*F*, respectively). Curves *C* and *G* correspond to *w*-GaN and *w*-AlN. The vertical arrows indicate the position of the A_1(LO) mode and of the GaN-like E_1(TO) mode of AlGaN.

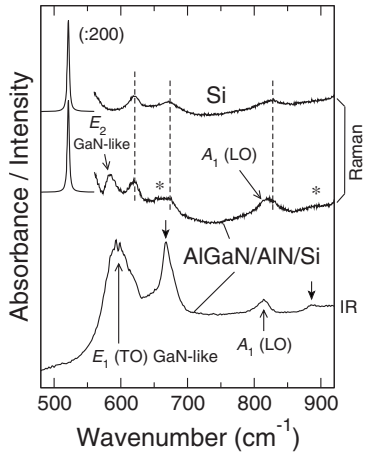

FIG. 7. Raman spectrum (middle curve) and far-IR absorbance spectrum at oblique incidence (lower curve) for an $Al_{0.29}Ga_{0.71}N$ epilayer grown on a Si(111) substrate with an AlN buffer (sample F). The upper curve shows the Raman spectrum of bulk Si(111). The asterisks in the Raman spectrum of the $Al_{0.29}Ga_{0.71}N$ epilayer indicate the position of the E_{2h} and A_1(LO) modes of the AlN buffer layer. The vertical arrows in the IR spectrum refer to the E_1(TO) and A_1(LO) modes of the AlN buffer layer.

the GaN-like E_1(TO) mode obtained from the transmission spectra as a function of x. The frequency of this mode increases monotonically with x, in agreement with the Raman results reported by Davydov *et al.*[17] on hexagonal AlGaN. Note that we do not observe the AlN-like E_1(TO) mode for any of our AlGaN epilayers. This is similar to the observations in Ref. 17, where no AlN-like E_1(TO) mode was found in the Raman spectra of $Al_xGa_{1-x}N$ for Al compositions up to $x \sim 0.6$.

On the other hand, we observe a clear, broad dip in all the spectra in Fig. 5 that can be the assigned to the A_1(LO) phonon mode of AlGaN. As discussed in detail in Ref. 17, both this mode and the E_1(LO) mode exhibit a one-mode behavior in this alloy system. We plot in the upper panel of Fig. 6 the composition behavior of this mode as obtained from the IR spectra. As in Ref. 17, we find that the A_1(LO) mode increases monotonically with increasing x. In the measurements performed under normal incidence, no residual signal of the A_1(LO) mode was detected. As in the case of AlN, no features corresponding to the E_1(LO) mode were observed in any of the oblique-incidence measurements on the *c*-oriented AlGaN epilayers.

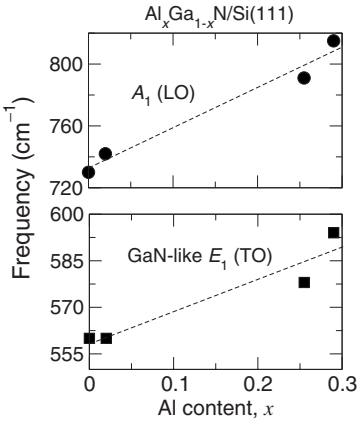

FIG. 6. Frequency behavior of the A_1(LO) (upper panel) and the GaN-like E_1(TO) (lower panel) phonon modes as obtained with the obliquely incident transmission measurements on the $Al_xGa_{1-x}N$ epilayers studied in this work. The dashed lines are guides to the eye.

Next, in order to assess the usefulness of the IR technique to study the group-III nitrides, we compare the IR transmission spectra of the AlGaN/AlN/Si(111) samples with the results of visible Raman scattering (λ_{exc}=514.5 nm). It should be first noted that the Raman efficiency of the different Raman-active phonon modes of $Al_xGa_{1-x}N$ depends on both x and on the energy of the excitation source used to perform the experiments. In other words, different laser wavelengths in the UV spectral range should be used to enhance the Raman signal of the different layers investigated. However, visible laser lines are commonly employed to study group-III nitrides. While for bulk samples or thick films the large scattering volumes involved yield strong Raman signals, weak Raman signals are expected in the case of very thin AlGaN films. In such case, the signal of the substrate material may also preclude the observation of the weakest peaks from the nitride layers.

In Fig. 7, we plot transmission and Raman spectra of one of the AlGaN/AlN/Si(111) epilayers studied in this work (sample F). For convenience, the vertical scale of the IR spectrum has been plotted as absorbance (lower curve). In the figure, we have included the Raman spectrum of bulk Si(111) for comparison (upper curve). In this curve, besides the strong first-order peak of Si at 521 cm^{-1}, three second-order features at about 620, 670, and 825 cm^{-1} are clearly visible. These three features are also detected in the Raman spectrum of sample F (intermediate curve) and overlap with some of the Raman peaks of the AlGaN and AlN layers. In particular, the A_1(LO) mode of AlGaN, located at ~815 cm^{-1}, overlaps with the Si-related band at 825 cm^{-1},

which might lead one to overestimate the frequency of the A_1(LO) mode from the Raman measurements. Contrary, as discussed above, the A_1(LO) mode is clearly visible in the IR oblique-incidence spectrum (see the lower curve in Fig. 7).

While in the IR spectrum of sample F the GaN-like E_1(TO) mode of AlGaN appears as a prominent feature at ~595 cm^{-1}, the nonpolar GaN-like E_{2h} mode of AlGaN can only be observed in the Raman spectrum as a weak band at ~585 cm^{-1}. For the AlN buffer only extremely weak Raman features corresponding to the E_{2h} and A_1(LO) modes are detected (peaks marked with an asterisk at ~650 and ~890 cm^{-1}). In contrast, clear E_1(TO) and A_1(LO) bands from the AlN buffer appear in the IR spectrum (peaks marked with an arrow at ~670 and ~890 cm^{-1}). These results show the usefulness of the IR technique for the direct detection of phonon peaks arising from very thin layers of semiconductor compounds whose scattering efficiency is low in visible Raman spectroscopy.

V. CONCLUSIONS

We have performed IR transmission experiments at normal and oblique incidence in a series of GaN, AlN, and AlGaN films grown by MBE on either GaAs and Si(111) substrates. We have observed clear signatures corresponding to both the TO and the LO modes in the cubic films, grown on (001)-GaAs, and in the wurtzite samples, grown on Si(111). In the case of the *c*-oriented *w*-AlGaN epilayers, the A_1(LO) and the GaN-like E_1(TO) modes are detected. The observation of transmission dips arising from the nitride phonons is possible because both the GaAs and Si(111) substrates are nearly transparent in the spectral region of interest (550–950 cm^{-1}). We have discussed our results in terms of the electromagnetic theory of IR transmission in cubic and wurtzite thin films. To explore the usefulness of the Berreman technique, we have compared the IR data with the results of visible Raman-scattering measurements. In the particular case of the samples grown on Si substrates, the strong first- and second-order Raman peaks of Si overlap with the phonon modes of the nitrides. In contrast, the Berreman technique makes it possible to unambiguously characterize the nitride films. Thus, we conclude that the IR transmission experiments at oblique incidence are particularly useful to complement Raman spectroscopy.

ACKNOWLEDGMENTS

This work was supported by the Spanish Ministry of Science and Technology (Contract No. MAT2007-63617 and the Ramon y Cajal Programme) and by the British EPSRC-GB.

[1] A. S. Barker and M. Ilegems, Phys. Rev. B **7**, 743 (1973).
[2] M. F. MacMillan, R. P. Devaty, and W. J. Choyke, Appl. Phys. Lett. **62**, 750 (1993).
[3] M. Giehler, M. Ramsteiner, O. Brandt, H. Yang, and K. H. Ploog, Appl. Phys. Lett. **67**, 733 (1995).
[4] C. Wetzel, E. E. Haller, H. Amano, and I. Akasaki, Appl. Phys. Lett. **68**, 2547 (1996).
[5] P. Perlin, E. Litwin, B. Suchanek, W. Knap, J. Camassel, T. Suski, R. Piotrzkowski, I. Grzegory, S. Porowski, E. Kaminska, and J. C. Chervin, Appl. Phys. Lett. **68**, 1114 (1996).
[6] G. Yu, H. Ishikawa, M. Umeno, T. Egawa, J. Watanabe, T. Soga, and T. Jimbo, Appl. Phys. Lett. **73**, 1472 (1998).
[7] G. Mirjalili, T. J. Parker, S. Farjami, M. M. Bulbul, S. R. P. Smith, T. S. Cheng, and C. T. Foxon, Phys. Rev. B **57**, 4656 (1998).
[8] P. Wisniewski, W. Knap, J. P. Malzac, J. Camassel, M. D. Bremser, R. F. Davis, and T. Suski, Appl. Phys. Lett. **73**, 1760 (1998).
[9] R. Y. Krupitskaya and G. W. Auner, J. Appl. Phys. **84**, 2861 (1998).
[10] M. Shubert, A. Kasic, T. E. Tiwald, J. Off, B. Kuhn, and F. Scholz, MRS Internet J. Nitride Semicond. Res. **4**, 11 (1999).
[11] H. Harima, T. Inoue, S. Nakashima, H. Okumura, Y. Ishida, S. Yoshida, T. Koizumi, H. Grille, and F. Bechstedt, Appl. Phys. Lett. **74**, 191 (1999).
[12] T. Prokofyeva, M. Seon, J. Vanbuskirk, M. Holtz, S. A. Nikishin, N. N. Faleev, H. Temkin, and S. Zollner, Phys. Rev. B **63**, 125313 (2001).
[13] M. Holtz, T. Prokofyeva, M. Seon, K. Copeland, J. Vanbuskirk, S. Williams, S. A. Nikishin, V. Tretyakov, and H. Temkin, J. Appl. Phys. **89**, 7977 (2001).
[14] M. Bickermann, B. M. Epelbaum, P. Heimann, Z. G. Herro, and A. Winnacker, Appl. Phys. Lett. **86**, 131904 (2005).
[15] E. Iborra, M. Clement, L. Vergara, A. Sanz-Hervas, J. Olivares, and J. Sangrador, Appl. Phys. Lett. **88**, 231901 (2006).
[16] H. Harima, J. Phys.: Condens. Matter **14**, R967 (2002).
[17] V. Y. Davydov, I. N. Goncharuk, A. N. Smirnov, A. E. Nikolaev, W. V. Lundin, A. S. Usikov, A. A. Klochikhin, J. Aderhold, J. Graul, O. Semchinova, and H. Harima, Phys. Rev. B **65**, 125203 (2002).
[18] A. Sanz-Hervas, E. Iborra, M. Clement, J. Sangrador, and M. Aguilar, Diamond Relat. Mater. **12**, 1186 (2003).
[19] D. W. Berreman, Phys. Rev. **130**, 2193 (1963).
[20] M. D. Sciacca, A. J. Mayur, E. Oh, A. K. Ramdas, S. Rodriguez, J. K. Furdyna, M. R. Melloch, C. P. Beetz, and W. S. Yoo, Phys. Rev. B **51**, 7744 (1995).
[21] M. Aigle, H. Pascher, H. Kim, E. Tarhan, A. J. Mayur, M. D. Sciacca, A. K. Ramdas, G. Springholz, and G. Bauer, Phys. Rev. B **64**, 035316 (2001).
[22] J. Ibáñez, E. Tarhan, A. K. Ramdas, S. Hernández, R. Cuscó, L. Artús, M. R. Melloch, and M. Hopkinson, Phys. Rev. B **69**, 075314 (2004).
[23] A. S. Barker, Phys. Rev. **132**, 1474 (1963).
[24] D. Pastor, J. Ibáñez, R. Cuscó, L. Artús, G. González-Díaz, and E. Calleja, Semicond. Sci. Technol. **22**, 70 (2007).
[25] T. Dumelow and D. R. Tilley, J. Opt. Soc. Am. A **10**, 633 (1993).
[26] L. Bergman, M. Dutta, C. Balkas, R. F. Davis, J. A. Christman, D. Alexson, and R. J. Nemanich, J. Appl. Phys. **85**, 3535 (1999).

Early View publication on www.interscience.wiley.com
(issue and page numbers not yet assigned;
citable using Digital Object Identifier – **DOI**)

phys. stat. sol. (b), 1–4 (2008) / **DOI** 10.1002/pssb.200743398

physica status solidi b
www.pss-b.com
basic solid state physics

Phonons in $B_xGa_{1-x}N$/GaN epilayers studied by means of UV Raman scattering

R. Cuscó[1], E. Alarcón-Lladó[1], J. Ibáñez[1], L. Artús[*,1], S. Gautier[2], and A. Ougazzaden[3]

[1] Institut Jaume Almera (CSIC), C. Lluís Solé i Sabarís s.n., 08028 Barcelona, Spain
[2] Laboratoire Matériaux Optiques, Photonique et Systèmes, UMR CNRS 7132, Université de Metz and SUPELEC, 2 rue E. Belin, 57070 Metz, France
[3] International Joint Research Unit "UMI 2958 GT–CNRS", Georgia Institute of Technology, School of Electrical and Computer Engineering, Atlanta, USA/Georgia Tech Lorraine (GTL), 2–3 rue Marconi, 57070 Metz, France

Received 24 July 2007, revised 26 September 2007, accepted 25 October 2007
Published online 15 January 2008

PACS 78.30.Fs, 78.66.Fd

[*] Corresponding author: e-mail lartus@ija.csic.es, Phone: +34-93-4095410, Fax: +34-93-4110012

We present UV Raman scattering measurements on $B_xGa_{1-x}N$ epilayers with boron composition up to 3.6%. The resonant enhancement of the longitudinal optical modes allows us to detect multiphonon scattering by A_1(LO) modes. For low boron compositions ($\lesssim$2%), both the E_2 and the A_1(LO) modes show a consistent frequency increase with boron composition due to alloying effects. Higher disorder and expansive strain are observed in alloys with higher boron content.

1 Introduction During the past few years GaN and related group-III nitrides have attracted considerable interest for their applications in light-emitting devices operating in the green, blue, and ultraviolet spectral regions. Alloying in group-III nitrides permits the band gap of the active layer to be adjusted in a wide range of energies. Novel wide band gap semiconductor alloys are being investigated as the demand of optoelectronic devices operating in the UV spectral range increases in applications such as optical storage, ophthalmic surgery, nanosurgery, and sterilization. Adding boron to GaN is expected to increase its band gap into the UV [1, 2], and if sufficient boron is incorporated, the alloy can be lattice matched with AlN and SiC substrates. However, the large lattice mismatch between GaN and BN results in considerable internal strain, making it difficult to grow BGaN with an appreciable boron concentration before phase separation occurs [3]. Successful growth of $B_xGa_{1-x}N$ alloys is achieved only for very low boron contents, typically $x \lesssim 3\%$ [4–6]. Since the formation enthalpy for $B_xGa_{1-x}N$ is similar in trend and magnitude to that of $GaAs_{1-x}N_x$, it has been suggested that high-quality BGaN single crystals with 5% boron may be possible [2].

In this work, we present a UV Raman scattering study of the dependence on boron content of the phonons of the BGaN alloy. While Raman spectroscopy has been widely used to investigate the lattice dynamics, the local composition, and the strain state of group-III nitrides [7], to date no Raman data on BGaN are available. Our Raman measurements confirm the incorporation of boron to the GaN lattice in samples previously characterized by means of high resolution X-ray diffraction (HRXRD) and secondary ion mass spectrometry (SIMS) measurements [4]. For low boron compositions, a consistent trend of phonon frequency blue shift with increasing B content of the alloy is observed. While the A_1(LO) mode maintains this trend up to the highest boron concentrations studied in this work, the blue shift of the E_2 mode markedly drops for boron concentrations of 3% and higher. We discuss this behavior in connection with the higher inhomogeneity in boron distribution in the samples with the highest boron content.

2 Experiment The BGaN layers used in this study were grown by metal-organic vapor-phase epitaxy (MOVPE) on 4 μm thick (0001) GaN templates on sapphire substrates. A 200 nm GaN buffer was grown prior to

the BGaN epilayers, with typical thicknesses between 120 nm and 350 nm. A thick ($d \approx 1.2$ μm) epilayer was also grown for comparison. The boron composition of the samples was estimated from HRXRD measurements to be 1.1%, 1.6%, 1.75%, 1.9%, 2.16%, 3.0%, and 3.6%. Details of the growth procedure, as well as structural and compositional characterization by means of HRXRD and SIMS, are given in Ref. [4].

Unpolarized Raman scattering measurements were carried out at room temperature in backscattering configuration on a (0001) face. The 325 nm line of a He–Cd laser was used as the excitation source. The scattered light was analyzed with a Jobin-Yvon T64000 spectrometer equiped with a LN_2-cooled charge-coupled device (CCD) detector, using the single-stage configuration with a notch filter. BGaN epilayer thicknesses were kept below the critical thickness to ensure smooth surface morphology [4]. Since BGaN is transparent to visible light, UV excitation had to be employed for such thin epilayers in order to enable the detection of Raman scattering signal limited to the BGaN epilayers.

3 Results and discussion The energy of the 325 nm excitation is ≈0.4 eV above the GaN band-gap energy and thus is strongly absorbed. Using the absorption coefficient of GaN [8], we estimate that the Raman signal comes from a surface layer of about 40 nm, which is well within the studied epilayer. In addition, the Raman spectra excited with this line are under near-resonant conditions, which leads to a strong enhancement of the A_1(LO) peaks through the Fröhlich mechanisms and allows us to observe multiphonon scattering. This is illustrated by the spectrum shown in Fig. 1, corresponding to the sample with 1.6% boron composition, where strong overtones of the A_1(LO) mode can be seen. The steeply increasing background observed at higher wavenumbers corresponds to the band-to-band emission of the GaN buffer, which acts as recombination well for the photoexcited carriers. Weak satellites are observed on either side of the mA_1(LO) peaks. These have been previously assigned to $E_2^{low} + mA_1(LO)$ and $E_2^{high} + mA_1(LO)$ combinations [9]. The weak peak observed at about 565 cm^{-1} corresponds to the E_2^{high} mode. In Fig. 2 we display the Raman spectra of three BGaN layers with increasing boron content, where the allowed E_2 and A_1(LO) modes can be seen. A narrow E_2 peak is observed at 564.7 cm^{-1} in the sample with the lowest boron content (1.1%). Note that the E_2 frequency measured in this sample is noticeably lower than the value of 569 cm^{-1} reported for high-quality thick GaN epilayers [10]. This frequency shift indicates the presence of a residual biaxial tensile strain field in the epilayer and/or the existence of point defects that give rise to an expansive hydrostatic strain [11].

As the boron content is increased, the E_2 peak significantly broadens, reflecting a higher degree of disorder in the BGaN layer. Also, the E_2 Raman peak tends to shift to higher frequencies for increasing boron concentration. Since boron incorporation reduces the alloy lattice parameter, it is expected to increase the tensile strain in the layers with higher boron content. This would lead to a redshift of the E_2 mode, contrary to the trend observed in our spectra, which indicates that alloying is the main effect driving the E_2 mode to higher frequencies. As can be seen in Fig. 2, the A_1(LO) mode, which is strongly enhanced by near-resonance Fröhlich mechanisms, also shifts to higher frequencies with increasing boron concentration. However, the increase in full width at half maximum (FWHM) is much less apparent than in the case of the E_2 mode. We shall discuss this behavior below. The data on the peak frequency and FWHM of the E_2 and A_1(LO) peaks are collected in Fig. 3 for all the epilayers studied. Note that the open symbols represent the data from the thick epilayer. As can be seen in Fig. 3(a), the E_2 FWHM increases roughly linearly for the set of thin epilayers, and it becomes larger by a factor of three when the boron composition increases from 1.1% up to 3.6%. In contrast, the FWHM of the A_1(LO) peak increases only by ≈3 cm^{-1} over the same range of boron composition [see Fig. 3(c)]. This suggests that, whereas the E_2 mode is probing the increased

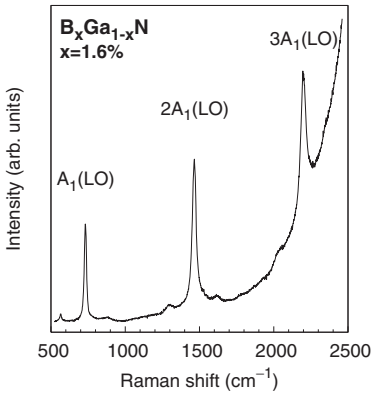

Figure 1 Multiphonon scattering by A_1(LO) modes in $B_xGa_{1-x}N$ for $x = 0.016$ under near-resonant conditions.

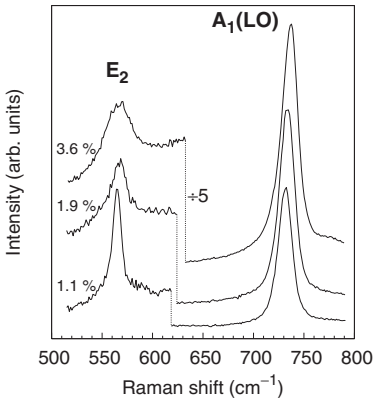

Figure 2 Room temperature Raman spectra of BGaN epilayers for increasing boron composition.

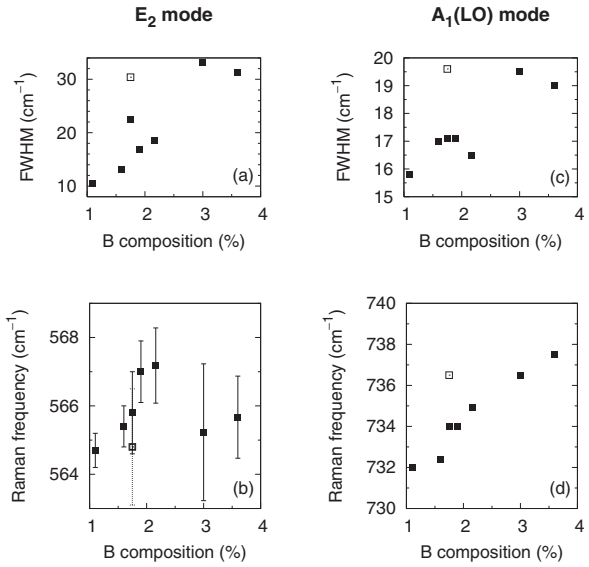

Figure 3 Frequency and full width at half maximum of the E_2 and A_1(LO) modes of BGaN for a range of boron compositions. The open squares correspond to the 1.2 μm thick epilayer.

average disorder of the layer, the A_1(LO) signal mainly arises from more homogenous regions, probably because of fluctuations in the boron composition and in the strain fields that may locally alter the band gap energy. Such composition fluctuations are known to give rise to selective excitation of the strongly resonant A_1(LO) mode in InGaN [12, 13], and could also explain the lower sensitivity to alloy disorder of the A_1(LO) peak observed in the BGaN alloys.

As to the mode frequencies, we can see from Fig. 3(b) that the E_2 mode exhibits a trend of increasing frequency for boron compositions up to 2.16%, and then falls back to values found in samples with lower boron content. Note, however, the large error bars associated with the uncertainty of determining the frequency of the weak, broad E_2 peak on a raising background. It is known that the incorporation of higher boron concentrations is difficult [5]. Then, the samples with the highest boron concentration (3.0% and 3.6%) probably contain substantial composition inhomogeneities and a high density of defects, and this may explain the low E_2 frequencies observed in these samples. On the one hand, the E_2 peak may contain contributions from regions with different boron compositions, which leads to the broadening of this peak. In addition, the increased disorder in the layers with high boron content partially relaxes the $k = 0$ selection rule, and the participation of $k \neq 0$ modes further broadens the E_2 peak toward low frequencies. On the other hand, the high density of defects may induce a hydrostatic expansive strain in the layers that contributes to lower the E_2 frequency. In contrast, as can be seen from Fig. 3(d), the A_1(LO) frequency consistently increases with the boron composition. As discussed above, this behaviour may be explained by the presence of regions with higher boron incorporation which are selectively excited in near-resonance conditions. Since the Raman resonance is expected to be enhanced for increasing boron compositions, as corroborated by the intensity increase of the A_1(LO) peak with boron content (see Fig. 2), the Raman signal from the domains containing the higher boron composition in those regions with significant composition fluctuations should dominate the A_1(LO) peak. The results shown in Fig. 3(d) indicate that the boron concentration in these regions increases with the boron content of the alloy.

Finally, we comment on the data from the thick BGaN layer (open squares in Fig. 3). The growth of BGaN epilayers beyond a critical thickness results in enhanced surface roughness and the appearance of cracks in the surface [4], so a lower crystalline quality of these samples is expected. Indeed, both the E_2 and A_1(LO) modes of this sample display FWHM values which are substantially higher than those observed in the thin epilayer of the same composition. It is interesting to note that the E_2 frequency of the thick sample is lower than that of the corresponding thin epilayer, whereas the opposite applies for the A_1(LO) mode [see Fig. 3(b) and (d)]. In fact, the frequency and width of both modes in the thick sample are similar to those observed in the epilayer with the highest boron compositions. As in that case, the reduction of the E_2 frequency suggests the incorporation of defects that contribute to the expansion of the lattice, whereas the increase of the A_1(LO) frequency may be indicative of the presence of regions with higher boron content.

4 Conclusion We have carried out a Raman scattering study of the composition dependence of the E_2 and A_1(LO) phonons in BGaN. For low boron compositions ($\lesssim$2%), both modes exhibit a parallel frequency increase as a result of alloying effects. For higher boron compositions, the E_2 peak broadens substantially and its frequency falls back to values similar to those of low boron composition samples. This suggests the presence of a higher degree of disorder and expansive strain associated with the incorporation of defects. Contrary, the A_1(LO) frequency maintains its trend of increasing frequency with boron composition, possibly due to selective excitation of regions with higher boron content.

Acknowledgements This work has been supported by the Spanish Ministry of Education and Science (Contract No. MAT2004-0664 and Ramón y Cajal Program).

References

[1] T. Honda, M. Shibata, M. Kurimoto, M. Tsubamoto, J. Yamamoto, and H. Kawanishi, Jpn. J. Appl. Phys. **39**, 2389 (2000).
[2] L. Escalanti and G. L. W. Hart, Appl. Phys. Lett. **84**, 705 (2004).
[3] L. K. Teles, L. M. R. Scolfaro, J. R. Leite, J. Furthmüller, and F. Bechstedt, Appl. Phys. Lett. **80**, 1177 (2002).

[4] A. Ougazzaden, S. Gautier, C. Sartel, N. Maloufi, J. Martin, and F. Jomard, J. Cryst. Growth **298**, 316 (2007).
[5] V. K. Gupta, C. C. Wamsley, M. W. Koch, and G. W. Wicks, J. Vac. Sci. Technol. B **17**, 1246 (1999).
[6] T. Honda, M. Kurimoto, M. Shibata, and H. Kawanishi, J. Lumin. **87–89**, 1274 (2000).
[7] H. Harima, J. Phys.: Condens. Matter **14**, R967 (2002).
[8] J. F. Muth, J. H. Lee, I. K. Shmagin, R. M. Kolbas, H. C. Casey, B. P. Keller, U. K. Mishra, and S. P. DenBaars, Appl. Phys. Lett. **71**, 2572 (1997).
[9] D. Pastor, J. Ibáñez, R. Cuscó, L. Artús, G. González-Díaz, and E. Calleja, Semicond. Sci. Technol. **22**, 70 (2007).
[10] T. Azuhata, T. Sota, K. Suzuki, and S. Nakamura, J. Phys.: Condens. Matter **7**, L129 (1995).
[11] C. Kisielowski, J. Krüger, S. Ruvimov, T. Suski, J. W. Ager III, E. Jones, Z. Liliental-Weber, M. Rubin, E. R. Weber, M. D. Bremser, and R. F. Davis, Phys. Rev. B **54**, 17745 (1996).
[12] D. Behr, J. Wagner, A. Ramakrishnan, H Oblob, and K.-H. Bachem, Appl. Phys. Lett. **73**, 241 (1998).
[13] S. Hernández, R. Cuscó, D. Pastor, L. Artús, K. P. O'Donnell, R. W. Martin, I. M. Watson, Y. Nanishi, and E. Calleja, J. Appl. Phys. **98**, 013511 (2005).

IOP PUBLISHING SEMICONDUCTOR SCIENCE AND TECHNOLOGY

Semicond. Sci. Technol. **22** (2007) 1145–1150 doi:10.1088/0268-1242/22/10/011

Raman scattering study of undoped and As-doped GaN grown with different III/V ratios

J Ibáñez[1], D Pastor[1], E Alarcón-Lladó[1], R Cuscó[1], L Artús[1], S V Novikov[2] and C T Foxon[2]

[1] Institut Jaume Almera, Consell Superior d'Investigacions Científiques (CSIC), Lluís Solé i Sabarís s.n., 08028 Barcelona, Catalonia, Spain
[2] School of Physics and Astronomy, University of Nottingham, Nottingham NG7 2RD, UK

Received 31 January 2007, in final form 26 July 2007
Published 7 September 2007
Online at stacks.iop.org/SST/22/1145

Abstract
We have used Raman scattering to investigate a series of undoped and As-doped GaN epilayers grown on sapphire substrates by plasma-assisted molecular beam epitaxy with different Ga-to-N ratios. We find that the frequency of the E_{2h} phonon mode of GaN is very sensitive to the Ga-to-N ratio used to grow both types of samples, which may be attributed to strain effects arising from the different growth conditions. We observe Raman signatures corresponding to the formation of submicron cubic domains in some of the spectra of the As-doped samples. We discuss the origin of a broad band located at 232 cm^{-1} that appears in both the undoped and the As-doped epilayers. We speculate that this band, reported in previous Raman studies on As-doped and Bi-doped GaN, may be attributed to the formation of Ga clusters.

1. Introduction

Group-III nitride semiconductors are currently being used to fabricate a wide variety of optical and electronic devices such as blue-ultraviolet light emitting diodes (LEDs) and field effect transistors (FETs) [1, 2]. The growth of high-quality material is essential to improve the performance of the GaN-based applications. The suitability of molecular beam epitaxy (MBE) to fabricate high-quality layers of group-III nitrides was already demonstrated in the last decade [3]. A great number of studies dealing with the MBE growth of GaN have been carried out over the last few years with different purposes: (i) to optimize the growth conditions; (ii) to determine the effect of different sources of N on the properties of the GaN epilayers; (iii) to find the optimal substrates; (iv) to investigate how the growth is affected by the presence of interlayers (for instance AlN or AlGaN buffer layers).

Both the growth temperature and the flux of species are crucial for MBE growth, and therefore they have to be carefully adjusted to obtain high-quality material. It has been shown that the III/V ratio strongly affects the morphology and the optical properties of MBE-grown wurtzite (w) GaN [4–7]. While nanocolumnar growth is observed under N-rich conditions [8], Ga droplets are formed in the Ga-rich regimes [6]. The III/V ratio also affects the quality of cubic (c) GaN and the transition between w-GaN and c-GaN [9].

The III/V ratio plays a very important role in the incorporation of impurities during the growth of semiconductor materials. For instance, in GaN films grown by plasma-assisted MBE (PA-MBE) with an additional As flux it has been observed that, depending on the Ga-to-N flux ratio, there is a transition from As-doped w-GaN, showing strong blue emission at 2.6 eV, to formation of GaNAs alloys, which results in a redshifted band-gap edge [10–12]. The interest in As-doped GaN is manifold: (i) arsenic acts as a surfactant and promotes the formation of the cubic phase during the growth of GaN [13]; (ii) the strong blue emission observed at room temperature in As-doped GaN might be used in optoelectronic devices working in the blue region [14, 15]; (iii) a large negative bowing in the energy band gap of $GaN_{1-x}As_x$ arising from valence-band hybridization has been observed for $x < 0.06$ [16, 17]. Such hybridization has been ascribed to the interaction between localized As states and the extended valence-band states of the GaN matrix. This is similar to what is observed in dilute nitrides (i.e. $GaAs_{1-y}N_y$ and $In_{1-x}Ga_xAs_{1-y}N_y$), where the N localized level interacts with the conduction band states of GaAs [18].

0268-1242/07/101145+06$30.00

Table 1. List of samples studied in this work. Samples A1 to A3 correspond to undoped GaN, while samples B1 to B7 were grown with an additional As flux ($\Phi_{As} \sim 4 \times 10^{-6}$ mbar). The flux of Ga and N_2, Φ_{Ga} and Φ_{N_2}, together with the Ga/N and As/Ga flux ratios, are listed for all samples. The last column displays the thickness of the epilayers.

Sample	Φ_{Ga} (mbar)	Φ_{N_2} (mbar)	Φ_{Ga}/Φ_{N_2}	Φ_{As}/Φ_{Ga}	Thickness
A1	8.0×10^{-7}	1.9×10^{-5}	1/24	0	$\sim$1 μm
A2	8.0×10^{-7}	3.6×10^{-5}	1/45	0	$\sim$1 μm
A3	8.0×10^{-7}	1.3×10^{-4}	1/162	0	$\sim$1 μm
B1	1.3×10^{-6}	3.0×10^{-5}	1/23	3	970 nm
B2	7.9×10^{-7}	3.1×10^{-5}	1/39	7	950 nm
B3	4.8×10^{-7}	3.1×10^{-5}	1/64	10	790 nm
B4	2.9×10^{-7}	3.0×10^{-5}	1/103	14	550 nm
B5	1.6×10^{-7}	3.0×10^{-5}	1/187	19	430 nm
B6	9.6×10^{-8}	3.2×10^{-5}	1/333	53	370 nm
B7	3.3×10^{-8}	3.1×10^{-5}	1/939	82	220 nm

Raman scattering is a very powerful, non-destructive technique that provides reliable information about the crystalline quality, the strain state and the composition of semiconductor materials and structures. Raman scattering is widely used to study GaN and related compounds [19]. In the present work we use Raman scattering to study the effect of the III/V ratio on the properties of two different sets of GaN thin films grown by PA-MBE on sapphire substrates: undoped GaN epilayers and As-doped GaN epilayers. We find that the frequency of the E_{2h} phonon mode of GaN in both types of samples is very sensitive to the III/V ratio, which indicates that the strain state of the epilayers is substantially affected by the growth conditions. We tentatively assign a feature that emerges at 232 cm^{-1} in some of the spectra to the formation of Ga clusters. In the case of the As-doped GaN epilayers, the Raman spectra reveal the presence of cubic domains in some of the samples. Our results show that Raman scattering is a well-suited tool to obtain valuable information for the optimization of the growth conditions of GaN epilayers and related compounds.

2. Experiment

The two sets of GaN epilayers studied in this work were grown by PA-MBE on sapphire substrates. Details of the growth procedure can be found elsewhere [11, 12]. Three undoped GaN epilayers (samples A1 to A3) and seven As-doped GaN epilayers (samples B1 to B7) were grown at 800 °C with different Ga-to-N flux ratios. All the undoped samples were grown with a constant Ga flux $\Phi_{Ga} \sim 8.0 \times 10^{-7}$ mbar (beam equivalent pressure, BEP), whereas the As-doped GaN epilayers were grown with a constant N_2 flux $\Phi_{N_2} \sim 3 \times 10^{-5}$ mbar and an intentional arsenic flux $\Phi_{As} \sim 4 \times 10^{-6}$ mbar. The layer characteristics of the samples can be found in table 1. It must be noted that the growth time for all the samples was the same (3 h). Thus, given that the growth rate is mainly determined by the Ga flux, the thickness of the GaN epilayers is larger for the samples grown with higher Ga fluxes. In the last column of table 1 we display the thickness of the epilayers studied in this work. While the thickness of the undoped films was estimated from the growth conditions and previous x-ray diffraction (XRD) measurements performed on similar samples, the thickness of the As-doped epilayers was obtained by optical reflectance measurements.

SIMS measurements were carried out in order to determine the As concentration of GaN samples similar to those studied here [10]. In that work, it was shown that the maximum concentration of arsenic that can be incorporated into GaN for this type of samples and growth conditions is around 6×10^{19} cm^{-3}. The SIMS experiments revealed that the concentration of As in the N-rich samples is around one order of magnitude higher than that found in the Ga-rich epilayers [10].

Room-temperature micro-Raman measurements were performed using a Jobin-Yvon T64000 spectrometer equipped with a liquid-nitrogen cooled charge coupled device (CCD) detector. The 514.5 nm line of an Ar^+ laser was used as an excitation source. The scattered light was collected in the $z(x, x)\bar{z}$ geometry through a $\times$100 objective. The confocal micro-Raman set-up allows a spatial resolution of $\sim$1 μm with a probing depth of $\sim$1 μm.

3. Results and discussion

3.1. Undoped GaN epilayers

It is well known that the III/V ratio affects the morphology, the crystalline quality, the optical properties and the nature of the electrically active defects of GaN. For undoped GaN grown by PA-MBE on sapphire, there is an optimum Ga-to-N flux ratio that gives rise to films with a good morphology and the highest room-temperature band-edge luminescence efficiency [20].

Figure 1 shows Raman spectra from three undoped GaN/sapphire epilayers grown by PA-MBE with different III/V ratios (samples A1 to A3). All the spectra display two main peaks corresponding to the E_{2h} and A_1(LO) modes of w-GaN, which are allowed in the Raman configuration used for the experiments. To facilitate the comparison of the spectra, we have normalized the intensity of the E_{2h} and A_1(LO) peaks in the spectra of samples A2 and A3 to their respective intensities in sample A1.

Whereas the E_{2h} peak is virtually identical for the Ga-rich sample (A1) and for the sample grown with an intermediate III/V ratio (A2), the E_{2h} peak is broadened and shifted to lower frequencies in the case of the N-rich sample (A3). The increased width of the E_{2h} peak observed for this sample

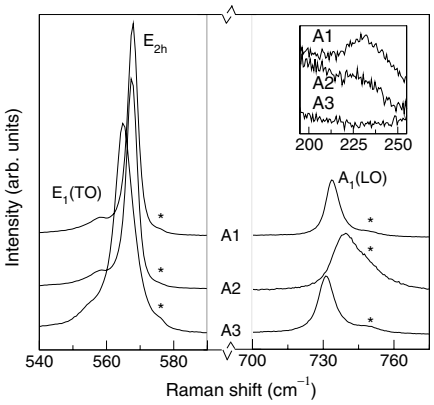

Figure 1. Raman spectra of three w-GaN epilayers grown by PA-MBE with different Ga-to-N ratios (samples A1 to A3). The inset shows the low-frequency spectral region, where a Raman feature at 232 cm^{-1} can be observed in some of the spectra. The peaks marked with an asterisk correspond to the sapphire substrate.

indicates a reduced crystalline quality, in agreement with the very weak PL emission of epilayers grown under similar conditions [20]. Given that GaN grown on sapphire is compressively strained [21], the redshift of the E_{2h} mode that we observe for the N-rich sample may be attributed to strain relaxation effects. Consequently, a higher density of dislocations is expected in this sample. Also, it should be noted that, under N-rich conditions, the PA-MBE growth of GaN is columnar [20]. Under such growth conditions, Sanchez-Garcia *et al* observed completely relaxed needles in GaN samples grown by PA-MBE on Si(111), as deduced from PL and x-ray diffraction data [7].

While the E_{2h} peaks are basically identical for samples A1 and A2, the A_1(LO) peaks are sizeably different for these two epilayers. In contrast, the A_1(LO) mode of sample A3 is only slightly redshifted with respect to that of sample A1, similarly to their respective E_{2h} peaks. The fact that the A_1(LO) peak for sample A2 is broadenend and shifted to higher frequencies with respect to the A_1(LO) peak of sample A1 may be attributed to the presence in sample A2 of free-carriers, whose collective excitations couple to the polar A_1(LO) phonon mode giving rise to an LO-plasmon coupled mode (LOPCM) [19]. Remarkably, the Ga-to-N flux ratio used to grow sample A2 is near to optimum conditions, giving rise to the highest room-temperature band-edge PL emission [20]. Given that the crystalline quality of samples A1 and A2 is similar, as revealed by the width of the E_{2h} peaks in the Raman spectra, we speculate that the growth under Ga-rich conditions introduces a sizeable density of non-radiative defects that eliminate the background electron concentration, giving rise to a weaker PL emission as reported in [20]. In the case of sample A3, no free carriers are present as a consequence of the poorer crystalline quality of this epilayer, in agreement with the broader E_{2h} peak observed for this sample. As expected, the A_1(LO) peak of sample A3 is slightly broader than that of sample A1.

Next, we would like to pay special attention to a feature that appears in the low-frequency region of the Raman spectra of sample A1 and, to a lower extent, in the spectra of sample A2 (see inset of figure 1). Note that this band, located at 232 cm^{-1}, does not appear in the spectra of the N-rich epilayer (sample A3). A similar feature was previously observed in Raman spectra of As-doped GaN [22] and of Bi-doped GaN [23], and was attributed to either As or Bi impurity modes. Given that this peak appears in the spectra of undoped GaN, it is clear that it is not related to As or Bi. On the other hand, it must be borne in mind that no disorder-activated modes appear in this frequency region in the Raman spectra of ion-beam implanted GaN [24]. Siegle *et al* [25] observed this feature in As-doped w-GaN and in c-GaN grown on GaAs and assigned it to a defect cluster. Such assignment was performed on the basis of the broad linewidth of this feature in comparison to that of the As-related impurity modes [25]. Since we observe that the intensity of the band at 232 cm^{-1} increases with increasing Ga flux (see inset of figure 1), and given that the frequency of the most prominent peak of solid Ga is found at 246 cm^{-1} [26], we speculate that this band may be related to the formation of Ga clusters in GaN. Then, the appearance of this feature in the spectra of As-doped and of Bi-doped GaN would indicate that a substantial fraction of As or Bi impurities, which are isoelectronic to N and therefore are expected to incorporate mainly on N sites, tend to incorporate on Ga sites. Such a result would be partly supported by the theoretical results of Van de Walle and Neugebauer [27], who studied the behavior of As impurities in GaN and found that the As_{Ga} impurity behaves as a deep donor with a very low formation energy comparable to that of As_N even under n-type conditions. More investigations are required to confirm that the 232 cm^{-1} band corresponds to the formation of Ga clusters.

Besides the E_{2h} and A_1(LO) peaks, an additional Raman feature appears in the low-frequency tail of the E_{2h} peak for all samples (see figure 1). For the Ga-rich epilayer and the intermediate sample, it is clear that such a feature, located at ∼558 cm^{-1}, corresponds to the forbidden E_1(TO) mode. In the case of the N-rich sample, this peak is located at ∼553 cm^{-1}. While the observed frequency is close to the TO frequency of cubic GaN, we believe that this peak actually corresponds to the E_1(TO) mode of w-GaN which, similarly to the E_{2h} mode, is shifted to lower frequencies due to strain relaxation effects. This is supported by the fact that no optical emission corresponding to the cubic phase (∼3.2 eV) [28] appears in the PL spectra of GaN epilayers grown under the same conditions as those used to grow our N-rich sample (see [20]). Also, the transition from w-GaN to c-GaN is usually observed at higher Ga fluxes, which further supports the assignment of the 553 cm^{-1} peak to the forbidden E_1(TO) mode of w-GaN.

3.2. As-doped GaN epilayers

The III/V ratio plays an important role in the incorporation of As into w-GaN [10–12]. In figure 2 we show the Raman spectra of samples B1, B3 and B5, which were grown with different Ga-to-N ratios and an additional As flux (see table 1). These epilayers have different thicknesses because they were grown with different Ga fluxes (see table). Thus, for comparison purposes, we have rescaled the intensity of the E_{2h} peaks that appear in figure 2. The figure clearly shows that,

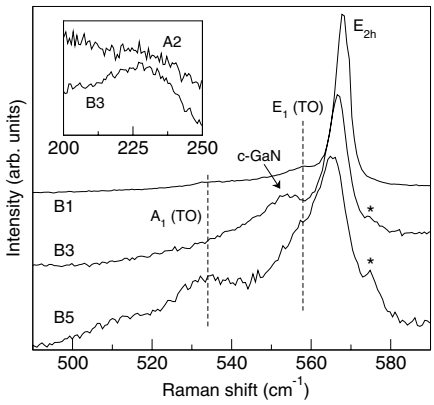

Figure 2. Raman spectra of three As-doped w-GaN epilayers grown by PA-MBE with different Ga-to-N ratios (samples B1, B3 and B5). The inset shows that the band at 232 cm^{-1} is more intense when the samples are grown with an additional As flux. The spectra of the inset correspond to samples A2 (undoped GaN) and B3 (As-doped GaN). The peaks marked with an asterisk correspond to the sapphire substrate.

similarly to the undoped epilayers, the E_{2h} peak undergoes a downward frequency shift with increasing As/Ga ratio. These shifts may arise from two different reasons: (i) a strain relaxation induced by the growth conditions, as in the case of the undoped samples; (ii) the effect of As incorporation into the GaN lattice. We will discuss about the origin of these shifts later on.

Figure 2 also shows that the E_{2h} peak progressively broadens with increasing As/Ga ratio, which indicates that the presence of As reduces the crystalline quality of the samples. The spectrum of sample B5 also displays a broad band at ∼533 cm^{-1} that can be assigned to the forbidden A_1(TO) mode of GaN. The increased intensity of this feature relative to the E_{2h} peak provides a further indication of the loss of crystalline quality induced by As. In the low-frequency tail of the E_{2h} peak of this curve (∼558 cm^{-1}), a broad feature that can mainly be attributed to forbidden E_1(TO) modes activated by disorder can also be observed. A weaker E_1(TO) feature appears in the spectrum of the sample grown with the lowest As/Ga ratio (sample B1).

An additional broad band, located at ∼555 cm^{-1}, can be observed in the spectrum of sample B3. This feature cannot be attributed to a strained E_1(TO) mode of w-GaN since it displays a sizable redshift relative to the E_1(TO) modes observed in the spectra of both Ga-rich epilayers (B1) and N-rich epilayers (B5). Given that the E_{2h} mode is highly sensitive to strain and it shows a monotonic shift as the As/Ga ratio increases, we may assume that the strain state of sample B3 lies between those of samples B1 and B5. Therefore the E_1(TO) frequency in sample B3 is also expected to be found between those observed in samples B1 and B5, and the significantly lower frequency of the additional feature in B3 rules out its attribution to the E_1(TO) mode. We assign the feature at ∼555 cm^{-1} to the TO mode of c-GaN, which is supported by the results of previous works on As-doped GaN films grown by PA-MBE, where the presence of c-GaN was confirmed by means of XRD measurements [11, 29]. As a result of those studies, it was concluded that the cubic phase predominantly exists at the substrate–epilayer interface of the PA-MBE grown samples [29]. The findings of the present Raman study are similar to those recently obtained in Bi-doped GaN epilayers grown by PA-MBE [23].

The As flux also affects the feature located at 232 cm^{-1} that we observed in the spectra of the undoped epilayers (inset of figure 1) and which we tentatively attributed to Ga clusters. In the inset of figure 2 we show the low-frequency region of the Raman spectra of samples A2 and B3. The As-doped sample (B3) was grown with a Ga-to-N ratio slightly lower than that used to grow the undoped sample (A2), and therefore a lower density of Ga clusters would be expected for this sample. Even so, the plot shows that the broad feature at 232 cm^{-1} is more pronounced in the spectrum of the As-doped sample. When we compare the spectra of the As-doped samples grown under Ga-rich conditions (samples B1 to B3) with the spectra of the undoped samples grown with similar III/V ratios (samples A1 and A2), we find that the feature at 232 cm^{-1} is consistently more intense in the As-doped samples. This result supports the idea that a significant fraction of As impurities may be incorporating into Ga sites. As in the case of the N-rich undoped epilayer, we do not observe the 232 cm^{-1} band in any of the As-doped samples grown under N-rich conditions (samples B4 to B7).

In order to shed additional light on the origin of this feature, we first note that Foxon *et al* [10–12], in several studies on the incorporation of As into GaN epilayers similar to the samples studied here, concluded that the transition from As-doped GaN to formation of GaNAs alloys (i.e., the incorporation of As on the N sites) takes place under N-rich conditions. For epilayers grown with an additional As flux and Ga-rich conditions, the PL, x-ray and SIMS data seem to suggest that As is incorporated predominantly in the Ga site [10], which could favor the formation of Ga clusters and account for the intensity increase of the 232 cm^{-1} peak that appears in the As-doped samples. Similar arguments could be applied to Bi-doped GaN. As already discussed, the incorporation of As on Ga sites might be favored by the relatively low formation energy of As_{Ga} impurities [27], which might be a reason for the difficulty in producing GaNAs alloys. The fact that the growth of the alloy by PA-MBE seems to require low Ga/N ratios could explain the absence of the 232 cm^{-1} band in the spectra of the As-doped samples grown under N-rich conditions, since Ga clusters would not be formed in these samples. More investigations are required to unambiguously ascertain the origin of the Raman band at 232 cm^{-1}, to understand the role of the III/V ratio on the growth of the GaNAs alloy by PA-MBE and to optimize the incorporation of As on the N sites.

Next, we discuss the downward frequency shift of the E_{2h} mode observed both in the undoped and in the As-doped GaN epilayers with decreasing Ga/N ratios. In figure 3 we plot the frequency of the E_{2h} mode for all the samples studied in this work. The figure illustrates the decrease of the E_{2h} phonon frequency with decreasing Ga/N ratio, which is of up to ∼3 cm^{-1} between the N-rich and Ga-rich ends of the graph. In the case of the As-doped samples, the fact that the thickness of the epilayers is different, which is due to the different Ga fluxes used to grow these samples (see table 1), could lead one

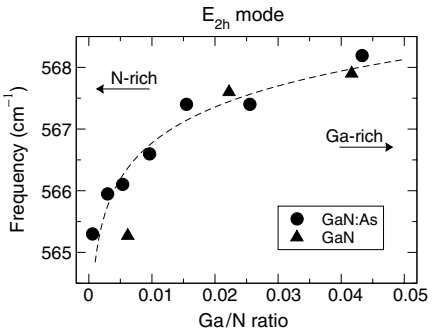

Figure 3. Frequency of the E_{2h} mode for the undoped and As-doped GaN samples studied in this work as a function of the Ga-to-N ratio used to grow the epilayers.

to conclude that the shifts of the E_{2h} mode may be originated by a thickness effect. However, since GaN grown on sapphire is compressively strained, and given that the strain relaxation is expected to be higher for thicker epilayers [30], a downward frequency shift of the E_{2h} mode with increasing thickness (i.e, with increasing Ga flux) should take place, which is contrary to our observations. Figure 3 shows that the frequency behavior of the E_{2h} mode of the undoped and of the As-doped samples is very similar. Thus, we conclude that in both types of samples the shifts of the E_{2h} mode can be mainly attributed to strain relaxation effects due to the different growth conditions. A higher density of dislocations is expected in the more relaxed samples (i.e., in the samples grown with the lowest Ga-to-N ratios).

The frequency of the E_{2h} mode for the undoped GaN sample grown with the lowest Ga/N ratio (sample A3, grown with $\Phi_{Ga}/\Phi_{N_2} = 6.2 \times 10^{-3}$) is slightly lower (about 0.8 cm^{-1}) than that of the As-doped epilayer grown with similar III/V ratios (sample B5, see figure 3). It should be noted that the thickness of these two samples differs significantly as a consequence of the different Ga fluxes used to grow them. Therefore, the higher E_{2h} frequency found for sample B5 is probably due to the fact that the residual compressive strain is more relaxed in the thicker A3 sample. However, the possibility that the growth mode and the subsequent final strain state of the As-doped epilayers is influenced by the presence of the additional As flux cannot be ruled out.

4. Conclusions

We have used Raman scattering to investigate the effect of the III/V ratio on the crystal quality and the strain properties of undoped and of As-doped GaN thin films grown by PA-MBE on sapphire. We have shown that in both types of samples the E_{2h} phonon mode of GaN displays a progressive downward frequency shift with decreasing Ga/N ratio that can be attributed to differences in the final strain state of the samples, suggesting that the density of dislocations is higher in the samples grown under N-rich conditions. We observe a band at 232 cm^{-1} in the spectra of the undoped samples that was related in previous works to As and Bi impurities. Based on the intensity dependence of this band on the Ga, N and As fluxes used to grow the epilayers, we tentatively assign it to the formation of Ga clusters. Signatures of the formation of submicron cubic domains have also been detected in some of the As-doped epilayers.

Acknowledgments

Work supported by the Spanish Ministry of Science and Technology (contract MAT2004-0664 and Ramon y Cajal Programme) and by the British EPSRC.

References

[1] Orton J W and Foxon C T 1998 *Rep. Prog. Phys.* **61** 1
[2] Pearton S J, Zolper J C, Shul R J and Ren F 1999 *J. Appl. Phys.* **86** 1
[3] Jain S C, Willander M, Narayan J and Van Overstraeten R 2000 *J. Appl. Phys.* **87** 965
[4] Cho S H, Hata K, Maruyama T and Akimoto K 1997 *J. Cryst. Growth* **173** 260
[5] Tarsa E J, Heying B, Wu X H, Fini P, DenBaars S P and Speck J S 1997 *J. Appl. Phys.* **82** 5472
[6] Heying B, Averbeck R, Chen L F, Haus E, Riechert H and Speck J S 2000 *J. Appl. Phys.* **88** 1855
[7] Sanchez-Garcia M A, Calleja E, Monroy E, Sanchez F J, Calle F, Muñoz E and Beresford R 1998 *J. Cryst. Growth* **183** 23
[8] Calleja E, Sanchez-Garcia M A, Sanchez F J, Calle F, Naranjo F B, Muñoz E, Jahn U and Ploog K 2000 *Phys. Rev.* B **62** 16826
[9] Shi B M, Xie M H, Wu H S, Wang N and Tong S Y 2006 *Appl. Phys. Lett.* **89** 151921
[10] Novikov S V, Winser A J, Bell A, Harrison I, Li T, Campion R P, Staddon C R, Davis C S, Ponce F A and Foxon C T 2002 *J. Cryst. Growth* **240** 423
[11] Foxon C T, Harrison I, Novikov S V, Winser A J, Campion R P and Li T 2002 *J. Phys.: Condens. Matter* **14** 3383
[12] Foxon C T, Novikov S V, Li T, Campion R P, Winser A J, Harrison I, Kappers M J and Humphreys C J 2003 *J. Cryst. Growth* **251** 510
[13] Okumura H, Hamaguchi H, Feuillet G, Ishida Y and Yoshida S 1998 *Appl. Phys. Lett.* **72** 3056
[14] Foxon C T, Novikov S V, Li T, Campion R P, Davis C S, Winser A J, Harrison I and Liao Y 2002 *Mater. Sci. Eng.* B **93** 35
[15] Winser A J, Novikov S V, Davis C S, Cheng T S, Foxon C T and Harrison I 2000 *Appl. Phys. Lett.* **77** 2506
[16] Kimura A, Paulson C A, Tang H F and Kuech T F 2004 *Appl. Phys. Lett.* **84** 1489
[17] Wu J, Walukiewicz W, Yu K M, Denlinger J D, Shan W, Ager J W III, Kimura A, Tang H F and Kuech T F 2004 *Phys. Rev.* B **70** 115214
[18] Shan W, Walukiewicz W, Ager J W III, Haller E E, Geisz J F, Friedman D J, Olson J M and Kurtz S R 1999 *Phys. Rev. Lett.* **82** 1221
[19] Harima H 2002 *J. Phys.: Condens. Matter* **14** R967
[20] Foxon C T, Novikov S V, Campion R P, Liao Y, Winser A J and Harrison I 2001 *Phys. Status Solidi* b **288** 219
[21] Kisielowski C *et al* 1996 *Phys. Rev.* B **54** 17745
[22] Kaczmarczyk G, Kaschner A, Hoffmann A and Thomsen C 2000 *Phys. Rev.* B **61** 5353
[23] Ibáñez J, Pastor D, Cuscó R, Artús L, Avella M, Jiménez J, Novikov S V and Foxon C T 2005 *Phys. Status Solidi* a **202** 850
[24] Limmer W, Ritter W, Sauer R, Mensching B, Liu C and Rauschenbach B 1998 *Appl. Phys. Lett.* **72** 2589

[25] Siegle H, Kaschner A, Hoffmann A, Broser I, Thomsen C, Einfeldt S and Hommel D 1998 *Phys. Rev.* B **58** 13619
[26] Creigton J A and Withnall R 2000 *Chem. Phys. Lett.* **326** 311
[27] Van de Walle C G and Neugebauer J 2000 *Appl. Phys. Lett.* **76** 1009
[28] As D J, Schmilgus F, Wang C, Schöttker B, Schikora D and Lischka K 1997 *Appl. Phys. Lett.* **70** 1311
[29] Li T *et al* 2002 *J. Cryst. Growth* **235** 103
[30] Kozawa T, Kachi T, Kano H, Nagase H, Koide N and Manabe K 1995 *J. Appl. Phys.* **77** 4389

References

[1] K. Takahashi, A. Yoshikawa, and A. Sandhu, *Wide Bandgap Semiconductors*. Springer-Verlag, Berlin, Germany, 2007.

[2] H. Harima *J. Phys. Condens. Matter*, vol. 14, p. R967, 2002.

[3] P. Perlin, C. Jauberthie-Carillon, J. P. Itie, A. San Miguel, I. Grzegory, and A. Polian *Phys. Rev. B*, vol. 45, p. 83, 1992.

[4] J. Groenen, R. Carles, G. Landa, C. Guerret-Piecourt, C. Fontaine, and M. Gendry *Phys. Rev. B*, vol. 58, p. 10452, 1998.

[5] V. Y. Davydov, I. N. Goncharuk, A. N. Smirnov, A. E. Nikolaev, W. V. Lundin, A. S. Usikov, A. A. Klochikhin, J. Aderhold, J. Graul, O. Semchinova, and H. Harima *Phys. Rev. B*, vol. 65, p. 125203, 2002.

[6] M. Giehler, M. Ramsteiner, O. Brandt, H. Yang, and K. H. Ploog *Appl. Phys. Lett.*, vol. 67, p. 733, 1995.

[7] D. J. As, D. Schikora, A. Greiner, M. Lubbers, J. Mimkes, and K. Lischka *Phys. Rev. B*, vol. 54, p. R11118, 1996.

[8] S. V. Novikov, K. W. Edmonds, A. D. Giddings, K. Y. Wang, C. R. Staddon, R. P. Campion, and B. L. Gallagher *Semicond. Sci. Technol.*, vol. 19, p. L13, 2004.

[9] L. Shunfend, J. Schomann, D. J. As, and K. Lischka *Appl. Phys. Lett.*, vol. 90, p. 071903, 2007.

[10] A. Kikuchi, T. Yamada, S. Nakamura, K. Kusakabe, D. Sugihara, and K. Kishino *Jap. J. Appl. Phys.*, vol. 39, p. L330, 2000.

[11] J. A. Sanjurjo, E. Lopez-Cruz, P. Vogl, and M. Cardona *Phys. Rev. B*, vol. 28, p. 4579, 1983.

[12] S. Reich, A. C. Ferrari, R. Arenal, A. Loiseau, I. Bello, and J. Rovertson *Phys. Rev. B*, vol. 71, p. 205201, 2005.

[13] R. Geick, C. H. Perry, and G. Rupprecht *Phys. Rev.*, vol. 146, p. 143, 1966.

[14] L. K. Teles, L. M. R. Scolfaro, J. R. Leite, J. Futhmueller, and F. Bechstedt *Appl. Phys. Lett.*, vol. 80, p. 1177, 2002.

[15] G. Orsal, N. Maloufi, S. Gautier, M. Alnot, A. A. Sirenko, M. Bouchaour, and A. Ougazzaden *J. Cryst. Growth*, vol. 310, p. 5058, 2008.

[16] S. Hernández, R. Cuscó, D. Pastor, L. Artús, K. P. O'Donell, R. W. Martin, I. M. Watson, Y. Nanishi, and E. Calleja *J. Appl. Phys.*, vol. 98, p. 013511, 2005.

[17] J. Neugebauer, T. Zywietz, M. Scheffler, J. E. Northrup, and C. G. Van de Walle *Phys. Rev. Lett.*, vol. 80, p. 3097, 1998.

[18] G. Feuillet, H. Hamaguchi, K. Ohta, P. Hacke, H. Okumura, and S. Yoshida *Appl. Phys. Lett.*, vol. 70, p. 1025, 1997.

[19] X. Li, S. Kim, E. E. Reuter, S. G. Bishop, and J. J. Coleman *Appl. Phys. Lett.*, vol. 72, p. 1990, 1998.

[20] J. I. Pankove and J. A. Hutchby *J. Appl. Phys.*, vol. 47, p. 5387, 1976.

[21] A. J. Winser, S. V. Novikov, C. S. Davis, T. S. Cheng, C. T. Foxon, and I. Harrison *Appl. Phys. Lett.*, vol. 77, p. 2506, 2000.

[22] A. Stoetzler, R. Weissenborn, M. Diecher, and ISOLDE collaboration *MRS Internet J. Nitride Semicond. Res.*, vol. 5S1, p. W12.9, 2000.

[23] C. T. Foxon, S. V. Novikov, R. P. Campion, Y. Liao, A. J. Winser, and I. Harrison *Phys. Status Solidi B*, vol. 288, p. 219, 2001.

[24] L. C. Jenkins, T. S. Cheng, C. T. Foxon, S. E. Hooper, J. W. Orton, S. V. Novikov, and V. V. Tretyakov *J. Vac. Sci. Technol. B*, vol. 13, p. 1585, 1995.

[25] G. Kaczmarczyk, A. Kaschner, A. Hoffmann, and C. Thomsen *Phys. Rev. B*, vol. 61, p. 5353, 2000.

[26] H. Siegle, A. Kaschner, A. Hoffmann, I. Broser, C. Thomsen, S. Einfeldt, and D. Hommel *Phys. Rev. B*, vol. 58, p. 13619, 1998.

[27] M. Ramsteiner, J. Menniger, O. Brandt, H. Yang, and K. H. Ploog *Appl. Phys. Lett.*, vol. 69, p. 1276, 1996.

[28] R. B. Barnes and M. Czerny *Z. Phys.*, vol. 72, p. 447, 1931.

[29] D. W. Berreman *Phys. Rev.*, vol. 130, p. 2193, 1963.

[30] C. T. Foxon, S. V. Novikov, T. Li, R. P. Campion, A. J. Winser, I. Harrison, M. J. Kappers, and C. J. Humphreys *J. Cryst. Growth*, vol. 251, p. 510, 2003.

[31] A. Ougazzaden, S. Gautier, C. Sartel, N. Maloufi, J. Martin, and F. Jomard *J. Cryst. Growth*, vol. 298, p. 316, 2007.

"All men by nature desire knowledge.

Aristotle

6

Raman Scattering in Undoped and Doped Dilute Nitrides

6.1 Introduction

Dilute nitrides are III-V compound semiconductors with low (typically $< 5\%$) composition of nitrogen in the lattice. $GaAs_{1-x}N_x$, $In_yGa_{1-y}As_{1-x}N_x$, $GaP_{1-x}N_x$, $InP_{1-x}N_x$ or $Al_yGa_{1-y}As_{1-x}N_x$ are some examples of dilute nitrides, and all of them exhibit a large scale bowing of the band gap among other interesting properties, which are of great interest from a fundamental and applied point of view [1,2]. Owing to the large difference in size and electro-negativity between N and As/P atoms, $N_{As/P}$ introduce quasi-localized electron states in the host matrix. These localized states strongly interact with the extended electronic band of the matrix material, and leads to a strong redshift of the fundamental band gap accompanied by a secondary electronic transition at higher energies, called E_+ [3].

In this study, we focus on the ternary and quaternary alloys $GaAs_{1-x}N_x$ and $In_yGa_{1-y}As_{1-x}N_x$, respectively. The first chapter of this thesis already introduced the interest of these compounds in optoelectronics and specially in telecommunications. $In_yGa_{1-y}As_{1-x}N_x$ is of particular interest since it can be used for a larger reduction of the band gap than the ternary compound and can be pseudomorphically grown on GaAs, which makes it very suitable for the GaAs technology. However, the study of

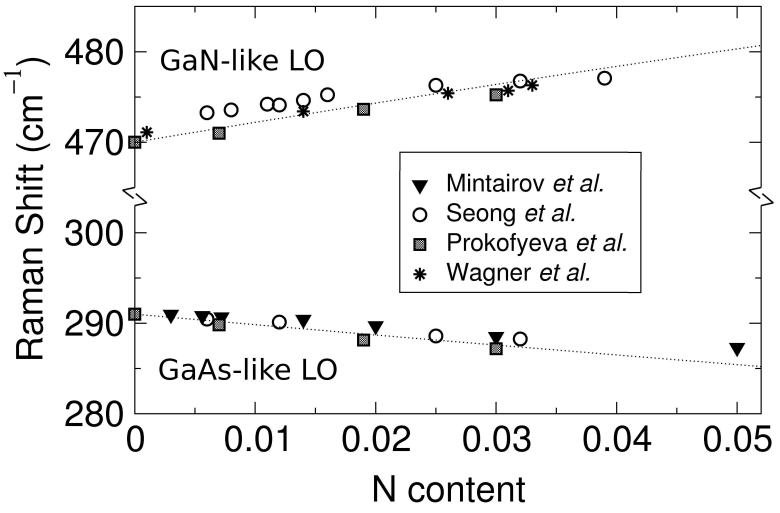

Figure 6.1: Raman shift of the GaAs-like and GaN-like longitudinal optical modes of coherently strained $GaAs_{1-x}N_x$ obtained by several authors. Dotted line is a guide-to-the-eye.

the ternary GaAsN alloy is very attractive from the fundamental point of view, as a tool to better understand the perturbation caused by N.

Some studies concerning the vibrational properties of $GaAs_{1-x}N_x$ alloys have already been published [4–9]. Dilute nitrides present a zinc-blende structure and show a two-mode behavior (see chapter 5) for the optical modes of the alloy in the dilute regime. This behavior is typical of alloys in which the atoms occupying equivalent lattice sites have significantly different masses. While the GaAs-like LO phonon shifts to lower frequencies with increasing N content, the GaN-like LO phonon monotonically shifts to higher frequencies and gains intensity. Since the alloy is within the dilute regime, the GaN-like LO mode can be considered as a nitrogen-related local vibrational mode in the GaAs host matrix.

A weak interaction between the GaAs-like optical phonons and the N impurity mode has been also described in these works. This fact makes the N impurity mode to be a very sensitive probe of the local environment of the N atoms. In the dilute regime, the GaN-like mode appears around the frequency of 470 cm^{-1} and has been proven to behave like a local vibrational mode of N substituting an As atom and surrounded by four Ga atoms [10].

The origin of the observed shifts in the optical phonons of $GaAs_{1-x}N_x$ is not fully understood yet, since all the published works have dealt with strained epilayers. The frequency shifts in the LO modes in $GaAs_{1-x}N_x$ alloys have been said to be due to

alloying and/or biaxial strain effects. These two phenomena are hardly separated in strained epilayers since $GaAs_{1-x}N_x$ compounds are relatively new. Calculation of strain effects on the normal modes requires assumptions on the variation of lattice parameters and elastic constants of the alloy with N fraction. Usually, a linear interpolation between the binary GaAs and *c*-GaN values is used (the well known Vegard's law). Although, Li *et al.* [11] and Fan *et al.* [12] agree that Vegard's law may be reliable for lattice parameters in alloys with N contents below 2%, the study of relaxed $GaAs_{1-x}N_x$ layers is of particular importance in dilute nitrides.

On the other hand, when In is added to $GaAs_{1-x}N_x$ the GaN-like LO mode slightly redshifts and two additional modes emerge in the nitrogen LVM region (at 430 and 488 cm^{-1} for room temperature measurements) [13–15]. Thermal annealing treatments increase the intensity of both new peaks relative to the LVM observed in samples without In. This suggests that the incorporation of In into the $GaAs_{1-x}N_x$ lattice changes the bonding environment of the N atoms. The LVM at $\sim$470 cm^{-1}, which is related to a NGa_4 configuration, is now strained by the presence of In (see figure 6.2a). Contrariwise, the peak at 488 cm^{-1} is given by the Ga_3InN configuration, i.e. N atoms bonded to three Ga atoms and one In atom (see figure 6.2b). The additional mode observed at 430 cm^{-1} still remains unassigned to specific N bonds and/or environment.

Most research into the $In_yGa_{1-y}As_{1-x}N_x$ system involves material grown on (100) oriented substrates. However, it has been proved in other semiconductors that their growth on higher-index planes offers potential advantages, such as larger critical thickness, higher impurity incorporation, improved electronic properties and lasing performance, as well as the appearance of piezoelectric effects. For instance, reduced threshold current densities were observed for (111)-oriented InGaAs single quantum well (SQW) lasers [16], and high-performance InGaAs/GaAs quantum dot (QD) lasers were achieved by using (311)-GaAs [17]. Regarding dilute nitrides, improved optical properties and longer PL wavelengths for (111) $In_yGa_{1-y}As_{1-x}N_x$ QWs were reported by Miguel-Sánchez *et al.* [18, 19].

Concerning the impurity incorporation, the atomic arrangement and dangling bonds of the substrate surface is expected to affect the ratio of N and In incorporated into GaAs. While larger atoms may be more easily incorporated at double dangling bond sites, such as in Ga-terminated surfaces (labelled B), the small N atom may prefer the single-dangling bond site, like in As-terminated planes (A-labelled). Previous studies in the ternary $GaAs_{1-x}N_x$ system confirmed the dependence of N

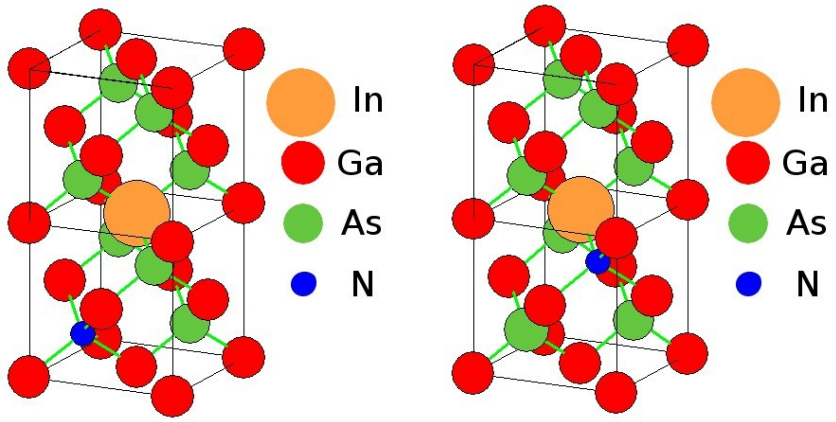

(a) (b)

Figure 6.2: Schematic showing GaAs lattice with isolated N and In atoms (a) and with an In atom next to the N atom (b).

incorporation to substrate orientation [20]. They reported a higher N incorporation for (111)A than for (100) oriented layers, and lower incorporation for (111)B. In this sense, a Raman study of the phonon modes of the alloy can give a qualitative measure of the alloy composition, local bonding of impurities and strain. Thus, investigations concerning the vibrational properties of $In_{1-y}Ga_yAs_{1-x}N_x$ can give further insight into the influence of substrate orientation to the nitrogen incorporation in the host lattice and its local environment.

Nonetheless, although the modified electronic and optical properties of dilute $In_yGa_{1-y}As_{1-x}N_x$ are particularly advantageous to fabricate optoelectronic devices, the use of dilute nitrides in device applications is still limited by their low *n*-type mobility [1]. The localized states associated with N clusters play a crucial role in the low carrier mobilities obtained in dilute nitrides. Indeed, such low mobilities can be explained mainly by two phenomena: a dramatic increase in the electron scattering rate and an increase of the effective mass due to the strong interaction between the extended states of the host crystal and the N localized electronic states. The band anti crossing (BAC) model is the most simple analytic model which accounts for the dependence on N content of the two energy states E_+ and E_-, where the E_- energy state defines the fundamental band gap of the alloy. The BAC model yields an analytical expression for the $E_\pm(k)$ dispersion, which suggests that the effective mass of the lower energy subband E_- is substantially increased relative to that of the III-V matrix. Moreover, it predicts a distinct flattening of the $E_-(k)$ subband for

electron energies approaching the energy of the localized N state.

Most of the optical experiments to determine the electron effective mass in dilute (In)$GaAs_{1-x}N_x$ were performed on undoped material (see for instance [21]). As a consequence, the electronic effective mass values obtained in those experiments correspond to the bottom of the E_- conduction subband effective mass m^*_{e0}. By optically probing highly doped n-type samples, the conduction band dispersion and $m^*_e(k)$ is investigated. Skierbiszewski *et al.* [22,23] experimentally confirmed by infrared reflectivity in $In_yGa_{1-y}As_{1-x}N_x$ layers the validity of the BAC model to account for the energy-wavevector dispersion. In contrast, recent magneto photoluminescence measurements on undoped $GaAs_{1-x}N_x$ suggested that the BAC model underestimates the band edge effective mass (m^*_{e0}) for N contents above 0.1% [24]. However, no experimental studies probing m^*_e above the conduction band edge are provided. Additional experiments are therefore necessary to determine how the conduction band dispersion $E(k)$ and the effective mass $m^*_e(k)$ depend on N content in dilute nitrides.

Raman scattering by LO phonon-plasmon coupled modes (LOPCMs) is very useful to probe the carrier density, mobility and optical effective mass of free carriers in a non-destructive way. Only a previous work has studied coupled modes in $GaAs_{1-x}N_x$ layers so far [25]. They report disorder-canceled coupled modes for N contents close to 3%. The investigation of LOPCMs provides a means of optically probing the energy wavevector dispersion $E(k)$ of the carriers in a polar semiconductor, since the frequency of these coupled modes strongly depend on the carrier effective mass. No studies by means of Raman scattering dealing with the effective mass and its wavevector dependence in dilute nitrides has been reported yet.

In this chapter, after a good knowledge of undoped, unstrained $GaAs_{1-x}N_x$ layers, the N incorporation in $InGaAs_{1-x}N_x$ epilayers as a function of substrate orientation will be evaluated. Next, we will study highly doped $GaAs_{1-x}N_x$ layers and the coupling between its LO phonons and the free carriers. We will assess the viability of the Raman spectroscopy as a non-destructive technique to obtain carrier densities, mobilities and lifetimes in dilute nitrides. Also, we will investigate the dependence of $m^*_e(k)$ in $GaAs_{1-x}N_x$ on the N content, and assess the role of m^*_e and the scattering rates in the dilute nitrides mobility.

6.1.1 Aim

In summary, the aim of the work on dilute nitrides is threefold:

- To discuss the origin of the alloying-induced frequency shifts in dilute $GaAs_{1-x}N_x$ optical phonons, by probing thick strain free $GaAs_{1-x}N_x$ epilayers with N contents up to 1.5%.

- To assess the effect of In incorporation to the $GaAs_{1-x}N_x$ lattice. To evaluate both alloying and strain-induced frequency shifts in the optical phonons of GaInAsN. Also, to investigate the possible influence of the substrate orientation on the N incorporation and strain state of the epilayers.

- To study the LO phonon-plasmon coupling in highly doped *n*-$GaAs_{1-x}N_x$. To optically obtain values of carrier densities and mobilities comparable to the Hall data. To analyze by means of Raman scattering the role of N in the reduced electron mobility of dilute nitrides , i.e. to assess the N effects on both the optical effective mass and the carrier scattering rate.

6.2 Groundwork

Previous to any analysis, we should first introduce some theoretical background to support the interpretation of the experimental results. In this section we discuss the frequency shifts of optical phonons induced by strain effects in pseudomorphically grown layers. Afterwards, an extension of the already described Hydrodynamical model is depicted, as a tool for calculating the carrier density, the optical effective mass and the mobility from LOPCMs in doped $GaAs_{1-x}N_x$. We will see that a model for the electronic band dispersion is required for these calculations, and hence the most accepted BAC model for highly mismatched alloys will be discussed.

6.2.1 Strain-induced frequency shifts of the optical phonons

Thin film growth technologies allow the growth of heteroepitaxial structures, in which the thin film and the substrate are different materials with different lattice parameters. The lattice mismatch between the layer and the substrate is accommodated by elastic distortion of the layer. As long as the film thickness does not exceed a critical value, the film will remain pseudomorphic (or coherent). This means that the strain in the layer is homogeneous (biaxial strain) and the in-plane lattice constant of the layer becomes the same as that of the substrate (see figure 6.3).

The lattice misfit f is defined as $f \equiv (a_s - a_0)/a_0$, where a_s and a_0 are the natural lattice parameters of the substrate and film materials, respectively. If the natural lattice parameter of the epilayer is larger than that of the substrate ($f < 0$), the layer is under compressive strain (figure 6.3a). Opposite, when the layer lattice parameter is shorter than the one of the substrate ($f > 0$), the layer is under tensile strain (figure 6.3b). Due to volume conservation of the unit cell, the epilayer strain in the growth direction is contrary to the in-plane strain. Namely, in an in-plane tensile strained layer, the layer is compressively strained in the growth direction.

Strain in semiconductor crystals can substantially modify their electronic, optical and vibrational properties. Regarding the vibrational properties, the changes in the atomic distances highly affect the intrinsic vibrations, and hence the Raman frequencies. Frequencies and strain are related by the stress tensor and elastic constants of the material, as we will see later on. It is worth noting that in the absence of strain,

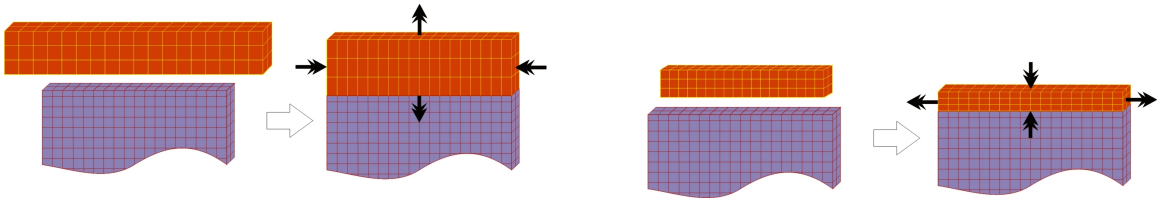

(a) In-plane compressively strained layer. The lattice parameter is larger than that of the substrate.

(b) In-plane tensile strained layer. The lattice parameter is smaller than that of the substrate.

Figure 6.3: Biaxial strain in pseudomorphically grown layers.

the optical phonons at the Γ point in a zinc-blende crystal are triply degenerate due to the cubic symmetry. However, we will see that uniaxial or biaxial stress removes the cubic symmetry and hence splits the triplet.

The strain in a crystal is defined by the amount of deformation experienced by the crystal compared to its original shape. The strain is written as a symmetric tensor ϵ_{ij}, where i and j designate the x, y or z directions. While diagonal elements (ii) refer to the typical compressive/tensile strain, crossed elements (ij with $j \neq i$) are the shear strain components. In the presence of strain, the dynamical equations to first order terms in strain for the $\vec{q} \sim 0$ triply degenerate optical modes of zinc-blende crystals have the form [26]

$$\mu\ddot{\eta}_i = -\sum_k K_{ik}\eta_k = -K_{ii}\eta_i - \sum_{klm} \frac{\partial K_{ik}}{\partial \epsilon_{lm}} \epsilon_{lm}\eta_k \qquad (6.1)$$

where η_i is the relative atomic displacement of the two atoms in the unit cell along the i-direction, μ is the reduced mass of the two atoms, K_{ij} is the spring constant of the zone center optical phonons, and i, k, l, and m designate the x, y, or z directions.

The first term on the right side of equation 6.1 is the dynamical term in absence of strain, and hence $K_{ii} = \mu\omega_0^2$, where ω_0 is the natural strain-free frequency of the crystal. In the second term, $\partial K_{ik}/\partial \epsilon_{lm}$ describes the changes of the spring constants in the presence of strain. From symmetry considerations, it can be shown that for zinc-blende crystals [26]

$$\frac{\partial K_{xx}}{\partial \epsilon_{xx}} = \frac{\partial K_{yy}}{\partial \epsilon_{yy}} = \frac{\partial K_{zz}}{\partial \epsilon_{zz}} \equiv \mu\tilde{K}_{11}, \qquad \frac{\partial K_{xx}}{\partial \epsilon_{yy}} = \frac{\partial K_{yy}}{\partial \epsilon_{zz}} = \frac{\partial K_{xx}}{\partial \epsilon_{zz}} \equiv \mu\tilde{K}_{12}$$
$$\frac{\partial K_{xy}}{\partial \epsilon_{xy}} = \frac{\partial K_{xz}}{\partial \epsilon_{xz}} \equiv \mu\tilde{K}_{44} \qquad (6.2)$$

$\tilde{K}_{ab}$ are the phonon deformation potential constants and stand for the frequency change per strain unit. Hence, different values are expected for TO and LO phonons.

Table 6.1: Deformation potential and elastic stiffness constants [10^{11} dyn/cm^2] for cubic GaAs, InAs and GaN materials. Values obtained from references [27–29]. Note that deformation potential values for cubic GaN are omitted, since no data for this material is found in the literature yet.

	$\tilde{K}_{11}^{\mathrm{LO}}$	$\tilde{K}_{12}^{\mathrm{LO}}$	$\tilde{K}_{44}^{\mathrm{LO}}$	$\tilde{K}_{11}^{\mathrm{TO}}$	$\tilde{K}_{12}^{\mathrm{TO}}$	$\tilde{K}_{44}^{\mathrm{TO}}$	C_{11}	C_{12}	C_{44}
GaAs	-2	-2.7	-0.53	-2.57	-2.87	-0.88	11.88	5.38	5.94
InAs	-1.75	-2.323	-0.76	-2.05	-2.62	-0.76	8.33	4.53	3.96
GaN							2.93	1.59	1.55

The phonon deformation potential constants $\tilde{K}_{ab}$ for GaAs and InAs optical phonons at the Γ point are listed in table 6.1. Using the considerations above, the frequencies of the optical phonons in the presence of strain are the solutions of the secular equation

$$\begin{vmatrix} [\tilde{K}_{11}\epsilon_{xx} + \tilde{K}_{12}(\epsilon_{yy}+\epsilon_{zz}) - \lambda] & 2\tilde{K}_{44}\epsilon_{xy} & 2\tilde{K}_{44}\epsilon_{xz} \\ 2\tilde{K}_{44}\epsilon_{yx} & [\tilde{K}_{11}\epsilon_{yy} + \tilde{K}_{12}(\epsilon_{xx}+\epsilon_{zz}) - \lambda] & 2\tilde{K}_{44}\epsilon_{yz} \\ 2\tilde{K}_{44}\epsilon_{xz} & 2\tilde{K}_{44}\epsilon_{yz} & [\tilde{K}_{11}\epsilon_{zz} + \tilde{K}_{12}(\epsilon_{xx}+\epsilon_{yy}) - \lambda] \end{vmatrix} = 0 \tag{6.3}$$

where $\lambda \equiv (\omega'^2 - \omega_0^2)/\omega_0^2$ and ω' is the strain-dependent frequency of the optical phonons. This secular equation yields a set of three eigenvectors of the optical phonons in the presence of strain.

As an example, let us consider the simplest case of a biaxial strain in the xy plane, which is the case for a pseudomorphic epilayer grown along the z direction. The in-plane strain coefficients are equal and correspond to the misfit between the epilayer and substrate ($\epsilon_{xx} = \epsilon_{yy} = f$). The shear strain is zero ($\epsilon_{ij} = 0, i \neq j$) and the strain in the growth direction can be obtained from the biaxial strain relationship [30]

$$\frac{\epsilon_{zz}}{\epsilon_{xx}} = -2\frac{C_{12}}{C_{11}} \tag{6.4}$$

where C_{ij} are the elastic constants of the epilayer (see table 6.1 for the values of some cubic crystals).

Hence, for biaxially strained epilayers the secular equation is easily solved and gives rise to one single degenerated and one double degenerated solutions [26, 30]

$$\Delta\omega)_s = \omega_0 \left[\tilde{K}_{12} - \frac{C_{12}}{C_{11}}\tilde{K}_{11}\right] f \tag{6.5}$$

$$\Delta\omega)_d = \omega_0 \left[\frac{1}{2}\tilde{K}_{11} + \tilde{K}_{12}\left(\frac{1}{2} - \frac{C_{12}}{C_{11}}\right)\right] f \tag{6.6}$$

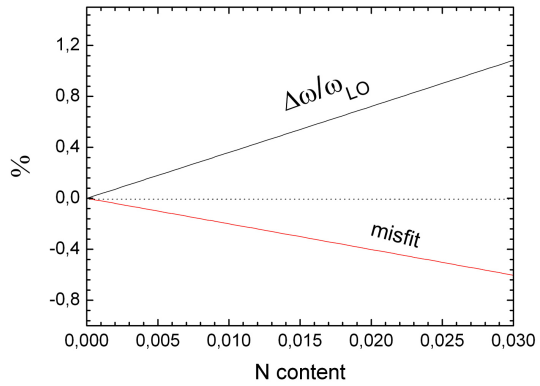

Figure 6.4: Misfit of a pseudomorphic $GaAs_{1-x}N_x$ layer over a GaAs substrate (red curve) and the consequent frequency shift of the LO phonon mode obtained from equation 6.6.

The vibrations for the singlet mode are along the (001) direction, while they are in-plane for the doublet mode. Then, LO phonons propagating along the (001) direction have a different frequency than those propagating in the xy plane. So, the threefold degeneracy of the Γ_{15} LO mode of zinc-blende crystals has broken.

For a pseudomorphically strained $GaAs_{1-x}N_x$ epilayer grown on GaAs substrate, the misfit f depends on the N content x, following

$$f(x) = \frac{x(a_{GaAs} - a_{GaN})}{a_{GaAs}(1-x) + a_{GaN}x} \tag{6.7}$$

where Vegard's law has been assumed for the lattice parameter of the $GaAs_{1-x}N_x$ alloy. Figure 6.4 shows strain frequency shifts of the Γ_{15} LO mode for a (001)-oriented $GaAs_{1-x}N_x$ as a function of the N content. For the calculations, interpolated elastic constants C_{ij} between the two cubic binaries GaAs and GaN have been used. Since the N content is small and phonon deformation potential values slightly vary from a material to another, $\tilde{K}_{ij}$ values of the GaAs have been used for the calculations.

As can be seen in the figure, for 3% of N content, the strain-related frequency shift is about $0.01 \cdot \omega_{LO} \sim 3$ cm^{-1}, which is of the order of alloy-related frequency shifts (assuming Vegard's law). For this reason, the study of strain-free $GaAs_{1-x}N_x$ is very interesting to really evaluate alloying effects on the optical phonons of the novel material and the validity of using Vegard's law in dilute nitrides.

6.2.2 LO-plasmon coupled modes in dilute nitrides

In the *Theoretical Framework* chapter, we have introduced the coupling phenomena between phonons and free carriers. We also stated that to account for the Raman frequencies of the LOPCMs is necessary an expression for the electronic susceptibility ($\chi_e(\omega)$). The evaluation of charge densities, optical effective masses and mobilities from LOPCM analysis relies heavily on the model used to account for the free charge contribution to $\chi_e(\omega)$.

We described the simplest approach to calculate the electronic susceptibility, the Drude model. This model is only a rough approximation and may be used in the case of single-component long-wavelength degenerate electron gas. The Drude model neglects wavevector dispersion of the plasmons, temperature effects, and non-parabolicity of the conduction band. For this reason we introduced the also classical Hydrodynamical (HD) model. While the HD model includes wavevector dispersion, non-parabolicity effects remain neglected. It should be noted that for the special case of dilute nitrides, the use of non-parabolic bands is crucial, as we have mentioned and will be further discussed later on. The incorporation of non-parabolocity effects together with thermal distribution of the free carriers leads to the Extended Hydrodynamical (EHD) model [31], which will be explained in the next section.

Extended Hydrodynamical model

To include the non-parabolicity and thermal distribution effects to the HD model, we consider a carrier density dependent effective mass, called optical effective mass (m^*_{opt}), instead of the constant m^*. The optical effective mass is calculated from the wavevector dependent electron conduction band and averaged over the thermal velocity of the free carriers according to [32]

$$\frac{1}{m^*_{opt}} = \frac{1}{3\hbar^3 N_e}\int_0^\infty \nabla_k^2 E \cdot n_{FD} g(E) dE \tag{6.8}$$

The density of states $g(E)$ and the Fermi-Dirac distribution n_{FD} have been already described in section 2.5. From its definition, the optical effective mass directly depends on the wavevector dispersion of the electronic band. Kane [33] found a secular equation to account for the dispersion curves of the conduction and valence bands of semiconductors from the $\vec{k}\cdot\vec{p}$ theory,

$$E'(E'+E_g)(E'+E_g+\Delta_{so}) - k^2p^2(E'+E_g+\frac{2}{3}\Delta_{so}) = 0, \tag{6.9}$$

where $E' = E - \hbar^2 k^2/(2m_e)$, p is the momentum matrix element between valence and conduction band, E_g is the band gap at the Γ point and Δ_{so} is the energy of the spin-orbit splitting. Blakemore [34] expanded the solution for the conduction band in powers of wavevector, and obtained the following expression to order k^4

$$E(k) \sim E_g + \frac{\hbar^2}{2m^*}k^2 + \frac{\alpha}{E_g}\frac{\hbar^4}{(2m^*)^2}k^4 \tag{6.10}$$

Here α is the non-parabolicity coefficient. Using this expression in eq. 6.8, the optical effective mass can be written in terms of the reduced Fermi energy ($\eta = E_F/k_BT$)

$$\frac{1}{m^*_{opt}} = \frac{1}{m^*_0}\left[1 + 5\alpha\frac{k_bT}{E_0}\frac{\mathscr{F}_{3/2}(\eta)}{\mathscr{F}_{1/2}(\eta)}\right] \tag{6.11}$$

$\mathscr{F}_{1/2}$ and $\mathscr{F}_{3/2}$ are the Fermi integrals, which are defined by equation 2.34 in section 2.5. Likewise, the electron density is calculated in terms of the Fermi energy and Fermi integrals by

$$N_e = \int_0^\infty n_{FD}g(E)dE = 2\left(\frac{K_BTm^*}{2\pi\hbar^2}\right)^{3/2}\mathscr{F}_{1/2}(\eta)\left[1 - \frac{15}{4}\alpha\frac{k_BT}{E_g}\frac{\mathscr{F}_{3/2}(\eta)}{\mathscr{F}_{1/2}(\eta)}\right] \tag{6.12}$$

Substituting equations 6.11 and 6.12 into the definition of the plasma frequency (equation 2.26), we obtain the frequency of the bare plasma in a non-parabolic conduction band to be

$$\omega_p^2 = \omega_{p0}^2 \cdot \mathscr{F}_{1/2}(\eta)\left[1 + \frac{5}{4}\frac{\alpha k_BT}{E_g}\frac{\mathscr{F}_{3/2}(\eta)}{\mathscr{F}_{1/2}(\eta)}\right] \tag{6.13}$$

where ω_{p0} is the natural frequency of a plasma in a parabolic band (equation 2.26).

For dilute nitrides, the wavevector dependence of the electronic band structure [$E(k)$] is however unknown. The study of LOPCMs can give valuable information about $E(k)$ through the optical effective mass. Vice versa, once an assumption is made for $E(k)$, information about carrier concentration and mobility can be obtained from LOPCMs. Some models have been developed to account for the dilute nitrides band gap reduction, but only the Band Anticrossing (BAC) model gives an expression for $E(k)$. Therefore, in the next section we focus on the BAC model for the electronic band structure in dilute nitrides.

The BAC model for the electronic band structure

One of the most attractive features of dilute nitrides is the unusually strong dependence of the fundamental band gap on the N content. Some models have been

proposed to explain this phenomena. The more widely accepted model is the so-called Band Anticrossing (BAC) model, which was suggested by Shan *et al.* [35] and is described below.

It is well known that replacing a single As atom by N introduces a highly localized acceptor-like level in (In)GaAs located slightly above (~ 0.3 eV) the conduction band minimum. This fact was demonstrated by pressure dependent PL measurements by Liu *et al.* [36]. The BAC model suggests that the narrow resonant band formed by N states strongly interact with the (In)GaAs conduction band, due to the highly localized nature of the perturbation induced by N atoms. Hence, the BAC model considers two interacting energy levels: the extended states of the host (In)GaAs matrix ($E_M(k)$) and the localized resonant energy state of a single N atom in the host material ($E_N = 1.64$ eV above the top valence band of the host material, at room temperature or $E_N = 1.72$ at 80K [37]). Assuming that the interaction between the two types of states can be treated as a perturbation, the energy state of the dilute nitride is given by solving the 2×2 eigenvalue problem:

$$\begin{vmatrix} E - E_M(k) & V_{MN} \\ V_{MN} & E - E_N \end{vmatrix} = 0 \qquad (6.14)$$

Both $E_M(k)$ and E_N are relative to the top of the valence band. V_{MN} describes the interaction between the two energy states and gives rise to the anticrossing of these states. This strength of the interaction was found to scale with the square root of the nitrogen content according to $V_{MN} = C_{MN}x^{1/2}$ [38]. Solving equation 6.14 we find the two subband solutions

$$E_{\pm}(k) = \frac{E_N + E_M(k)}{2} \pm \frac{1}{2}\sqrt{(E_N - E_M(k))^2 + 4xC_{MN}^2} \qquad (6.15)$$

To illustrate the two resulting subbands proposed by the BAC model, the $E_+(k)$ and $E_-(k)$ dispersion curves derived from equation 6.15 are plotted in figure 6.5 for the GaAsN alloy with 0.5% of N. The parameters used for the calculations are listed in the table beside, and correspond to values at 80K. The scenario of the unperturbed conduction band of GaAs and the localized N energy state are also plotted for comparison purposes. The downward energy shift of the lower subband $E_-(k)$ with respect to the unperturbed band of GaAs accounts for the experimentally observed reduction of the fundamental band gap in dilute nitrides. On the other side, the secondary electronic transition at higher energies can be regarded as a transition from the valence band to the upper subband $E_+(k)$ [35, 39].

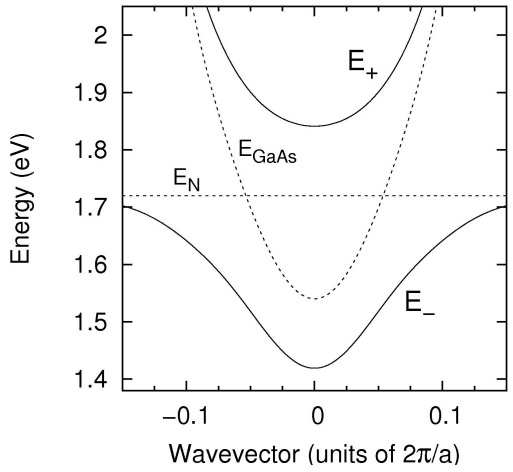

BAC model parameters	
$E_M(k)$	$E_0 + (\hbar^2/2m^*)k^2$
E_0	1.54 eV
m^*	$0.066m_e$
E_N	1.72 eV
C_{MN}	2.7 eV

Figure 6.5: Band structure of $GaAs_{1-x}N_x$ alloy with a 0.5% of N calculated within the framework of the BAC model. The parameters that enter the BAC model correspond to values at 80K, and are listed in the table. The solid curves are two non-parabolic subbands E_+ and E_- obtained from the BAC model. The dashed lines represent the unperturbed conduction band of GaAs $E_M(k)$ and the dispersionless N state E_N.

The BAC model was firstly tested by hydrostatic pressure experiments, since the band edge of the host matrix behaves differently from the localized N state under hydrostatic pressure, and hence the repulsion effects can be continuously tuned. The model has been further successfully used to quantitatively describe the dependencies of the upper and lower subband energies on hydrostatic pressure and on N content in $Al_yGa_{1-y}As_{1-x}N_x$, $InP_{1-x}N_x$ and $GaP_{1-x}N_x$ alloys [40].

This model does not only explain the band gap reduction and its behavior under hydrostatic pressure in III-N_x-V_{1-x} alloys, but it also predicts that the N-induced modifications to the conduction band may have profound effects on the transport properties of this material system. In particular, the wavevector dispersion of the $E_-(k)$ band given by the model predicts an enhancement of the optical effective mass.To clarify this assumption, we will obtain an analytic expression for the optical effective mass in dilute nitrides within the BAC model framework.

For the sake of simplicity the degenerate limit is considered, which is a valid assumption in heavily doped $GaAs_{1-x}N_x$ at 80 K. In this regime, the optical effective

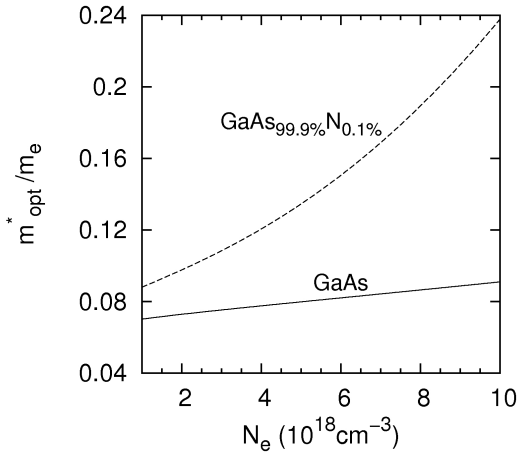

Figure 6.6: Optical effective mass versus electron density for GaAs and $GaAs_{99.9\%}N_{0.1\%}$ calculated by equations 6.11 and 6.17, respectively, in the degenerate limit.

mass calculation reduces to

$$\frac{1}{m^*_{\text{opt}}} = \frac{1}{\hbar^2 k_F}\left|\frac{\partial E(k)}{\partial k}\right|_{k_F} \tag{6.16}$$

where the Fermi wavevector is $k_F = (3\pi^2 N_e)^{1/3}$ in the degenerate limit. Within the BAC model framework, equation 6.16 leads to the following expression for the optical mass of the low energy band $E_-(k)$

$$m^{*^{-1}}_{\text{opt}}(N_e, x) = \frac{1}{2m^{\text{GaAs}}_{\text{opt}}(k_F)}\left[1 - \frac{E_M(k_F) - E_N}{\sqrt{(E_N - E_M(k_F))^2 + 4xC^2_{MN}}}\right] \tag{6.17}$$

As can be seen in figure 6.6, the optical effective mass dependence on the electron density is plotted for the host GaAs and GaAsN alloys by using equation 6.17. The BAC model predicts a large increase of the electron optical effective mass in dilute nitrides even for nitrogen concentrations as low as 0.1%. Since the electron mobility (μ) is inversely proportional to the effective mass, the mobility should decrease in dilute nitrides due to the perturbation of nitrogen on the conduction band.

By contrast, μ is directly proportional to the carrier lifetime τ, which is accounted for by the scattering rate of free carriers with impurities, phonons, etc. Considering that the electronic and crystal structures of dilute nitrides are highly perturbed, it is expected that the carrier lifetime of free carriers is also strongly affected by the presence of nitrogen. The effects of an increased carrier lifetime on the Raman scattering by coupled modes are discussed next.

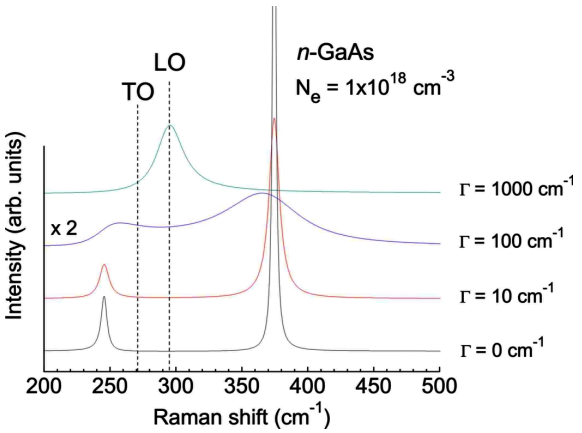

(a) Calculated Raman spectra of the coupled plasmon-phonon modes using different values of the electronic damping parameter for a *n*-GaAs sample with an electron concentration of 1×10^{18} cm^{-3}.

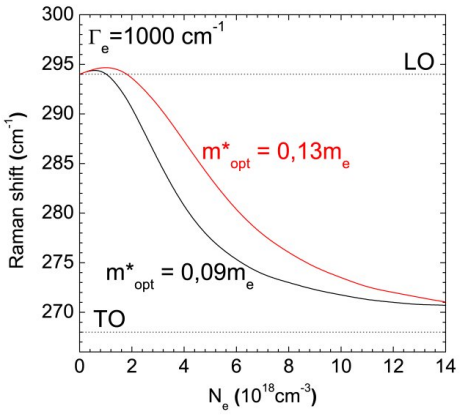

(b) Calculated N_e-dependence of the frequency of heavily damped LOPCM (Γ_e = 1000 cm^{-1}) in GaAs for two different values of the optical effective mass, $m^*_{opt} = 0.13$ and $0.09m_e$.

Figure 6.7: Overdamped LOPCMs in *n*-type GaAs.

Overdamped LOPCMs

As mentioned in the introductory section, the origin of the low mobility of carriers in dilute nitrides is thought to be two-fold: an increase of the optical effective mass and large carrier scattering rates. The former has been discussed in the previous section by considering highly non-parabolic bands, and the latter is the focus of the present section.

The lifetime of LOPCMs τ is reduced by the scattering of free carriers. The phenomenological damping parameter Γ_e (electronic damping) can be related to the LOPCM lifetime through the energy-time uncertainty relation $\tau^{-1} = 2\pi c\Gamma_e$. Hence, an increase of the free carrier scattering rate translates into an increase of the damping parameter Γ_e.

Changes in Γ_e result in variations of the frequencies and widths of the LOPCMs and even affect their coupling strenght. In figure 6.7, different calculated Raman spectra for *n*-GaAs with several electronic damping values are plotted. As shown in the figure, the coupled modes become much broader as the plasma damping constant increases. For Γ_e values much larger than the phonon and plasma energies ($\Gamma_e \gg 325$ cm^{-1} for *n*-GaAs with $N_e = 1 \times 10^{18}$ cm^{-3}), the LOPCMs become overdamped. In this regime, the plasmons and LO phonons are almost decoupled and a single mode is observed between the TO and LO frequencies of the lattice [41].

The energy of the typical L^+ coupled mode detected in *n*-type III-V semiconductors, such as in *n*-GaAs, is very sensitive to N_e variations. In contrast, from an overdamped plasma only one Raman feature in the range of the optical phonon frequencies is observed, even in the presence of a large carrier density. Such single LOPCM has been previously observed in *p*-GaAs samples, where the large effective mass of light and heavy holes give rise to the overdamping [42].

Heavily-damped LOPCM peaks can still be used to obtain relevant information about the investigated materials. For instance, the LOPCM energy behavior highly depends on the optical effective mass, as can be seen in figure 6.7b. The frequency dependence of the overdamped LOPCM in low-mobility *n*-GaAs on the carrier density is plotted for optical effective masses of $0.09m_e$ and $0.13m_e$. The two curves evidence that m^*_{opt} yields substantial differences in tendency of the overdamped LOPCM as a function of the carrier density.

6.3 The dilute nitride samples

The unusual physical properties of III-V-N alloys are consequences of the exceptional chemical characteristics of the nitrogen compared to the other elements of the groups III and V. In turn, these chemical characteristics lead to difficulties in the creation of these alloys. The incorporation of nitrogen is not straightforward, since clusters and pairs of N are usually formed, and phase segregation may also occur. The most promising range of N composition in the Ga(In)AsN system is to be less than 2%, in which the band gap reduction is sharp and the crystal quality of the material is still good. In this work, we study samples with nitrogen concentrations up to 1.5%. Strong non-equilibrium methods together with a highly reactive nitrogen precursor are necessary to overcome the immiscibility of N into the III-V host lattices.

The Molecular Beam Epitaxy (MBE) method has been widely adopted as a standard method for the growth of dilute nitride layers, although they have also been grown by other epitaxial techniques, such as Organo-Metallic Vapor Phase Epitaxy (OMVPE) and Chemical Beam Epitaxy (CBE), and also by N implantation on GaAs [43]. The techniques used for the growth of our dilute nitride samples are either Radio-Frequency MBE (RF-MBE) or Metal-Organic MBE (MOMBE). The growth and the main characteristics of the samples studied in this chapter will be explained next.

Strain-free $GaAs_{1-x}N_x$ layers

The thick strain-free $GaAs_{1-x}N_x$ samples were grown in the *EPSRC National Center for III-V Technologies* at the University of Sheffield (UK). The MBE facility consists of a VG V80H MBE system equipped with an Oxford Applied Research HD25 radio-frequency plasma source for nitrogen with a maximum power of 600W. Arsenic was obtained from a valved cracker, whereas Ga source was solid.

The relaxed $GaAs_{1-x}N_x$ epilayers were grown on n^+-type (001)-oriented GaAs substrates, with a 25nm-AlAs/100nm-GaAs buffer layers to relieve the mismatch strain between the substrate and $GaAs_{1-x}N_x$ layers (see sketch in figure 6.8). The buffer layers were grown at 600°C, while the growth for the $GaAs_{1-x}N_x$ films was performed at 450°C. The plasma intensity and the RF power were varied to obtain different N concentrations in the layers. The resulting epilayers were 1.5 μm thick with nitrogen contents from 0.05% to 1.5%. The nominal N fraction was checked

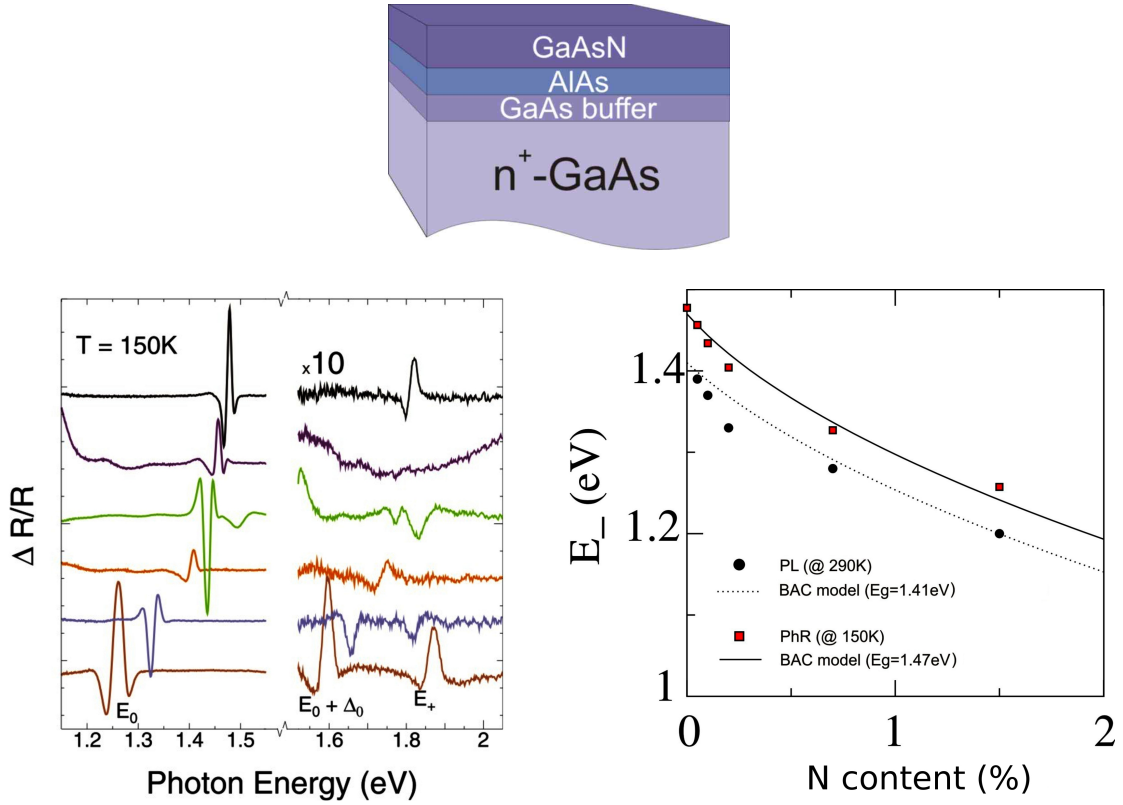

Figure 6.8: (top) Structural scheme of the strain-free $GaAs_{1-x}N_x$ samples. (bottom left) Photomodulated reflectance (PhR) spectra obtained from $GaAs_{1-x}N_x$ samples, with nitrogen contents up to 1.5%. (bottom right) Comparison between E_- values calculated by the BAC model and the experimental values measured by PL at 290 K and by PhR at 150 K.

by XRD and Photomodulated reflectance (PhR) measurements. PhR curves (figure 6.8) also revealed no-strain related features, which means that the epilayers are fully relaxed. Also, the PhR signal from the E_- transition highly agrees with the theoretically expected values within the BAC model theory.

$InGaAs_{1-x}N_x$ layers grown on misoriented GaAs

$InGaAs_{1-x}N_x$ samples were grown in the same laboratory as the strain-free $GaAs_{1-x}N_x$ epilayers. 100nm thick $InGaAs_{1-x}N_x$ films were grown simultaneously at 400°C on different epiready GaAs substrates with the orientations: (100), (111)A, (311)A, (411)A, and (511)A. In this notation, "A" stands for As-terminated plane. Over the GaAs substrate, a 0.2μm thick GaAs buffer was first deposited at 590°C. Then, the temperature was lowered to 400°C and a 0.1μm thick undoped GaAs layer was deposited, followed by the $InGaAs_{1-x}N_x$ layer (see sketch in figure 6.9a).

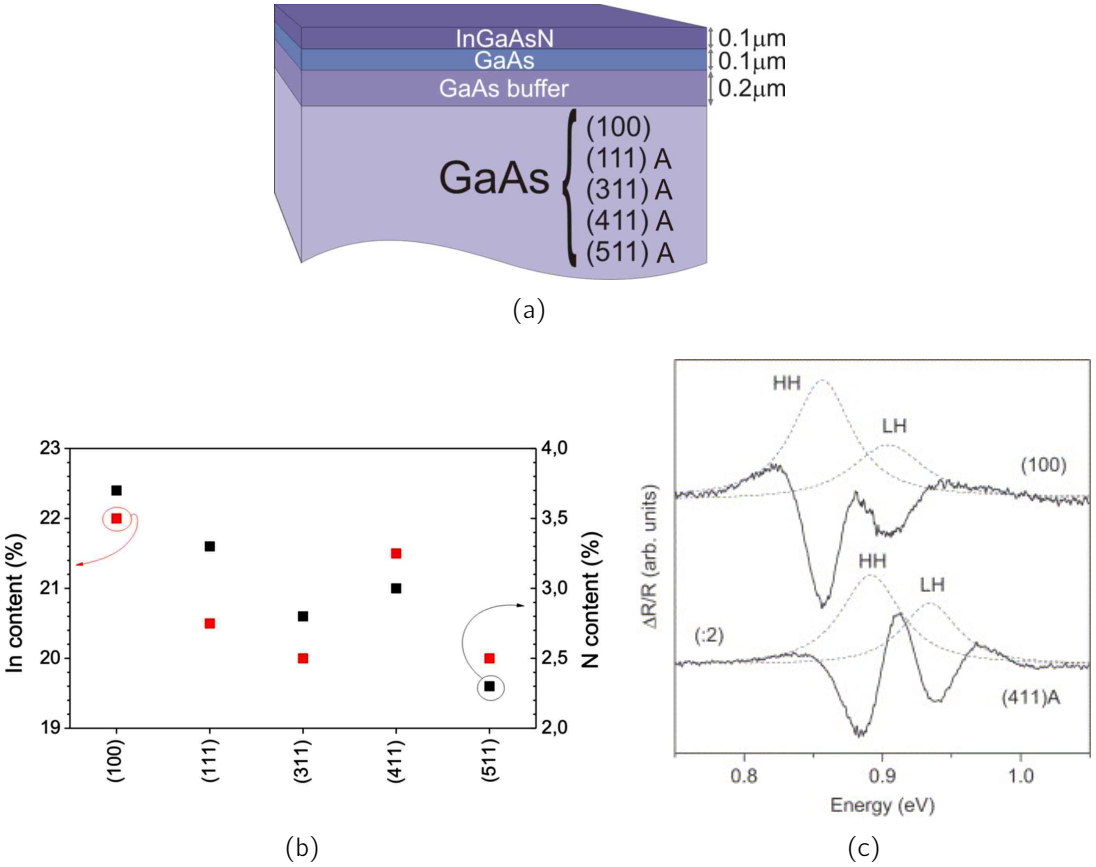

Figure 6.9: (a) Structural scheme of the $InGaAs_{1-x}N_x$ samples. (b) Experimental In and N content of the samples grown on the (100) and (a11)-oriented substrates, obtained from HR-XRD and PhR measurements. (c) PhR spectra of two of the samples reflecting the degeneracy break of the upper valence band of the samples, and hence their strain state.

The nominal In and N compositions are 20% and 3%, respectively, which were chosen to obtain optical emission in the $1.3-1.5\mu$m region, which is of relevance in the fiber telecommunications field.

In previous studies, the samples were characterized by means of photoluminescence, photomodulated reflectance, high-resolution X-ray diffraction, and X-ray wavelength dispersion spectroscopy to check their optical quality and composition [44, 45]. The nitrogen and indium contents were found to be close to the nominal values, as can be seen in figure 6.9b. Figure 6.9c shows the PhR measurements of two different $InGaAs_{1-x}N_x$ thin films grown on differently orientated GaAs substrates. The PhR measurements revealed an energy splitting between the light and heavy hole bands, which indicate that the $InGaAs_{1-x}N_x$ thin films are fully strained, contrary to the thick $GaAs_{1-x}N_x$ epilayers of the previous section.

Se-doped $GaAs_{1-x}N_x$ layers

For the highly doped $GaAs_{1-x}N_x$ samples, we used selenium as the donor impurity. Se-doped dilute nitrides were grown at the *Research Institute for Electronic Science*, Hokkaido University (Japan), with a Metal-Organic MBE (MOMBE) growth system. The metal-organic precursors were triethylgallium (TEGa), monomethylhydrazine (MMHy) and trisdimethylaminoarsenic (TDMAAs) for $GaAs_{1-x}N_x$, and ditertiarybutylselenide (DtBSe) for Se dopants. Arsenic, nitrogen and selenium pressures were varied in order to obtain several N fractions and Se concentrations. The N content of the studied samples ranges from 0.1 to 0.3%.

The layers were grown on a semi-insulating GaAs substrate with a GaAs buffer layer under a growth temperature of 600°C (see figure 6.10). The resulting thicknesses of the epilayers are ∼170nm for all the films.

Hall measurements revealed electron concentrations from 0.5 to 1.5 $\times 10^{19}$cm^{-3}. Temperature dependent Hall measurements showed a low dependence of the electron mobility as a function of temperature, which suggests that impurity scattering may be the predominant process which limits the mobility in the samples.

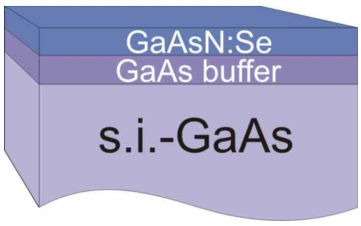

Sample N	Thickness (μm)	N_e (10^{18}cm^{-3})	μ_{Hall} (cm$^2/Vs$)
0%	0.19	7.7	607
0.1%	0.18	5.3	101
0.2%	0.14	9.0	88
0.23%	0.13	7.8	61
0.3%	0.14	15.0	46

Figure 6.10: Structural scheme and Hall data of the Se-doped $GaAs_{1-x}N_x$ samples.

6.4 Results and Discussion: Related Publications

The results and discussions concerning the studies on dilute nitrides can be found in the following publications:

Optical phonon behavior in strain-free dilute Ga(As,N) studied by Raman scattering
Journal of Applied Physics **102** 013502 (2007)

Dilute (In,Ga)(As,N) thin films grown by molecular beam epitaxy on (100) and non-(100) GaAs substrates: a Raman scattering study
Journal of Materials Science: Materials in Electronics **20** S116 (2009)

LO phonon-plasmon coupled modes and carrier mobilities in heavily Se-doped Ga(As,N) thin films
Journal of Materials Science: Materials in electronics **20** S425 (2009)

Electron effective mass and mobility in heavily doped n-$GaAs_{1-x}N_x$ probed by Raman scattering
Journal of Applied Physics **103** 103528 (2008)

JOURNAL OF APPLIED PHYSICS **102**, 013502 (2007)

Optical phonon behavior in strain-free dilute Ga(As,N) studied by Raman scattering

J. Ibáñez, E. Alarcón-Lladó, R. Cuscó, and L. Artús[a)]
Institut Jaume Almera, Consell Superior d'Investigacions Científiques (CSIC), Lluís Solé i Sabarís s.n., Barcelona 08028, Catalonia, Spain

M. Hopkinson
Department of Electronic and Electrical Engineering, University of Sheffield, S3 3JD Sheffield, United Kingdom

(Received 22 March 2007; accepted 9 May 2007; published online 3 July 2007)

We present a Raman-scattering study on strain-free dilute Ga(As,N) epilayers grown by molecular beam epitaxy. The aim of our work is to discriminate the effect of alloying from the effect of biaxial strain on the frequency behavior of the optical phonon modes of Ga(As,N). In the relaxed epilayers, we observe the following: (i) for the GaN-like LO mode, an upward frequency shift with increasing N which is larger than previously observed in strained samples; (ii) for the GaAs-like LO mode, a redshift with increasing N content which is lower than those reported in the literature on strained samples; and (iii) for the GaAs-like TO mode, we observe a very minor blueshift with increasing N fraction. We discuss the origin of the observed shifts, with particular attention to the reduction of the GaAs-like TO-LO splitting in Ga(As,N). Our data and analysis suggest that such reduction cannot be explained only by a reduction of the total number of Ga–As oscillators due to the substitution of As by N. We discuss the effects of disorder and of ionic plasmon coupling between the GaAs and GaN sublattices of Ga(As,N) on the behavior of the GaAs-like LO mode of the alloy. We conclude that the behavior of this mode is determined by long-range effects. © *2007 American Institute of Physics*. [DOI: 10.1063/1.2749491]

I. INTRODUCTION

Dilute Ga(As,N) alloys and related compounds have recently attracted much attention due to their unique optical properties, which could be exploited to develop optoelectronic devices operating in the 1.3–1.55 μm range of interest for optical fiber communications. Raman spectroscopy is a standard technique to characterize the strain and composition of III-V alloys. Several works have used resonant and nonresonant Raman scattering to investigate dilute $GaAs_{1-y}N_y$ layers.[1–7] In particular, the resonant Raman studies have provided valuable information about the wave function symmetry of the E_- and E_+ subbands of Ga(As,N) observed by reflectance spectroscopy.[3–5]

The optical phonons of Ga(As,N) exhibit a two-mode behavior in the dilute regime. It has been shown that the GaAs-like longitudinal optical (LO) branch of $GaAs_{1-y}N_y$ ($y \lesssim 5\%$) shifts to lower frequencies with increasing y.[1,2,5] In contrast, no appreciable frequency variation with composition of the GaAs-like transverse optical (TO) phonon mode of Ga(As,N) has been observed. The GaN-like LO phonon of Ga(As,N) appears at $\sim 470\ cm^{-1}$ and shifts to higher frequencies with increasing y.[1,4–6] Prokofyeva *et al.*[1] studied a series of strained Ga(As,N) epilayers grown pseudomorphically on GaAs and showed that the downward frequency shifts of the GaAs-like LO mode arise from two different causes: (i) biaxial strain and (ii) alloying effects. The interest of studying relaxed Ga(As,N) layers to confirm that alloying redshifts this mode was recognized in that work.[1] Such type of study on strain-free samples is of particular importance in dilute Ga(As,N) because the elastic constants of this compound might exhibit some deviation from Vegard's law,[8] and this would affect the analysis of the strain-induced phonon frequency shifts in the strained epilayers. Likewise, the frequency shifts observed for the GaN-like LO mode in previous works are likely influenced by biaxial-strain effects. Thus, it would be desirable to study unstrained epilayers in order to discriminate the effect of alloying from that of strain on the frequency behavior of this mode.

In the present work we use the Raman scattering to investigate the behavior of the optical phonons of unstrained dilute $GaAs_{1-y}N_y$. For this purpose, we study a series of relaxed $GaAs_{1-y}N_y$ thick layers grown by molecular beam epitaxy (MBE) on (100)-GaAs substrates (y=0.05%, 0.1%, 0.2%, 0.7%, and 1.5%). To measure the frequency of the forbidden GaAs-like TO modes, we have carried out Raman experiments with the samples tilted about 60° off-normal incidence. We show that the GaAs-like LO branch of strain-free Ga(As,N) displays a downward frequency shift with increasing y, which confirms that this phonon branch is affected by alloying. In contrast, we find that the GaAs-like TO mode exhibits a slight upward shift with increasing N content. With regard to the GaN-like LO mode, we find that this mode blueshifts with increasing y in the unstrained epilayers. The observed blueshift is larger than previously observed in biaxially strained Ga(As,N).

We discuss the origin of the alloying-induced frequency shifts observed in our strain-free Ga(As,N) samples. We

[a)]Electronic mail: lartus@ija.csic.es

show that the reduction of the number of Ga–As bonds due to the incorporation of substitutional N together with the presence of N-related disorder may account for the observed reduction of the GaAs-like TO-LO splitting. The role of ionic plasmon coupling between the GaAs and GaN sublattices of Ga(As,N) on the frequency of the LO phonon modes is also discussed. We conclude that long-range effects dominate the phonon behavior of the GaAs-like LO branch of Ga(As,N).

II. EXPERIMENTAL DETAILS

Strain-free, 1.5-μm-thick $GaAs_{1-y}N_y$ layers with $y=0.05\%$, 0.1%, 0.2%, 0.7%, and 1.5% were grown by MBE on (100)-GaAs substrates. The composition of the samples was checked by low-temperature photoluminescence (PL), while the relaxed strain state of the films was confirmed by low-temperature photoreflectance (PR) measurements, which did not show any of the strain-related features that appear in Ga(As,N) or (In,Ga)(As,N) grown pseudomorphically on GaAs.[9,10]

Raman measurements were excited at room temperature and at 80 K with the 514.5 nm line of an Ar^+ laser. The spectra were recorded with a Jobin-Yvon T64000 Raman spectrometer equipped with a charge coupled device (CCD) detector. The experiments were performed on a (100) face by using either the double subtractive or the triple additive configuration of the spectrometer with 100 μm slits. To obtain a higher accuracy in the measurement of the frequency of the GaAs-like TO modes of Ga(As,N) as a function of composition, we carried out Raman measurements with the samples tilted about 60° off-normal incidence. With this procedure, the selection rules for the TO phonon modes of zinc-blende semiconductors, forbidden in backscattering on a (100) face, are circumvented, and thus the intensity of the TO peaks is enhanced (see, for instance, Ref. 11). The measurements in off-normal incidence were performed at room temperature by using the triple additive configuration of the spectrometer and 100 μm slits.

III. RESULTS AND DISCUSSION

Figure 1(a) shows a typical room-temperature Raman spectrum of the strain-free $GaAs_{1-y}N_y$ epilayers studied in this work ($y=0.7\%$). As in the case of coherently grown Ga(As,N) thin films,[1,2,5] the spectrum of the unstrained sample is dominated by the GaAs-like LO mode located at $\sim$290 cm^{-1}. The forbidden GaAs-like TO mode, centered at 269 cm^{-1}, is also observed in the spectrum of the strain-free sample. On the low-frequency tail of the TO peak we observe a weak shoulder at $\sim$255 cm^{-1} that has been previously attributed to the TO(X) phonon mode, activated by disorder.[5] Second-order features appear in the 300–400 and 480–600 cm^{-1} ranges.[1] As in the case of the strained Ga(As,N), we observe the GaN-like LO mode at $\sim$470 cm^{-1}.[1,5]

Next, we carry out a detailed analysis of the frequency behavior of the different first-order optical modes of strain-free, dilute Ga(As,N). We will pay special attention to the TO-LO splitting of the GaAs-like phonon modes.

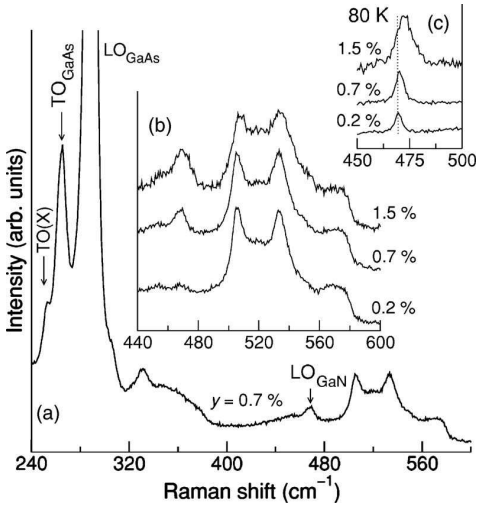

FIG. 1. (a) Raman spectrum of a relaxed $GaAs_{1-y}N_y$ epilayer acquired at room temperature ($y=0.7\%$). (b) Detailed spectra, acquired at room temperature, showing the second-order optical peaks and the evolution of the GaN-like LO mode with increasing y of three different $GaAs_{1-y}N_y$ epilayers ($y=0.2\%$, 0.7%, and 1.5%). (c) Detailed spectra, acquired at 80 K, showing the evolution of the GaN-like LO mode with increasing y of three different $GaAs_{1-y}N_y$ epilayers ($y=0.2\%$, 0.7%, and 1.5%).

A. GaN-like LO mode

Figure 1(b) shows the 440–600 cm^{-1} spectral region for our $GaAs_{1-y}N_y$ samples with higher N content ($y=0.2\%$, 0.7%, and 1.5%). The spectra were acquired at room temperature. Besides the second-order optical peaks above 480 cm^{-1}, the GaN-like LO mode at $\sim$470 cm^{-1} is visible in all spectra, even in the case of the sample with $y=0.2\%$. As expected, the intensity of this peak increases with increasing y.

As can be seen in Fig. 1(b), the GaN-like LO mode gives rise to a weak and broad feature for all samples, in particular, for the sample with $y=0.2\%$. As a consequence, it was not possible to measure with high accuracy the frequency of this mode from the room-temperature spectra. In order to determine the composition dependence of the GaN-like mode in our samples, we carried out Raman measurements at 80 K. In Fig. 1(c) we plot the spectral region at 80 K of the GaN-like LO mode for the samples with $y=0.2\%$, 0.7%, and 1.5%. For $y<0.2\%$, the GaN-like mode was not observed. As expected, the peaks are much sharper at low temperature, enabling us to measure their frequency position. As is clear from Fig. 1(c), the peak for the sample with $y=1.5\%$ is blueshifted, around 3 cm^{-1}, with respect to that of the sample grown with $y=0.2\%$. From a linear fit to the frequency of the GaN-like LO peaks of these three samples, we obtain the following composition dependence for this mode in relaxed Ga(As,N):

$$\omega(\mathrm{LO_{GaN}})\ (\mathrm{cm^{-1}}) = (470 \pm 1) + (2.5 \pm 0.5)y(\%), \qquad (1)$$

where the $y=0$ value corresponds to the frequency of the Ga–N impurity mode in bulk GaAs at 80 K. Although more samples would be required to reduce the error of the slope thus obtained, our results already indicate that the blueshift of the GaN-like LO mode in the strain-free samples

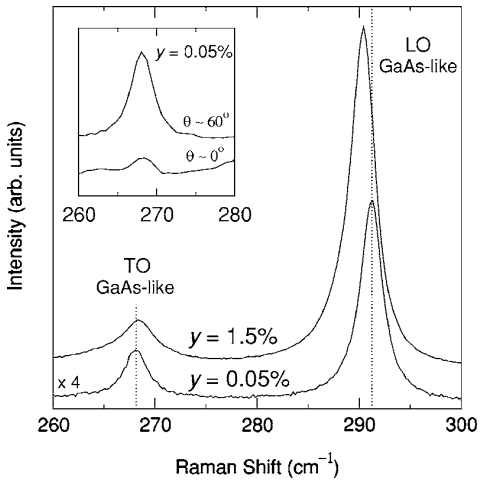

FIG. 2. Room-temperature Raman spectra of two $GaAs_{1-y}N_y$ epilayers, with $y=0.05\%$ and $y=1.5\%$, acquired off-normal incidence to enhance the intensity of the TO peaks. Inset: detail of the TO peak for the $GaAs_{1-y}N_y$ epilayer with $y=0.05\%$, acquired in backscattering configuration ($\theta\sim0°$) and off-normal incidence ($\theta\sim60°$).

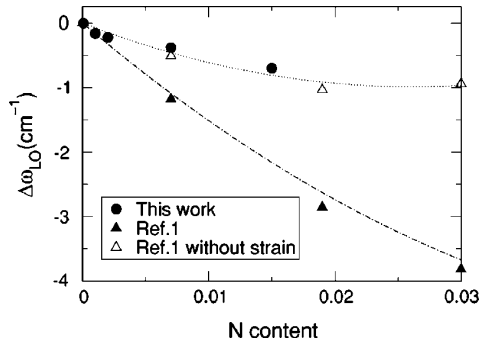

FIG. 3. Frequency of the GaAs-like LO mode obtained from the Raman spectra of our $GaAs_{1-y}N_y$ epilayers (closed circles). For comparison purposes, the LO frequencies measured by Prokofyeva *et al.* in Ref. 1 on coherently strained Ga(As,N) samples are also plotted with closed triangles. The open triangles show the corresponding LO frequency values obtained by subtracting the strain-induced shifts from the experimental values of Ref. 1.

$[2.5y(\%)\ \text{cm}^{-1}]$ is larger than that found in previous works on strained epilayers. While in Ref. 1 the observed blueshifts were of about $1.97y(\%)\ \text{cm}^{-1}$ for $y\lesssim3\%$, shifts of $\sim1.53y(\%)\ \text{cm}^{-1}$ for $y\lesssim2\%$ were found in Ref. 5. It may be noted that the frequency dependence observed in Ref. 5 above $y\sim3\%$ was not linear, which may be due to the presence of biaxial strain in the samples or to the effect of nonsubstitutional N in the crystal lattice.

B. GaAs-like optical modes

In backscattering configuration from a (100) face of a zinc-blende compound, the LO modes are allowed and the TO modes are forbidden. Accordingly, the GaAs-like TO peak is very weak in the Ga(As,N) samples with lower N content; only in the samples with higher N content are the GaAs-like TO peaks clearly visible due to a disorder-induced relaxation of the selection rules. To study simultaneously the frequency behavior of the GaAs-like TO and LO modes in all our samples, we carried out Raman measurements with the samples tilted about 60° off-normal incidence to circumvent the selection rules for the TO phonons. We plot in Fig. 2 the corresponding spectra for the $GaAs_{1-y}N_y$ epilayers with $y=0.05\%$ and 1.5%. In the two curves, acquired at room temperature, both the GaAs-like TO ($\sim268\ \text{cm}^{-1}$) and LO modes ($\sim290\ \text{cm}^{-1}$) are visible. The spectrum of the sample with $y=0.05\%$ is virtually identical to that of undoped GaAs. To illustrate the relaxation of the selection rules for the TO mode when the spectra are acquired off-normal incidence, we plot in the inset of Fig. 2 two Raman spectra of the sample with $y=0.05\%$, in the frequency region of the TO peak, acquired in normal incidence (i.e., in backscattering geometry) and with the sample tilted about 60° off-normal incidence. The figure shows the sizeable intensity increase of the TO peak achieved when the sample is tilted. The weak intensity of the TO peak in backscattering geometry is a consequence of the good crystal quality of this sample. As expected, the frequency of the TO peaks remains unchanged regardless of the incidence angle.

As can be observed in Fig. 2, the LO peak of the sample with $y=1.5\%$ is shifted to lower frequencies, around $0.7\ \text{cm}^{-1}$, with respect to the sample with $y=0.05\%$. This result, which we obtain in strain-free samples, confirms that alloying effects in Ga(As,N) redshift the GaAs-like LO phonon mode. We plot in Fig. 3 the frequency of the GaAs-like LO mode measured in all our samples (closed circles). The figure shows the progressive redshift of this mode with increasing y in the relaxed epilayers. From a linear fit to these data, we obtain the following composition dependence for the GaAs-like LO mode in relaxed Ga(As,N) ($y\lesssim1.5\%$):

$$\omega(\text{LO}_{\text{GaAs}})\ (\text{cm}^{-1}) = (290\pm1) - (0.42\pm0.05)y(\%). \quad (2)$$

The shift that we obtain is virtually identical to that found in Ref. 1, where the redshift component attributed to alloying effects (i.e., after subtraction of the strain effects originated by the pseudomorphic growth of the samples) was estimated to be around $-0.4y(\%)\ \text{cm}^{-1}$ for $y\lesssim3\%$. For comparision purposes, we have also plotted in Fig. 3 the LO frequencies measured by Prokofyeva *et al.*[1] on strained Ga(As,N) epilayers grown on GaAs (closed triangles), together with the corresponding LO frequency values obtained by subtracting from the experimental frequencies the strain-induced shifts (open triangles). As explained in Ref. 1, the strain-induced shifts amount to approximately $-0.96y(\%)\ \text{cm}^{-1}$, as estimated from biaxial-strain effects in Ga(As,N) epilayers coherently grown on GaAs substrates. Figure 3 shows that the experimental LO frequencies measured in our samples and those of Ref. 1 are in good agreement once the biaxial-strain effects are taken into account.

From the spectra acquired under off-normal incidence (Fig. 2), we find that for the sample with $y=1.5\%$ the GaAs-like TO mode is scarcely blueshifted, around $0.3\ \text{cm}^{-1}$, with respect to the sample with $y=0.05\%$. This result is in agreement with the upward frequency shift expected for the GaAs-like TO frequency of strain-free dilute $GaAs_{1-y}N_y$ with increasing y due to the smaller size of N atoms (i.e., smaller

interatomic distances in $GaAs_{1-y}N_y$ with increasing y should yield tighter spring constants). Whereas no data on the TO phonon frequencies of Ga(As,N) were provided in Refs. 1 and 5, in Ref. 7 it was reported that the GaAs-like TO mode does not show any measurable shift with composition in coherently grown epilayers. In contrast, a very small redshift, which could be attributed to biaxial-strain effects, was observed in Ref. 2. With regard to this, we would like to remark that the determination of the frequency of the GaAs-like TO peaks performed in the previous works was hampered by the fact that this mode is forbidden due to the selection rules, giving rise to weak, broad features in the Raman spectra. As discussed above, here we have overcome this limitation by performing the experiments under off-normal incidence.

C. GaAs-like TO-LO splitting

Our measurements reveal that the TO-LO splitting for the GaAs-like optical modes in strain-free $GaAs_{1-y}N_y$, $\omega(LO_{GaAs})-\omega(TO_{GaAs})$, is reduced by about 1 cm^{-1} from $y=0.05\%$ to $y=1.5\%$. This result cannot be accounted for by short-range effects (i.e., by a change in the spring constant or disorder effects), because these should affect both TO and LO modes in a similar manner. On the contrary, we have observed that the GaAs-like TO mode exhibits a small blueshift, while the GaAs-like LO mode redshifts with increasing N content.

Some authors have attributed the shifts of the GaAs-like LO mode of Ga(As,N) to disorder and have used the spatial correlation model (SCM), based on finite-size effects on the phonon frequencies,[12] to determine phonon correlation lengths as a function of the N content.[7,13] With regard to this, it should be mentioned that previous works have shown that the SCM fails to explain simultaneously the frequency behavior of the TO and LO peaks in disordered GaAs.[14,15] Despite its usefulness to account for the phonon shifts in microcrystals, the SCM has several limitations. First, the SCM predicts larger confinement-induced frequency shifts for the TO mode than for the LO mode of GaAs, as deduced from Raman scattering results on GaAs/AlAs superlattices.[14,16] However, such TO phonon shifts are not observed experimentally in disordered GaAs.[14,17] In addition, to fit the Raman data with the SCM in disordered GaAs one has to arbitrarily change the phonon amplitude at the boundary of the microcrystalline regions from $1/e$ to $\exp(-4\pi^2)$.[15] An alternative account of the shifts and broadening of the optical phonon Raman peaks of disordered GaAs was provided by Burns *et al.*, who considered both strain effects and a change in the TO-LO splitting due to the presence of vacancies, antisites, and interstitials in order to explain their results in ion-bombarded GaAs.[14] The long-range effects associated with LO phonons (i.e., the macroscopic ionic polarization) may also play an important role in the behavior of the GaAs-like LO branch of Ga(As,N).

Next, we analyze the effect of long-range effects on the frequency of the GaAs-like LO phonon branch of Ga(As,N). For undoped GaAs, the ionic plasma frequency associated with the LO phonons, $\Omega_{GaAs}=(\omega_{LO}^2-\omega_{TO}^2)^{1/2}$, is given by[18,19]

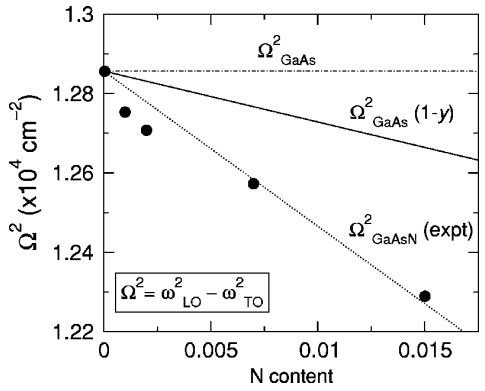

FIG. 4. Squared ionic plasmon frequency, $\Omega^2_{GaAsN}(\text{expt})=\omega^2(LO_{GaAs})-\omega^2(TO_{GaAs})$, associated with the GaAs-like LO mode of Ga(As,N) as determined from the GaAs-like TO and LO frequencies measured in the samples studied in this work (closed circles). For comparison purposes, the progressive reduction of the squared ionic plasmon frequency of the GaAs-like LO mode resulting from the substitution of As by N, i.e., $\Omega^2_{GaAs}(1-y)$, is also plotted. Ω^2_{GaAs} is the squared ionic plasmon frequency for bulk GaAs.

$$\Omega^2_{GaAs}=\frac{4\pi N e^{*2}_{T,GaAs}}{\epsilon_\infty V \mu_{GaAs}}, \tag{3}$$

where ω_{LO} and ω_{TO} are the long-wavelength LO and TO phonon frequencies of bulk GaAs, respectively μ_{GaAs} is the Ga–As reduced mass, $e^*_{T,GaAs}$ is the transverse effective charge for the longitudinal Ga–As oscillators, N is the total number of Ga–As bonds (i.e., N is the number of primitive cells, so there are $2N$ atoms in the GaAs crystal), V is the volume of the crystal ($V=Na_0^3/4$, where a_0 is the lattice parameter of the conventional cell), and ϵ_∞ is the high-frequency dielectric constant of GaAs.

To understand why the TO-LO splitting is reduced in Ga(As,N) with increasing N content, we first note that $\epsilon_\infty(\text{GaAsN})<\epsilon_\infty(\text{GaAs})$, as can be concluded from the corresponding values for GaAs and c-GaN. Thus, the variation of ϵ_∞ cannot explain the observed reduction of Ω_{GaAsN}. Similarly, as expected from the smaller lattice parameter of c-GaN with respect to GaAs, the lattice parameter of Ga(As,N), and therefore the total volume of the crystal, decreases with increasing y,[20] which neither can explain the observed reduction in the TO-LO splittings. On the other hand, it is expected that $e^*_{T,GaAs}$ remains basically unchanged for the Ga–As oscillators within the GaAs sublattice of the Ga(As,N) ternary alloy.[19] This is particularly true in the dilute regime. In contrast, the total number of Ga–As oscillators is reduced when N is incorporated substitutionally into GaAs. In this case, the total number of Ga–As bonds N has to be replaced by $N(1-y)$ in Eq. (3), giving rise to a reduction of the TO-LO splitting.

We plot in Fig. 4 (solid line) the squared ionic plasmon frequency associated with the GaAs-like LO mode of Ga(As,N) that results from considering only substitutional nitrogen, i.e., $\Omega^2_{GaAs}(1-y)$ (here we neglect the changes in ϵ_∞ and a_0, the effects of which are expected to be much smaller than those related to the reduction of the number of oscillators). For comparison, we also plot the squared ionic plasmon frequency as determined from the Raman measurements

in our samples, i.e., $\Omega^2_{GaAsN}(expt)=\omega^2(LO_{GaAs})-\omega^2(TO_{GaAs})$ (closed circles). Surprisingly, the experimental $\Omega^2_{GaAsN}(expt)$ values are appreciably lower than $\Omega^2_{GaAs}(1-y)$ (see Fig. 4). Consequently, most of the TO-LO splitting reduction (and therefore most of the LO phonon shifts) that we observe in our samples still remain to be explained. By subtracting $\Omega^2_{GaAs}(1-y)$ from $\Omega^2_{GaAsN}(expt)$ in Fig. 4, we find that the deviation between the experimental data and the theoretical TO-LO splitting, obtained assuming only substitutional N, is $\Delta\Omega^2=\Omega^2_{GaAsN}(expt)-\Omega^2_{GaAs}(1-y)\approx -0.02\Omega^2_{GaAs}y(\%)$; this amounts to more than 60% of the total TO-LO splitting reduction observed in our samples.

Here, we speculate that the fraction of $\Omega^2_{GaAsN}(expt)$ reduction that remains to be explained may be attributed to the presence of defects (interstitials, vacancies, and antisites). Such defects were shown to give rise to a sizeable reduction of Ω^2_{GaAs} in disordered GaAs.[14] Following the arguments of Burns *et al.*,[14] we find that a ratio of vacancies (antisites) to atoms of ~0.5% (~0.3%) in the sample with $y=1.5\%$ may account for our Raman data. With regard to this, one should keep in mind that dilute nitrides contain a high density of defects, mainly N interstitials, Ga vacancies, and N clusters, which are responsible for the low luminescence efficiency of the as-grown materials.[21,22] Thus, it is likely that a combination of such defects lowers the total number of Ga–As oscillators and/or changes the high-frequency dielectric constant of the material, giving rise to an important part of the observed LO phonon shifts.

Finally, we consider the effect of ionic plasmon coupling on the frequency of the GaAs-like LO mode of Ga(As,N), which may also explain part of the shifts observed for this phonon mode. As it is well known, the LO phonon branches of ternary alloys may display appreciable bowings as a consequence of the long-range Couloumb interactions involved in the long-wavelength LO phonons. This is the case, for instance, of (In,Ga)As.[19] Accordingly, it cannot be ruled out that the behavior of the GaAs-like LO mode of Ga(As,N) be a consequence of the electrostatic coupling between the GaAs and GaN sublattices of this compound, yielding a downward (upward) frequency shift of the GaAs-like (GaN-like) LO mode. To test this hypothesis we used the repulsion model outlined in Ref. 19, which allows one to determine the LO frequencies of ternary alloys without any adjustable parameters, in order to estimate the effect of ionic plasmon coupling on the GaAs-like LO branch of $GaAs_{1-y}N_y$. This model has successfully accounted for the LO phonon behavior[19] and LO-plasmon coupling phenomena[23,24] in (In,Ga)As ternary alloys. For the calculations, which we restricted to the dilute regime, we used the following data: for the GaAs-like TO branch of Ga(As,N), we used the experimental frequency dependence, as obtained from Fig. 2; and for the GaN-like branches, we used Vegard's law together with the frequency of the TO and LO modes of *c*-GaN (555 and 742 cm^{-1}, respectively) and the frequency of the Ga–N impurity mode in GaAs (470 cm^{-1}). Our analysis indicates that only around 10% of the reduction of the TO-LO splitting observed in our samples may be originated by coupling between the two polar sublattices. Thus, we conclude that the observed TO-LO splitting reduction in dilute Ga(As,N) is primarily due to the reduction in the number of Ga–As bonds caused by the substitutional N and by the increased amount of point defects and clusters induced by the presence of N.

IV. CONCLUSIONS

We have used Raman scattering to investigate the behavior of the optical phonons of unstrained, dilute $GaAs_{1-y}N_y$ ($y\lesssim 1.5\%$), where the phonon frequency shifts can be solely attributed to alloying effects. We find that the GaN-like LO mode blueshifts with increasing y in the strain-free epilayers. The observed shifts, of about $2.5y(\%)$, are higher than those previously observed in strained samples. In turn, we have found that the GaAs-like LO mode in unstrained $GaAs_{1-y}N_y$ exhibits a downward frequency shift with increasing y. The observed redshift amounts to about $-0.42y(\%)$, in good agreement with previous estimations of the alloying effect in strained epilayers.

Given that the frequency of the GaAs-like TO mode does not change significantly in this composition range, the redshift of the GaAs-like LO mode cannot arise from short-range effects. The observed shifts imply an appreciable reduction of the GaAs-like TO-LO splitting that cannot be explained solely by the reduction of Ga–As oscillators due to the substitution of As ions by N ions. A disorder-induced reduction of the number of Ga–As oscillators that contributes to the long-range effects and a minor contribution of ionic plasmon coupling between the GaAs and GaN sublattices of Ga(As,N) may account for the observed behavior of the GaAs-like LO mode of this material. We conclude that long-range effects determine the behavior of the GaAs-like LO mode of dilute Ga(As,N).

ACKNOWLEDGMENTS

This work was supported by the Spanish Ministry of Science and Technology (Contract No. MAT2004-0664 and Ramon y Cajal Program). We would like to thank Amalia Patanè for the PL and PR data.

[1] T. Prokofyeva, T. Sauncy, M. Seon, M. Holtz, Y. Qiu, S. Nikishin, and H. Temkin, Appl. Phys. Lett. **73**, 1409 (1998).
[2] A. M. Mintairov, P. A. Blagnov, V. G. Melehin, N. N. Faleev, J. L. Merz, Y. Qiu, S. A. Nikishin, and A. Temkin, Phys. Rev. B **56**, 15836 (1997).
[3] M. J. Seong, A. Mascarenhas, and J. F. Gaisz, Appl. Phys. Lett. **79**, 1297 (2001).
[4] M. J. Seong, M. C. Hanna, and A. Mascarenhas, Appl. Phys. Lett. **79**, 3974 (2001).
[5] A. Mascarenhas and M. J. Seong, Semicond. Sci. Technol. **17**, 823 (2002).
[6] J. Wagner, T. Geppert, K. Köhler, P. Ganser, and N. Herres, J. Appl. Phys. **90**, 5027 (2001).
[7] H. F. Liu, N. Xiang, S. Tripathy, and S. J. Chua, J. Appl. Phys. **99**, 103503 (2006).
[8] M. Reason, X. Weng, W. Ye, D. Dettling, S. Hanson, G. Obeidi, and R. S. Goldman, J. Appl. Phys. **97**, 103523 (2005).
[9] Y. Zhang, A. Mascarenhas, H. P. Xin, and C. W. Tu, Phys. Rev. B **61**, 4433 (2000).
[10] J. Ibáñez, R. Kudrawiec, J. Misiewicz, M. Schmidbauer, M. Henini, and M. Hopkinson, J. Appl. Phys. **100**, 093522 (2006).
[11] L. Artús, R. Cuscó, J. Ibáñez, N. Blanco, and G. González-Díaz, Phys. Rev. B **60**, 5456 (1999).
[12] H. Richter, Z. P. Wang, and L. Ley, Solid State Commun. **39**, 625 (1981).
[13] E. K. Koh, Y. J. Park, E. K. Kim, S. Min, and S. H. Choh, Phys. Rev. B **57**, 11919 (1998).
[14] G. Burns, F. H. Dacol, C. R. Wie, E. Burstein, and M. Cardona, Solid State

Commun. **62**, 449 (1987).
[15]I. H. Campbell and P. M. Fauchet, Solid State Commun. **58**, 739 (1986).
[16]A. K. Sood, J. Menendez, M. Cardona, and K. Ploog, Phys. Rev. Lett. **54**, 2111 (1985).
[17]K. Tiong, P. M. Amirtaraj, F. Pollak, and D. E. Aspnes, Appl. Phys. Lett. **44**, 122 (1984).
[18]G. Lukovsky, R. M. Martin, and E. Burstein, Phys. Rev. B **4**, 1367 (1971).
[19]J. Groenen, R. Carles, G. Landa, C. Guerret-Piécourt, C. Fontaine, and M. Gendry, Phys. Rev. B **58**, 10452 (1998).
[20]See, for instance, W. J. Fan, S. F. Yoon, T. K. Ng, S. Z. Wang, W. K. Loke, R. Liu, and A. Wee, Appl. Phys. Lett. **80**, 4136 (2002), and references therein.
[21]W. Li, M. Pessa, T. Ahlgren, and J. Decker, Appl. Phys. Lett. **79**, 1094 (2001).
[22]J. Toivonen, T. Hakkarainen, M. Sopanen, H. Lipsanen, J. Oila, and K. Saarinen, Appl. Phys. Lett. **82**, 40 (2003).
[23]R. Cuscó, L. Artús, S. Hernández, J. Ibáñez, and M. Hopkinson, Phys. Rev. B **65**, 035210 (2002).
[24]J. Ibáñez, E. Tarhan, A. K. Ramdas, S. Hernández, R. Cuscó, L. Artús, M. R. Melloch, and M. Hopkinson, Phys. Rev. B **69**, 075314 (2004).

J Mater Sci: Mater Electron (2009) 20:S116–S119
DOI 10.1007/s10854-007-9462-7

Dilute (In,Ga)(As,N) thin films grown by molecular beam epitaxy on (100) and non-(100) GaAs substrates: a Raman-scattering study

Jordi Ibáñez · Esther Alarcón-Lladó · Ramon Cuscó · Lluís Artús · Mohamed Henini · Mark Hopkinson

Received: 19 July 2007 / Accepted: 25 October 2007 / Published online: 15 November 2007

Abstract We use Raman scattering to investigate a series of $In_xGa_{1-x}As_{1-y}N_y$ epilayers ($x \sim 20\%$ and $y \sim 3\%$) coherently grown on (100) and on (N11) GaAs substrates ($N = 1$, 3, 4, and 5). We use biaxial-strain theory to evaluate the effect of N alloying on the frequency of the GaAs-like phonon optical modes of dilute InGaAsN. We find that N alloying reduces the TO–LO splitting of the GaAs-like modes. We investigate the effect of substrate orientation on the N-related vibrational modes. Our results suggest that the growth direction does not affect substantially the local bonding of N atoms in InGaAsN.

1 Introduction

Dilute In(Ga)AsN semiconductor alloys have recently attracted much attention due to their remarkable properties and their potential application for the fabrication of optoelectronic devices working in the 1.3–1.5 μm region [1]. Despite much work dealing with the optical and electronic properties of dilute nitrides grown on (100) substrates, relatively little is known about their non-(100) counterparts. High-index surfaces pose particular interest for the growth of dilute nitrides, since both the incorporation of N and the type of N-related defects may be strongly affected by substrate orientation.

Raman scattering is widely used to investigate the lattice dynamics, the crystal quality, the composition and the strain of III–V semiconductors. Raman scattering also provides information about the local bonding of impurities, as for instance N into In(Ga)As. In the present work we use Raman scattering to investigate a series of strained $In_xGa_{1-x}As_{1-y}N_y$ epilayers ($x \sim 20\%$ and $y \sim 3\%$) grown by molecular beam epitaxy (MBE) on different (100) and non-(100) GaAs substrates. The aim of this work is twofold: (i) to evaluate the effect of N on the frequency of the InAs- and GaAs-like phonon modes of dilute InGaAsN by studying samples with an appreciable N content ($x \sim 3\%$); (ii) to investigate the vibrational properties of the InGaAsN system as a function of the growth direction, with special emphasis on the N-related vibrational modes.

To assess the effect of N-related alloying on the frequency of the InAs-like and GaAs-like phonon modes of InGaAsN, we have evaluated the strain-induced frequency shifts by using standard biaxial-strain theory. We discuss the possible mechanisms involved in the alloying-induced frequency shifts of InGaAsN. We do not find significant changes in the N-related vibrational modes with substrate orientation, which suggests that the local bonding of N atoms in InGaAsN is not substantially affected by the growth direction.

2 Experiment

Five 100-nm thick $In_xGa_{1-x}As_{1-y}N_y$ films ($x \sim 20\%$, $y \sim 3\%$) were grown by solid-source MBE at 400 °C on

J. Ibáñez (✉) · E. Alarcón-Lladó · R. Cuscó · L. Artús
Institut Jaume Almera, Consell Superior d'Investigacions Científiques (CSIC), 08028 Barcelona, Catalonia, Spain
e-mail: jibanez@ija.csic.es

M. Henini
School of Physics and Astronomy, University of Nottingham, Nottingham NG7 2RD, UK

M. Hopkinson
Department of Electronic and Electrical Engineering, University of Sheffield, Sheffield, UK

J Mater Sci: Mater Electron (2009) 20:S116–S119

different GaAs substrates with the following orientations: (100), (111)A, (311)A, (411)A, and (511)A. For the growth, a 0.2-μm-thick undoped GaAs buffer layer was first deposited directly on the epiready substrates (T = 590 °C). Then, the temperature was lowered to T = 400 °C and a 0.1-μm-thick undoped GaAs layer was deposited, followed by the $In_xGa_{1-x}As_{1-y}N_y$ film.

A combination of high-resolution X-ray diffraction (HRXRD) and photoreflectance (PR) measurements were performed to determine the In and N composition of the films. Details can be found elsewhere [2, 3]. The HRXRD measurements showed that the epilayers are coherently grown on the GaAs substrates.

Room temperature and low temperature (80 K) Raman-scattering measurements were excited in a backscattering configuration with the 514.5-nm line of an Ar^+ laser. Given the absorption coefficient of $In_{0.20}Ga_{0.80}As$ for this wavelength [4], the Raman measurements are only probing the InGaAsN epilayers. The spectra were recorded with a Jobin-Yvon T64000 Raman spectrometer equipped with a charge coupled device detector cooled with liquid nitrogen. The measurements were performed with the double subtractive configuration of the spectrometer and 100-μm slits.

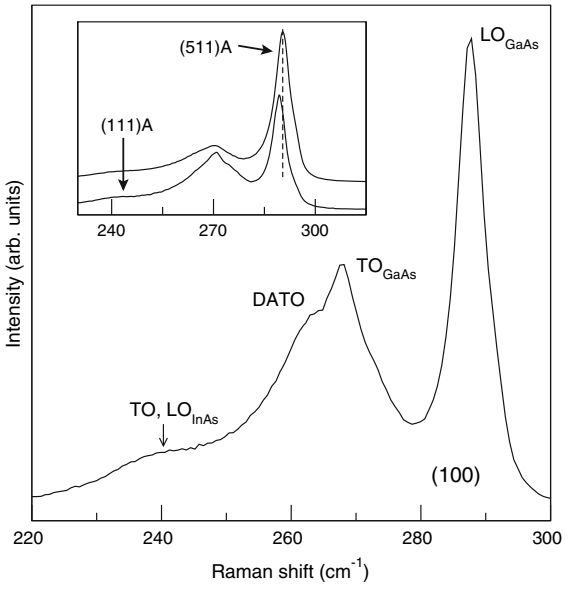

Fig. 1 Room-temperature $x(yz)\bar{x}$ Raman spectrum of a $In_xGa_{1-x}As_{1-y}N_y$ epilayer grown on (100)-GaAs (x = 22%, y = 3.7%). Inset: Raman spectra acquired in a parallel polarization configuration of the (111)A and (511)A $In_xGa_{1-x}As_{1-y}N_y$ epilayers studied in this work

3 Results and discussion

Figure 1 shows a $x(yz)\bar{x}$ Raman spectrum of the $In_xGa_{1-x}As_{1-y}N_y$ film grown on (100)-GaAs (x = 22%, y = 3.7%) [2]. As expected, owing to the selection rules for backscattering on a (100) face in zincblende compounds, the spectrum of this sample is dominated by the GaAs-like LO mode, located at $\sim$288 cm^{-1}. The peak at $\sim$268 cm^{-1} corresponds to the forbidden GaAs-like TO mode, while the broad feature that appears just below the GaAs-like TO peak has been previously observed in $In_xGa_{1-x}As$ and assigned to a disorder-activated TO (DATO) mode [5]. The weak, broad feature located at $\sim$239 cm^{-1} can be assigned to the InAs-like LO mode, with possibly some small contribution of the forbidden InAs-like TO mode. These two modes cannot be resolved because they are very close in frequency, as occurs in $In_xGa_{1-x}As$ for similar In compositions [5].

Due to the effect of N-related alloy disorder, a clear signature of the forbidden GaAs-like TO mode is observed in the spectrum of (100)-InGaAsN (Fig. 1). A strong forbidden GaAs-like LO peak in the $x(yy)\bar{x}$ configuration is also observed (not shown). These findings are similar to those reported in Ref. [6] in $In_xGa_{1-x}As_{1-y}N_y$ with lower In content (x = 6%). In that work, the strong depolarization of the GaAs-like modes was tentatively explained by the strong microscopic strain fields introduced by N in the InGaAs matrix.

The inset of Fig. 1 shows Raman spectra of two of the non-(100) samples investigated in this work [(111)A and (511)A epilayers]. As can be observed in the figure, the intensity of the different InAs- and GaAs-like first-order optical peaks varies with the growth direction due to the selection rules. However, as occurs in the (100) sample, we also observe an overall relaxation of the selection rules in all the non-(100) samples. Again, this strong depolarization effect can be attributed to N-related disorder.

The frequency of the different first-order optical modes of $In_xGa_{1-x}As_{1-y}N_y$ grown on GaAs is determined by x, y, and by biaxial strain. As a consequence, it is expected that the frequency of the InAs- and GaAs-like peaks varies slightly from sample to sample, since small compositional and strain-state differences exist in these epilayers [2]. This is illustrated in the Inset of Fig. 1, which shows that the frequency of the GaAs-like LO mode for the (111)A sample is slightly redshifted, by about 1.2 cm^{-1}, with respect to the (511)A sample. As discussed in detail in Ref. [2], these two samples have a comparable In content but a dissimilar N concentration (y = 2.3% and y = 3.3% for the (511)A and (111)A epilayers, respectively). The different N content gives rise to measurable differences in the vertical lattice spacings (i.e., the lattice spacings along the growth direction) as determined by HRXRD. Then, the observed phonon frequency shifts between these two samples can be mainly attributed to the following effects: (i) the different strain state of the epilayers as a

consequence of their different N composition; (ii) N alloying effects. Note that in GaAsN the GaAs-like LO mode is redshifted due to N alloying [7, 8]. Thus, it is expected that the Ga(In)As-like optical modes of InGaAsN are also affected by N.

Next, in order to gain information about the behavior of the Ga(In)As optical modes of InGaAsN as a function of N composition, we perform a calculation of the frequency of the GaAs-like TO and LO modes for a $In_xGa_{1-x}As$ epilayer grown on (100)-GaAs with the same In content, $x = 22\%$, and the same strain state as those of our (100) sample. To include the latter, we use the lattice spacings measured by HRXRD [2]. Then, the difference between the calculated and the experimental phonon frequencies will provide an indication of the alloying-induced shifts in InGaAsN. We do not consider the InAs-like modes because the TO mode is not observed in the Raman spectra. For the calculations, we use conventional biaxial-strain theory [9] and neglect the effect of N on the phonon deformation potentials of $In_xGa_{1-x}As_{1-y}N_y$ (i.e., we take the values of bulk $In_xGa_{1-x}As$). We use the data and analysis of Ref. [5] to obtain the frequency of the optical phonon modes of bulk (unstrained) $In_xGa_{1-x}As$ ($x = 22\%$). In Table 1, we display the strained GaAs-like TO and LO frequencies obtained from the calculations. For comparison, we display the frequency of these modes as determined from the Raman spectra of the (100) sample (Fig. 1). The experimental and calculated values displayed in Table 1 suggest that, similarly to what occurs in dilute GaAsN [7, 8], N alloying induces a redshift (blueshift) of the GaAs-like LO (GaAs-like TO) mode of InGaAsN. In the particular case of the TO mode, the estimated blueshift is appreciably larger than that observed in GaAsN [8]. These results indicate that the TO–LO splitting for the GaAs-like optical modes of InGaAsN is sizably reduced by N alloying. This is similar to what has been previously reported in GaAsN, where the observed TO–LO splitting reduction was mainly attributed to the decrease of the total number of Ga–As bonds due to the incorporation of substitutional N as well as to the presence of N-related disorder [8].

Table 1 Frequency of the GaAs-like TO and LO phonon modes measured in the (100) InGaAsN epilayer ($\omega_{exp.}$). To evaluate N alloying effects on the frequency of these modes, calculated frequencies for a (100) InGaAs epilayer with the same In content and the same strain state than the InGaAsN sample are given ($\omega_{calc.}$)

	$\omega_{exp.}$ (cm^{-1})	$\omega_{calc.}$ (cm^{-1})	($\omega_{exp.} - \omega_{calc.}$) ($cm^{-1}$)
GaAs-like LO mode	287.7	289.1	− 1.4
GaAs-like TO mode	267.8	264.5	+ 3.3

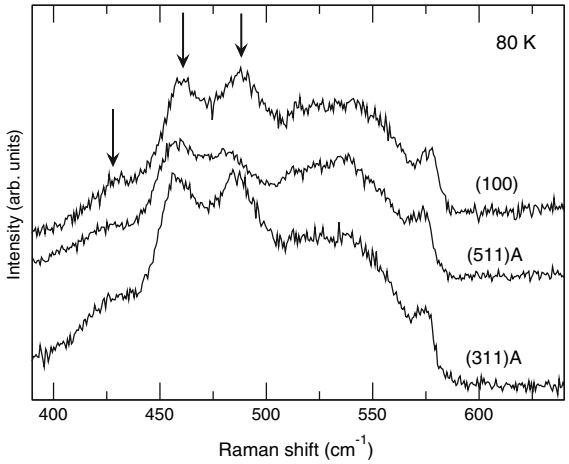

Fig. 2 Detailed spectra, acquired at 80 K in a parallel polarization geometry, showing the N-related vibrational modes and the second-order optical peaks of three of the InGaAsN epilayers studied in this work

Finally, we shift our attention to the N-related local vibrational modes (LVMs) of as-grown InGaAsN. Figure 2 shows the 400–600 cm^{-1} spectral range for the (100), (511)A and (311)A samples as obtained in a parallel polarization configuration. Similar spectra were obtained for the (411)A and (111)A epilayers (not shown for scaling reasons). These spectra were acquired at 80 K to better resolve the LVM peaks. The bands that appear above 500 cm^{-1} are also observed in InGaAs and correspond to GaAs-like second-order optical bands. In contrast, the three features marked in the figure with an arrow and located at about 430, 458 and 487 cm^{-1}, do not appear in the Raman spectrum of InGaAs. These features can be assigned to N-related LVMs. Similar LVM peaks at 425, 458, and 480 cm^{-1} were reported for $In_xGa_{1-x}As_{1-y}N_y$ with $x = 12\%$ and $y = 4\%$ in a previous study [10]. Bearing in mind that N introduces a single LVM in GaAs [7, 10], the presence of these peaks suggests that the incorporation of In into GaAsN changes the bonding environment of the N atoms, giving rise to In–N bonds ($NInGa_3$ configuration) in addition to the Ga–N bonds (NGa_4 configuration) [10, 11]. As observed in previous works, the bonding environment in InGaAsN is modified by annealing [6, 11], leading to a blueshift of the bandgap energy [12].

It is noteworthy that the intensity of the LVM peaks is larger in $x(yy)\bar{x}$ geometry than in $x(yz)\bar{x}$ geometry, which is a consequence of their A_1 character. While the intensity and width of these peaks display small changes from sample to sample that can be mainly attributed to minor compositional variations (see Fig. 2), the overall shape of the LVM spectrum, in particular the number of N-related

J Mater Sci: Mater Electron (2009) 20:S116–S119

peaks, is the same for all our (100) and non-(100) epilayers. Thus, we conclude that the atomic environment of N in InGaAsN (i.e., the number of In–N bonds formed during the growth and the resulting strain distribution around the N atoms) is not affected in a substantial manner by the growth direction.

4 Conclusions

The Raman spectrum of InGaAsN is affected by N-related disorder. Besides a strong depolarization effect, observed regardless of the growth direction, N-related disorder reduces the total number of Ga–As bonds, giving rise to a reduction of the TO–LO splitting for the GaAs-like optical modes. Our Raman spectra indicate that the local atomic environment around N is very similar for (100) and non-(100) InGaAsN.

Acknowledgements Work supported by the Spanish Ministry of Education and Science under Contract Ref. MAT2004-0664 and the Ramon y Cajal Program.

References

1. M. Henini (ed.), *Dilute Nitride Semiconductors* (Elsevier, 2005)
2. J. Ibáñez, R. Kudrawiec, J. Misiewicz, M. Schmidbauer, M. Henini, M. Hopkinson, J. Appl. Phys. **100**, 093522 (2006)
3. J. Ibáñez, M. Henini, R. Kudrawiec, J. Misiewicz, M. Schmidbauer, M. Hopkinson, J. Cryst. Growth **301–302**, 552 (2007)
4. Landolt-Börnstein, in *New Series III*, vol. 17. ed. by O. Madelung, Pt. a (Springer-Verlag, Berlin, 1982)
5. J. Groenen, R. Carles, G. Landa, C. Guerret-Piecourt, C. Fontaine, M. Gendry, Phys. Rev. B **58**, 10452 (1998)
6. S. Shirakata, M. Kondow, T. Kitatani, J. Phys. Chem. Solids. **66**, 2119 (2005)
7. T. Prokofyeva, T. Sauncy, M. Seon, M. Holtz, Y. Qiu, S. Nikishin, H. Temkin, Appl. Phys. Lett. **73**, 1409 (1998)
8. J. Ibáñez, E. Alarcón-Lladó, R. Cuscó, L. Artús, M. Hopkinson, J. Appl. Phys. **102**, 013502 (2007)
9. B. Jusserand, M. Cardona, in *Light Scattering in Solids V*, ed. by M. Cardona, G. Güntherodt (Springer, Berlin, 1989)
10. J. Wagner, T. Geppert, K. Köhler, P. Ganser, N. Herres, J. Appl. Phys. **90**, 5027 (2001)
11. S. Kurtz, J. Webb., L. Gedvilas, D. Friedman, J. Geisz, J. Olson, R. King, D. Joslin, N. Karam, Appl. Phys. Lett. **78**, 748 (2001)
12. P.J. Klar, H. Grüning, J. Koch, S. Schäfer, K. Volz, W. Stolz, W. Heimbrodt, A.M. Kamal Saadi, A. Lindsay, E.P. O'Reilly, Phys. Rev. B **64**, 121203(R) (2001)

J Mater Sci: Mater Electron (2009) 20:S425–S429
DOI 10.1007/s10854-008-9661-x

LO phonon–plasmon coupled modes and carrier mobilities in heavily Se-doped Ga(As, N) thin films

J. Ibáñez · E. Alarcón-Lladó · R. Cuscó · L. Artús · D. Fowler · A. Patanè · K. Uesugi · I. Suemune

Received: 19 July 2007 / Accepted: 15 February 2008 / Published online: 5 March 2008

Abstract We use Raman scattering to study the LO–plasmon coupled modes (LOPCMs) of *n*-type $GaAs_{1-x}N_x$ epilayers grown by molecular beam epitaxy ($0.1\% \leq x \leq 0.36\%$). We find that the LOPCMs are heavily damped in *n*-$GaAs_{1-x}N_x$ even for *x* as low as 0.1%. From a lineshape analysis based on the hydrodynamical model, we evaluate the lifetime of the LOPCMs in our samples. We compare the values thus obtained with the corresponding Hall mobilities. We find that both quantities decrease strongly with increasing *x*, which can be attributed to N-related alloy scattering of conduction band electrons in the $GaAs_{1-x}N_x$ alloy.

1 Introduction

Dilute nitride semiconductor alloys such as $GaAs_{1-x}N_x$ and $Ga_{1-y}In_yAs_{1-x}N_x (x \lesssim 5\%)$ have recently been the subject of intense research effort due to their remarkable optical and electronic properties, which could be exploited to develop GaAs-based long-wavelength photodetectors, diode lasers and high-performance solar cells [1].

Owing to the large difference in size and electronegativity between N and As atoms, N_{As} introduce quasi-localized electron states in Ga(In)As. These N-related states strongly interact with the extended band states of the matrix material, leading to a strong redshift of the band gap and to the splitting of the conduction band into two highly non-parabolic subbdands, E_- and E_+ [1].

Although the modified electronic band structure of Ga(In)AsN could be particularly advantageous to fabricate specific types of devices such as low-noise avalanche photodiodes [2] or terahertz emitters, [3] in general the use of dilute nitrides in device applications is currently limited by the drastic reduction of the *n*-type mobility of these compounds. Such low mobilities can be explained by the strong interaction between extended and localized electronic states, giving rise to a dramatic increase in the electron scattering rate. As recently shown by Fahy et al. [4] by means of a tight-binding model of the electronic structure of substitutional N in GaAs, localized states associated with N clusters play a crucial role in the low carrier mobilities measured in dilute nitrides.

Raman scattering by LO phonon–plasmon coupled modes (LOPCMs) is widely used to evaluate the free charge density of polar semiconductors. Also, it provides useful information about carrier lifetimes and effective masses in these compounds [5]. While several Raman investigations on undoped GaAsN and InGaAsN have been carried out [6–9], only a few studies have used Raman scattering to study the LOPCMs in dilute nitrides [10, 11].

Here we present a Raman-scattering investigation of the LOPCMs in heavily Se-doped, *n*-type $GaAs_{1-x}N_x$ thin films grown by metal-organic molecular beam epitaxy

J. Ibáñez (✉) · E. Alarcón-Lladó · R. Cuscó · L. Artús
Institut Jaume Almera, Consell Superior d'Investigacions Científiques (CSIC), 08028 Barcelona, Catalonia, Spain
e-mail: jibanez@ija.csic.es

D. Fowler · A. Patanè
School of Physics and Astronomy, University of Nottingham, Nottingham NG7 2RD, UK

K. Uesugi
Faculty of Engineering, Muroran Institute of Technology, Mizumotocho, Muroran, Hokkaido 050-8585, Japan

I. Suemune
Research Institute for Electronic Science (RIES), Hokkaido University, Sapporo 060-0812, Japan

S426 J Mater Sci: Mater Electron (2009) 20:S425–S429

(MOMBE) with x in the 0.1–0.36% range. We find that, on account of the reduced n-type mobility in the $GaAs_{1-x}N_x$ alloy, only a heavily-damped LOPCM appears in the Raman spectra even for x as low as 0.1%. We analyze our Raman spectra with a lineshape model based on the hydrodinamical model [12]. From fits to the spectra we evaluate the lifetime (τ) of the LOPCMs as a function of x. We find that τ is strongly quenched as x increases. We compare our results with the electron mobilities determined from Hall measurements and with the calculated n-type mobilities of GaAsN reported by Fahy et al. [4].

2 Experiment

Six Se-doped $GaAs_{1-x}N_x$ epilayers, with x in the 0.1–0.36% range, were grown by MOMBE on (001) semi-insulating GaAs substrates. Details of the growth conditions can be found in Ref. [13]. The N content of the samples, which was determined by high-resolution X-ray diffraction (HRXRD) measurements, is given in Table 1. For comparison purposes, two Se-doped GaAs epilayers were also grown. The thickness of all the epilayers was evaluated from an analysis of the HRXRD curves and was found to lie between 120 and 220 nm. Hall measurements at different temperatures were performed to obtain the carrier concentrations (N_e) and Hall mobilities (μ_{Hall}) of the samples. The second and third columns of Table 1 display the corresponding values at 100 K. In the temperature range studied (4.2–300 K), both N_e and μ_{Hall} exhibit very weak temperature dependence for all the $GaAs_{1-x}N_x$ epilayers.

Raman spectra were recorded at 80 K using the high-resolution triple additive configuration of a Jobin-Yvon T64000 spectrometer equipped with a CCD detector. The 100-μm slits were used to acquire the spectra. The Raman measurements, performed in a backscattering geometry on a (001) face, were excited with the 514.5-nm line of an Ar^+ laser.

Table 1 List of Se-doped $GaAs_{1-x}N_x$ samples studied in this work. The N content (x), the carrier concentration (N_e), the electron mobility (μ_{Hall}), and the electronic damping parameter (Γ_e) as determined from a lineshape analysis of the Raman spectra, are listed

N content (x) (%)	N_e (cm^{-3})	μ_{Hall} (cm^2/Vs)	Γ_e (cm^{-1})
0	7.7×10^{18}	607	200
0	1.0×10^{19}	406	270
0.10	5.3×10^{18}	101	625
0.20	7.6×10^{18}	114	565
0.20	9.0×10^{18}	88	780
0.23	7.8×10^{18}	61	850
0.30	1.5×10^{19}	46	1,450
0.36	1.5×10^{19}	51	1,235

3 Results and discussion

Figure 1 shows $z(xy)\bar{z}$ Raman spectra of two of the samples investigated in this work. Curve A corresponds to a Se-doped GaAs epilayer with $N_e = 1.0 \times 10^{19}$ cm^{-3}, while curve B corresponds to a Se-doped $GaAs_{1-x}N_x$ epilayer with $x = 0.2\%$ and $N_e = 9.0 \times 10^{18}$ cm^{-3}. Curve A is a typical spectrum of heavily-doped n-type GaAs. This spectrum is dominated by a strong peak at ~ 271 cm^{-1} that can be attributed to a L^- coupled mode arising from the coupling between the LO phonons and the collective excitations of the free carriers (plasmons) [5]. The corresponding L^+ coupled mode [5] for this sample appears as a broad band centered at around 1,150 cm^{-1} (see the inset of Fig. 1). The frequency at which the L^+ mode is observed is in good agreement with the results of previous Raman studies on heavily doped n-GaAs [14]. The weaker peak at ~ 294 cm^{-1} corresponds to the LO phonon mode of GaAs

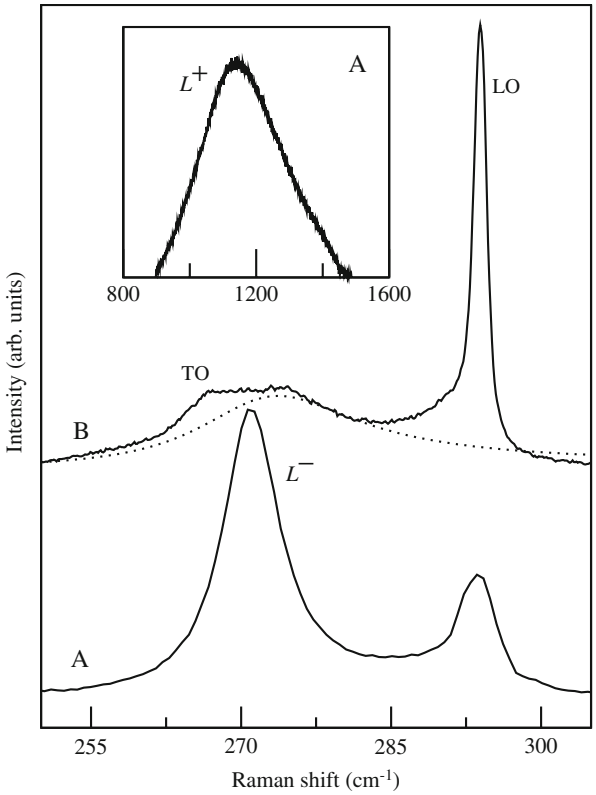

Fig. 1 Raman spectra of n-type GaAs with $N_e = 1.0 \times 10^{19}$ cm^{-3} (curve A) and of a n-type $GaAs_{1-x}N_x$ epilayer with $x = 0.2\%$ and $N_e = 9.0 \times 10^{18}$ cm^{-3} (curve B). The inset shows the L^+ band that is observed in the case of the n-GaAs epilayer. No L^+ band is observed in any of the spectra of the n-$GaAs_{1-x}N_x$ samples

J Mater Sci: Mater Electron (2009) 20:S425–S429

arising from the surface depletion region, which is well-known to exist in the (100) surface of GaAs [5, 15].

In the case of the $GaAs_{1-x}N_x$ epilayer with $x = 0.2\%$ and $N_e = 9.0 \times 10^{18}$ cm^{-3} (curve B), three features can be observed. Similar spectra are obtained for the rest of $GaAs_{1-x}N_x$ samples. The most intense peak, located at $\sim$294 cm^{-1}, corresponds to the GaAs-like LO mode of $GaAs_{1-x}N_x$ from the surface depletion region. Note that the thickness of these epilayers is large compared to $1/2\alpha$ [16], where α is the absorption coefficient of GaAs for the 514.5-nm radiation. As a consequence, the contribution of the GaAs substrate to the Raman signal is negligible. As discussed in Refs. [6] and [9], the frequency of the GaAs-like LO mode of $GaAs_{1-x}N_x$ is progressively redshifted with increasing x due to strain, N alloying and disorder. However, for the N contents involved in our samples, such shifts can be neglected. The peak located at $\sim$268 cm^{-1} corresponds to the forbidden TO mode of $GaAs_{1-x}N_x$. The frequency of this mode is barely shifted with respect to GaAs [6, 9]. Besides these two peaks, an additional broad feature emerges between the TO and LO phonons of $GaAs_{1-x}N_x$. As occurs in p-type GaAs [17, 18], where the LOPCMs are heavily damped owing to the low mobility of the free holes, this feature can be assigned to a heavily-damped LOPCM [19]. The strong damping of this mode can be attributed to the disorder introduced by N. We observe this heavily-damped coupled mode in all samples, even in the epilayer with x as low as 0.1%.

The energy of the L^+ coupled mode detected in n-type III–V semiconductors such as n-GaAs or n-InP is very sensitive to N_e variations. In contrast, the heavily-damped LOPCM observed in p-GaAs or in n-$GaAs_{1-x}N_x$ does not show such high sensitivity. These heavily-damped LOPCM peaks, however, can still be used to obtain relevant information about the investigated materials. For instance, Limmer et al. [18] performed a full lineshape analysis of the Raman spectra of p-GaMnAs layers to evaluate hole concentrations and mobilities. These type of analyses necessarily rely on the Lindhard–Mermin (LM) dielectric function, since only this model allows one to include finite-temperature and nonparabolicity effects as well as Landau damping effects [12, 20]. In the case of $GaAs_{1-x}N_x$, the LM model cannot be used because the dispersion of the conduction band of this compound is not well known. In contrast, simpler models such as the hydrodynamical (HD) model do not have this limitation. The HD approach neglects important effects, but it still allows one to take into account the spatial dispersion of plasmons (i.e., wave-vector effects) through a wave-vector dependent electric susceptibility [12]. The HD model can be extended to include temperature effects and the dependence on N_e of the electron effective mass provided that the conduction-band dispersion is known [20].

Here, we perform a lineshape analysis of the Raman spectra based on the conventional HD model with the aim of evaluating the lifetime, τ, of the free carriers. For this purpose, we calculate LOPCM lineshapes using a fluctuation–dissipation formalism and the HD susceptibility for the free electrons [12, 21]. The calculated lineshapes are then fitted to the experimental Raman spectra. For the sake of simplicity, we neglect the nonparabolicity of the conduction band of dilute nitrides for the present analysis and we use the electron effective-mass values recently measured by Masia et al. [22] with magnetophotoluminescence spectroscopy in $GaAs_{1-x}N_x$. In the composition range $0.2\% \leq x \leq 0.36\%$ the effective mass can be well approximated by a constant value $m^* = 0.13m_e$, whereas for $x = 0.1\%$ we take $m^* = 0.1m_e$ [22]. For the samples with $x = 0\%$ we take $m^* = 0.09m_e$ from Ref. [23].

For the fits, it would be in principle possible to treat the carrier concentration N_e and the phenomenological electronic damping parameter Γ_e, both of which enter the electric susceptibility of the electron gas [12], as free parameters. However, in the case of heavily-damped LOPCMs this yields some degree of ambiguity in the lineshape analysis, since different combinations of N_e and Γ_e may lead to satisfactory fits (see the discussion in Ref. [18]). To avoid this problem, here we use the N_e values obtained from Hall measurements (Table 1) for the fitting procedure and we leave Γ_e as the only fitting parameter. The lifetime of the LOPCMs can then be derived via the energy-time uncertainty relation, $\tau^{-1} = 2\pi c\Gamma_e$, where c is the speed of light in vacuum and Γ_e is expressed in wavenumber units (cm^{-1}).

As mentioned above, nonparabolicity effects are neglected throughout this work. This is expected to yield increased Γ_e values as extracted from the fits, which can be shown by comparing LOPCM lineshapes calculated with different values of m^* and Γ_e. Nevertheless, for the low N composition of the samples studied in this work, the m^* values that we take from Ref. [22] are not too different from the values predicted by the BAC model for n-GaAsN with 5×10^{18} cm^{-3} $< N_e <$ 1.5×10^{19} cm^{-3} [24]. Consequently, bearing in mind the controversial nature of the conduction band of GaAsN [25] and the lack of electron effective-mass measurements in this compound as a function of N_e, for the present analysis we rely on the experimental data of Ref. [22].

In Fig. 1 (dashed line), we show the fit of the theoretical LOPCM lineshapes to the experimental spectrum for the n-$GaAs_{1-x}N_x$ epilayer with $x = 0.2\%$ and $N_e = 9.0 \times 10^{18}$ cm^{-3}. A value of $\Gamma_e = 780$ cm^{-1}, corresponding to $\tau = 6.8 \times 10^{-15}$ s, was extracted from this fit. Prior to the fits, the Raman peaks from the TO and LO modes were fitted by Lorentzian lineshapes and substracted from the Raman spectra.

S428 J Mater Sci: Mater Electron (2009) 20:S425–S429

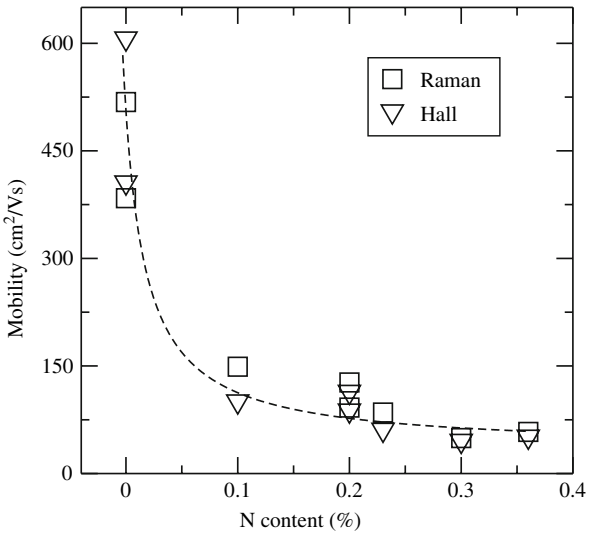

Fig. 2 Mobility versus N content for the samples studied in this work as determined by Hall measurements and from a lineshape analysis of the LOPCM peaks

In the last column of Table 1 we display the value of Γ_e obtained from the lineshape fits for all the samples studied in this work. Clearly, the coupled-mode lifetime tends to decrease with increasing N content as occurs with the Hall mobility. To compare Γ_e with μ_{Hall}, we plot in Fig. 2 the value of $\mu_{\text{Raman}} = e/(2\pi c\Gamma_e m^*)$ as a function of x for all our samples (open squares). In the last expression, e denotes the electron charge. For the n-GaAs samples ($x = 0\%$), the Raman mobilities were determined by fitting the L^- and L^+ coupled mode peaks. In Fig. 2, we also plot the electron mobility as determined from Hall measurements (open triangles). As can be observed in the figure, good agreement is found between the Hall measurements and our Raman analysis. Both techniques show that the electron mobility (and therefore the electron lifetime) is abruptly reduced with the addition of just 0.1% of N in GaAs, which may be mainly attributed to electron scattering by localized electron states associated with N impurities and clusters [4]. An additional contribution to the observed mobility reduction may also arise from the increased electron effective mass in the $GaAs_{1-x}N_x$ alloy, which is expected to be more important in the degenerate limit [26]. Owing to the increased amount of N-related disorder in the samples, a progressive reduction of the mobility is observed with increasing x for $x > 0.1\%$.

With regard to the results of Fig. 2, we would like to remark that intrinsic differences exist between the optical and the transport measurements. While the former probe the lifetime of the LOPCMs (i.e., the lifetime of the collective excitations of the conduction electrons) through a lineshape analysis of the Raman spectra, the Hall mobilities are derived from the transport properties of free electrons. Note also that the presence of N-related localized electronic states in n-$GaAs_{1-x}N_x$ modifies the scattering rate of the free carriers, leading to a more complex picture in which the electron mobility shows a $1/\sqrt{m^*}$ dependence [4]. While the lifetime of the LOPCMs is expected to be affected by the N localized states, the evaluation of such effect is clearly beyond the scope of this work.

Finally, we note that the Hall mobilities measured in our $GaAs_{1-x}N_x$ samples (< 120 cm^2 V^{-1} s^{-1}) are sizeably lower that those predicted in Ref. [4]. Also, the mobilty of our n-GaAs samples is already below the predictions of Ref. [4]. Thus, we conclude that other scattering mechanisms not related to the N impurities are present in these epilayers. In particular, the high density of ionized Se donors may be greatly responsible for the low electron mobilities of our samples. As reported by Fowler et al. [27], the conductivity is significantly enhanced in modulation-doped $GaAs_{1-x}N_x$ heterostructures. In such type of structures, the electron mobility has also shown to be strongly limited by N-related scattering [27], in agreement with the considerations of Ref. [4] and with the Hall and Raman data obtained in our samples.

4 Conclusion

The LO-plasmon coupled modes (LOPCMs) in dilute $GaAs_{1-x}N_x$ are heavily damped, which is attributed to carrier scattering by N-related localized electronic states. We have carried out a lineshape analysis based on the hydrodynamical model to evaluate the lifetime of the free carriers. Our calculations show that in the high damping regime a single LOPCM is expected between the TO and LO modes of GaAsN. The lifetimes of the LOPCMs as obtained from our analysis are in good agreement with the measured Hall mobilities. The introduction of only a 0.1% of N into GaAs dramatically reduces both the lifetime and the Hall mobility of the free carriers.

Acknowledgements Work funded by the Spanish Ministry of Education and Science under Contracts Ref. MAT2004-0664, MAT2007-63617 and by the Ramon y Cajal Program.

References

1. Special issue III-V-N Semiconductor alloys, Semicond. Sci. Technol. **17** (2002)
2. A.R. Adams, Elec. Lett. **40**, 1086 (2004)
3. A. Ignatov, A. Patanè, O. Makarovsky, L. Eaves, Appl. Phys. Lett. **88**, 032107 (2006)
4. S. Fahy, A. Lindsay, H. Ouerdane, E.P. O'Reilly, Phys. Rev. B **74**, 035203 (2006)
5. Abstreiter et al., in *Light Scattering in Solids IV*, ed. by M. Cardona, G. Güntherodt (Springer-Verlag, Berlin, 1984)

J Mater Sci: Mater Electron (2009) 20:S425–S429 S429

6. T. Prokofieva, T. Sauncy, M. Seon, M. Holtz, Y. Qiu, S. Nikishin, H. Temkin, Appl. Phys. Lett. **73**, 1409 (1998)
7. A. Mascarenhas, M.J. Seong, Semicond. Sci. Technol. **17**, 823 (2002)
8. H.F. Liu, N. Xiang, S. Tripathy, S.J. Chua, J. Appl. Phys. **99**, 103503 (2006)
9. J. Ibáñez, E. Alarcón-Lladó, R. Cuscó, L. Artús, M. Hopkinson, J. Appl. Phys. **102**, 013502 (2007)
10. T. Tite, O. Pagès, M. Ajjoun, J.P. Laurenti, D. Bormann, E. Tournié, O. Maksimov, M.C. Tamargo, Solid State Electr. **47**, 455 (2003)
11. P.A. Grandt, A.E. Griffith, M.O. Manasreh, D.J. Friedman, S. Dogan, D. Johnstone, Appl. Phys. Lett. **85**, 4905 (2004)
12. L. Artús, R. Cuscó, J. Ibáñez, N. Blanco, G. González, Phys. Rev. B **60**, 5456 (1999)
13. I. Suemune, K. Uesugi, T.Y. Seong, Semicond. Sci. Technol. **17**, 755 (2002)
14. M. Ramsteiner, J. Wagner, P. Hiesinger, K. Köhler, U. Rössler, J. Appl. Phys. **73**, 5023 (1993)
15. H. Shen, F.H. Pollak, R.N. Sacks, Appl. Phys. Lett. **47**, 891 (1985)
16. D.E. Aspnes, A.A. Studna, Phys. Rev. B **27**, 985 (1983)
17. K. Wan, J.F. Young, Phys. Rev. B **41**, 10772 (1990)
18. W. Limmer, M. Glunk, S. Mascheck, A. Koeder, D. Klarer, W. Schoch, K. Thonke, R. Sauer, A. Waag, Phys. Rev. B **66**, 205209 (2002)
19. J. Ibáñez et al., in *Physics of Semiconductors*, ed. by J. Menendez, C.G. VanDeWalle (Aip Conference Proceedings, New York 2005), pp. 293–294
20. J. Ibáñez, R. Cuscó, L. Artús, Phys. Stat. Sol. (b) **223**, 715 (2001)
21. R. Cuscó, J. Ibáñez, L. Artús, Phys. Rev. B **57**, 12197 (1998)
22. F. Masia et al., Phys. Rev. B **73**, 073201 (2006)
23. H.R. Chandrasekhar, A.K. Ramdas, Phys. Rev. B **21**, 1511 (1980)
24. C. Skierbiszewski et al., Appl. Phys. Lett. **76**, 2409 (2000)
25. A. Lindsay, E.P. O'Reilly, Phys. Rev. Lett. **93**, 196402 (2004)
26. M.P. Vaughan, B.K. Ridley, Phys. Rev. B **75**, 195205 (2007)
27. D. Fowler, O. Makarovsky, A. Patanè, L. Eaves, L. Geelhaar, H. Riechert, Phys. Rev. B **69**, 153305 (2004)

JOURNAL OF APPLIED PHYSICS **103**, 103528 (2008)

Electron effective mass and mobility in heavily doped *n*-GaAsN probed by Raman scattering

J. Ibáñez,[1] R. Cuscó,[1] E. Alarcón-Lladó,[1] L. Artús,[1,a)] A. Patanè,[2] D. Fowler,[2] L. Eaves,[2] K. Uesugi,[3] and I. Suemune[4]
[1]*Institut Jaume Almera, Consell Superior d'Investigacions Científiques (CSIC), Lluis Solé i Sabarís s.n., 08028 Barcelona, Catalonia, Spain*
[2]*School of Physics and Astronomy, University of Nottingham, NG7 2RD Nottingham, United Kingdom*
[3]*Faculty of Engineering, Muroran Institute of Technology, Mizumotocho, Muroran, Hokkaido 050-8585, Japan*
[4]*Research Institute for Electronic Science (RIES), Hokkaido University, Sapporo 060-0812, Japan*

(Received 5 December 2007; accepted 18 March 2008; published online 27 May 2008)

We investigate inelastic light scattering by longitudinal optic phonon-plasmon coupled modes (LOPCMs) in a series of heavily Se-doped, *n*-type $GaAs_{1-x}N_x$ epilayers with $x<0.4\%$. We perform a line shape analysis of the LOPCM spectra to estimate the optical effective mass, m^*_{opt}, and the scattering time of the conduction electrons in GaAsN. We use these results to evaluate an effective carrier mobility for our samples. The values thus obtained, which we compare with measured electron Hall mobilities, indicate that the *x*-dependence of the mobility in $GaAs_{1-x}N_x$ is dominated by the scattering time, rather than by the variation of the electron effective mass. The Raman analysis yields m^*_{opt} values that are lower than those obtained from the band anticrossing model.
 [DOI: 10.1063/1.2927387]

I. INTRODUCTION

[1]Dilute nitride compounds, in particular GaAsN and GaInAsN, have attracted much interest over the last decade because of their remarkable physical properties and their potential for device applications in long-wavelength optoelectronics.[1] It has been established that the incorporation of a few atomic percent of N into the Ga(In)As alloy system leads to a substantial band-gap reduction, as well as to the splitting of the conduction band of the III–V matrix into two highly nonparabolic subbands, E_+ and E_-.[2–5] The simple two-level band anticrossing (BAC) model[2] provides a reasonably accurate description of the dependence on N content of the energies of E_+ and E_-. Also, it predicts a substantial increase in the effective mass (m^*_e) for the lower energy subband E_- relative to the III–V matrix.[6,7] However, a complete description of the band structure of dilute nitrides requires detailed calculations of the localized electronic states introduced by N and their interaction with the extended conduction states of the host matrix.[4,5] While magneto-tunneling measurements have revealed the admixed character of the N-induced states and the anticrossing behavior of the E_- and E_+ subbands in $GaAs_{1-x}N_x$ quantum wells,[8,9] optical and transport techniques have confirmed the increase of m^*_e of conduction electrons in both GaAsN and GaInAsN.[6,7,10–13]

Most of the optical experiments to determine m^*_e in dilute Ga(In)AsN were performed on undoped material. As a consequence, the m^*_e values obtained in those experiments correspond to the bottom of the E_- conduction subband (m^*_{e0}). In order to use optical techniques to investigate the conduction band (CB) dispersion of Ga(In)AsN and determine m^*_e far above the zone-center minimum of E_-, heavily doped *n*-type samples are required. Studies on highly doped material tend to confirm the validity of the BAC model as a description of the energy-wave vector dispersion, $E(k)$, in the case of the GaInAsN quaternary alloy.[6,7] In contrast, magnetophotoluminescence measurements on undoped $GaAs_{1-x}N_x$ suggest that the BAC model underestimates m^*_{e0} for $x \gtrsim 0.1\%$,[12] while experimental studies probing m^*_e in this compound at energies above the CB minimum are presently lacking. Additional experiments are therefore necessary to determine how $E(k)$ and $m^*_e(k)$ depend on N content both in GaAsN and GaInAsN.

Raman scattering by longitudinal optical (LO) phonon-plasmon coupled modes (LOPCMs) has been widely reported in the literature as a method for determining the free-carrier concentration in polar semiconductors.[14–19] Conversely, the investigation of LOPCMs can also be used to optically probe the CB dispersion of the compound under study if the carrier concentration, N_e, is known from independent measurements, since the frequency of the LOPCMs strongly depends on m^*_e. It should be recalled that optical experiments probe the optical effective mass of the carriers, m^*_{opt}, which exhibits a marked N_e-dependence in nonparabolic bands.[20,21]

In the present work, we use Raman scattering to investigate the LOPCMs in a series of heavily doped *n*-type $GaAs_{1-x}N_x$ epilayers ($0\%<x<0.4\%$). From the line shape analysis of the LOPCM spectra, we estimate m^*_{opt} and the scattering time, τ, of conduction electrons in our samples. We use the values of m^*_{opt} and τ to obtain an effective electron mobility which we compare with the Hall effect mobility. We find that the values of m^*_{opt} are lower than those predicted by the BAC model. Our analysis suggests that the

a)Electronic mail: lartus@ija.csic.es.

TABLE I. List of *n*-type Se-doped $GaAs_{1-x}N_x$ epilayers studied in this work.

Sample	x	N_e (cm^{-3})	μ_{Hall} (cm^2/Vs)	m^*_{opt}/m_e	Γ_e (cm^{-1})	μ_{Raman} (cm^2/Vs)
A	0%	1.0×10^{19}	406	0.09	270	384
B	0.10%	5.3×10^{18}	101	0.09	688	151
C	0.20%	7.6×10^{18}	114	0.13	563	127
D	0.23%	7.8×10^{18}	61	0.12	1009	77
E	0.30%	1.5×10^{19}	46	0.13	1346	53
F	0.36%	1.5×10^{19}	51	0.11	1555	55

x-dependence of the mobility in n-$GaAs_{1-x}N_x$ with $x<0.4\%$ is controlled by the carrier lifetime rather than by the variation of m^*_e.

II. EXPERIMENT

Six Se-doped, n-type $GaAs_{1-x}N_x$ epilayers ($0\%<x<0.4\%$) were grown on (001) semi-insulating GaAs substrates by metal-organic molecular beam epitaxy. The growth conditions can be found elsewhere.[22,23] Se was used as the n-type dopant instead of Si because Si and N passivate each other in Si-doped GaAsN due to the formation of Si–N complexes.[24] The N concentrations of the films (samples A–F), as determined by high-resolution x-ray diffraction (HRXRD) measurements,[25] are given in Table I. The thickness of the epilayers is in the 120–220 nm nm range, as obtained from the analysis of the HRXRD scans. Hall measurements at different temperatures were carried out in order to determine N_e and the Hall mobility (μ_{Hall}) of the layers. The third and fourth columns of Table I display N_e and μ_{Hall} as obtained at 100 K. Owing to the high N_e values measured ($N_e>5\times10^{18}$ cm^{-3}), it can be assumed that the free carriers are degenerate in all the samples studied.

Raman measurements were performed at 80 K in a backscattering geometry on the (001) face. The spectra were obtained with the 514.5 nm line of an Ar^+ laser as excitation. Given that the penetration depth of the 514.5 nm light is appreciably smaller than the thickness of the GaAsN epilayers, the contribution of the GaAs substrate to the Raman signal is negligible. A Jobin-Yvon T64000 spectrometer equipped with a charge-coupled device detector was used to record the Raman measurements. The spectra were acquired with the high-resolution triple additive configuration of the spectrometer, with 100 μm slits.

III. RESULTS AND DISCUSSION

Figure 1 shows $z(xy)\bar{z}$ Raman spectra of our Se-doped GaAsN layers (samples B–F). Three main features can be observed in all the spectra. The most intense peak is located at $\sim$294 cm^{-1} and corresponds to the GaAs-like LO phonon of GaAsN.[26,27] In the case of n-type material, the LO peaks arise from the surface depletion region of the samples.[14] The broad band centered at $\sim$268 cm^{-1} can be assigned to the GaAs-like TO mode of GaAsN.[26,27] An additional broad feature that is not observed in undoped GaAsN and whose frequency and width change from sample to sample emerges between the TO and LO GaAs-like phonons. We assign this feature to a heavily damped LOPCM. Similar heavily damped LOPCM bands have been observed in p-GaAs,[28] and in n-type InGaAs lattice matched to InP.[19] While the LOPCMs in p-GaAs are heavily damped due to the very low hole mobility, Landau damping effects associated with the low electron effective mass of InGaAs are responsible for the low LOPCM lifetimes in this compound. In the case of n-type GaAsN, the observation of heavily damped LOPCMs instead of the well-known L^- and L^+ coupled modes[14] might be at first sight surprising. Note that, as expected, we observe both the L^+ and L^- bands in the Raman spectra of our n-GaAs sample (inset of Fig. 1), while no L^+ band is observed for any of the n-GaAsN epilayers.

To confirm that the features observed in the spectra of Fig. 1 correspond to a heavily damped LOPCM, we show in Fig. 2 the calculated LOPCM frequency versus N_e for n-GaAs in the high damping regime (solid curve). This curve was obtained by calculating Raman line shapes at different N_e values by using the fluctuation-dissipation formalism of Hon and Faust and the hydrodynamical (HD) model (see Refs. 16 and 29 for details), taking the maxima of the calculated LOPCM curves. For the sake of simplicity, we used for the calculations a constant value of $m^*_{opt}=0.09m_e$, which is the value found in heavily doped n-GaAs for $N_e\sim1$

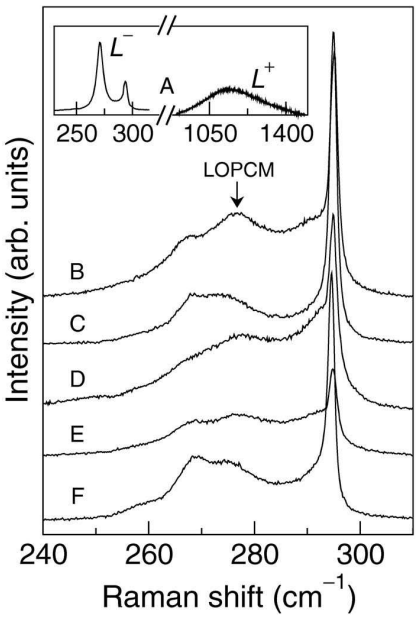

FIG. 1. Raman spectra acquired at 80 K of the n-GaAsN epilayers studied in this work (samples B–F). The inset shows the Raman spectrum of the n-GaAs epilayer (sample A).

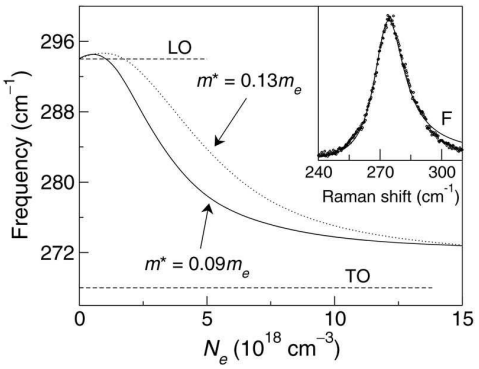

FIG. 2. Calculated N_e-dependence of the frequency of the heavily damped LOPCM in low mobility n-GaAs. The solid curve was calculated with $m^*_{opt}=0.09m_e$ and the dashed curve with $m^*_{opt}=0.13m_e$. Inset: LOPCM line shape fit (solid line) to the Raman spectrum of sample F (dots).

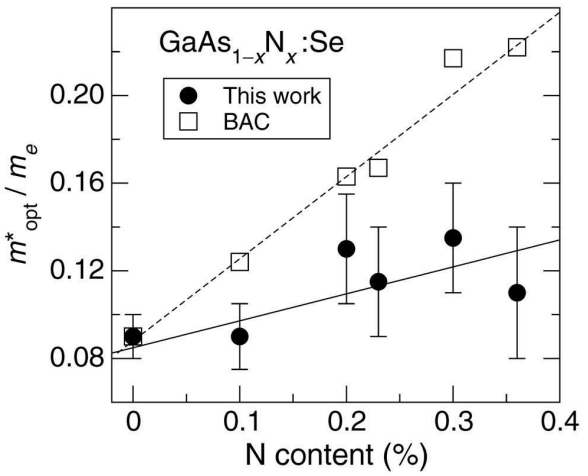

FIG. 3. Optical effective mass values, m^*_{opt}, extracted from the analysis of the Raman measurements (dots) and values predicted by the two-level BAC model for the N composition and N_e of the studied samples (open squares). The solid (dashed) line is intended only as a guide to the eye to show the increasing trend of m^*_{opt} with N content in our samples, as derived from the Raman spectra (BAC model).

$\times 10^{19}$ cm^{-3}.[20] A phenomenological electronic damping parameter $\Gamma_e=1000$ cm^{-1}, consistent with the low electron mobilities measured in our heavily doped samples (see Table I and Ref. 30), was used. The resulting curve confirms that, as for the case of p-GaAs,[28] in n-GaAs with low electron mobility only a single LOPCM is expected between the TO and LO phonon modes of GaAs. In the case of GaAsN, the low (high) μ_{Hall} (Γ_e) values are a consequence of the N-related disorder.[31,32] With regard to this, we would like to note that both N_e and μ_{Hall} exhibited a weak temperature dependence in our samples. This suggests that the contribution of N-related alloy scattering to τ in these layers is much stronger than the contribution of other relaxation mechanisms such as inelastic phonon scattering.

The L^+ mode observed in n-GaAs is particularly sensitive to variations in N_e and in m^*_{opt}. However, the heavily damped LOPCM does not display such high sensitivity. We therefore need to evaluate the effect of m^*_{opt} on the LOPCM frequency in order to determine whether the Raman spectra are sufficiently sensitive to effective mass variations, in which case valuable information about m^*_{opt} can be obtained from the LOPCM spectra. Thus, we repeated the calculation of the frequency of the heavily damped LOPCM in n-GaAs as a function of N_e by using a higher value of $m^*_{opt}=0.13m_e$. This is close to the values measured by Masia *et al.* in undoped GaAs$_{1-x}$N$_x$ samples with N contents similar to those of our samples[12] and also to the value obtained from magnetophonon resonance measurements in moderately doped GaAs$_{1-x}$N$_x$ with $x=0.1\%$.[13]

The resulting curve, plotted in Fig. 2 (dashed curve), shows that the frequency of the heavily damped LOPCM is higher (i.e., closer to the uncoupled LO mode) when m^*_{opt} is increased. This result demonstrates that a change in m^*_{opt} has measurable effects on the LOPCM frequency, and hence that the analysis of the Raman spectra can provide useful information about m^*_e in dilute n-GaAsN.

To determine m^*_{opt} in our samples, we have carried out a line shape analysis of the Raman spectra based on the HD mode in the degenerate limit (see Refs. 16 and 29). The calculated line shapes are fitted to the experimental Raman spectra using the N_e values obtained from Hall measurements (Table I) and leaving m^*_{opt} and Γ_e as free parameters. Note that the lifetime τ of the LOPCMs, and hence the scattering time of the free carriers, is related to Γ_e through the energy-time uncertainty relation $\tau^{-1}=2\pi c\Gamma_e$. To avoid possible ambiguities in the fitting procedure, since different combinations of the fitting parameters may lead to satisfactory fits (see for instance Ref. 17 for the case of p-GaAs), we restrict m^*_{opt} and Γ_e to vary within meaningful ranges, compatible with our measured Hall-effect carrier mobilities and with the m^*_e values reported in the literature.[12,13]

We plot in the inset of Fig. 2 (solid line) the resulting line shape fit to the Raman spectrum of one of the analyzed n-GaAsN films (sample F). Note that prior to the fits the Raman peaks from the TO and LO phonon modes of GaAsN were fitted by Lorentzian line shapes and subtracted from the Raman spectra. Values of $m^*_{opt}=0.11m_e$ and $\Gamma_e=1555$ cm^{-1} were extracted from this fit. As can be seen in the figure, the HD model provides good fits to the heavily damped LOPCM line shapes. We show in the fifth and sixth columns of Table I the m^*_{opt} and Γ_e values obtained from the fits. In the particular case of the n-GaAs epilayer (sample A), m^*_{opt} and Γ_e were obtained from a fit to the L^+ band. The last column of the table shows the mobility of the samples as estimated from $\tau=1/(2\pi c\Gamma_e)$ and m^*_{opt} with the expression $\mu_{Raman}=e\tau/m^*_{opt}$. As can be seen in the table, both μ_{Hall} and μ_{Raman} tend to decrease with increasing x. Interestingly, a quite good agreement between the transport and the Raman mobilities is found, which provides support for the reliability of the Raman analysis.

In Fig. 3, we plot as a function of x the m^*_{opt} values extracted from the fits for all the samples studied in this work (dots). Error bars have been drawn in the figure to take into account possible uncertainties in the determination by Hall-effect measurements of N_e. These uncertainties also lead to significant relative errors in Γ_e, which we estimate to be around 10–20%. For comparison, we also plot in Fig. 3 the

m^*_{opt} values predicted by the two-level BAC model for the N composition and N_e of our samples (open squares). We use the analytical expressions for the effective mass given in Refs. 6 and 7, where the Fermi wave vector k_F is evaluated in the degenerate limit as $k_F=(3\pi^2N_e)^{1/3}$. To obtain the parameters that enter the BAC model at 80 K, we extrapolate the values given in Ref. 33. As can be seen in Fig. 3, the m^*_{opt} values obtained with the BAC model increase as expected with increasing x. Note that the large m^*_{opt} values obtained with the BAC model for the samples with the highest N content (samples E and F, with $x=0.30$ and 0.36%, respectively) are due to the high free-electron density of these two epilayers (see Table I). For such high doping levels, the BAC model predicts a large CB nonparabolicity, i.e., increased m^*_{opt} values. As can be seen from the figure, however, for the N concentrations of the samples studied in this work, the m^*_{opt} values extracted from the LOPCM spectra are appreciably lower than those predicted by the two-level BAC model.

Although the discrepancy between the Raman data and the predictions of the two-level BAC model could be a consequence of intrinsic uncertainties in the analysis of the LOPCM spectra, it is quite likely that the BAC model offers a too simplistic description of the electron effective mass in GaAsN. The BAC model seems to correctly predict the large N-induced increase of m^*_e for $x>1\%$ in n-type $In_yGa_{1-y}As_{1-x}N_x$.[6] However, in the case of undoped GaAsN, magnetophotoluminescence measurements have revealed that m^*_{e0} is sizably higher than that predicted by the BAC model for the composition range of the samples studied here. These experimental results can be understood in terms of a description based on a linear combination of isolated nitrogen states,[5] which shows that for the particular case of $0.1\%<x<0.2\%$ the CB-edge electronic states of $GaAs_{1-x}N_x$ are strongly hybridized with N cluster states. Such a strong hybridization is responsible for the large m^*_{e0} values measured in this composition range.[12] However, for heavily doped n-$GaAs_{1-x}N_x$ and the N compositions of the samples studied here, the Fermi energy lies well above the N cluster states (i.e., hundreds of meV depending on x and N_e), and therefore only a weak interaction exists between the extended electronic states around the Fermi surface and the N-related localized cluster states. As a consequence, the enhancement of the electron effective mass due to the hybridization with N cluster states should play a much weaker role in our samples. These arguments can explain why, unlike the m^*_{e0} values measured by magnetophotoluminescence in undoped GaAsN, the m^*_{opt} values extracted from the LOPCM spectra are not larger than the values predicted by the two-level BAC model. However, the fact that the Raman data are below the predictions of the BAC model (Fig. 3) remains unexplained. Further work is necessary to confirm these results and to ascertain how m^*_e is affected by N_e.

Interestingly, the fact that m^*_{opt} is lower than predicted by the BAC model has important implications for the mechanisms responsible for the low electron mobility of heavily doped GaAsN. The m^*_{opt} values derived from our analysis, together with the x-dependence of μ_{Hall} and μ_{Raman}, indicate that the electron mobility in GaAsN is limited more by the decrease of the electron scattering time with increasing N content as a consequence of N-related disorder than by changes of m^*_{opt} with increasing N-content and/or carrier concentration.

IV. CONCLUSION

We have found that N-related disorder in n-$GaAs_{1-x}N_x$ gives rise to a single heavily damped LOPCM even for N contents as low as 0.1%. Despite the lower sensitivity to N_e or m^*_e variations of the heavily damped LOPCM in comparison to the L^+ coupled-mode branch observed in n-GaAs, a careful analysis of the Raman spectra provides a means of estimating the optical effective mass of the free electrons, m^*_{opt}, in the n-$GaAs_{1-x}N_x$ epilayers. We find that the m^*_{opt} values obtained from the fits are lower than those predicted by the BAC model in heavily doped n-GaAsN. These results suggest that the x-dependence of the measured electron mobility is mainly determined by the scattering time.

ACKNOWLEDGMENTS

This work is supported by the Spanish Government (Projects MAT 2004-0664 and MAT2007-63617, and Ramon y Cajal Program) and the EPSRC, United Kingdom.

[1] M. Henini, *Dilute Nitride Semiconductors* (Elsevier Science, Amsterdam, 2005).
[2] W. Shan, W. Walukiewicz, J. W. Ager III, E. E. Haller, J. F. Geisz, D. J. Friedman, and J. M. Olson and S. R. Kurtz, Phys. Rev. Lett. **82**, 1221 (1999).
[3] J. D. Perkins, A. Mascarenhas, Y. Zhang, J. F. Geisz, D. J. Friedman, J. M. Olson, and S. R. Kurtz, Phys. Rev. Lett. **82**, 3312 (1999).
[4] P. R. C. Kent and A. Zunger, Phys. Rev. Lett. **86**, 2613 (2001).
[5] A. Lindsay and E. P. O'Reilly, Phys. Rev. Lett. **93**, 196402 (2004).
[6] C. Skierbiszewski, P. Perlin, P. Wisniewski, W. Knap, T. Suski, W. Walukiewicz, W. Shan, K. M. Yu, J. W. Ager III, E. E. Haller, J. F. Geisz, and J. M. Olson, Appl. Phys. Lett. **76**, 2409 (2000).
[7] C. Skierbiszewski, P. Perlin, P. Wisniewski, T. Suski, J. F. Geisz, K. Hingerl, W. Jantsch, D. E. Mars, and W. Walukiewicz, Phys. Rev. B **65**, 035207 (2001).
[8] J. Endicott, A. Patanè, J. Ibáñez, L. Eaves, M. Bissiri, M. Hopkinson, R. Airey, and G. Hill, Phys. Rev. Lett. **91**, 126802 (2003).
[9] J. Endicott, A. Patanè, D. Maude, L. Eaves, M. Hopkinson, and G. Hill, Phys. Rev. B **72**, 041306 (2005).
[10] P. N. Hai, W. M. Chen, I. A. Buyanova, H. P. Xin, and C. W. Tun, Appl. Phys. Lett. **77**, 1843 (2000).
[11] F. Masia, A. Polimeni, G. Baldassarri, M. Bissiri, M. Capizzi, P. J. Klar, and W. Stolz, Appl. Phys. Lett. **82**, 4474 (2003).
[12] F. Masia, G. Pettinari, A. Polimeni, M. Felici, A. Miriametro, M. Capizzi, A. Lindsay, J. B. Healy, E. P. O'Reilly, A. Cristofoli, G. Bais, M. Piccin, S. Rubini, F. Martelli, A. Franciosi, P. J. Klar, K. Volz, and W. Stolz, Phys. Rev. B **73**, 073201 (2006).
[13] G. Allison, S. Spasov, A. Patanè, L. Eaves, A. Ignatov, D. K. Maude, M. Hopkinson, and R. Airey, Phys. Rev. B **75**, 115325 (2007).
[14] G. Abstreiter, M. Cardona, and A. Pinczuk, in *Light Scattering in Solids IV*, edited by M. Cardona and G. Güntherodt (Springer-Verlag, Berlin, 1984), Vol. 54.
[15] R. Cuscó, J. Ibáñez, and L. Artús, Phys. Rev. B **57**, 12197 (1998).
[16] L. Artús, R. Cuscó, J. Ibáñez, N. Blanco, and G. Gonzalez-Diaz, Phys. Rev. B **60**, 5456 (1999).
[17] W. Limmer, M. Glunk, S. Mascheck, A. Koeder, D. Klarer, W. Schoch, K. Thonke, R. Sauer, and A. Waag, Phys. Rev. B **66**, 205209 (2002).
[18] P. A. Grandt, A. E. Griffith, M. O. Manasreh, D. J. Friedman, S. Dogan, and D. Johnstone, Appl. Phys. Lett. **85**, 4905 (2004).
[19] R. Cuscó, L. Artús, S. Hernández, J. Ibáñez, and M. Hopkinson, Phys. Rev. B **65**, 035210 (2001).
[20] H. R. Chandrasekhar and A. K. Ramdas, Phys. Rev. B **21**, 1511 (1980).
[21] M. Cardona, Phys. Rev. B **121**, 752 (1961).
[22] I. Suemune, K. Uesugi, and T. Y. Seong, Semicond. Sci. Technol. **17**, 755

(2002).
[23]K. Uesugi and I. Suemune, Appl. Phys. Lett. **79**, 3284 (2001).
[24]K. M. Yu, W. Walukiewicz, J. Wu, D. E. Mars, D. R. Chamberlin, M. A. Scarpulla, O. D. Dubon, and J. F. Geisz, Nat. Mater. **1**, 185 (2002).
[25]K. Uesugi, N. Morroka, and I. Suemune, Appl. Phys. Lett. **74**, 1254 (1999).
[26]T. Prokofyeva, T. Sauncy, M. Seon, M. Holtz, Y. Qiu, S. Nikishin, and H. Temkin, Appl. Phys. Lett. **73**, 1409 (1998).
[27]J. Ibáñez, E. Alarcón-Lladó, R. Cuscó, L. Artús, and M. Hopkinson, J. Appl. Phys. **102**, 013502 (2007).
[28]K. Wan and J. F. Young, Phys. Rev. B **41**, 10772 (1990).
[29]J. Ibáñez, R. Cuscó, and L. Artús, Phys. Status Solidi B **223**, 715 (2001).
[30]M. Ramsteiner, J. Wagner, P. Hiesinger, K. Köhler, and U. Rössler, J. Appl. Phys. **73**, 5023 (1993).
[31]S. Fahy, A. Lindsay, H. Ouerdane, and E. P. O'Reilly, Phys. Rev. B **74**, 035203 (2006).
[32]M. P. Vaughan and B. K. Ridley, Phys. Rev. B **75**, 195205 (2007).
[33]A. Grau, T. Passow, and M. Hetterich, Appl. Phys. Lett. **89**, 202105 (2006).

References

[1] M. Henini, *Dilute Nitride Semiconductors: Physics and Technology*. Oxford, UK: Elsevier Science Ltd, 2005.

[2] I. A. Buyanova and W. M. Chen, *Physics and Applications of Dilute Nitrides*. New York, USA: Taylor & Francis Books Inc., 2004.

[3] "Special issue: III-N-V semiconductor alloys," *Semicond. Sci. Technol.*, vol. 17 Num. 8, 2002.

[4] M. Mintairov, P. A. Blagnov, V. G. Melehin, N. N. Faleev, V. M. Tretyakov, J. L. Merz, Y. Qiu, S. A. Nikishin, and H. Temkin *Phys. Rev. B*, vol. 56, p. 15836, 1997.

[5] T. Prokofyeva, T. Sauncy, M. Seon, M. Holtz, Y. Qiu, S. Nikishin, and H. Temkin *Appl. Phys. Lett.*, vol. 73, p. 1409, 1998.

[6] A. Mascarenhas and M. J. Seong *Semicond. Sci. Technol.*, vol. 17, p. 823, 2002.

[7] M. Gungerich, P. J. Klar, W. Heimbrodt, J. Koch, W. Stolz, M. P. Halsall, and P. Harmer *Phys. Rev. B*, vol. 71, p. 075201, 2005.

[8] P. H. Tan, Z. Y. Xu, X. D. Luo, W. K. Ge, Y. Zhang, A. Mascarenhas, H. P. Xin, and C. W. Tu *Appl. Phys. Lett.*, vol. 89, p. 101912, 2006.

[9] H. F. Liu, N. Xiang, S. Tripathy, and S. J. Chua *J. Appl. Phys.*, vol. 99, p. 103503, 2006.

[10] H. C. Alt, A. Y. Egorov, H. Riechert, B. Wiedemann, J. D. Meyer, R. W. Michelmann, and K. Bethge *Physica B*, vol. 302, p. 282, 2001.

[11] W. Li, M. Pessa, and J. Likonen *Appl. Phys. Lett.*, vol. 78, p. 2864, 2001.

[12] W. J. Fan, S. F. Yoon, W. K. Cheah, W. K. Loke, T. K. Ng, S. Z. Wang, R. Liu, and A. Wee *J. Cryst. Growth*, vol. 268, p. 470, 2004.

[13] S. Shirakata, M. Kondow, and T. Kitatani *J. Phys. Chem. Solids*, vol. 66, p. 2119, 2007.

[14] J. Wagner, T. Geppert, K. Koehler, P. Ganser, and N. Herres *J. Appl. Phys.*, vol. 90, p. 5027, 2001.

[15] R. Srnanek, A. Vincze, J. Kovac, I. Gregora, D. S. McPhail, and V. Gottschalch *Mat. Sci. Eng. B*, vol. 91, p. 87, 2002.

[16] G. E. Dialynas, G. Deligeorgis, N. L. Thomas, Z. Hatzopoulos, and N. T. Pelekanos *Physica E*, vol. 23, p. 329, 2004.

[17] A. Polimeni, M. Henini, A. Patanè, L. Eaves, P. Mai, and G. Hill *Appl. Phys. Lett.*, vol. 73, p. 1415, 1998.

[18] J. Miguel-Sánchez, A. Guzmán, J. M. Ulloa, A. Hierro, and E. Muñoz *Appl. Phys. Lett.*, vol. 84, p. 2524, 2004.

[19] J. Miguel-Sánchez, M. H. M. Gutiérrez, P. Navaretti, H. Y. Liu, A. Guzmán, J. M. Ulloa, A. Hierro, and E. Muñoz *J. Cryst. Growth*, vol. 270, p. 62, 2004.

[20] A. Arnoult, F. Gonzalez-Posada, S. Blanc, V. Bardinal, and C. Fontaine *Physica E*, vol. 23, p. 352, 2004.

[21] P. N. Hai, W. M. Chen, I. A. Buyanova, H. P. Xin, and C. W. Tu *Appl. Phys. Lett.*, vol. 77, p. 1843, 2000.

[22] C. Skierbiszewski *Semicond. Sci. Technol.*, vol. 17, p. 803, 2002.

[23] C. Skierbiszewski, P. Perlin, P. Wisniewski, T. Suski, J. F. Geisz, K. Hingerl, W. Jantsch, D. E. Mars, and W. Walukiewicz *Phys. Rev. B*, vol. 65, p. 035307, 2001.

[24] F. Masia, G. Pettinari, A. Polimeni, M. Felici, A. Miriametro, M. Capizzi, A. Lindsay, S. B. Healy, E. P. O'Reilly, A. Cristofoli, G. Bais, M. Piccin, S. Rubini, F. Martelli, A. Franciosi, P. J. Klar, K. Volz, and W. Stolz *Phys. Rev. B*, vol. 73, p. 073201, 2006.

[25] T. Tite, O. Pagès, M. Ajjoun, J. P. Laurenti, D. Bormann, E. Tournié, O. Maksimov, and M. C. Tamargo *Solid State Electron.*, vol. 47, p. 455, 2003.

[26] F. Cerdeira, C. J. Buchenauer, F. H. Pollak, and M. Cardona *Phys. Rev. B*, vol. 5, p. 580, 1972.

[27] J. Ibáñez, R. Cuscó, S. Hernández, L. Artús, M. Henini, A. Patanè, L. Eaves, M. Roy, and P. A. Maksym *J. Appl. Phys.*, vol. 99, p. 043501, 2006.

[28] K. Takahashi, A. Yoshikawa, and A. Sandhu, *Wide Bandgap semiconductors: Fundamental Properties and Modern Photonic and Electronic Devices*. Berlin, Germany: Springer, 2005.

[29] Landoelt-Boernstein, *Numerical Data and Functional Relationships in Science and Technology*. Berlin, Germany: Springer-Verlag, 1982.

[30] J. Groenen, C. Priester, and R. Carles *Phys. Rev. B*, vol. 60, p. 16013, 1999.

[31] J. Ibáñez, R. Cuscó, and L. Artús *Phys. Status Solidi B*, vol. 223, p. 715, 2001.

[32] M. Cardona *Phys. Rev.*, vol. 121, p. 752, 1961.

[33] E. O. Kane *J. Phys. Chem. Solids*, vol. 1, p. 249, 1957.

[34] J. S. Blakemore *J. Appl. Phys.*, vol. 53, p. R123, 1982.

[35] W. Shan, W. Walukiewicz, J. W. Ager III, E. E. Haller, J. F. Geisz, D. J. Friedman, J. M. Olson, and S. R. Kurtz *Phys. Rev. Lett.*, vol. 82, p. 1221, 1999.

[36] X. Liu, M. E. Pistol, L. Samuelson, S. Schwetlick, and W. Seifert *Appl. Phys. Lett.*, vol. 56, p. 1451, 1990.

[37] A. Grau, T. Passow, and M. Hetterich *Appl. Phys. Lett.*, vol. 89, p. 202105, 2006.

[38] J. Wu, W. Shan, and W. Walukiewicz *Semicond. Sci. Technol.*, vol. 17, p. 860, 2002.

[39] J. Endicott, A. Patanè, J. Ibáñez, L. Eaves, M. Bissiri, M. Hopkinson, R. Airey, and G. Hill *Phys. Rev. Lett.*, vol. 91, p. 126802, 2003.

[40] P. J. Klar, J. Teubert, M. Guengerich, T. Niebling, H. Gruening, W. Heimbrodt, K. Volz, W. Stolz, A. Polimeni, M. Capizzi, E. P. O'Reilly, A. Lindsay, M. Galluppi, L. Geelhaar, H. Riechert, and S. Tomic *Phys. Status Solidi B*, vol. 244, p. 24, 2007.

[41] D. T. Hon and W. L. Faust *Appl. Phys.*, vol. 1, p. 241, 1973.

[42] K. Wan and J. F. Young *Phys. Rev. B*, vol. 41, p. 10772, 1990.

[43] K. M. Yu, W. Walukiewicz, J. Wu, J. W. Beeman, J. W. Ager III, E. E. Haller, W. Shan, H. P. Xin, C. W. Tu, and M. C. Ridgway *Appl. Phys. Lett.*, vol. 90, p. 2227, 2001.

[44] J. Ibáñez, R. Kudrawiec, J. Misiewicz, M. Schmidbauer, M. Henini, and M. Hopkinson *J. Appl. Phys.*, vol. 100, p. 093522, 2006.

[45] J. Ibáñez, M. Henini, R. Kudrawiecs, M. Schmidbauer, and M. Hopkinson *J. Cryst. Growth*, vol. 301-302, p. 552, 2007.

"If I have a thousand ideas
and only one turns out
to be good, I am satisfied."
Alfred Bernhard Nobel

7

Summary and Conclusions

The present work has been aimed to provide a deeper insight of the Raman scattering processes that take place in doped and undoped leading semiconductors in the optoelectronics. In this chapter we present a list of the main results and conclusions reached throughout the work.

Raman scattering in as-grown and implanted ZnO

- We have carried out a comprehensive Raman study on the first and second order modes in as-grown high-quality bulk ZnO. We have unambiguosly determined all the first order Raman active modes by using different geometry conditions and considering the Raman selection rules. We have shown that, contrary to DFT calculations, the energy of the E_1(LO) mode is higher than that of the A_1(LO) at $q \sim 0$.

- The symmetry and nature of all the second-order modes has been identified by analyzing Raman spectra obtained in several geometries, and according to DFT-calculated phonon density of states. Also, we have unambiguously assigned the mode at 333 cm^{-1}, which was previously attributed to TA[M] overtones, to the difference mode $E_2^{\text{high}} - E_2^{\text{low}}$ by means of temperature-dependent Raman scattering.

- We have performed temperature-dependent high-resolution Raman spectra of the E_2^{high}, A_1(LO) and E_1(LO) modes. The high-resolution Raman spectra revealed an asymmetric E_2^{high} mode in ZnO. We have explained this asymmetry

in terms of anharmonic decay and the presence of a ridge-like structure in the two-phonon DOS around the E_2^{high} frequency, which gives rise to a non-uniform frequency-dependent imaginary part of the phonon self-energy. By contrast, we have observed symmetric lineshapes for the polar A_1 and E_1 longitudinal optical modes, as a consequence of the almost uniform two-phonon DOS around their frequencies.

- We have determined the effective third-order anharmonic coupling constants of the E_2^{high}, A_1(LO) and E_1(LO) modes, by analyzing our temperature-dependent Raman measurements and considering the DFT-calculated phonon DOS of ZnO. The best fit to our data for the E_2^{high} mode reveals that the main anharmonic decay mechanisms of this mode are phonon-sum decay channels into combinations of the TA and LA bands in the vicinity of the K point.

- By contrast, we have shown that the temperature dependence of the frequency and FWHM of the A_1(LO) and E_1(LO) modes can be satisfactorily explained assuming a simple generalized Ridley channel, i.e. the decay into a pair TO and TA phonons whose frequencies correspond to maxima of the phonon DOS. The branches in which the A_1 and E_1 modes decay, are splitted due to anisotropy forces in the wurtzite structure. Our anharmonic decay analysis showed that the E_1(LO) mode is more affected by impurity/defect scattering, which reveals a possible anisotropy in the distribution of defects between the in-plane and c-direction in ZnO.

- Phonon lifetimes have been extracted from the FWHM of the Raman lineshapes in as grown ZnO. The LO modes have lifetimes around 0.5 ps at 300 K, which is close to that reported for high-quality AlN and one order of magnitude lower than that for GaN. For this reason, we state that ZnO is more suited for high-speed devices than GaN, since hot-phonon effects should play a less relevant role in carrier relaxation.

- We have performed a systematic and accurate frequency determination of the polar modes as a function of the phonon propagation direction. We have explained this angular dependence by means of Loudon's model for uniaxial crystals. The quasimodes frequency behavior may be useful to determine crystal orientation in ZnO-based nanostructures. From the angular and polarization dependence of the LO and TO modes, we suggest that although birefringence is important in several optical studies, it may be neglected when dealing with

quasiphonons in ZnO.

- We have uniformly implanted ZnO with several atomic species and we have shown that the DALO band is a good indicator of the degree of implantation-induced lattice damage. We have seen that the intensity of this band scales linearly with the mass of the implanted ion. After a RTA at 950° for 10 s under a continuous O_2 gas flow, the DALO bands are fully removed from the Raman spectra, which indicates the high degree of lattice recovery even for the heavily damaged ZnO samples.

- We have observed additional Raman modes only for the ZnO:N^+ sample. We have ruled out their origin to be intrinsic to lattice defects, since the modes do not appear for the samples implanted with the native species. To obtain further information about the origin of the additional modes appearing in ZnO:N^+, we have performed an isotopic study by implanting ZnO with ^{14}N and ^{15}N ions. We have seen that the frequency of the additional modes does not change with the N isotope. Thus, our experiments conclude that the additional modes appearing in ZnO:N are wrongly atributed to LVMs of nitrogen in a substitutional position in the host lattice. From this study, we suggest that N atoms induce local distortions in the ZnO lattice or forms complex defects that does not occur for other atomic species.

Raman scattering in GaN-related materials

- We have performed a comparative study between the IR-transmission and Raman techniques to investigate the *w*-AlGaN system, including the binaries GaN and AlN. IR-transmission experiments at oblique incidence clearly reveal simultaneously the GaN-like $E_1(\mathrm{TO})$ and $A_1(\mathrm{LO})$ modes of the AlGaN alloy system. By contrast, the Raman spectra from the AlGaN epilayers show the GaN-like E_2^{high} mode and a weak $A_1(\mathrm{LO})$ mode, which is overlapped with second-order features related to the Si substrate. This fact may give rise to a frequency overestimation of the Raman allowed modes.

- From the IR measurements, we have observed a monotonical frequency increase of the $A_1(\mathrm{LO})$ and the GaN-like $E_1(\mathrm{TO})$ modes with the Al content, which agrees with previous Raman studies on thick AlGaN layers. Also, the IR-technique has allowed us to detect a clear $E_1(\mathrm{TO})$ and the $A_1(\mathrm{LO})$ modes from the AlN buffer under the AlGaN epilayer, while no signal from this layer

is observed in the Raman spectra. Therefore, the IR technique at oblique incidence can ve very useful to complement Raman spectroscopy for the detection of phonons arising from very thin layers of semiconductor compounds with low Raman efficiencies, such as the AlGaN alloy system.

- We have explored the use of Berreman-IR-transmission measurements for the study of *c*-GaN, and the effects caused by the presence of an AlN buffer layer. The TO and LO modes of *c*-GaN are clearly detected by both techniques, Raman and IR-transmission, but signal from *w*-GaN has been only detected by Raman scattering (a sharp E_2^{high} peak). *w*-GaN domains are not noticed by IR transmission since the frequency of the IR active LO and TO modes for both phases is very similar and the transmission dips are much broader than the corresponding Raman peaks. By contrast and similar to the AlGaN samples, no signal from the AlN buffer layer appears in the Raman spectra, whereas dips associated to the TO and LO modes of the *c*-AlN layer are unambiguously detected by IR transmission with the Berreman technique.

- We have carried out the first Raman scattering study of the phonon composition dependence in *w*-$B_xGa_{1-x}N$, for $x < 4\%$. For low boron contents ($x < 2\%$), both E_2^{high} and $A_1(LO)$ modes exhibit a similar frequency increase as a result of alloying effects. For boron contents $2 < x < 4\%$, the E_2^{high} peak broadens substantially and its frequency falls back to values similar to those of low boron composition samples. Contrary, the $A_1(LO)$ frequency maintains its trend of increasing frequency with boron composition. We have explained these results by the presence of a higher degree of disorder and strain with increasing x associated with the incorporation of defects, and composition inhomogeneities, which give rise to a selective excitation of regions with higher boron content.

- We have used Raman scattering to investigate undoped and As-doped *w*-GaN epilayers grown on sapphire substrates by PA-MBE with different III/V ratios. We have found that the frequency of the E_2^{high} phonon mode displays a progressive downward frequency shift with decreasing III/V ratio, regardless of the presence of As during growth. This shift can be attributed to strain relaxation of the epilayers, suggesting N-rich conditions yield layers with higher density of dislocations.

- From the analysis of peak broadenings and disorder-activated modes for the As-

doped GaN epilayers, we state that the presence of As in GaN epilayers reduces the crystal quality of the samples. Also, we have observed the existence of cubic GaN domains in some of the As-doped samples.

- In both As-doped and undoped Ga-rich GaN epilayers, we have observed a feature at $\sim$232 cm^{-1}, which was previously assigned to As or Bi impurities in As- and Bi-doped GaN, respectively. Given that this band is also present in the undoped samples and its intensity increases with the Ga flux, we relate this band to Ga clusters in GaN. Also, we have observed that this Raman feature is more intense for the As-doped than undoped epilayers grown under similar III/V ratio conditions, which may indicate that a small fraction of As is incorporated in the Ga site. However, the band at $\sim$232 cm^{-1} is not detected for the N-rich GaN:As epilayer, which suggest that N-rich conditions may favor the formation of the GaNAs alloy.

Raman scattering in undoped and doped dilute nitrides

- We have performed a Raman study on thick strain-free $GaAs_{1-x}N_x$ layers with $x \leq 1.5\%$ to discriminate the effects of alloying from that of biaxial strain on the optical modes frequencies in dilute nitrides. We have observed that the GaN-like LO mode blueshifts when increasing the N content with a $2.5 \pm 0.5x(\%)$ cm^{-1} slope for measurements at 80 K. Despite the large error, the blueshift in the strain-free samples is larger than that found for strained layers (around $1.5x(\%)$ and $1.9x(\%)$) in previous works. This difference is due to the partial frequency compensation induced by tensile strain. Ignoring the strain-induced frequency shift leads to an overstimation of the alloy compositions in thin GaAsN films, when extracted from Raman scattering measurements.

- We have studied the GaAs-like polar modes as a function of the N content in the strained-free GaAsN epilayers. We performed Raman measurements under off-normal incidence to study simultaneously for the first time the frequency behavior of the GaAs-like TO and LO modes in dilute nitrides. While the TO mode is scarcely blueshifted with increasing N, the LO mode linearly redshifts by about $0.42 \pm 0.05x(\%)$ cm^{-1}. The GaAs-like LO frequency shift is virtually identical to that found in previous works on strained epilayers once pseudomorphic strain effects are substracted.

- The frequency behavior of the GaAs-like modes in the strain-free GaAsN sam-

ples reveal that long-range effects may have an important role in the TO-LO splitting reduction. Therefore, we have analyzed the long-range effects on the GaAs-like LO mode through the ionic plasma frequency associated to this mode ($\Omega^2_{\mathrm{GaAsN}}$). We find Ω^2_{GaAsN} values which are noticeably lower than those expected by the reduction in the Ga-As oscillators due to substitutional nitrogen. We speculate that this additional shift arises from presence of defects like N interstitials, Ga vacancies and N clusters in GaAsN.

- We have investigated a series of $In_yGa_{1-y}As_{1-x}N_x$ epilayers coherently grown on (100) and (n11) GaAs substrates (n =1, 3, 4, and 5), for $y \sim 20\%$ and $x \sim 3\%$. The Raman spectra are dominated by the GaAs-like modes, a weak InAs-like signal, a disorder-activated TO band and the N-related LVMs between the 400-600 cm^{-1}. We observe a depolarization of the TO mode possibly due to strong strain fields around the N atoms, which is not substantially affected by the substrate orientation. We have found a reduction of the LO-TO splitting to the GaAs-like optical modes induced by N-related disorder and alloying, like in strain-free GaAsN epilayers. Also, the overall shape of the LVM spectrum is the same for all the samples. Therefore, we conclude that the substrate orientation does not affect neither the crystalline quality of the InGaAsN layers nor the N local environment.

- We have identified heavily damped LOPCMs in Se-doped $GaAs_{1-x}N_x$ epilayers ($0.1 \leq x \leq 0.36\%$), which indicates the great impact of N to the GaAs matrix even for nitrogen contents as low as 0.1%. We have analyzed the overdamped LOPCMs by evaluating the free-electron susceptibility by the Extended Hydrodynamical (EHD) model, allowing us to obtain the LOPCMs lifetimes, which are strongly quenched as the N content increases. We remark that electron mobilities calculated from this analysis are highly consistent with those determined by Hall, which provides support for the reliability of the Raman analysis. The electron mobility is reduced by 4 when introducing only a 1% of N, which accounts for the existance of heavily damped LOPCMs in the samples.

- From fits to the LOPCM spectra for the GaAsN:Se samples, we have estimated the optical effective mass, m^*_{opt} of the free electrons. m^*_{opt} values extracted from the Raman spectra show a progressive increase with the N content, and are close to values obtained by magnetophotoluminescence in samples with similar N contents. This enhancement is however appreciably lower than those predicted by the two-level BAC model. Then, our results suggest that the

low electron mobility in GaAsN layers is mainly determined by the reduced scattering rate of free carriers, than by the increase in their optical effective mass.

"One never notices what has been done; one can only see what remains to be done."

Marie Curie

A

Present Situation and Future Works

The main objective of this work has been to study the vibrational properties of bulk ZnO, some GaN-related materials and dilute nitrides. The studies presented in this PhD thesis suggest different topics that can be addressed in the future. Here we outline our prospective works that can be regarded as a natural continuation of this thesis, and the most recent studies developed in our group to reach their aim.

A.1 Nanostructured ZnO

In the introductory chapter of this dissertation, the importance of ZnO in microelectronics and optoelectronics has been described. Nowadays, nanostructured ZnO materials have recieved broad attention due to their promising application in high-performance electronics, optics and photonics arising from their crystalline structure and morphology. Beside the practical importance of the great variety of growth morphologies available for ZnO such as nanobelts, nanohelices, nanowires, etc. [1], their study is also of benefit for understanding fundamental phenomena in low-dimensional systems.

Raman scattering is widely used to characterize and study the optical and vibrational properties of nanostructures, where Raman peak shifts and broadenings provide valuable information about strain, composition, phonon confinement and temperature (as it has been demonstrated in chapter 4 for layers and single crystals) [2–9].

The deep understanding of the Raman spectrum of bulk ZnO described in chapter 4 is essential to study and analyze novel optical properties of ZnO nanostructures,

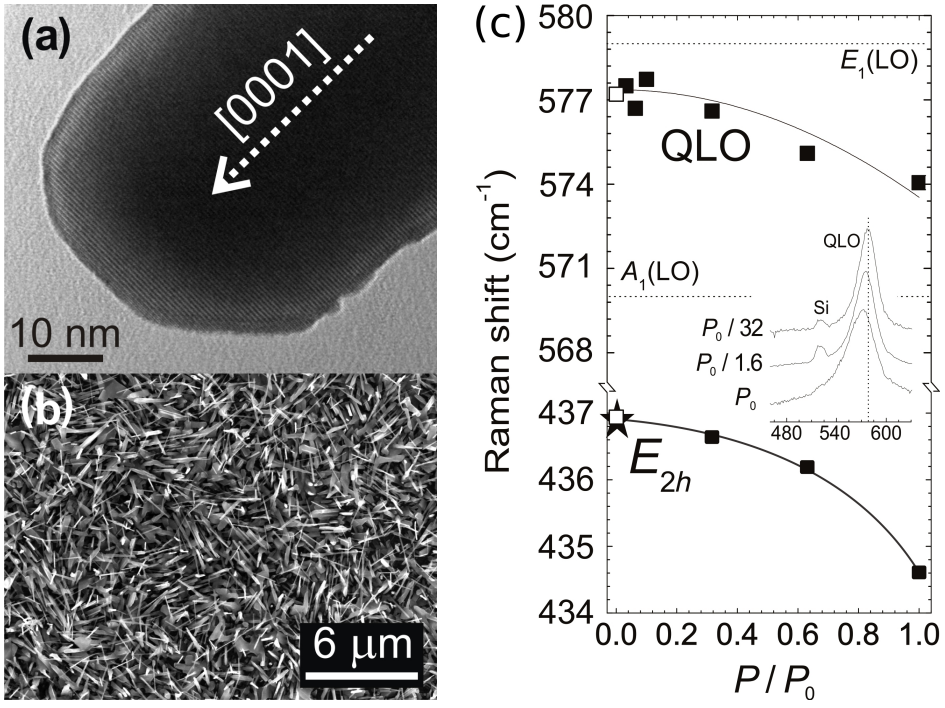

Figure A.1: (a) High-resolution TEM image taken from a single nanowire. The growth direction is along the [0001]. (b) SEM image of the as-grown ZnO nanowires. (c) Raman frequencies of the E_2^{high} and polar optical modes for the mechanically removed nanowires (filled squares) as a function of the excitation power (P). The black curves may serve as guide to the eye. The frequencies for the as-grown nanowires (empty squares) and bulk ZnO (black star for the E_2^{high} mode and dotted lines for the polar modes) are plotted only for $P \to 0$ since they do not vary with the incident power. The inset shows three representative spectra of the mechanically removed nanowires obtained with different P.

which will be the focus of our future work on ZnO.

As we have seen in chapter 4, the Raman spectrum of anisotropic crystals is sensitive to the crystal orientation. Thus, the polar optical modes observed in a collection of randomly oriented ZnO structures are no longer well-described by the bulk data, and quasimode effects must be considered. The aim of our most immediate work is to explain the frequency shift of the different features that appear in the resonant Raman spectra of randomly-aligned ZnO nanowires, with special emphasis on the longitudinal optical modes. For this purpose we firstly probe thick ZnO nanowires, for which phonon confinement effects are not expected. The nanowires that we have studied so far were grown via an Au-catalized vapor-phase carbothermal transport process on SiO_2/Si substrates (growth details can be found in [10]),

and were supplied by the *Electronics Department* of the *Universitat de Barcelona*. TEM measurements (see figure A.1.a) confirmed the presence of strain-free wurtzite (0001)-oriented ZnO nanowires with mean radius $r \sim 40$ nm and lengths up to 3 μm. SEM images of the as-deposited nanowires (figure A.1.b) reveal that their c-axis is randomly aligned with respect to the substrate.

To overcome possible difficulties when analyzing the as-grown product, such as strong elastically-scattered light or intense Raman signals from some sort of substrates, it is common to probe the nanowires removed from the substrate. For this reason, we probe nanowires both as-grown and mechanically removed from the SiO_2/Si substrate and transferred to a clean Si wafer.

The UV-Raman spectrum of the as-grown nanowires show a weak E_2^{high} mode and an intense resonant LO-like mode. While the frequency of the E_2^{high} mode corresponds to that for bulk ZnO, the LO-like mode frequency does not match with neither those of A_1(LO) nor E_1(LO) modes for the bulk material.

On the other hand, the frequency of the E_2^{high} and LO modes is visibly lower in the spectrum for the mechanically removed nanowires, than for the as-grown sample. These shifts may have two possible origins: local heating and/or crystallites alignment. In low dimensional structures, local heating induced by the excitation laser might be important, specially in free-standing structures such as the mechanically removed nanowires. As shown in chapter 4, a temperature increase in ZnO induces a downward shift and a broadening of both polar and non-polar modes. On the other hand, if the as-grown nanowires had a preferential alignment, the frequency of the LO peak would not match that of the mechanically removed nanowires, which are randomly distributed through the clean Si wafer.

To substract the possible heating effects in our measurements, we record Raman spectra by using different excitation powers (P). As-grown nanowires are not affected by laser heating since the Raman spectra is invariant to the exciting laser power. By contrast, the Raman frequencies for the mechanically removed nanowires tend to those of the as-grown when decreasing P (see figure A.1.c).

From this experiment we can conclude that: a) the nanowires in the as-grown sample are efectively randomly aligned, b) the frequency shift of the LO feature in the Raman spectra of nanowires is not fully explained by local heating effects, as claimed in other works. This difference is accounted for by the excitation of quasimodes.

At present, we are developing a model to predict the LO frequency for uniaxial-material–based nanostructures, where the nanocrystallites show different relative

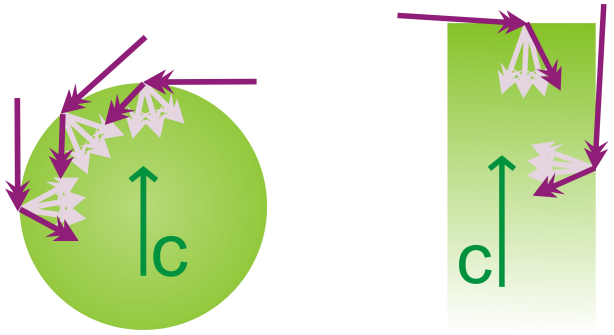

(a) Light propagation directions which are available in spherical nanocrystallites if refraction is considered.

(b) Light propagation directions which are possible in column-like nanocrystals if refraction is taken into account.

Figure A.2: Illustration of the refraction-induced limits to the light propagation in spherical- and column-like crystallites. Notice that for an spherical shape, light can propagate in any direction, but some directions are restricted for column-like structures.

alignment and morphology (for instance, well-aligned nanocolumns or randomly-aligned nanoplates). A model has been already proposed for ZnO nanocrystallites [6]. In such model, light can propagate in every direction in the nanocrystal, which is equivalent to assume an spherical morphology (see figure A.2a).

By contrast, the column-like structure restrains the available directions of light propagation in the crystal due to refraction by the enclosing surfaces (see figure A.2b). In our samples, top and side surfaces are enclosed by *c*- and *m*-planes, respectively, which means that light can propagate with angles from 0° to $\sim$ 30° and from $\sim$ 60° to 90° with respect to the *c*-axis. Also, the difference in area between the top and lateral surfaces of a column-like morphology results into a different cross-section for light scattering. Hence, the resulting LO frequency in randomly aligned nanowires depends on their diameter-to-length ratio, due to the different contribution to the quasimode frequency.

In our model, we consider these two effects in column-like structures (light refraction and cross-section). An accurate prediction of the LO signal is highly important for a further analysis of the Raman spectra, since the LO bulk data is no longer a fixed reference. Ignoring the quasinature of the LO-like feature could result into a misleading analysis of strain, phonon confinement, temperature and/or electron-phonon coupling in ZnO nanostructures.

A.2 Narrow Band Gap Group-III Nitrides

In this thesis, we have studied group-III nitrides with band gap energies in the near UV and above (AlN, GaN, BN and related alloys). InN is the group-III nitride alternative to extend the range of applications to the visible and IR spectral region. Also, InN is very promising for high-speed devices and high-efficiency photovoltaic applications due to its small electron effective mass, small band gap, high electron mobility and high drift velocity.

However, indium-rich-based materials are hardly understood and subject to many strong localization phenomena. Indeed, the InN binary is a semiconductor with several controversies around its physics and dynamics. For instance, its band-gap energy was longly thought to be 1.9 eV until experimental observations developed by *Davydov et al.* [11] and *Wu et al.* [12] in 2002 indicated a much smaller direct band gap (0.7 eV). Also, InN is unique among III-V semiconductors in that it exhibits an extreme electron accumulation at the surface [13, 14], due to ionized donor-type surface states that pin the surface Fermi level high above the conduction band minimum.

High quality InN films are difficult to grow and a large density of dislocations and native defects occur, which affect the optical and electrical properties of the resulting material [15]. Indeed, large residual electron densities are found in as-grown InN layers, which may partially arise from N vacancies, O impurities and charged dislocations [15, 16].

In the recent years, improvements in epitaxial growth techniques have led to the availability of InN films with considerably lower electron concentrations and much higher electron mobilities. Background electron concentrations in mid-10^{17} cm^{-3} with room-temperature bulk electron mobilities above 1000 cm^2/Vs have been achieved [11, 17, 18]. On the other hand, the growth of nanostructured InN, such as InN nanocolumns [19], has attracted much attention since this is a well-known method to obtain high-quality crystals free of dislocations. Nanostructured InN may offer additional advantages such as ultra-high conversion efficiencies in photonic device applications [20].

Regarding the vibrational properties of the wurtzite material, the presence of the large residual electron densities, together with the existence of an electron accumulation layer at the surface, has led to some controversies in the interpretation of the Raman spectra of InN layers and nanostructures. Indeed, for such doping levels with such large mobilities, plasma modes coupled to the InN LO modes are expected

in the Raman spectra as explained in chapter 2. However, research groups dealing with InN have not come to an agreement regarding the observation of such coupled modes (LOPCMs) and the scattering mechanisms involving the Raman process.

The typical features observed in $z(xx)\bar{z}$ Raman spectra of InN are an intense non-polar E_2^{high} mode, a clear peak at the LO frequency region and a weak feature around the TO frequency region. Several authors ascribed the LO-like structure to an L^- coupled mode and invoked wave-vector non-conserving scattering processes to explain their results [21–24]. Some of these authors concluded that the main scattering mechanism in their samples was the forbidden impurity-induced Fröhlich mechanism [21, 23], whereas others claimed instead the charge-density fluctuations as the main scattering mechanism [22].

Concerning the weak TO-like structure in InN layers, it has been assigned either to a disorder-activated A_1(TO) mode [21,24,25] or to an L^- coupled mode [26–29]. Also, the observation of L^- coupled modes at the TO-frequency region has been reported for InN nanocolumns, which were related to free charge at lateral surface [30, 31].

Our group has very recently demonstrated that Raman scattering by long- wavelength coupled modes takes place in InN layers by studying high-quality samples with background electron densities spanning a whole order of magnitude [32]. The samples were grown at *Ritsumeikan University* (Japan), and Hall measurements revealed background electron densities from $\sim 4{\cdot}10^{18}$ to $\sim 2{\cdot}10^{19}$ cm^{-3}. In this study, Raman measurements were performed by using two different excitation wavelengths, 514.5 and 780 nm, with the macrocamera configuration. For both excitation wavelengths, the Raman spectra revealed a clear shift to higher frequencies and a sharpening of the TO-like peak with increasing residual electron density in the samples (see figure A.3.a). In fact, the frequency of this peak agrees well with that expected for an L^- coupled mode in samples with such N_e if a wavevector-conserving scattering process is assumed (see inset of figure A.3.a). Hence, the TO-like feature is unambiguosly assigned to an L^- coupled mode.

To corroborate that the Raman process is wavevector-conserving, Raman scattering measurements were performed by using a longer excitation wavelength. The frequencies of the L^- mode are visibly lower in the spectra recorded under 780 nm excitation (red dots in figure A.3.a) than in those excited with the 514.5 nm line (green dots in figure A.3.a). As described in section 2.5, this is the expected behavior for LOPCMs when wavevector dispersion of the plasma oscillations is taken into ac-

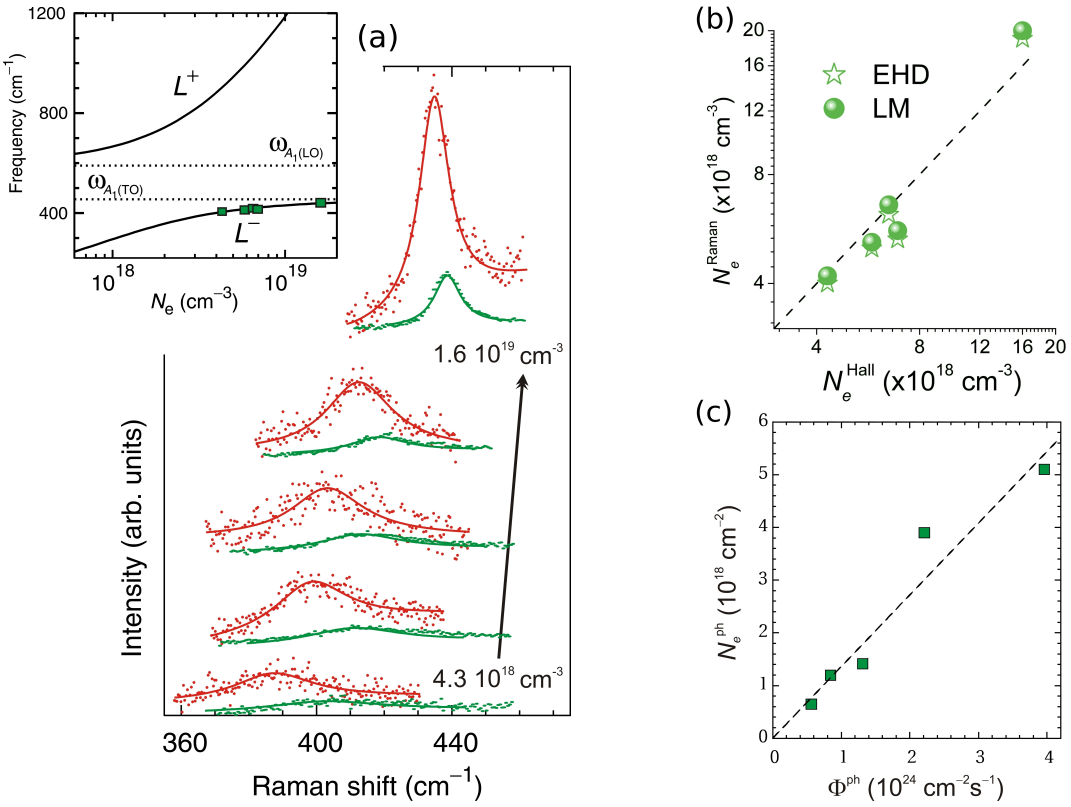

Figure A.3: (a) Raman spectra of the TO-like feature for the InN epilayers taken under 514.5 nm (red dots) and 780 nm (green dots) -wavelength excitation at 80 K. Green and red solid lines are LM-lineshape fits to the Raman spectra. The intensities are scaled to yield an E_2^{high} mode with equal intensity. Inset: Free-electron density dependence of LOPCMs as calculated from the LM model, and experimental frequencies of the TO-like feature vs the Hall-derived electron densities (green squares). (b) Raman- vs Hall- derived electron densities for the InN epilayers, by using the LM (dots) and the EHD (stars) models in the Raman analysis. (c) Photogenerated carriers in a InN epilayer as a function of the incident photon flux.

count. Hence, our result rules out that the Raman scattering process is wave-vector non-conserving in InN, as many authors have previously claimed [21–24].

Since our analysis demonstrates that the TO-like peak is an L^- mode, it is noteworthy that no L^+ signal is detected. We explain the absence of the L^+ peak in the Raman spectra in terms of inhomogeneous broadening induced by fluctuations of the electron density accross the crystal. These fluctuations mainly affect the L^+ coupled mode due to its strong plasma-like character for such doping levels, as compared to the phonon-like character of the L^- mode.

Besides, the free electron density in the InN films can obtained from suitable

line-shape fits to the L^- Raman peak [32]. By using the standard dielectric line-shape model developed by Hon and Faust (described in chapter 2) and evaluating the free-electron susceptibility by the Lindhard-Mermin (LM) model, values for the free electron densities in our samples have been found. Similarly, evaluating the L^- Raman peak by the classical Extended Hydrodynamical (EHD) model for the electronic susceptibility, the resulting electron density values are 4-6% lower than those predicted by the more accurate LM model (see figure A.3.b).

The resulting N_e values from the Raman lineshape analysis are in very good agreement with those determined by Hall experiments (figure A.3.b), although an homogeneous plasma was considered for calculation simplicity [32]. Hall data are usually strongly affected by the electron accumulation region in InN thin layers. However, the samples under study are thick enough to consider that N_e^{Hall} values are mainly related to free charge in the bulk. This assumption is compatible with our Raman results, bearing in mind the good agreement between the N_e^{Hall} and N_e^{Raman}. Ideed, plasma modes are hardly expected to exist in a few nm-thick layer (which is the theoretical thickness given for the electron accumulation region in InN) and, hence, we suggest that the L^- coupled mode is related to the free-charge in the bulk.

As just discussed, electrons in the surface accumulation layer are confined. Also, the small thickness of this region yields to wavevector uncertainities much larger than the Thomas-Fermi screening wavevector (q_{TF}). Consequently, the large electron density at the surface accumulation layer is not capable to screen the macroscopic electric field associated to the LO mode. Within the electron accumulation layer, the confining potential gives rise to extremely high electric fields. Bearing in mind these considerations, in our study we propose that the LO-like feature appearing in the Raman spectra of InN, is an unscreened A_1(LO) mode, which is enhanced by surface-field-induced Raman scattering mechanisms in the accumulation layer. We are planning to perform further analysis to corroborate the origin of the observed A_1(LO) mode.

The unambiguous assignment of the TO-like Raman feature to be a long-wavelength L^- coupled mode, is the first step which opens a wide window of oportunities to deeper understand the physics in InN. For instance, bulk N_e values obtained by Hall are strongly disturbed by the electron acumulation layer in InN thin films. Hence, we suggest that Raman scattering may be an alternative technique to probe background N_e in InN thin films, since carrier densities obtained from Raman lineshape analysis are mainly related to residual free electrons in the bulk.

On the other hand, we have very recently observed photoexcited carriers in our Raman experiments for InN films when excited with high laser power densities. The Raman analysis for doped semiconductors with photoexcited carriers is quite more complicated than for simply doped crystals. In this case, a multicomponent plasma (electrons, light holes and heavy holes) has to be considered. A preliminary analysis of the photoexcited carriers in the InN layers, reveals a nearly linear increase of N_e^{ph} with the photon density flux of the exciting light. As can be seen in figure A.3.c, the photoexcited carrier density reaches up to $\sim 5 \cdot 10^{18}$ cm^{-3} values for the highest photon fluxes. This behavior suggests that the surface recombination velocity of excitons in InN is very small. One of our most inmediate aims is to further investigate on the surface recombination velocity in the samples with different residual electron densities. Also, we aim to study by means of Raman scattering how this velocity is affected by the surface Fermi level pinning.

Likewise, our future work with III-nitrides will focus on the study of InN nanocolumns, epitaxially and lithographically grown. The reason to study InN nanocolumns is twofold. First, nanocolumns are expected to have lower dislocation densities, and consequently low background electron densities (10^{16} cm^{-3} or less). We intend to analyze the features emerging in their Raman spectra whose nature may be related to the residual electron densities (three dimensional plasma) and/or to the electron accumulation layer at the lateral surfaces (two dimensional plasma). Second, we aim to evaluate the surface recombination velocity in InN and assess how it may be affected by the high surface-to-volume ratio of nanocolumn structures.

References

[1] Z. L. Wang *Mat. Today*, vol. 7, p. 26, 2004.

[2] M. Rajalakshmi, A. K. Arora, B. S. Bendre, and S. Mahamuni *J. Appl. Phys.*, vol. 87, p. 2445, 2000.

[3] R. P. Wang, G. Xu, and P. Jin *Phys. Rev. B*, vol. 2004, p. 113303, 2004.

[4] Y. Zhang, H. Jia, R. Wang, C. Chen, X. Luo, and D. Yu *Appl. Phys. Lett.*, vol. 83, p. 4631, 2003.

[5] L. L. Yang, J. H. Yang, D. D. Wang, Y. J. Zhan, Y. X. Wang, H. L. Liu, H. G. Fan, and J. H. Lang *Physica E*, vol. 40, p. 920, 2008.

[6] L. Bergman, X. Chen, J. Huso, J. L. Morrison, and H. Hoeck *J. Appl. Phys.*, vol. 98, p. 093507, 2005.

[7] F. Demangeot, V. Paillard, P. M. Chassaing, C. Pagès, M. L. Kahn, A. Maisonnat, and B. Chaudret *Appl. Phys. Lett.*, vol. 88, p. 071921, 2006.

[8] K. A. Alim, V. A. Fonoberov, M. Shamsa, and A. A. Balandin *J. Appl. Phys.*, vol. 97, p. 124313, 2005.

[9] K. A. Alim, V. A. Fonoberov, and A. A. Balandin *Appl. Phys. Lett.*, vol. 86, p. 053103, 2005.

[10] J. D. Prades, R. Jiménez-Díaz, F. Hernández-Ramírez, L. Fernández-Romero, T. Andreu, A. Cirera, A. Romano-Rodríguez, A. Cornet, J. R. Morante, S. Barth, and S. Mathur *J. Phys. Chem. C*, vol. 112, p. 14639, 2008.

[11] V. Y. Davidov, A. A. Klochikhin, R. P. Seisyan, V. V. Emtsev, S. V. Ivanov, F. Bechstedt, J. Furthmueller, H. Harima, A. V. Mudryi, J. Aderhold, O. Semichinova, and J. Graul *Phys. Status Solidi B*, vol. 229, p. R1, 2002.

[12] J. Wu, W. Walukiewicz, K. M. Yu, J. W. Ager III, E. E. Haller, H. Lu, W. J. Schaff, Y. Saito, and Y. Nanishi *Appl. Phys. Lett.*, vol. 80, p. 3967, 2002.

[13] H. Lu, W. J. Shaft, L. F. Eastman, and C. E. Stutz *Appl. Phys. Lett.*, vol. 82, p. 1736, 2003.

[14] I. Mahboob, T. D. Veal, C. F. McConville, H. Lu, and W. J. Schaff *Phys. Rev. Lett.*, vol. 92, p. 036804, 2004.

[15] A. G. Bhuiyan, A. Hashimoto, and A. Yamamoto *J. Appl. Phys.*, vol. 94, p. 2779, 2003.

[16] L. F. J. Piper, T. D. Veal, C. F. McConville, H. Lu, and W. J. Schaff *Appl. Phys. Lett.*, vol. 88, p. 25109, 2006.

[17] D. C. Look, H. Lu, W. J. Schaff, J. Jasinski, and Z. L. Weber *Appl. Phys. Lett.*, vol. 80, p. 258, 2002.

[18] T. Inushima, V. V. Mamutin, V. A. Vekshin, S. V. Ivanov, T. Sakon, M. Motokawa, and S. Ohoya *J. Cryst. Growth*, vol. 227, p. 481, 2001.

[19] M. A. Sánchez-García, J. Grandal, E. Calleja, S. Lazic, J. M. Calleja, and A. Trampart *Phys. Status Solidi B*, vol. 243, p. 1490, 2006.

[20] A. Sood and R. Welser *SPIE Newsroom*, vol. 94, p. DOI 10.1117/2.1200807.1207, 2008.

[21] J. S. Thakur, D. Haddad, V. M. Naik, R. Naik, G. W. Auner, H. Lu, and W. J. Schaff *Phys. Rev. B*, vol. 71, p. 115203, 2005.

[22] F. Demangeot, C. Pinquier, J. Frandon, M. Gaio, O. Briot, B. Maleyre, S. Ruffenach, and B. Gil *Phys. Rev. B*, vol. 71, p. 104305, 2005.

[23] J. W. Pomeroy, M. Kuball, C. H. Swartz, T. H. Myers, H. Lu, and W. J. Schaff *Phys. Rev. B*, vol. 75, p. 035205, 2007.

[24] A. Kasic, M. Schubert, Y. Saito, Y. Nanishi, and G. Wagner *Phys. Rev. B*, vol. 65, p. 115206, 2002.

[25] T. Inushima, M. Higashiwaki, and T. Matsui *Phys. Rev. B*, vol. 68, p. 235204, 2003.

[26] V. Y. Davidov, V. V. Emtsev, I. N. Goncharuk, A. N. Smirnov, V. D. Petrikov, V. V. Mamutin, V. A. Vekshin, S. V. Ivanov, M. B. Smimov, and T. Inushima *Appl. Phys. Lett.*, vol. 75, p. 3297, 1999.

[27] E. Kurimoto, M. Hangyo, H. Harima, M. Yoshimoto, T. Yamaguchi, T. Araki, and Y. Nanishi *Appl. Phys. Lett.*, vol. 84, p. 212, 2004.

[28] Y. M. Chang, H. W. Chu, C. H. Shen, H. Y. Chen, and S. Gwo *Appl. Phys. Lett.*, vol. 90, p. 072111, 2007.

[29] Y. M. Chang, C. T. Chuang, C. T. Chia, K. T. Tsen, H. Lu, and W. J. Schaff *Appl. Phys. Lett.*, vol. 85, p. 5224, 2004.

[30] S. Lazic, E. Gallardo, J. M. Calleja, F. Agulló-Rueda, J. Grandal, M. A. Sánchez-Garcia, E. Calleja, E. Luna, and A. Trampert *Phys. Rev. B*, vol. 76, p. 205319, 2007.

[31] J. Segura-Ruiz, N. Garro, A. Cantarero, C. Denker, J. Malindretos, and A. Rizzi *Phys. Rev. B*, vol. 79, p. 115305, 2009.

[32] R. Cuscó, J. Ibáñez, E. Alarcón-Lladó, L. Artús, T. Yamaguchi, and Y. Nanishi *Phys. Rev. B*, vol. 79, p. 1, 2009.

B

List of Publications

Ref.	Title	Authors	Reference	IF index
4.1	Study of the temperature dependence of E2 and A1(LO) modes in ZnO	E. Alarcón-Lladó, R. Cuscó, J. Ibáñez, L. Artús, J. Jimenéz, B. Wang, and M. Callahan	Mater. Res. Soc. Symp. Proc. **957** 0957-K07-11	-
4.2	Temperature dependence of Raman scattering in ZnO	R. Cusco, E. Alarcón-Lladó, J. Ibáñez, L. Artús, J. Jiménez, B. Wang, and M. Callahan	Physical Review B **75** 165202	3.172
4.3	Raman scattering of quasimodes in ZnO	E. Alarcón-Lladó, R. Cuscó, L. Artús, J. Jimenéz, B. Wang, and M. Callahan	J. Phys.: Condens. Matter **20** 445211	1.886
4.4	Raman scattering characterization of implanted ZnO	E. Alarcón-Lladó, R. Cuscó, L. Artús, G. González-Díaz, I. Martil, J. Jimenéz, B. Wang, and M. Callahan	Mater. Res. Soc. Symp. Proc. **957** 0957-K07-24	-

4.5	Isotopic study of the nitrogen-related modes in N^+-implanted ZnO	L. Artús, R. Cuscó, E. Alarcón-Lladó, G. González-Díaz, I. Martil, J. Jimenéz, B. Wang, and M. Callahan	Applied Physics Letters **90** 181911	3.596
5.1	Raman scattering study of undoped and As-doped GaN grown with different III/V ratios	J. Ibánez, D. Pastor, E. Alarcón-Lladó, R. Cuscó, L. Artús, S.V. Novikov, C.T. Foxon	Semicond. Sci. Tech. **22** 1145	1.899
5.2	Far-infrared transmission in GaN, AlN, and AlGaN thin films grown by molecular beam epitaxy	J. Ibánez, S. Hernández, E. Alarcón-Lladó, R. Cuscó, L. Artús, S.V. Novikov, C.T. Foxon, and E. Calleja	J. Appl. Phys. **104**, 033544	2.171
5.3	Phonons in $B_xGa_{1-x}N$/GaN epilayers studied by means of UV Raman scattering	R. Cuscó, E. Alarcón-Lladó, J. Ibánez, L. Artús, S. Gautier, and A. Ougazzaden	Phys. Stat. Solidi b **245** 731	1.071
6.1	Optical phonon behavior in strain-free dilute Ga(As,N) studied by Raman scattering	J. Ibánez, E. Alarcón-Lladó, R. Cuscó, L. Artús, and M. Hopkinson	J. Appl. Phys. **102**, 013502	2.171
6.2	Dilute (In,Ga)(As,N) thin films grown by molecular beam epitaxy on (100) and non-(100) GaAs substrates: a Raman scattering study	J. Ibánez, E. Alarcón-Lladó, R. Cuscó, L. Artús, M. Henini, and M. Hopkinson	J. Mater. Sci.: Mater. Electron. **20**, S116	0.947

6.3	LO phonon-plasmon coupled modes and carrier mobilities in heaavily Se-doped Ga(As,N) thin films	J. Ibánez, E. Alarcón-Lladó, R. Cuscó, L. Artús, D. Fowler, A. Patanè, K. Uesugi, and I. Suemune	J. Mater. Sci.: Mater. Electron. **20**, S425	0.947
6.4	Electron effective mass and mobility in heavily doped *n*-GaAsN probed by Raman scattering	J. Ibánez, R. Cuscó, E. Alarcón-Lladó, L. Artús, A. Patanè, D. Fowler, L. Eaves, K. Uesugi, and I. Suemune	J. Appl. Phys. **103**, 103528	2.171

"Cridem qui som i que tothom ho escolti. I en acabat, que cadascú es vesteixi com bonament li plagui, i via fora! Que tot està per fer i tot és possible."

Miquel Marí i Pol
(Ara Mateix)

C

Resum en Català

Introducció

En els últims anys, la recerca en el món de la microelectrònica s'ha centrat en trobar nous materials per tal de satisfer un mercat en demanda contínua. La revolució de la indústria en l'electrònica que ha tingut lloc en les últimes dècades ha transformat la nostra vida diària d'una manera que ningú podia preveure anys ençà, quan el primer transistor fóu inventat. Aquest esdeveniment va suposar un gran avenç en l'estudi dels semiconductors, en entendre la seva física i conseqüentment, en permetre desenvolupar l'electrònica d'avui dia.

El mercat de circuits integrats per la computació, intercanviadors de potència, emmagatzament de dades i comunicació, està dominat principalment pel silici (Si). La tecnologia de fabricació d'aquest semiconductor s'ha desenvolupat de tal manera al llarg dels anys que avui dia el cost de la seva manufactura és molt reduït. Malauradament, el Si semiconductor té un salt d'interbandes indirecte, fet que porta a l'arsenur de gal.li (GaAs) com al material més adequat sobre el qual basar els dispositius optoelectrònics, ja que té un salt de banda prohibida directe i mobilitats dels portadors majors que les del Si.

Tanmateix, el GaAs i derivats no permeten cobrir tot el rang especral, des de l'ultravioleta (UV) fins l'infraroig (IR). El què s'anomena enginyeria de l'ample de banda prohibida, *band-gap engineering* en anglès, ja permet fabricar dispositius optoelectrònics basats en aliatges de GaAs que operen des de l'IR fins el groc. Per tant, cal investigar materials amb ample de banda prohibida (E_g) majors per tal d'extendre

el rang d'operació dels dispositius optoelectrònics fins al verd/blau/UV.

Els materials amb un E_g superior als $\sim$ 2 eV es coneixen com a *wide-band-gap*, dins els quals es troba el carbur de silici (SiC), el selenur de zinc (ZnSe), el nitrur de gali (GaN) i l'òxid de zinc (ZnO). Els materials *wide-band-gap* no només són interessants pel seu E_g ideal per operar en l'UV/blau, sinó que també ofereixen molts avantatges en termes de potència i de resistivitat a la radiació d'alta energia, altes temperatures i freqüències.

L'interès en materials *wide-band-gap* va començar a finals dels anys 80, quan va sortir a la venda el primer LED emissor de llum blava basat en SiC. Apart del SiC i del diamant, que tenen salts de banda prohibida inderecte i per tant baixes eficiències òptiques, es pot parlar de tres tipus de semiconductors *wide-band-gap*: les calcogenites del grup III, com ara el ZnSe; els òxids del grup II, com el ZnO; i els nitrurs del grup III, com seria el GaN.

A principis dels anys 90, el primer làser de díode pulsat emissor de llum blava es basava en ZnSe. Malgrat els avenços científics i tecnològics en aquest material, la ràpida degradació dels materials relatius representa encara un un punt feble. Des de llavors, el GaN ha rebut molta atenció en el món de la recerca sobre làsers i LEDs emissors en el blau i l'UV. L'any 1993, l'investigador Shuji Nakamura va obtenir el primer LED emissor de llum blava/UV d'alta brillantor, utilitzant l'aliatge de InGaN com a material emissor. L'interès en el ZnO va començar més endavant, quan es van haver desenvolupat noves tecnologies per a fabricar tant cristalls com capes primes epitaxials d'alta qualitat. Durant l'última dècada s'ha aconseguit créixer molts tipus d'estructures de ZnO tant a escales *macro* com *nano*. Després d'haver sigut àmpliament utilitzat en la cosmètica, com a sensor de gasos i per la fabricació de transistors, el ZnO va esdevenir un bon candidat per ser utilitzat en aplicacions optoelectròniques. En efecte, la primera emissió en l'UV del ZnO va ser observada per *Zu et al.* l'any 1997 en ZnO microcristal.lí.

Tant el GaN com el ZnO presenten propietats molt similars. Mentre que l'ample de banda prohibida a temperatura ambient del ZnO és de 3.37 eV, el del GaN és de 3.39 eV. Els dos materials tenen paràmetres de xarxa molt similars, i per aquesta raó són bons candidats a fer de substracte l'un de l'altre en creixement epitaxial. Tot i que els aliatges basats en qualsevol dels dos semiconductors cobreixen gairebé el mateix rang d'energies d'emissió/absorció, s'espera que el ZnO permeti faricar díodes de làser amb menor voltatge llindar, ja que els seus excitons poden existir a més temperatura. De fet, l'energia de lligam dels excitons en el ZnO és d'uns 60 meV, que és més del doble de la dels excitons en el GaN (26 meV). Aquest fet porta

a una emisssió excitònica al fons de la banda molt intensa per temperatures fins i tot superiors a l'ambient. Fins avui dia s'ha aconseguit que capes de ZnO altament texturades laserin en l'UV quan són bombejades òpticament.

Per altra banda, en l'última dècada s'ha desenvolupat molts estudis sobre el creixement i l'aplicació d'estructures de ZnO de baixa dimensió. Aquestes estructures són unes grans candidates per a ser usades en biosensors, detectors d'UV i dispositius d'un únic xip. Malgrat tot, encara cal superar un problema per què el ZnO pugui fer camí en el món de la optoelectrònica: aconseguir capes conductives tipus p de manera reproduïble. Tot i el gran progrés que s'ha dut a terme en la fabricació de ZnO tipus p, encara no s'ha aconseguit capes d'alta qualitat de manera reproduïble. Una de les possibles causes a aquest problema són els defectes intrínsecs del cristall, que es creu que compensen la càrrega tipus p. De fet, s'ha demostrat que tant el zinc intersticial com les vacants d'oxigen presenten una entalpia de formació molt baixa. Per tal de superar aquest coll d'ampolla i obtenir un control sobre les propietats del material, és imprescindible entendre els processos físics que es duen a terme en el ZnO dopat, sense oblidar l'objectiu d'aconseguir ZnO d'alta qualitat amb nivells baixos de dopants residuals tipus n.

Tot i el gran interès pel ZnO, els nitrurs del grup III no han deixat de ser objecte d'investigació. Ben al contrari, els nitrurs del grup III han estat reconeguts com el sistema de materials més important per la fabricació de dispositius optoelectrònics operant en el verd, blau i l'UV. De fet, el làser de díode més potent del món emissor en el blau/UV l'ha produït l'empresa Sanyo molt recentment, i es basa en GaN.

Un dels principals candidats dins el grup de nitrurs per tal d'extendre la fabricació d'emissors i detectors en l'UV és el sistema $Al_xGa_{1-x}N$. Quan s'afegeix Al al GaN, l'ample de banda s'extén des dels 3.39 eV fins als 6.2 eV, que correspon a l'E_g del AlN d'estructura hexagonal. A més a més, el salt de banda és directe per tot el rang de composicions de Al. El sistema $Al_xGa_{1-x}N$ també és molt atractiu per la possibilitat que ofereix de ser integrat en la tecnologia del Si. El principal problema d'aquest aliatge però és la presència de tensions, dislocacions, dominis d'inversió i piràmides hexagonals superficials, que empitjoren les propietats electròniques i optoelectròniques de les seves capes.

Un altre candidat per al *band-gap engineering* és el sistema BGaN. De manera similar al cas del $Al_xGa_{1-x}N$, s'espera que el BGaN tingui l'ample de banda prohibida major que la del GaN, ja que l'E_g del BN és de 5.5 eV a temperatura ambient. Tot

i que amb una quantitat adequada de B, l'aliatge té el mateix paràmetre de xarxa que els substractes de 6H-SiC, la gran diferència de paràmetres de xarxa entre els binaris GaN i BN fa que sigui complicat obtenir dapes de BGaN unifàsic amb concentracions majors al 2% de B. Malauradament, hi ha molt poca informació sobre les propietats físiques d'aquest aliatge. De fet, aquest és un material molt nou i encara es troba en estat de desenvolupament, però tenint en compte el l'interès creixent en el seu estudi, sembla possible que aviat hi hagi capes de millor qualitat i amb major concentració de bor.

No només és interessant créixer aliatges basats en el GaN utilitzant espècies atòmiques del grup III, sinó també fent servir les del grup V. La unió entre el GaN, d'E_g gran, i el GaAs, d'E_g mitjà, sembla evident ja que els costos de producció del GaAs i relatius són baixos, els seus processos de producció estan ben desenvolupats i la tecnologia dels nitrurs ha patit grans avenços en els últims anys. Si es pogués créixer l'aliatge GaNAs al llarg de tot el rang de composicions, aquest es podria utilitzar en dispositius que operin des de l'UV fins l'IR.

S'ha descobert que la incorporació de As a la xarxa del GaN provoca la formació d'un estat localitzat a la banda de València de la seva matriu. Aquest fet dóna lloc a una reducció de l'E_g molt poc lineal (*band gap bowing*). A més a més, la luminiscència de la banda blava de mostres de GaN dopades amb As (fomant o no l'aliatge GaNAs) és més intensa que l'emissió al fons de la banda en mostres sense dopar, fet ue n'augmenta la potencial aplicació d'aquests compostos. Cal destacar també que el As té un efecte surfactant en el GaN, fet que en millora la funcionalitat. Malauradament, créixer aliatges de GaNAs ordenats i unifàsics no és trivial i, ara per ara, només s'ha aconseguit incorporar petites quantitats de As.

De la mateixa manera que s'introdueix As al GaN, també es pot intentar incorporar N al GaAs per augmentar-ne l'ample de banda prohibida. Sorprenentment, l'any 1992 *Weyers et al.* van observar l'efecte contrari a l'esperat: l'E_g era molt menor en les mostres dopades que en les no dopades. Aquest comportament tant inusual va causar un gran interès tant des del punt de vista de la física fonamental, com des del punt de vista aplicat. La reducció de l'ample de banda prohibida és notable fins i tot per concentracions de nitrogen tan baixes com un 0.0032%. Aquests nous aliatges de propietats físiques tan inusuals, es coneixen avui dia com a nitrurs diluïts. Tot i que les primeres capes epitaxials de nitrurs diluïts eren de poca qualitat cristal.lina i presentaven eficiències òptiques baixes, fet que no és del tot sorprenent

en un material nou, l'interès en l'estudi dels nitrurs diluïts no ha parat de créixer. El principal problema és que la introducció de N al GaAs en redueix ràpidament la qualitat cristal.lina. La gran diferència entre les mides dels àtoms de N i As causa grans tensions a la xarxa del GaAs. Una solució és la introducció d'àtoms de In al sistema, els quals compensen la mida reduïda dels àtoms de N a la vegada que provoquen una disminució addicional de l'E_g. Així doncs, l'aliatge InGaAsN és un material molt interessant per l'optoelectrònica en el rang espectral de les telecomuinicacions (1.3-1.5 μm). A més a més, quan la fracció de In és tres vegades major a la del N, aquest aliatge quaternari té el mateix paràmetre de xarxa que el GaAs, i per tant es pot integrar dins la seva tecnologia una vegada es tingui un bon coneixement de les seves propietats físiques.

Tot i que tots aquests materials són molt prometedors i que en els últims anys se n'ha obtingut resultats molt sorprenents, encara hi ha un llarg camí per recórrer dins la recerca sobre aquests. Es necessiten estudis per tal de comprendre millor els mecanismes que dónen lloc a les seves propietats físiques, millorar-ne els sistemes de creixement, i així, optimitzar el funcionament dels dispositius.

L'espectre fonònic de qualsevol material és una de les seves característiques més fonamentals. L'espectroscòpia Raman és una tècnica molt potent i no-destructiva que permet avaluar les propietats vibracionals dels cristalls. Les mesures Raman poden donar informació sobre la qualitat cristal.lina del material, de la mateixa manera que permeten analitzar aspectes més concrets de la dinàmica de la xarxa, com ara efectes isotòpics, anharmonicitat, vides mitjes dels fonons, defectes de la xarxa, ... L'espectroscòpia Raman també és molt útil per l'estudi d'aliatges i heteroestructures, ja que permet obtenir informació sobre la seva composició, tensions i *intermixing*. A més a més, si el material presenta càrrega lliure, la tècnica pot proporcionar informació sobre la interacció càrrega-fonó i sobre transicions òptiques assistides per fonons, les quals tenen un paper molt important en el funcionament dels dispositius. Per tant, l'estudi de la dinàmica de la xarxa no només és interessant des del punt de vista fonamental, sinó també per tal d'entendre millor els paràmetres estructurals que són responsables de l'eficiència dels dispositius microelectrònics i optoelectrònics, transport de calor, l'electrònica quànitca i fins i tot de la superconductivitat.

Aquesta tesi

Aquesta tesi està centrada en l'anàlisi i l'estudi de les propietats vibracionals de semiconductors d'actual interès en l'optoelectrònica tant en l'UV com en el rang de les telecomunicacions. Amb aquesta fi, s'ha utilitzat principalment l'espectroscòpia Raman com a tècnica d'anàlisi de la seva dinàmica de la xarxa.

La tesi està dividida en tres grans blocs, segons la relació de compostos estudiats: ZnO verge i implantat, nitrurs del grup III *wide-band gap* i nitrurs diluïts dopats i sense dopar. A continuació es farà un resum dels principals resultats obtinguts en cadascun d'aquests blocs.

ZnO verge i implantat

Els últims estudis sobre les proprietats vibracionals del ZnO daten dels anys seixanta i setanta. A la literatura hi ha estudis del seu espectre Raman tant sota condicions de resonància com de no-resonància. Tot i així, la baixa resolució espectral dels equips d'ençà i la poca qualitat cristal.lina que presentava el ZnO llavors, va crear certes controvèrsies en la freqüència i assignament de modes de primer i segon ordre, i en l'assimetria de certs pics.

Fins fa ben poc no hi havia disponible cristalls volúmics de ZnO d'alta qualitat i per tant el coneixement sobre la dinàmica de la xarxa d'aquest és força limitat. De fet, molt recentment s'ha publicat les primeres mesures experimentals de dispersió inelàstica de neutrons (INS) sobre les branques òptiques i acústiques del ZnO al llarg de certes línies d'alta simetria de la zona de Brillouin. Fins llavors, l'única guia per a interpretar els resultats experimentals sobre la dinàmica de la xarxa eren càlculs teòrics DFT de la dispersió de fonons del ZnO.

L'adopció que s'ha fet en els últims anys del ZnO com a material clau dins l'electrònica i optoelectrònica, demana que es duguin a terme estudis fonamentals, acurats i fiables de la seva dinàmica de la xarxa.

Espectre Raman de primer i segon ordre en el ZnO verge

Un dels objectius d'aquesta tesi és dur a terme un estudi profund, detallat i precís dels modes Raman de primer i segon ordre en mostres de ZnO d'alta qualitat.

Les mostres utilitzades en els nostres estudis són cristalls volúmics d'estructura *wurtzita* que han estat crescuts pel mètode hidrotermal. Abans de realitzar els estudis vibracionals, hem investigat la degradació òptica de la superfície del ZnO en patir

processos de polit mecànics. Mitjançant mesures de càtodo-luminiscència resoltes en l'espai, hem observat com la pressió provocada per un poliment mecànic afecta considerablement la qualitat òptica de la superfície. Per tal d'eliminar la superfície alterada, aquesta s'ha de tractar químicament. Tenint en compte que les propietats òptiques de la superfície poden afectar els espectres Raman, les mostres estudiades en aquest treball han estat polides per l'empresa *Nova SiC*, líder mundial en el poliment del ZnO.

Hem realitzat espectres Raman en condicions fóra de resonància i en diverses configuracions de dispersió per tal d'observar tots els modes de primer ordre del ZnO (inclòs el mode E_1(LO), que s'observa en condicions de dispersió poc habituals). Gràcies a aquestes mesures hem pogut corroborar que el mode E_1(LO) té una energia major que el A_1(LO) a centre zona ($q \sim 0$), per contra del què preveien certs càlculs DFT.

Els experiments en diverses geometries de dispersió ens han permès determinar la simetria de tots els modes de segon ordre que es troben dins el rang de 100-1200 cm^{-1}. El mode de segon ordre més intens a la regió de baixes freqüències (pic a ~ 333 cm^{-1}) és força controvers pel que fa a la seva assignació. A partir de mesures Raman a diverses temperatures, hem pogut observar com el comportament de la intensitat d'aquest pic es correspon a la d'un mode diferència. Analitzant la densitat d'estats a un sol fonó (1-DOS) del ZnO, hem determinat que el pic a ~ 333 cm^{-1} és el mode diferència $E_2^{high} - E_2^{low}$.

Per altra banda, hi ha molts camps de la física i la tecnologia dels semiconductors que es veuen molt afectats pels mecanismes de decaïment i vides mitjes dels fonons. L'estudi d'aquests es pot dur a terme amb l'anànlisi de les corbes Raman, i és rellevant per al desenvolupament i millora dels dispositius. Els fonons òptics longitudinals tenen un paper molt important en els límits fonamentals i pràctics dels dispositius. La seva vida mitja i les interaccions que pateixen amb la càrrega lliure determinen paràmetres tant importants com la velocitat de saturació i la termalització dinàmica de les càrregues. Mentre que els temps de vida mitja dels fonons del AlN i GaN ja es coneixen, no hi ha gaire informació sobre aquests paràmetres en el ZnO.

Així doncs, un altre dels objectius d'aquesta tesi ha sigut determinar els temps de vida mitja i els mecanismes de decaïment dels fonons del ZnO associats als modes LO. A partir de les amplades a mitja alçada dels pics Raman, hem extret els temps de vida mitja dels fonons dels modes LO. Hem obtingut un temps de vida mitja al voltant dels 0.5 ps per als dos modes LO del ZnO, valor que és molt similar al dels

fonons LO en el AlN i menors dels del GaN. Segons aquest resultat podem afirmar que el ZnO és més apropiat per la fabricació de dispositius d'alta potència, ja que patirà menys efectes relacionats amb els anomenats *hot phonons*.

També hem realitzat un anàlisi complet i exhaustiu de les freqüències i amplades de pic dels modes A_1(LO) i E_1(LO) en funció de la temperatura. Hem vist com l'eixamplament i desplaçament cap a baixes freqüències dels pics Raman en augmentar la temperatura, és degut a l'expansió tèrmica de la xarxa i al decaïment anharmònic dels modes en fonons TO i TA corresponents a màxims de la 1-DOS. Aquest tipus de decaïment és força comú en modes LO, i s'anomena decaïment a través del canal Ridley. L'anàlisi de decaïment anharmònic en funció de la temperatura també ens ha permès calcular el que s'anomena l'eixamplament natural del mode a temperatura 0 K (Γ_0), que dóna una idea de la contribució de les imperfeccions de la xarxa al decaïment dels fonons. Curiosament, Γ_0 és major pel mode E_1(LO) que no pas pel mode A_1(LO), fet que indica una possible anisotropia en la distribució dels defectes en el ZnO. O sigui, la direcció en l'eix *c* sembla presentar menys defectes que el pla perpendicular.

Per altra banda, també ens hem interessat pel mode E_2^{high}, ja que és el més intens de l'espectre Raman del ZnO. Tal i com havien previst antics treballs, aquest mode té una corba Raman assimètrica. Aquest fet provoca que el càlcul del temps de vida mitja i l'anàlisi del decaïment anharmònic dels fonons no sigui directe. De fet, s'ha de recórrer al què s'anomena l'enrgia pròpia del fonó (*phonon self-energy*), la qual depèn de la densitat d'estats a dos fonons del material (2-DOS). Utilitzant càlculs teòrics DFT de la literatura i la *self-energy*, hem explicat com una 2-DOS irregular al voltant de la freqüència del mode E_2^{high} provoca l'assimetria del pic Raman d'aquest. Analitzant la corba del mode E_2^{high} a diverses temperatures hem pogut determinar amb poca ambigüetat els seus mecanismes de decaïment: el mode decau principalment en la suma de fonons de les bandes TA i LA.

Un altre punt important a tenir en compte sobre els fonons òptics en materials anisotròpics, com ara el ZnO, és que quan els eixos d'alta simetria del cristall estàn desviats respecte la direcció de propagació del fonó, els modes es *barrejen*. Aquesta *barreja* de modes polars dóna lloc al què s'anomena *quasimodes*, la freqüència dels quals depèn de la direcció de propagació de la llum. Apart de l'interès intrínsec des del punt de vista fonamental, la dependència dels quasimodes amb la direcció de la llum incident és rellevant en l'anàlisi fonònic de ZnO nano-estructurat, ja que en aquestes els eixos d'alta simetria poden estar orientats aleatòriament. L'espectroscòpia Raman

és una tècnica molt utilitzada per estudiar nano-estructures per tal d'avaluar-ne les propietats vibracionals i òptiques i d'extreure'n informació addicional sobre tensions, composició, confinament, temperatura, acoblament fonó-càrrega, ... Per tant, si s'ignora la presència de quasimodes es pot arribar a errors en l'anàlisi de qualsevol de les propietats just comentades.

S'ha publicat alguns treballs sobre quasimodes en cristalls de AlN i GaN, però només s'ha publicat un parell de treballs als anys 60 sobre cristalls de ZnO on es mostra només una direcció de propagació de quasimodes. Tenint en compte la importància que té avui dia el ZnO per la fabricació de dispositius d'alta velocitat, d'alta potència i optoelectrònics, hem realitzat un estudi complet i sistemàtic dels quasimodes en el ZnO.

Hem dut a terme experiments Raman no-resonants en ZnO volúmic variant l'angle d'incidència del feix d'excitació. En variar l'angle, hem observat com els modes polars perden el seu caràcter A_1 i E_1, mantenint-ne el de transversal òptic i longitudinal òptic. És a dir, hem detectat la presència de modes quasi-TO i quasi-LO quan la direcció de propagació del fonó no coincideix amb els eixos principals del cristall. La freqüència d'aquests quasimodes en funció de l'angle de propagació es pot explicar a través del model de Loudon per medis uniaxials. Altrament, realitzant les mesures amb diferents estats de polarització de la llum incident, hem pogut determinar que la birrefringència no té un paper important en l'estudi de quasimodes en el ZnO.

Modes locals de vibració en el ZnO implantat

Cal recordar que per tal de poder fabricar dispositius basats en el ZnO és essencial aconseguir tant capes de tipus *n* com de tipus *p*. Com ja s'ha comentat anteriorment, obtenir ZnO tipus *p* encara representa un repte. Una de les tècniques més atractives per introduir dopants és la implantació iònica, ja que el dopatge és molt selectiu i controlat. Malauradament, el feix d'ions fa malbé la xarxa, la qual s'acostuma recuperar a partir de tractaments tèrmics.

La majoria dels estudis en materials implantats iònicament es centra en entendre diferents aspectes fonamentals, com ara el grau de dany del cristall, la naturalesa dels defectes induïts pel feix d'ions, el grau d'incorporació a la xarxa dels ions implantats... Mentre que les tècniques més comunment utilitzades per estudiar la qualitat òptica dels materials (com ara la fotoluminiscència) no permeten avaluar el grau de dany al cristall i la seva recuperació, l'espectroscòpia Raman ho permet. En espectres Raman de ZnO danyat per un feix d'ions, s'ha observat certes branques dels fonons

longitudinals òptics que han sigut activats pel desordre i han desaparescut després de sotmetre les mostres a recuïts d'altes temperatures.

Els tractaments tèrmics no només es duen a terme per a millorar l'estat de la xarxa cristal.lina, sinó també per aconseguir que les impureses implantades s'emplacin en posicions substitucionals i s'activin elèctricament. La tècnica de caracterització Hall proporciona informació sobre la densitat de càrrega lliure i la mobilitat de les capes implantades. Mitjançant mesures Hall, s'ha trobat que el grau d'activació de les impureses en el ZnO és molt baix, ja sigui perquè l'energia d'activació elèctrica és elevada, per la compensació per defectes natius o per la formació de complexes elèctricament inactuis. En aquest context, l'espectroscòpia Raman pot proporcionar informació sobre la incorporació de les impureses a la xarxa i sobre la possible formació de complexes. En concret, els modes de vibració local (LVM) es poden tractar com les *empremtes* d'impureses incorporades a la xarxa i/o formant complexes.

Així com el N és un dels candidats més importants per aconseguir ZnO tipus p, la termodinàmica de la seva incorporació a la xarxa és complicada. A la literatura es troba diversos estudis centrats en caracteritzar la incorporació del N a la xarxa del ZnO i la formació de complexes que per ventura poden reduir l'eficiència del ZnO:N. Aquests estudis mostren com l'espectre Raman del ZnO:N presenten estructures característiques a les freqüències de 275, 510 i 644 cm^{-1}. L'origen d'aquests pics és encara font de debat. Hi ha autors que afirmen que els pics són LVMs. En canvi d'altres asseguren que són modes intrínsecs a la xarxa del ZnO, ja que també els observen en mostres dopades amb Fe, Sb i Al. De manera paral.lela, *Manjón et al.* suggereixen que els pics corresponen a modes *silent* del ZnO, i que han estat activats pel desordre i per la presència d'impureses. En canvi, *Wang et al.* presenten una sèrie de càlculs teòrics combinats amb mesures experimentals per determinar que un dels modes (275 cm^{-1}) està relacionat amb complexes de zinc, i que la resta de pics són deguts al desordre.

Fins avui, no hi ha cap evidència experimental de la participació directa del N en aquests modes. És per això que en aquest treball volem estudiar quin paper té el N en la vibració dels modes addicionals mitjançant mostres de ZnO implantades amb N^+. Abans però, cal esbrinar quin és el dany provocat per la implantació iònica i si podem recuperar la cristal.linitat de la xarxa mitjançant recuïts tèrmics. Per consegüent, hem implantat mostres de ZnO amb diferents espècies atòmiques (N, P, O, Zn) sota el mateix perfil d'implantació uniforme. En primer lloc, hem observat que en totes les mostres implantades apareix una banda ampla a la regió de les frqüències longitudinals òptiques. Aquesta banda correspon a modes de la branca LO de $q \neq 0$

que han estat activats pel desordre (banda DALO). En segon lloc, veiem com la intensitat d'aquesta banda creix de manera lineal amb la massa de l'ió implantat. Per tant, creiem que la banda DALO pot ser un bon indicador del grau de dany en la xarxa cristal.lina del ZnO.

Per tal de recuperar la xarxa cristal.lina, hem sotmès totes les mostres sota un recuït tèrmic ràpid (RTA) a 950° durant 10s sota un flux constant de O_2. Després del recuït, la banda DALO no s'observa en cap de les mostres implantades, fet que demostra un alt grau de recuperació de la seva xarxa.

Referent als modes addicionals, només aquests apareixen en l'espectre Raman de la mostra dopada amb N. Ja que els modes no s'observen en les mostres implantades amb les espècies natives, hem descartat que aquests estiguin relacionats amb defectes intrínsecs a la xarxa del ZnO. Per tal de guanyar més informació sobre l'orígen d'aquests modes, hem implantat ZnO amb dos isòtops diferents de nitrogen: ^{14}N i ^{15}N. L'orígen d'aquest estudi isotòpic es basa en què la freqüència dels modes vibracionals està directament relacionada amb la massa dels àtoms vibrants. Per tant, diferents isòtops de N donarien lloc a LVMs a diferent freqüència. Per contra, els pics experimentals en qüestió presenten la mateixa freqüència per als dos isòtops de N. Conseqüentment, hem conclòs que els modes addicionals que apareixen en mostres de ZnO:N no són modes LVM de nitrogen en posició substitucional. Segons els nostres resultats suggerim que el N indueix distorcions locals a la xarxa del ZnO o crea complexes de defectes, fet que no succeeix per altres espècies atòmiques.

Nitrurs del grup III

Tal i com s'ha comentat anteriorment, el creixement i les propietats dels nitrurs del grup III han sigut el focus de molts estudis des de l'aparició del primer LED emissior en el blau als anys 90.

Hi ha estudis que tracten els fonons d'alguns dels compostos basats en el GaN, ja sigui mitjançant espectroscòpia Raman o d'infraroig. A temperatura ambient, l'espectre Raman del GaN d'estructura *wurtzita* sota la configuració $z(xx)\bar{z}$ està dominat pels modes E_2^{low} i E_2^{high} i, amb menys intensitat, els mode polar A_1(LO). La resta de modes Raman actius del GaN també han estat identificats utilitzant confiduracions de dispersió vàries.

L'interès particular en aliatges ternaris i quaternaris basats en els niturs s'esdevé de la possibilitat que ofereixen ajustar l'ample de la banda prohibida, aconseguint valors inaccessibles a través de compostos binaris. Mentre que l'E_g de l'aliatge es

pot estimar en força casos a través d'una interpolació lineal entre els valors dels binaris (per exemple, el cas del $Al_xGa_{1-x}N$), existeixen sistemes, com el GaAsN, on hi ha grans desviacions o *band gap bowing*.

Des del punt de vista vibracional, els fonons d'un aliatge segueixen una tendència característica per cada sistema. Normalment, els modes es deplacen en freqüència segons la composició, ja que la massa reduïda dels àtoms en vibració varia. Típicament, els modes d'un aliatge poden seguir dues tendències: d'un únic tipus (*one-mode*), de tipus doble (*two-mode*). La freqüència dels modes de comportament *one-mode* d'un aliatge $A_xB_{1-x}C$ qualsevol varia de manera contínua des de les d'un binari (AB) a l'altre (AC). Per contra, pels modes *two-mode* apareixen dos conjunts de modes, un per cada binari. La freqüència d'aquests és similar a la dels binaris corresponents i la seva intensitat depèn de la fracció molar de cada component. És a dir, si un aliatge té un mode LO tipus *two-mode*, hi haurà dos modes LO, les freqüències dels quals aniran des d'un dels binaris (AC o BC) fins al mode d'impuresa d'aquest dins l'altre binari ($BC:A$ o $AC:B$).

Transmissió infraroja en els sistemes *w*-$Al_xGa_{1-x}N$ i *c*-GaN/AlN

Pel què respecta les propietats vibracionals de l'aliatge $Al_xGa_{1-x}N$, *Davydov et al.* van estudiar de manera molt completa el comportament de tots els seus modes Raman en funció de la fracció de Al. Els seus experiments mostren com els modes A_1(LO) i E_1(LO) segueixen un comportament *one-mode*, mentre que la resta segueixen el *two-mode*. Aquest estudi es va realitzar sobre capes gruixudes de $Al_xGa_{1-x}N$. Avui dia però, el $Al_xGa_{1-x}N$ s'utilitza en forma de capa prima per la fabricació de dispositius. L' estudi de capes tan primes de $Al_xGa_{1-x}N$ per Raman esdevé força problemàtic ja que aquest material té molt poca eficiència Raman, sobretot quan la fracció de Al és elevada. A més a més, la senyal Raman del substracte pot *eclipsar* els pics associats a l'aliatge. Alguns autors han augmentat la senyal de la capa prima de $Al_xGa_{1-x}N$ a partir d'experiments Raman sota condicions de resonància excitant amb llum UV. Malauradament, la forta absorció del material a aquestes energies fa que només s'estigui avaluant la regió més superficial de la capa (els primers 100 nm o menys).

Nosaltres en aquest treball proposem utilitzar l'espectroscòpia d'IR com a tècnica complementària al Raman per obtenir informació dels fonons en capes primes de $Al_xGa_{1-x}N$. Amb aquest propòsit, hem analitzat capes primes de $Al_xGa_{1-x}N$ sobre AlN/Si(111) amb $x \sim 2, 25.5, 29\%$. Les mesures convecionals de transmissió d'IR (en incidència normal) només permeten observar modes que ipliquen oscil.lacions atòmiques paral.leles a la superfície de la capa. Per contra, si el feix és del tipus

TM (camp magnètic perpendicular al pla d'incidència) i la seva incidència és oblíqüa, llavors es poden observar tant modes TO com LO. Aquest és el que s'anomena *efecte Berreman*.

En materials uniaxials, com és el cas de les capes de AlGaN, l'orientació de l'eix extraordinari respecte la superfície de la capa determina la simetria dels modes que s'observaran. Les nostres capes de AlGaN tenen l'eix òptic (c) normal a la superfície. Seguint la teoria electromagnètica de transmissió de l'IR, el mode E_1(TO) del tipus GaN i el mode A_1(LO) haurien de veure's reflectits en els espectres de transmissió d'IR en incidència oblíqüa. Efectivament, tot i el poc gruix de les capes, els espectres de transmissió d'IR experimentals mostren unes valls pronunciades referents a aquests dos modes, la freqüència dels quals es desplaça en canviar la concentració de Al en concordància amb la literatura. Per contra, la senyal de la capa de AlGaN no és tan clara en els espetres Raman. El mode A_1(LO) es troba superposat a una banda de segon ordre del substracte de Si i el mode E_1(TO) és molt complicat d'observar en capes primes ja que segons les regles de selecció només està permès quan la incidència del feix és per al cara lateral. El que sí permet analitzar l'espectroscòpia Raman és el mode E_2^{high} del tipus GaN, el qual és IR inactiu.

Per altra banda, els espectres de transmissió IR també mostren els modes E_1(TO) i A_1(LO) de la capa de AlN intermitja, els quals són imperceptibles en els espectres Raman.

Els estudis de transmissió d'IR en el GaN d'estructura *wurtzita* són escassos, ja que moltes vegades el substracte utilitzat és el safir, el qual és molt absorbent en tota la regió dels modes de primer ordre del GaN. En canvi, el GaN d'estructura cúbica, el qual té certes avantatges respecte el d'estructura hexagonal en termes de dopatge i propietats elèctriques, s'acostuma a créixer sobre substractes de GaAs. No es troba gaires estudis sobre c-GaN ja que és difícil de créixer. Sovint s'incorpora una capa prima de AlN entre la capa i el substracte, per tal de millorar la qualitat del c-GaN, a més a més d'evitar possibles difusions de As provinent del substracte.

En els nostres estudis hem volgut comparar la informació que proporcionen les tècniques de transmissió IR i de Raman a l'hora d'estudiar capes primes de c-GaN crescudes sobre GaAs amb i sense una capa intermitja de AlN. Hem observat que les dues tècniques permeten identificar clarament els modes TO i LO del c-GaN. Tanmateix, amb l'espectre de transmissió d'IR també hem identificat els modes TO i LO de la capa de AlN intermitja, fet que no ho permet l'espectre Raman. Per contra, l'espectre Raman manifesta la presència de facetes de GaN hexagonal en la mostra que conté la capa de AlN. Els modes polars del c-GaN i w-GaN són força

amples i són molt propers en freqüència, de manera que la tècnica de transmissió d'IR no permet observar com la capa intermitja de AlN potencia la presència de GaN hexagonal.

Sistema *w*-$B_xGa_{1-x}N$

Un altre sistema interessant per a extendre l'operativitat dels sistemes III-N cap a l'UV és l'aliatge BGaN. Aquest és un sistema molt novell i encara es troba en fase de desenvolupament. Per aquesta raó encara no hi ha molta informació sobre les seves propietats físiques, com ara la dinàmica de xarxa. Tot i que hi ha molt poques referències respecte l'espectre Raman del binari BN, les freqüències dels modes òptics d'aquest material es troben per sobre dels 1000 cm^{-1}, tant per el BN d'estructura cúbica com hexagonal. Per tant, a l'incorporar B al GaN s'espera que les freqüències dels modes òptics augmentin.

El problema principal per analitzar aquest sistema és que no és fàcil créixer capes de BGaN relaxades i unifàsiques per fraccions de bor superiors a un 4%. La tècnica Raman però pot ser útil per identificar aquestes tensions i inhomogeneïtats de composició. Per exemple, un estudi realitzat al nostre grup sobre capes de InGaN mostra com la tècnica Raman detecta inhomogeneïtats en la comosició de l'aliatge per mitjà de resonàncies selectives i desplaçments en freqüència dels modes polars. Sota condicions properes a la resonància, els modes polars pateixen un augment considerable de la seva intensitat degut a la interacció *Fröhlich* electró-fonó. Fins i tot es detecten multi-fonons de segon ordre (2LO) i superiors (3LO, 4LO, ...). L'augment d'intensitat induït per *Fröhlich* depèn molt de la diferència entre les energies d'excitació i l'E_g del material. Per tant, inhomogeneitats espaials en la composició dónen lloc a inhomogeneitats espaials de l'E_g, que a la vegada causen resonàncies selectives. Això implica que donada una energia d'excitació, la senyal Raman provindrà principalment de les regions on l'E_g n'és més proper.

Coneixent la problemàtica que existeix en el sistema BGaN i la informació que pot proporcionar la tècnica Raman en condicions properes a la resonància, un altre dels objectius d'aquesta tesi ha sigut estudiar capes de *w*-BGaN en el rang de composicions disponibles fins la data ($x < 4\%$). El mode polar $A_1(LO)$ predomina l'espectre Raman de totes les mostres, seguit per el mode E_2^{high} força més feble. Segons la tendència de les seves freqüències en funció de la concentració de bor, es pot distingir clarament dos règims. El primer (per $x < 2\%$) es correspon a un increment de freqüència força lineal per als dos modes i en concordància amb l'esperat com a resultat de l'aliatge. En el segon règim en canvi (per $2 < x < 4\%$), el mode E_2^{high}

s'eixampla i dismineuix en freqüència mentre que el mode A_1(LO) segueix amb la mateixa tendència que en el primer règim. Aquest fet indica que per continguts de B superiors al 2%, hi ha força desordre i tensions associats a l'augment de defectes. A més a més, també indica que es produeixen inhomogeneitats en la composició de l'aliatge, i la senyal Raman del mode A_1(LO) prové precisament de les regions amb un major contingut de B.

Efecte del coeficient III/V en el GaN dopat amb As

La incorporació de As al GaN ha anat creixent en interès en els últims anys degut a tres grans raons:

a) El As té une efecte surfactant en el GaN i en promou la fase cúbica, de manera que ofereix la possibilitat de créixer capes de nitrurs més gruixudes.

b) L'aliatge GaNAs pateix una reducció molt significativa de l'E_g respecte del GaN. Malauradament, la incorporació de As a la xarxa del GaN és molt complicada.

c) El GaN dopat amb As té una emissió molt intensa en la regió del blau, relacionada amb els àtoms de As.

És ben conegut que el coeficient entre els fluxes de Ga i N (o coeficient III/V) durant el creixement per MBE afecta considerablement la morfologia, la qualitat cristal.lina i les propietats òptiques i elèctriques de la capa resultant. També s'ha insinuat que el coeficient III/V té un paper important al créixer GaN sota fluxos de As, a l'hora de determinar si la capa resultant és GaN dopat amb As o l'aliatge GaNAs. L'espectroscòpia Raman pot donar informació sobre la posició del As a través de l'estudi de modes LVM i efectes d'aliatge sobre els modes òptics. Un estudi realitzat per *Kaczmarczyk et al.* conclou que la presència d'impureses de As isolades en el GaN dónen lloc a modes LVM entre les freqüències de 95-200 cm^{-1}, i que clústers de As es reflectirien a l'espectre Raman al voltant de 235 cm^{-1}. Per altra banda, si el As s'incorporés a la xarxa, així formant l'aliatge GaNAs, els modes òptics tipus GaN s'haurien de desplaçar cap a baixes freqüències.

Per tant, hem aplicat l'espectroscòpia Raman per esbrinar com afecta el coeficient III/V a la qualitat i incorporació d'impureses al GaN. Per tal d'assolir aquest objectiu hem estudiat mostres de *w*-GaN, dopades amb As i sense dopar, crescudes per MBE sota diferents condicions de coeficient III/V.

Els espectres Raman de les mostres de *w*-GaN sense dopar indiquen clarament com créixer sota condicions riques en Ga dóna lloc a capes de millor qualitat cristal.lina. També hem vist com en augmentar la presència de Ga durant el creixement, apareix una estructura al voltant de 232 cm^{-1}, el qual estava atribuït a clústers de As fins llavors. Els nostres resultats experimentals indiquen que aquesta banda podria estar relacionada amb clústers de Ga. A mesura que augmenta el coeficient III/V de les mostres, el mode E_2^{high} es desplaça cap a baixes freqüències i apareixen modes activats per el desordre, denotant la relaxació de les capes per la creació de dislocacions/defectes.

Les mostres de *w*-GaN crescudes sota un flux addicional de As presenten un espectre Raman similar al de les no dopades. En concret, la freqüència del mode E_2^{high} segueix la mateixa tendència respecte el coeficient III/V en els dos tipus de mostra. Per contra, l'amplada del pic associat a aquest mode augmenta progressivament en incrementar el coeficient As/Ga, fet que indica que la presència de As durant el creixement empitjora la qualitat cristal.lina de les capes. Pel què respecta la banda a ~ 232 cm^{-1}, aquesta és significativament més intensa en les capes dopades riques en Ga que no pas en les no dopades que han estat crescudes en condicions similars. Aquest fet indica, que tot i millorar-ne la qualitat cristal.lina, créixer el GaN sota condicions riques en Ga afavoreix la incorporació del As a la posició del Ga. Per tant, per tal d'aconseguir l'aliatge GaNAs caldria créixer les mostres sota condicions riques en N.

Finalment, també cal destacar que en algunes de les mostres dopades amb As s'ha observat el mode TO associat al *c*-GaN. És a dir, que la presència de As durant el creixement afavoreix la creació de sub-dominis de GaN cúbic.

Nitrurs diluïts

Els nitrurs diluïts són compostos III-V amb concentracions baixes de N a la xarxa (concentracions habitualment menors d'un 5%). Els compostos GaAsN, InGaAsN, GaPN, InPN o AlGaAsN formen part d'aquest grup de materials anomenats nitrurs diluïts. Tots ells manifesten una reducció drstica de l'E_g que se surt de la típica linealitat (*band-gap bowing*). Aquest fenòmen fa que els nitrurs diluïts siguin molt interessants tant des del punt de vista aplicat com des del punt de vista fonamental. Degut a la gran diferència entre les electro-negativitats dels àtoms de N i As/P, substituir àtoms de N en la posició del As/P introdueix estats elecrònics quasi-localitzats a la xarxa del material hoste. Aquests estats quasi-localitzats interactuen amb la banda

electrònica de la xarxa, provocant que el salt energètic fonamental d'interbandes es desplaci considerablement cap a baixes energies, a més a més de crear una segona transició electrònica a més altes energies, anomenada E_+.

En aquest estudi ens hem centrat en els aliatges GaAsN i InGaAsN, l'interès dels quals ja s'ha destacat a la secció introductòria. Tot i que el quaternari InGaAsN té especial interès en el món de les telecomunicacions, el ternari GaAsN és molt atractiu des del punt de vista fonamentali ens permetrà entendre millor la perturbació causada pel N.

Efectes d'aliatge en els fonons òptics del GaAsN

S'ha publicat alguns estudis referent a les propietats vibracionals d'aliatges GaAsN. Els nitrurs diluïts són d'estructura zinc-blenda i els seus modes TO i LO són del tipus *two-mode*, fet que no sorprèn en aquest aliatge on el N i el As tenen masses tant diferents. Això significa que, tenint en compte les freqüències dels modes impuresa respectius, el mode LO tipus GaAs decreix en freqüència i el mode LO tipus GaN es desplaça cap a ferqüències majors a mesura que augmenta la concentració de N. Com que es tracta d'aliatges en el règim molt diluït, es pot dir que el mode LO tipus GaN és un mode LVM de nitrogen substituïnt un àtom de As. Aquests treballs també s'expliquen com la interacció entre els modes òptics referents a les dues subxarxes és força feble. Això dóna lloc a què el mode LVM de N sigui molt sensible a variacions de l'estat i ambient local dels àtoms de N. S'ha demostrat que en el GaAsN el mode local de N té una freqüència al voltant de 470 cm^{-1} i correspon a vibracions d'àtoms de N envoltats per quatre àtoms de Ga.

Respecte els modes tipus GaAs de l'aliatge ternari, aquests també pateixen desplaçaments en freqüència en funció de la fracció de N. Malgrat tot, fins avui dia no s'ha discernit entre el deplaçament causat per tensions pseudomòrfiques de la xarxa i el causat per efectes d'aliatge, ja que tots els estudis s'han realitzat en capes primes tensionades.

Per tant, en aquesta tesi s'ha estudiat capes gruixudes i relaxades de GaAsN amb concentracions fins a un 1.5% de N. A l'igual que en estudis anteriors, el mode LO tipus GaN es desplaça cap al blau, mentre que el mode local de N es desplaça cap al vermell a mesura que augmenta la concentració de N. L'augment de freqüència del mode local de N en les mostres relaxades és major que el publicat sobre mostres tensionades. Per contra, el pendent de disminució de freqüència del mode LO del tipus GaAs és menor que en les mostres tensionades. El creixement pseudomòrfic de capes fines dóna lloc a estrès biaxial en les capes, degut a la diferència de paràmetres

de xarxa entre el material d'aquesta i el del substracte. Hem observat que la diferència de pendents en la freqüència del mode LO tipus GaAs en les nostres mostres i les estressades d'altres autors, es pot explicar perfectament si suposem que les capes estressades pateixen estrès biaxial i que es compleix la llei de Vegard per al rang de composició en qüestió.

Per atra banda, el mode TO tipus GaAs no ha estat gaire estudiat prèviament, ja que en la configuració Raman de retrodispersió en incidència normal és prohibit. Per això, hem dut a terme experiments Raman en incidència oblíqüa, permetent així la presència dels modes TO i LO simultàniament. En el nostre estudi hem observat per primera vegada un lleuger desplaçament cap al blau del mode TO tipus GaAs en augmentar la concentració de N.

Donat que els desplaçaments en freqüència del mode TO tipus GaAs són molt lleugers, creiem que el desplaçament del corresponent mode LO no pot ser degut només a effectes de curt-abast (els quals afecten de la mateixa manera als dos modes). Per entendre millor l'origen d'aquests desplaçaments hem estudiat com varia la freqüència de plasma iònica associada al mode LO del tipus GaAs ($\Omega_{\mathrm{GaAs}} = (\omega_{\mathrm{LO}}^2 - \omega_{\mathrm{TO}}^2)^{1/2}$) en funció de la fracció de N. Segons la teoria electro-magnètica, aquesta freqüència depèn principalment de la quantitat d'oscil.ladors de la xarxa involucrats. Els nostres resultats indiquen que el nombre d'oscil.ladors Ga-As en l'aliatge no només es redueix per la substitució d'àtoms de As per àtoms de N, sinó també per altres efectes de llarg abast, com serien defectes intersticials o vacants promoguts pel N. D'aquest resultat també en podem concloure que el fort desplaçament del mode LO tipus GaAs és degut principalment a efectes de llarg abast.

Efecte de la orientació del substracte en capes de InGaAsN

En termes de fonons, quan s'afegeix In al GaAsN el mode LO tipus GaN es desplaça cap al vermell i apareixen dos modes addicionals a la regió del mode LVM de N, en concret a 430 i 488 cm^{-1}. Quan es duen a terme recuïts tèrmics, la intensitat d'aquests modes addicionals augmenta respecte la del LVM de N, fet que suggereix que el In modifica l'ambient local dels àtoms de N. És a dir, la presència de In tensiona els lligams NGa_4, els quals ssón responsables del mode LVM a 470 cm^{-1}. Per altra banda, mentre que l'origen del mode addicional a 488 cm^{-1} s'ha relacionat amb la configuració NGa_3In, encara no s'ha assignat el mode a 430 cm^{-1} a cap configuració concreta. Per tant, l'estudi d'aquests modes permeten avaluar els lligams entre les diferents espècies atòmiques i com és el seu voltant.

Tot i que la majoria d'estudis que s'ha publicat respecte l'aliatge de InGaAsN es refereix a mostres crescudes sobre substractes orientats segons la direcció (100), s'ha demostrat que créixer capes sobre plans d'índex majors ofereix moltes avantatges, com ara un augment del gruix crític, una millor incorporació de les impureses o fins i tot l'aparició d'efectes piezo-elèctrics. Per una banda, substractes orientats de diferent manera implica que la disstribució atòmica i els enllaços lliures de la superfície no siguin els mateixos, el qual pot afectar la incorporació d'impureses. Per exemple, àtoms grans com el In, s'incorporen millor en posicions amb enllaços lliures dobles, com els que disposa la superfície del GaAs que acaben amb Ga (anomenades cares B). Per contra, els àtoms petits de N prefereixen posicions amb enllaços lliures simples, com ara les cares acabades amb As (anomenades A). De fet, ja s'ha publicat algun treball on es parla de la millor incorporació de N al sistema GaAsN si la superfície del substracte és (111)A.

Sota aquest context, hem volgut estudiar mitançant l'espectroscòpia Raman, com afecta la orientació del substracte en la incorporació i ambient local del N i en la cristal.linitat de capes de InGaAsN. Amb aquesta finalitat hem analitzat mostres de InGaAsN amb un $\sim 20\%$ de In i $\sim 3\%$ de N, crescudes sobre substractes de GaAs orientats en les direccions (100) i (n11), on $n = 1, 3, 4, 5$.

L'espectre Raman del quaternari mostra els modes TO i LO del tipus GaAs molt intensos i els de tipus InAs de manera molt feble. Tot i la presència d'una banda TO activada pel desordre (DATO), la qualitat cristal.lina de les capes de InGaAsN no sembla estar afectada per l'orientació del substracte. Segons les orientacions de les capes, el mode TO no està pas prohibit i per això s'observa amb claredat. Tot i així, les regles de selecció en prediuen intensitats menors respecte les del mode LO. És a dir que el mode TO es troba lleugerament despolaritzat degut a camps de tensions molt forts al voltant dels àtoms de N. Aquesta despolarització, però, no es veu afectada per l'orientació del substracte.

Pel què respecta al desdoblament TO-LO del tipus GaAs, observem un comportament similar al de les capes de GaAsN de l'estudi anterior. En canvi, observem com els modes LVM pateixen canvis d'intensitat i amplada. Aquest fet és degut a petits canvis en la composició, la qual concorda amb mesures de HRXRD. Malgrat tot, la forma general de la regió dels modes LVM no canvia entre les diferents mostres, fet que indica que la orientació del substracte no afecta sustancialment l'ambient local dels àtoms de N i In.

Modes acoblats LO-plasmó en GaAsN altament dopat amb Se

L'aplicabilitat dels nitrurs diluïts encara està limitada per les baixes mobilitats que presenten les seves capes tipus *n*. Els estats localitzats de N tenen un paper molt important en les baixes mobilitats dels nitrurs diluïts, que poden arribar inferiors a 100 cm^2/Vs. De fet, l'origen d'aquestes mobilitats tan baixes s'associa principalment a dos fenòmens: un augment dràstic del ritme de dispersió dels electrons i un augment de la massa efectiva dels portadors. L'augment de la massa efectiva es deu a la forta interacció entre els estats extesos del cristall hoste i els estats electrònics localitzats de N. El model d'anti-creuament de bandes (*Band Anti-Crossing* o BAC) proposa una manera simple i analítica de tractar aquesta interacció entre estats electrònics. El model de BAC explica la dràstica reducció en funció de la fracció de N de l'estat E_-, que representa l'E_g fonamental, i la presència de l'estat energètic superior E_+. El model també proporciona expressions analítiques per la dispersió de les dues bandes resultants de la interacció ($E_+(k)$ i $E_-(k)$), les quals resulten ser altament no-parabòliques. La dispersió de la banda $E_-(k)$ que proposa el model de BAC prediu que la massa efectiva dels electrons lliures augmenta en presència del N. No només això, sinó que també prediu que la massa efectiva òptica (és a dir, la massa efectiva promig al voltant del nivell de Fermi) és més gran a mesura que el nivell de Fermi s'apropi a l'energia dels nivells localitzats de N.

La major part dels treball publicats per determinar la massa òptica dels nitrurs diluïts, es realitzen amb mostres amb nivells molt baixos de dopatge. Conseqüentment, la massa efectiva que avaluen es correspon a la massa effectiva al mínim de la banda $E_-(k)$, m^*_{e0}. Si es realitzéssin mesures òptiques sobre mostres amb diferents nivells de dopatge (és a dir, diferents posicions del nivell de Fermi), es podria determinar $m^*_e(k)$ i la pròpia banda $E_-(k)$. *Skierbiszewski et al.* mitjançant l'espectroscòpia de reflectivitat d'IR va confirmar les previsions del model de BAC respecte la dispersió de la banda $E_-(k)$ en mostres de InGaAsN. Per contra, *Masi et al.* han observat molt recentment mitjançant mesures de magneto-fotoluminiscència que el model de BAC subestima la m^*_{e0} del GaAsN per fraccions de N superiors al 0.1%. Fins avui no s'ha realitzat experiments per determinar la massa efectiva dels electrons més amunt del mínim de la banda de conducció.

Així doncs, en aquesta tesi hem estudiat mostres de GaAsN:Se amb un alt nivell de dopatge i diferents continguts de N, per mirar d'obtenir informació sobre la massa effectiva i la mobilitat dels portadors en funció del N mitjançant l'espectroscòpia Raman.

L'anàlisi de masses efectives a través de l'espectroscòpia Raman és a partir dels

què s'anomenen modes acoblats fonó-plasmó. Els portadors lliures presents en un semiconductor també dónen lloc a fenòmens de dispersió ineslàstica de la llum. En particular, les oscil.lacions col.lectives dels portadors lliures (plasmons) interaccionen amb el camp elèctric associat als fonons longitudinals òptics (LO) dels materials polars. Aquesta interacció dóna lloc als modes acoblats LO-plasmó, o LOPCs. La freqüència d'aquests modes depèn típicament de la densitat de càrrega en el material. Quan els modes LOPC no estan sobreesmorteïts existeixen dos tipus de modes, els L^- i L^+. Per a densitats de càrrega altes, el mode L^- és més aviat de tipus fonó i tendeix a la freqüència del mode TO del material, que no deixa de ser el mode LO apantallat per la càrrega lliure. Per contra, en aquest règim de dopatge la branca L^+ tendeix assimptòticament a la freqüència dels modes de plasma purs i prèn caràcter plasmònic.

Tanmateix, els espectres Raman de les mostres de GaAsN:Se no presenten signes de l'existència de modes L^- i L^+, sinó que apareix una única estructura addicional entre les freqüències dels modes TO i LO. La freqüència d'aquest pic varia lleugerament de mostra a mostra i, en una primera instància, suggerim que es correspon al mode acoblat sobreesmorteït. Quan els modes LOPC estan sobreesmorteïts, existeix un únic mode la freqüència del qual es belluga entre les del LO i del TO. En el nostre estudi hem demostrat com a partir del model hidrodinàmic per descriure els portadors lliures, les baixes mobilitats de les capes de GaAsN:Se dónen lloc al sobreesmorteïment dels modes acoblats.

Tot i que el mode LOPC sobreesmorteït no és tant sensible a variacions de la densitat de càrrega com n'és el mode L^+, en aquest estudi demostrem que, tot i així, aquest pot proporcionar molta informació sobre els portadors (massa efectiva, ritme de dispersió i mobilitat).

Per tal d'extreure informació dels modes acoblats, hem ajustat les corbes Raman segons el model de fluctuació-dissipació de Hon i Faust, on la contribució del gas d'electrons a la funció dielèctrica total ha estat calculada mitjançant el model hidrodinàmic.

Hem ajustat els espectres Raman prenent les densitats de càrrega obtingudes per Hall i hem deixat com a paràmetres lliures la massa efectiva òptica i el què s'anomena dàmping electrònic, el qual està directament relacionat amb el temps mig de dispersió de les càrregues lliures (τ_s). Els valors obtinguts de τ_s mostren com la presència de tan sols un 0.1% de N disminueix considerablement la vida mitja de les càrregues lliures per efectes de dispersió. A partir d'aquests valors hem calculat la mobilitat dels electrons lliures segons la relació $\mu_e^{\text{Raman}} = e\tau_s/m_e^*$. Els valors resultants mostren

un gran acord amb els obtinguts a través de mesures Hall, fet que determina que la mobilitat en els nitrurs diluïts es veu molt afectada per efectes de dispersió.

Per altra banda, els valors de m_e^* són força similars als obtinguts per *Masia et al.* a partir de mesures de magneto-fotoluminiscència en mostres sense dopar. Hem calculat els valors de m_e^* esperats pel model de BAC per a aquests alts nivells de dopatge i els hem comparat amb els nostres. Hem observat que el model de BAC prediu valors de massa effectiva majors als obtinguts per Raman, ja que el nivell de Fermi és força proper al nivell localitzat de N i en aquesta regió la banda $E_-(k)$ es preveu força plana. L'anàlisi dels espectres Raman determina, dins el grau d'incertesa dels ajustos, una no-parabolicitat menys accentuada de la banda $E_-(k)$, respecte la prevista pel model de BAC.

En conseqüència, aquest estudi demostra la utilitat de l'espectroscòpia Raman com a tècnica no destructiva per a determinar la mobilitat, massa efectiva i efectes de dispersió dels portadors lliures, fins i tot en mostres de baixa mobilitat. A més a més, hem vist que l'anàlisi de modes LOPC ens pot ajudar a avaluar la curvatura de la banda de conducció per vectors d'ona $\neq 0$.

Conclusions

Dins els estudis realitzats per aquesta tesi hem vist com les regles de selecció Raman juntament amb un anàlisi de les amplades dels pics, ens dóna informació sobre la qualitat cristal.lina de capes primes i cristalls volúmics. A través de l'estudi de modes locals de vibració, hem avaluat el grau d'impureses que s'incorporen a la xarxa en materials dopats i com es veu afectat l'ambient que les envolta en canviar certes condicions del procés de creixement o dopatge. També hem tractat amb la interacció entre fonons i càrrega lliure en semiconductors dopats de baixa mobilitat, de la qual n'hem extret informació tan rellevant com la massa efectiva dels portadors i la seva mobilitat.